# A Study of Heat Transport Processes in the Wake of a Stationary and Oscillating Circular Cylinder Using Digital Particle Image Velocimetry / Thermometry

Thesis by

Han G. Park

In Partial Fulfillment of

the Requirements for the Degree of

Doctor of Philosophy

California Institute of Technology

Pasadena, California

1998

(Submitted May 12, 1998)

# Acknowledgements

I would like to express my gratitude to everyone who assisted in this study. Foremost, I would like to thank my advisor, Prof. Mory Gharib, who gave me the opportunity, support, and freedom that I needed to conduct this research. I would like to thank Dr. Dana Dabiri for transferring all his knowledge about DPIV/T to me and helping to find the data acquisition system. I would like to thank Prof. George Karniadakis and Dr. Xia Ma for their computational results for comparison.

I would like to thank Profs. Tony Leonard, Melany Hunt, Dale Pullin, and Joe Shepherd for graciously being on my thesis committee.

I would like to thank Steve Haase and Ken Chadwick for designing much of the hardware used for this experiment. I would also like to thank Frederic Taugwalder for his assistance on computer matters. I am especially indebted to Alan Goudy who helped build and test all the hardware and instrumentation.

I would like to thank all of my colleagues, Brad Dooley, Michael Ol, Patrice Maheo, and Doug Shiels, who made life at GALCIT both interesting and enjoyable. I would also like to thank David Jeon for all his late night help in running the experiments and Jerry Shan for his friendship.

Finally, this work could never have been completed without the unselfish help of Dr. Flavio Noca. I would like to thank him for the countless hours of discussion about fluid mechanics and his sincere interest in my research. He has been both a trusted colleague and mentor to me during my stay at GALCIT.

This research has been supported by NSF Grant CTS-9418973.

This work is dedicated to my parents
for their constant (ᄂᆞᆫ한결ᄀᆞᆺᄒᆞᆫ) support and love.

# Abstract

An experimental investigation is carried out on the processes of heat transfer associated with a heated circular cylinder in crossflow. Two studies are made. First, a study of the transport of heat in the near wake ($x/D<5$) of a stationary and transversely oscillated cylinder is made at Reynolds number of 610. Second, a study is made of the surface heat transfer from a cylinder which is undergoing forced oscillations in the transverse direction.

The studies are made using the technique of Digital Particle Image Velocimetry/Thermometry (DPIV/T) which allows simultaneous measurements of both the velocity and temperature fields of the flow. The temperature is measured by seeding the flow with thermochromic liquid crystal (TLC) particles which change their reflected wavelength as function of temperature. By calibrating reflected wavelength versus temperature using a color multi-CCD camera, the local temperature of the flow may be deduced. The velocity is measured by using the same particles as Lagrangian flow tracers, and local velocity or displacement of the flow may be measured by cross-correlating two sequential images. A limitation of DPIV/T, which is the low level of precision (5% - 20% of the temperature span of TLC particles), may be overcome by a process in which the temperature at a given location is computed by averaging the temperatures of the particles within a specified sampling window. This process increases the precision to 2% - 10%.

In the study of the heat transport in the near wake, the velocity and temperature measurements obtained from DPIV/T are decomposed into their mean, coherent, and incoherent components using the triple decomposition. It is found that the heat from the cylinder is transported down the wake mostly by the mean heat flux and is laterally transported out of the wake by the coherent and the incoherent heat fluxes. In examining the direction of the turbulent heat flux vectors, the vectors are found not to be co-linear with the gradient of mean temperature. This misalignment implies that the gradient transport models are inappropriate for modeling the turbulent heat transport in the near wake of a circular cylinder. In examining the production of

turbulence, it is found that that kinetic energy fluctuations are produced in the saddle regions (regions where the fluid is being stretched in one direction and compressed in another) while the temperature fluctuations are produced at the edges of center regions (regions where the fluid is rotating), i.e., the edges of the vortex cores.

From the study of the heat convection from a cylinder as function of forced oscillation frequency ($0<St_c<1$) and amplitudes (A/D=0.1, 0.2), it is found that besides the previously known increase near the natural vortex shedding frequency, there also exists a large increase in the heat transfer at approximately three times this frequency for A/D=0.1. For A/D=0.2, there exist large increases at roughly two and three times the natural vortex shedding frequency. From a DPIV/T study, it is found that the wake pattern becomes synchronized with the mechanical oscillation of the cylinder at these frequencies where the heat transfer increases significantly. At the frequencies corresponding to roughly two and three times the unforced vortex shedding frequency, the wake pattern may become synchronized by processes of period doubling and tripling with respect to the cylinder oscillation period, respectively. The increase in the heat transfer rate is found to correlate with the distance at which vortices roll-up behind the cylinder. The distance is observed to decrease sharply at the frequencies corresponding to a sharp increase in the heat transfer. Therefore, the near wake is found to play a critical role in the heat transfer from the surface of a circular cylinder, and the cause of the increase in heat transfer is believed to the removal of the stagnant and low heat convecting fluid at the base of the cylinder during the roll-up of the vortices.

# Table of Content

# List of Figures

# List of Tables

# List of Symbols

*English Alphabet*

| | |
|---|---|
| A | amplitude of oscillation |
| B | blue intensity |
| Bi | Biot number ($\frac{hD}{k}$) |
| b | normalized blue intensity |
| $b_\lambda$ | transmission of blue |
| $C_p$ | heat capacity |
| D | diameter of cylinder |
| f | frequency |
| $f_c$ | frequency of cylinder oscillation |
| G | green intensity |
| Gr | Grashof number ($\frac{g\beta(T_c - T_\infty)D^3}{\nu^2}$) |
| g | normalized green intensity |
| $g$ | acceleration of gravity |
| $g_\lambda$ | transmission of green |
| H | hue |
| h | convection heat transfer coefficient |
| I | intensity |
| k | thermal conductivity |
| $k_{CO}$ | thermal conductivity of outer shell of cylinder |
| $k_{CI}$ | thermal conductivity of heat coil inside cylinder |
| L | span of cylinder |
| $\dot{m}$ | mass flux |
| Nu | Nusselt number ($\frac{hD}{k}$) |
| $Nu_o$ | Nusselt number of stationary cylinder |

| | |
|---|---|
| $\bar{n}$ | surface normal vector |
| P | pressure |
| $P$ | first invariant of velocity gradient tensor |
| $P_\lambda$ | spectrum of light source |
| $P_k$ | production of kinetic energy fluctuations |
| Pr | Prandtl number $(\frac{\nu}{\alpha})$ |
| $Pr_t$ | turbulent Prandtl number |
| $p$ | helical pitch of liquid crystal |
| $P_T$ | production of temperature fluctuations |
| $Q$ | second invariant of velocity gradient tensor |
| $\dot{Q}$ | heat input |
| $\dot{q}$ | heat input per unit mass |
| R | red intensity |
| $R$ | third invariant of velocity gradient tensor |
| $R_1$ | inner radius of heating coil inside cylinder |
| $R_2$ | outer radius of heating coil inside cylinder |
| $R_2$ | outer radius of cylinder |
| $R_\lambda$ | reflectance of surface |
| Re | Reynolds number $(\frac{U_\infty D}{\nu})$ |
| r | normalized red intensity |
| $\hat{r}$ | orientation vector of liquid crystal |
| $r_\lambda$ | transmission of red |
| S | saturation |
| St | Strouhal frequency $(\frac{fD}{U_\infty})$ |
| $St_c$ | Strouhal frequency of cylinder $(\frac{f_c D}{U_\infty})$ |
| T | temperature |

| | |
|---|---|
| $T_\infty$ | freestream temperature |
| $T_c$ | surface temperature of cylinder |
| $T_{tc}$ | temperature of thermocouple inside cylinder |
| $t$ | time |
| $U_\infty$ | freestream velocity |
| $\vec{u}$ | velocity vector |
| $u_i$ | i'th velocity component |
| $V_e$ | effective velocity of cylinder |
| $V_v$ | RMS of transverse velocity of oscillating cylinder |
| $v_1$ | first hue – saturation vector |
| $v_2$ | second hue – saturation vector |

*Greek Alphabet*

| | |
|---|---|
| $\alpha$ | heat diffusion coefficient $(\frac{k}{\rho C_p})$ |
| $\alpha_t$ | turbulent thermal diffusivity |
| $\beta$ | coefficient of thermal expansion |
| $\delta_T$ | thickness of temperature profile |
| $\delta_U$ | thickness of velocity profile |
| $\Gamma$ | circulation |
| $\lambda$ | wavelength |
| $\lambda_i$ | i'th eigenvalue of velocity gradient tensor |
| $\lambda_M$ | Taylor microscale |
| $\lambda_T$ | temperature microscale |
| $\rho$ | density |
| $\nu$ | kinematic viscosity |
| $\nu_t$ | turbulent eddy viscosity |
| $\omega$ | vorticity |

# Chapter 1

# Introduction

## 1.1 Introduction

The transport of heat associated with bluff bodies is of great importance in engineering. From heat exchangers to flame holders, heat transport processes associated with bluff bodies are used to cool, heat, and mix fluids in various applications. The transport of heat can be divided into two distinct processes. The first is the transfer of heat from the surface of a bluff body to the surrounding fluid. This is the process which cools or heats the body and is the most important consideration in the design of a device such as a cooling system for an electronic component or a heat engine. The second process is the convective transport of heat in the wake of a bluff body. This is the process by which the fluid is mixed downstream of the body and is the most important consideration in the design of a device such as a flame holder or a mixer.

This thesis presents results from an experimental study of both heat transport processes associated with a bluff body. The quintessential bluff body, the circular cylinder, is chosen for this study. Using the technique of Digital Particle Image Velocimetry and Thermometry (DPIV/T), the heat transport processes in the near wake of the circular cylinder are studied. Additionally, the variation of the heat transfer rate from the surface when the cylinder is oscillated transversely to the oncoming fluid is studied.

## 1.2 Reviews

### 1.2.1 Wake of the Circular Cylinder

Despite its simple shape, a circular cylinder generates a wake which is both varied and complex. The most essential parameter which characterizes the wake of a

smooth circular cylinder is the Reynolds number, $Re = U_\infty D/\nu$, where $U_\infty$ is the freestream velocity, D is the diameter, and $\nu$ is the kinematic viscosity. At less than $Re \approx 5$, the wake is steady and the boundary remains attached. Above $Re \approx 5$, the boundary layers on top and bottom separate (Taneda, 1956) which gives rise to a pair of steady symmetric vortices in the wake. The vortices become elongated as the Reynolds number is increased until the symmetry is broken at $Re \approx 40$, where the wake becomes unsteady, and the Karman vortices appear downstream. Above $Re \approx 90$, the wake is characterized by alternate shedding of vortices at the top and bottom of the cylinder with opposite signs of vorticity, a process termed "vortex shedding." While unsteady, the flow remains laminar and two-dimensional until $Re \approx 180$ (Williamson, 1988), above which the wake becomes three-dimensional and "turbulent." At above $Re \approx 1000$, the separated shear layers, which roll-up to form the vortices, become turbulent, and the wake progressively grows more turbulent. Finally, above $Re \approx 200{,}000$, or the "critical" Reynolds number, the boundary layer on the cylinder surface becomes turbulent, and the wake narrows to produce a large reduction in drag. A review of this Reynolds number region is given by Bearman (1969). Beyond this Reynolds number, little is known about the structure of the wake of a circular cylinder.

Thus by varying the Reynolds number, a rich set of flow patterns is observed, but even more wake patterns are observed by forced oscillation of the cylinder. Under forced transverse oscillations, various vortex shedding patterns are possible by varying the oscillation frequency and amplitude. An extensive review of the wake patterns are given by Williamson and Roshko (1988), and some possible patterns are shown in Fig. 1.1(a,b). At oscillation frequencies below the vortex shedding frequency of a stationary cylinder, the vortices may be shed and paired in various different ways as shown in Fig. 1.1(b). At oscillation frequencies above the vortex shedding frequency of a stationary cylinder, the cylinder may shed small vortices which then coalesce into large vortices as shown in Fig. 1.1(b). For small amplitudes ($A/D<0.5$), the large vortices may recover to the Karman vortex street farther downstream. The wake patterns at high oscillation frequencies have been studied by Ongoren and Rockwell (1988) who reported that the large vortices, which form in the

near wake (x/D<5) by the coalescence of smaller vortices, shed at or near the vortex shedding frequency of a stationary cylinder. At the super-harmonic frequencies, i.e., multiples of the vortex shedding frequency of a stationary cylinder, they observed organized vortex shedding patterns where a pair of small vortices are shed for each cycle of cylinder oscillation and coalesce with nearby vortices to form the large vortices. Their model of the coalescence of the small vortices is shown in Fig. 1.2.

### 1.2.2 Heat/Mass Transport in the Wake

In light of the previous sections, the most prominent features of the wake behind a circular cylinder are the vortices, and it is these structures which govern the transport of heat/mass in the wake. The process of entrainment of the freestream fluid by the motion of the vortices is the principal method of exchange of heat/mass in the wake. Within the wake, the vortices transport heat/mass out of themselves either through molecular diffusion and turbulent heat/mass exchange with the entrained fluid. Because of the significant role which vortices play in the transport of heat/mass in the wake of circular cylinder, recent studies have employed phase averaging techniques to study the net contribution of the coherent and random, i.e., "turbulent," motions of the vortices to the net heat/mass transport out of the wake.

Cantwell and Coles (1983) studied the mass entrainment characteristics of the vortices in the near wake (x/D<10) of a circular cylinder at Reynolds number of 140,000, and their conclusion was that the mass exchange in the wake is accomplished by the entrainment of fluid from adjacent saddle regions (regions where the fluid is being stretched in one direction and compressed in another) into the wake by the vortices. The entrainment of the fluid into the vortex itself was found to be of different rates on different sides, the highest being on the side of the wake opposite to that from which the vortex was shed. A more recent study by Matsumura and Antonia (1993) focused on the heat transfer from the vortices in the intermediate wake (10<x/D<40) of a circular cylinder at Reynolds number 5,830. They concluded that the coherent motion of the vortices transport heat in the lateral direction more effectively than momentum, especially for 10<x/D<20. The lateral coherent heat flux, i.e., contribution due to the coherent motion of the vortices, was found to

contribute more to the overall lateral heat flux than the coherent momentum flux to the overall lateral momentum flux. In other words, the transport of heat out of the wake is mainly accomplished by the coherent motion of the vortices, while the transport of momentum out of the wake is mainly accomplished by the incoherent motions or "turbulence."

### 1.2.3 Modeling of Turbulent Heat Transport in the Wake

In solving practical problems of turbulent flows such as the wake of a circular cylinder, one encounters a closure problem where there are more unknowns than equations. Therefore, to "close" the problem, a model must be made of the turbulent transport processes. One of the most widely used model in computing turbulent flows is the gradient transport model (Boussinesq model), where the turbulent transport is assumed to occur in the direction of the gradient of the mean (or spatially filtered) value of the quantity being transported. However, it has been long argued that the classical gradient transport model does not correspond to the actual turbulent transport in a turbulent flow. Tennekes and Lumley (1972) have argued that because the size of the largest eddies in a turbulent flow is of the local length scale, the gradient transport model cannot be justified. It has been argued by Roshko (1992), as well as Tennekes and Lumley (1972), that the mixing length theory and eddy viscosity theories, which are gradient transport based theories, work well in the far fields of jets, shear layers, and wakes because there is just one set of length and velocity scales in these problems, not because they represent the physics of turbulence. Recently, studies from Direct Numerical Simulations (DNS) (Fureby et al., 1997) and detailed experiments (Franke et al., 1989, Liu et al., 1994) have demonstrated that gradient transport models such as the k-ε model (Launder and Spalding, 1974) used in Reynolds Averaged Navier-Stokes (RANS), unsteady RANS, or the eddy viscosity model (Smagorinsky, 1963) in Large Eddy Simulations (LES) do not correspond to the actual turbulent transport in the flow. Karniadakis and Brown (1995) have shown that transport of vorticity is not well modeled by a gradient transport model because of three-dimensional stretching and tilting of the filaments of vorticity. For shear layers, Dimotakis (1991) has stated that the turbulent mixing

process of scalars is not well described by the gradient transport models. With a mountain of data against the validity of the gradient transport models for turbulent transport of various quantities, the gradient transport model commonly used in transport of heat has become suspect, and it may be prudent to test the model for an actual wake of a heated circular cylinder.

### 1.2.4 Effect of Transverse Oscillation on Surface Heat Transfer

It is intuitive to believe that oscillating a cylinder in a fluid will increase its heat transfer from its surface. Martinelli and Boelter (1938) measured that the heat transfer from the surface of a cylinder is increased up to 500 percent compared to that of free convection by oscillating it in water. Surprisingly, for the case of forced convection over a circular cylinder ($5{,}000<Re<25{,}000$), Sreenivasan and Ramachandran (1961) found no appreciable increase in heat transfer for large forced transverse oscillation amplitudes of $A/D=0.43$ and 3.7 as compared to that of a stationary cylinder. The oscillation frequencies they concentrated on were well below the vortex shedding frequency of a stationary cylinder. A similar study by Kezios and Prasanna (1966) ($5{,}500<Re<14{,}000$) found that the surface heat transfer increased by approximately 20%, even for small amplitudes ($0.02<A/D<0.075$), if the cylinder was forced to oscillate at a frequency corresponding to the vortex shedding frequency of a stationary cylinder. They noted that the increase in heat transfer could not be accounted for by the relative increase in the freestream velocity due to the transverse motion of the cylinder. Saxena and Laird (1978) found that a large increase (40% to 60%) in heat transfer occurs in water as the forced oscillation frequency approached the vortex shedding frequency of a stationary cylinder for large oscillation amplitudes ($0.89<A/D<1.99$) at $Re=3{,}500$. The maximum frequency reached was 0.8 times the shedding frequency. More recently, Karanth et al. (1994) conducted a computational study at $Re=200$ where increases of 1.2% and 3% in the surface heat transfer were observed for forced transverse oscillations amplitudes of $A/D=0.25$ and 0.5, respectively. Cheng and Hong (1997), in another computational study at $Re=200$, observed that the heat transfer increased 1.6%, 3.9%, 7.5%, and 12.5% for $A/D=0.14$, 0.3, 0.5, and 0.7, respectively. Following their computational

study, Cheng et al. (1997) measured increases in the surface heat transfer from 3% to 30% for A/D=0.138, 0.314, 0.628 at Re=200, 500, and 1,000 when the cylinder was forced to oscillate at the vortex shedding frequency of a stationary cylinder.

The authors of the previous studies have cited the phenomenon of "lock-in" or the synchronization of the vortex shedding with the mechanical oscillation of the cylinder as the reason for the increase in the surface heat transfer. When the vortex shedding becomes synchronized with the mechanical oscillation, a pair of vortices is always shed for each cycle of cylinder oscillation. However, it has never been fully explained why this synchronization leads to higher surface heat transfer. In addition, Cheng et al. (1997) noticed that past this synchronization frequency, the heat transfer continued to increase for large amplitudes (A/D=0.626), decreased then increased for medium amplitudes (A/D=0.314), or returned to close to the value of the stationary cylinder for small amplitudes (A/D=0.138), as shown in Fig. 1.3. The study stopped at 1.5 times the synchronization frequency, and the increase in the heat transfer for larger oscillation amplitudes at higher frequencies was attributed to the "turbulence" effect. The "turbulence" effect was left unclear and is presumed to be connected to some unsteadiness in the wake or boundary layer of the cylinder. Thus the issue of why synchronization of the vortex shedding with the mechanical oscillation increases the heat transfer from the surface of a circular cylinder, as well as the "turbulence" effect, remains unresolved.

### 1.2.5 DPIV/T

To study the unsteady heat transport process in the wake of a heated body, an experimental method is needed which can measure simultaneously the velocity and temperature of the flow. The traditional method is a combination probe of a hot-wire and a cold-wire. The velocity of the fluid is obtained from a hot-wire by measurement of the rate of heat transfer from a heated wire, while the temperature is obtained from a cold-wire by measurement of the resistance of a wire which changes as function of temperature. In a cold-wire setup, as opposed to a hot-wire setup, only a small current, just enough to measure the resistance, is passed through the wire, and the temperature is deduced from the thermoresistive characteristics of the wire. This

is the technique employed by Matsumura and Antonia (1993) to study the heat transfer in the intermediate wake of a circular cylinder. While the combination probe has excellent sensitivity and time-response, it is intrusive to the flow and cannot be used near a body without resorting to complicated "flying" setup.

An alternative method may be an optical technique called DPIV/T (Digital Particle Image Velocimetry/Thermometry). This method is based on seeding the flow with thermochromic liquid crystal (TLC) particles which change their reflected wavelength, i.e., color, as function of temperature. By taking a sequence of digital color images, the velocity and temperature may be extracted by measuring the displacement and the color of these particles. This technique has already been employed by Dabiri and Gharib (1991) to study the temperature distribution of a heated laminar vortex ring. The main advantage of this method is that the velocity and temperature of the whole field may be measured instantaneously rather than of a single point as with a combination probe of a hot-wire and a cold-wire. The shortcoming of DPIV/T at this stage of development is its poor precision in the temperature measurement which reduces its effectiveness in measuring turbulent temperature fluctuations. Therefore, the issue of temperature precision in DPIV/T must be addressed before accurate turbulent measurements are to be made using this technique.

## 1.3 Objectives

The objective of this thesis is to study experimentally the processes of heat transport related to circular cylinders. To achieve this objective, the technique of DPIV/T needs to be improved and made suitable for the measurement of turbulent flows. Having achieved this, the questions to be addressed are:

Heat Transport in the Wake of Circular Cylinder

1. How is the heat transported into, out of, and within the near wake of a circular cylinder?
2. Where are the turbulent temperature fluctuations generated?
3. How valid is the gradient transport model in predicting the turbulent transport of heat in the near wake of a circular cylinder?

Surface Heat Transfer for Transversely Forced Oscillating Cylinder

1. Why does the surface heat transfer increase when the cylinder is forced to oscillate at the vortex shedding synchronization frequency?
2. How does the surface heat transfer vary as the frequency is increased beyond the vortex shedding frequency of a stationary cylinder? What is the "turbulence" effect as described by Chen et al. (1997)?

### 1.4 Contributions

Some of the contributions of this research are:

1. Development, characterization, and use of DPIV/T for turbulent flows.
2. Detailed look at the process of heat transport in the near wake of a circular cylinder.
3. Examination of the validity of the gradient transport model in modeling the transport of heat in a turbulent wake.
4. Map of surface heat transfer from a transversely forced oscillating circular cylinder for a range of frequencies, including frequencies above the vortex shedding frequency of a stationary cylinder.
5. A link between the process of roll-up of the vortices and the surface heat transfer for a transversely forced oscillating circular cylinder.

### 1.5 Organization of Thesis

The present chapter has reviewed the heat transport processes associated with a circular cylinder, the current state of DPIV/T, and the objective of the thesis. In Chapter 2, the various methods of calibrating thermochromic liquid crystals for temperature measurements are reviewed, and an enhanced DPIT/V technique to measure temperatures more precisely is presented. In Chapter 3, the experimental setup is described. In Chapter 4, the results from a study of the heat transport in the wake of a stationary and transversely oscillating cylinder are presented, as well as a test of the gradient transport model. In Chapter 5, the experimental results from a study measuring the surface heat transfer as function of frequency and amplitude for a forced transverse oscillating cylinder are presented. In Chapter 6, the role which the near wake flow field plays on determining the surface heat transfer from a forced transverse oscillating cylinder is examined using DPIV/T. Finally, in Chapter 7, the conclusions from the study are presented along with some future recommendations.

# Chapter 2

# Digital Particle Image Velocimetry / Thermometry

## 2.1 Introduction

Digital Particle Image Velocimetry/Thermometry (DPIV/T) is a set of experimental techniques to measure simultaneously both velocity and temperature fields of a flow. The temperature is measured by seeding the flow with thermochromic liquid crystal (TLC) particles which change their reflected wavelength as function of temperature. By calibrating reflected wavelength versus temperature using a color multi-CCD camera, the local temperature of the flow may be deduced. The velocity is measured by using the same particles as Lagrangian flow tracers. Using standard DPIV, the local velocity or displacement of the flow can be measured by cross-correlating two sequential images.

In this chapter, the temperature calibration procedure for TLC particles is presented. Since various calibration methods are available, the uncertainties and benefits of each method are carefully studied and discussed. Finally, the implementation of DPIV/T in a water tunnel facility used for the measurement of heat transport in the wake of a heat circular cylinder is presented.

## 2.2 Thermochromic Liquid Crystals

A complete description of the thermochromic liquid crystals (TLC) and their behavior can be found in Parsley (1991). To summarize, TLC are made up of long-chain organic molecules which can exist in either the smectic or the nematic phase. In the smectic phase, all the molecules are layered with long axes oriented (or oriented nearly) in one particular direction, $\hat{r}$, as shown in Fig. 2.1(a). In the nematic phase, the molecules are not layered, but the long axes of nearby molecules are still oriented nearly in one particular direction as shown in Fig. 2.1(b). If the molecules in the nematic phase are also chiral, i.e., the molecules are not symmetric about their

long axis, the molecules become rotated slightly with respect to adjacent molecules forming a helical structure as shown in Fig. 2.2. This helical structure defines a pitch, $p$, which is the distance over which $\hat{r}$ rotates 360 degrees.

A light which hits this layer of TLC is both transmitted and reflected if its wavelength matches the pitch, $p$, as shown in Fig. 2.3. The light which is circularly polarized with the same hand sign as the helix is transmitted, while the light with the other hand sign is reflected. All other wavelengths (in the visual range) are transmitted. Therefore, when white light is shone on a chiral nematic TLC, a light of only one particular wavelength is reflected. It is this property, along with the property that the pitch of the TLC changes as function of temperature, which allows the TLC to be used to measure temperature by observing its reflected wavelength. The pitch typically changes inversely with temperature, hence, a sequence of colors from red, green, to blue is observed as the temperature is increased.

The TLC come in two packaged forms, raw mixtures and micro-encapsulated particles. In the micro-encapsulated form, the TLC are sealed in polymer shells to form discrete particles. The size of the particles is controlled during manufacture and can range from 1 micrometer to nearly a millimeter. The advantage of micro-encapsulation is that the TLC is protected from external contamination such as water. Thus micro-encapsulated TLC particles have much longer life than unprotected raw TLC particles which are made by dicing raw TLC mixtures. The disadvantage of micro-encapsulation is that the light must pass through a polymer shell which may distort the color and produce color variations from particle to particle. While raw TLC particles may have potential for better color consistency, the problems of contamination, degradation, and coalescence of particles are found to be too large to overcome, and only micro-encapsulated TLC particles are used for the studies in water. As a good compromise, a custom batch of micro-encapsulated TLC particles, which are made with very thin polymer shells to maximize consistency of reflected colors, are used for this DPIV/T study.

## 2.3 Calibration of Thermochromic Liquid Crystals

To measure temperature with the TLC, a calibration must be made of the reflected wavelength as a function of temperature. One possible method is to use an imaging spectrometer to measure the reflected light spectrum at every picture element. Unfortunately, imaging spectrometers are extremely expensive, are difficult to build, and require massive storage devices. The more sensible method is to use a camera with a limited number of spectral filters and infer the reflected wavelength by measuring the projections onto the spectral filters. The transmission characteristics of the spectral filters, therefore, form a set of basis vectors for a color space. For standard NTSC color cameras, three basis vectors, i.e., filters, whose transmission curves are given by $r_\lambda$, $g_\lambda$, and $b_\lambda$ are used as shown in Fig. 2.4. The magnitude of the projections onto these basis vectors, R, G, and B, are given by:

$$\begin{aligned} R &= \int_0^\infty R_\lambda P_\lambda r_\lambda d\lambda, \\ G &= \int_0^\infty R_\lambda P_\lambda g_\lambda d\lambda, \\ B &= \int_0^\infty R_\lambda P_\lambda b_\lambda d\lambda, \end{aligned} \tag{2.1}$$

where $R_\lambda$ is the spectral reflectance of an object, $P_\lambda$ is the spectral power distribution of the light source, and $\lambda$ is the wavelength. It is more convenient to work with values of R, G, and B which are normalized, where:

$$\begin{aligned} r &= \frac{R}{R+G+B} \\ g &= \frac{G}{R+G+B}. \\ b &= \frac{B}{R+G+B} \end{aligned} \tag{2.2}$$

For a monochromic reflecting object, the set of values of r, g, and b is unique and is simply the set of values of $r_\lambda$, $g_\lambda$, and $b_\lambda$ at the given wavelength. If the reflected wavelength from the TLC is monochromic or nearly so, a simple look-up table is sufficient to deduce the wavelength and hence the temperature. Unfortunately, the

reflected wavelength of the TLC is not perfectly monochromic as expected from theory given in Section 2.2. Instead, there is a dominant wavelength and a distribution spread about this wavelength. If the spread is large and/or the reflected light is contaminated by other wavelengths, there is no guarantee that the set of r, g, and b is unique. This is the drawback of having limited set of filters instead of a large set of filters as in an imaging spectrometer. Fortunately, in most cases the set of r, g, and b of the reflect light from the TLC is unique as function of temperature, since there exists a dominant wavelength. If we assume that the dominant wavelength is a unique function of temperature, then the set of r, g, and b is also a unique function of temperature.

Having a unique function for the set of r, g, and b for a given temperature, it is then possible to construct a temperature calibration curve. The most straightforward calibration may be the curves of r, g, and b (or simply r and g, since $b = 1 - r - g$) as function of temperature, i.e., $T = f(r,g,b)$. A typical calibration curve of r, g, and b is plotted in Fig. 2.5. It is observed that the set of values of r, g, and b is unique as function of temperature. This calibration method was used by Kimura et al. (1993). A difficulty of this method is that a fit to a function of three input variables (r, g, and b) and one output variable (temperature) must be found. It is difficult to find an optimal-fit function using simple polynomial expansions, and Kimura et al. (1993) trained a neural-network to find this optimal-fit function. Unfortunately, because of non-uniformity during the manufacture of the TLC, there exist variations in the reflected wavelength from particle to particle, even at the same temperature. This scatter in the values of r, g, and b at a given temperature can cause unpredictable behavior in the output temperature from either a trained neural-network or a polynomial curve-fit. This is because the training or the curve-fit is made with a restricted set of input variables, and any values outside the set can produce somewhat unpredictable results. Nevertheless, a satisfactory calibration can be made using this method.

Another method of calibration is to create a temperature function of a single input variable which is created from some combination of values of r, g, and b, i.e., $T = f(g(r,g,b))$. The advantage of reducing the input to a single variable is that the

calibration function can be more robust and simpler to evaluate. It is much easier to fit optimally a function of one variable with either polynomials or a neural-network, and if the function is chosen correctly, the scatter in the values of r, g, and b is unlikely to generate unpredictable behavior of the output temperature. The disadvantage of this method is that it may be difficult to find an input variable from a combination of r, g, and b which uniquely spans the temperature range of the TLC. Finding an appropriate combination is a trial and error process. It is from the author's experience that b, (b – r), and (b – r)/(1 - g) are good input variables which can span uniquely almost the full temperature range of the TLC. The input variable (b – r) generated from r, g, and b curves of Fig. 2.5 is shown in Fig. 2.6. It is observed that (b – r) is monotonic and can uniquely span the temperature range.

The most popular method of calibration using a single input variable has been the use of the hue variable (Dabiri and Gharib, 1991; Camci et al., 1992; Behle et al., 1996; Hay and Hollingsworth, 1996). The hue variable, H, comes from transforming R G B color space into H S I color space, or Hue, Saturation, and Intensity, respectively. One possible transformation from R G B to H S I space is given by:

$$\begin{bmatrix} v_1 \\ v_2 \\ I \end{bmatrix} = \begin{bmatrix} 2/\sqrt{6} & -1/\sqrt{6} & -1/\sqrt{6} \\ 0 & 1/\sqrt{6} & -1/\sqrt{6} \\ 1/3 & 1/3 & 1/3 \end{bmatrix} \begin{bmatrix} R \\ G \\ B \end{bmatrix}, \tag{2.3}$$

$$H = \tan^{-1}(v_1 / v_2), \tag{2.4}$$

$$S = \sqrt{v_1^2 + v_2^2}\,. \tag{2.5}$$

The H S I color space relative to the R G B color space is shown in Fig. 2.7. The intensity variable, I, is the measure of the brightness of the light. The saturation, S, is the measure of the purity of the color. If the R, G, and B values lie close to the intensity vector, the light has low saturation or is nearly colorless since equal parts of R, G, and B is defined to be white. Away from the intensity vector, the light has high saturation or is nearly pure in color since there is little white component. Finally, the hue, H, is the measure of the color or the dominant wavelength of the light. Therefore, it is a most natural definition or variable for the temperature calibration of

TLC. The hue curve as function of temperature generated from r, g, and b values in Fig. 2.5 is shown in Fig. 2.8.

The definition for the H S I space is not unique. Depending on the color basis vectors or the white (colorless) point, the transformation from R G B to H S I space may be different from Equation (2.4). In formulating a definition for hue, there are some criteria which should be satisfied. Strictly speaking, hue should be insensitive to white light, i.e., insensitive to saturation. It can be seen in Equation (2.4) that adding any constant to R, G, and B values on the right does not alter the value of hue, although the saturation (Equation 2.5) is altered. Hue should also be insensitive to intensity, and it can been seen in Equation (2.4) that multiplying R, G, and B values with any constant value does not alter the hue. In fact, there is an infinite number of definitions of hue which satisfy these criteria, and any angle between two independent vectors perpendicular to the intensity vector will satisfy. However, some authors (Farina et al., 1992; Hiller et al., 1993) have used alternate definitions. Farina et al. (1992), for example, have used:

$$\begin{bmatrix} v_1 \\ v_2 \\ I \end{bmatrix} = \begin{bmatrix} -1/4 & -1/4 & 1/2 \\ 1/4 & -1/2 & 0 \\ 1/3 & 1/3 & 1/3 \end{bmatrix} \begin{bmatrix} R \\ G \\ B \end{bmatrix}, \tag{2.6}$$

$$\begin{aligned} H &= \tan^{-1}(v_1 / v_2) \\ S &= \sqrt{v_1^2 + v_2^2} \end{aligned} . \tag{2.7}$$

which do not satisfy the strict criteria of hue. The hue curve using this definition is shown in Fig. 2.9. Nevertheless, these alternate definitions may work equally well in generating a temperature calibration as will be shown in Section 2.4.5.

## 2.4 Implementation

### 2.4.1 DPIV/T Setup

The DPIV/T experimental setup is shown in Fig. 2.10. The test section is made of 1.27 cm thick clear plexiglas™ and has an internal cross-sectional area of 15.2 cm by 15.2 cm. The tunnel can operate at flow speeds between 3 cm/s to 50 cm/s. The flow is seeded with encapsulated TLC particles and is illuminated by a

reflector assembly which produces a sheet of light at the center of the test section. The light reflector assembly is a mirror surfaced elliptical cylinder with a thin slit on top as shown in Fig. 2.11. The light, which is produced by two 25 cm long xenon flashtubes located at the foci of the ellipse, escapes through the slit and is collimated by two lenses to form a light sheet of 2 – 3 mm thickness. Each flashtube fires at 15 Hz with a flash duration of 150 microseconds and an energy of 8 J. By alternately firing the two flashtubes, synchronization with the frame rate of the video camera at 30 Hz is achieved with sufficient power and cooling.

The flow is imaged from the side of the water tunnel using a 3-CCD color camera (Sony DXC-9000) which has a standard set of NTSC color filters. The R, G, and B color video signals are recorded on a real-time digital video recorder.

### 2.4.2 Data Processing

The R, G, and B color channels are digitized to 24-bit color resolution (8-bits/channel) using an analog-to-digital frame grabber (Coreco RGB-SE) to form a 640 pixel by 480 pixel RGB color image. Before digitization, the offset and the gains of the analog-to-digital converters are adjusted to ensure that the dark current, i.e., pedestal, of each CCD is removed and the dynamic range maximized.

The TLC particles must be first located since the color information is contained only within them. To locate the particles, an intensity image, $Img_1$, is generated from a RGB color image. A second contrast enhanced image, $Img_2$, is created from $Img_1$, and a threshold operation is applied to $Img_2$ to create a list of particles. Then the precise centroid location of each TLC particle is found by locating the intensity maximum in $Img_1$. The r, g, and b values of each TLC particle are computed by conditionally averaging the centroid pixel and the eight pixels in the surrounding the centroid pixel as shown in Fig. 2.12. The conditional averaging procedure rejects r, g, and b values from pixels which have low saturation, i.e., no color. The procedure has two benefits. First, bright spots, i.e., regions of clipped signals, on a TLC particle, such as the ones near the particle centroid, do not skew the average. Second, dust or contamination particles, which are sometimes unavoidable

in a water tunnel, are automatically rejected because they are usually colorless and/or reflect much more intensely than TLC particles.

After the average values of R, G, and B of each particle are determined, the values to the input of the temperature calibration are computed. The input values may be of any form as discussed in Section 2.3. The temperature of each TLC particle is then estimated by evaluating the output of a pre-trained neural-network. The details of the neural-network are given in Section 2.4.4. Because there is typically a large uncertainty in the temperature of individual TLC particles (Section 2.4.5), the temperature at any point in the image is computed by averaging the temperatures of particles which lie within a specified (32 pixel by 32 pixel) window centered about the point. This averaging procedure is consistent with the technique of DPIV which computes the velocity, i.e. displacement, at any point by averaging the velocity of particles which lie within a specified window (Willert and Gharib, 1991). Thus the velocity and temperature reported by technique of DPIV/T at a given location is the average velocity and temperature of set of particles within a common specified window.

The computation of the velocity field is straightforward and is made by applying standard DPIV cross-correlation technique on a pair of intensity images. The interrogation window size is 32 pixel by 32 pixel with grid spacing of 8 pixels for window overlap of 75 percent. As noted above, the temperature field is computed with the same window size and grid spacing.

### 2.4.3 Temperature Calibration Procedure

The calibration of the TLC is made *in-situ* in the water tunnel facility prior or following the experiments. Because the reflected wavelength of TLC is function not only of temperature but also of viewing and illumination angles (Fergason, 1968; Parsley, 1991), the exact same viewing, illumination, and distance arrangements as the experiments must be maintained during the calibration. The tunnel is set to a constant speed, and the flow is seeded with micro-encapsulated TLC particles (Hallcrest BM40C26W20). These TLC have a temperature range of 20 °C under on-axis lighting arrangement, i.e., same illumination and viewing locations, but the 90°

off-axis lighting arrangement used for the experiments reduces the range to about 2.5 °C, or a range from approximately 26 °C to 28.5 °C. Starting from a temperature of colorlessness of the TLC particles (< 25 °C ), the temperature of the tunnel is slowly elevated. The water temperature is measured using a RTD temperature probe (Fluke 2180A) which has a resolution of 0.01 °C. A set of images is taken at each temperature increment of 0.1 °C up to 30 °C.

The r, g, and b values of the TLC particles are then extracted from the images of uniform temperature through a process discussed in Section 2.4.2. The mean values of r, g, and b of the entire image are then computed to produce calibration curves of r g b versus temperature. These curves in the useful temperature range of TLC were shown in Fig. 2.5. All other calibration curves are generated from these curves of mean r, g, and b values. The calibration curves of (b - r), H, and hue as defined by Farina et al. (1994) are shown in Fig. 2.6, 2.8, and 2.9, respectively. It should be noted that all single input calibration curves are monotonic although not linear.

### 2.4.4 Neural-Network Training

The fits to the calibration curves are made by training a neural-network, similar to the method used by Kimura et al. (1993). The neural-network arrangements for single and multi-input variables are shown in Fig. 2.13. Four neurons in the hidden layers are used for single input variable, and five neurons for multi-input variables. The network is trained by using the mean calibration curves (Fig. 2.5, 2.6, 2.8, and 2.9) as the training vectors and the measured temperatures as the target vectors. Using a standard back-propagation technique, the weights and biases of each node (neuron) are adjusted until the root-mean sum of the difference between the actual and the evaluated values of the target vectors from the set of training vectors is minimized. Typically, 1000 epochs or iterations are used to train the neural-network, and the fit is excellent with error of less than 0.05% through each target value in the temperature range.

### 2.4.5 Uncertainties

The uncertainty in the measured temperature of individual TLC particles comes from the non-uniformity in the manufacture of the TLC particles. Even under uniform temperature and lighting conditions, there are color variations between particles. This effect could be due to a variation in the chemical composition since the TLC are made from a complicated mixture of organic compounds. For the micro-encapsulated TLC particles, the variation in the thickness of the polymer shell can also affect the color by introducing light refraction effects. In addition, the TLC are sensitive to external stress which can mechanically change the helical pitch, and the process of encapsulating the TLC with a polymer shell may have introduced some residual stresses.

The scatters of r, g, and b values of individual particles are shown in Fig. 2.14. The scatters are obtained by computing the standard deviations of r, g, and b values from a set of 3000 to 5000 particles at each temperature. This can be translated into an uncertainty in the measured temperature as shown in the '+' symbols in Fig. 2.15. The uncertainty using the calibration curves of mean r g b versus temperature varies from 5% in the middle temperature ranges to 20% in the upper ranges. To reduce the uncertainty, the temperatures of the TLC particles within a specified window may be averaged. The results of this averaging procedure for 32 pixel by 32 pixel window is shown in the 'o' symbols in Fig. 2.15. The uncertainty is reduced to 4% in the middle ranges to 10% in the upper ranges. The price for this reduction in the uncertainty is a reduction in spatial resolution. However, as discussed in Section 2.4.2, the price paid is somewhat minimal since only the average velocity of the particles in the same specified window can be obtained using standard DPIV.

The uncertainties in the temperature using various calibration curves are shown in Fig. 2.16 - 2.18. The trends in the uncertainties of all the calibration curves are very similar. There are large uncertainties at the extreme ranges, and smaller uncertainties in the middle ranges. It is also important to note that the uncertainty levels using various calibration curves do not differ significantly. Whether hue or an algebraic combination of r, g, and b values is used, the uncertainty level is not affected greatly. The two definitions of hue, either standard or one used by Farina et

al. (1994), have similar uncertainty levels. This result somewhat contradicts findings of Hay and Hollingsworth (1996) who found that standard hue definition has lower uncertainty level than one used by Farina et al. (1994). However, the difference in the uncertainty levels between the two definitions was not very significant in the study by Hay and Hollingsworth (1996) and may be dependent on the types of TLC formulations.

The only exception to the similar levels of uncertainty is the computation of the temperatures using multi-input values of all three r, g, and b values. The uncertainty levels are much higher because the output of the multi-input neural-network is less robust than a single input neural-network. The input variable space is greatly expanded when using multi-inputs, i.e., factor of power 3, but the number of training vectors increase only slightly, i.e., factor of 3. Thus the neural-network becomes trained for a very narrow set of input values, and any set of input values outside this space may produce unexpected or unpredictable behavior. The scatter in r, g, and b values of individual TLC particles can therefore be amplified when computing the temperature.

The selected calibration curve for this study is the standard hue. This is for two reasons. The standard hue does not appear to do as well as the hue defined by Farina et al. (1994) in reducing the uncertainties, but the standard hue is believed to be more robust since it is invariant to saturation. This is an important consideration because changes in the seeding density, which may occur during the course of the experiment when heavier TLC particles settle to the bottom of the tunnel, may change the mean saturation level of the images. The standard hue also has very low and flat uncertainties in the normalized temperature range of 0.2 – 0.6 where most of the temperature measurements are to lie.

The accuracy error of the mean temperature, computed from a large number of individual measurements, is estimated to be on the order of 2%. The accuracy of the mean is determined by the shifts in the calibration curve. One cause of shift is the degradation of the TLC particles which can occur after several hours (> 8 hrs) of exposure to water. During the experiments, the TLC particles are stabilized in water for an hour or so and are then flushed after a few hours (~ 6 hrs). Therefore, the TLC

particles can be used only for a limited time if accurate mean temperature is desired. Other sources of shift can include changes in the viewing angle and seeding density. The shift in the calibration curve after a day of exposure to water is shown in Fig. 2.19.

The uncertainty in the velocity in a specified window using DPIV is of the order 1% (Willert and Gharib, 1991). The accuracy error in the mean velocity is estimated to be on the order of 1% (Huang, 1997). The combined uncertainty in the velocity-temperature correlation ($u_i$'T') for individual 32 pixel by 32 pixel window is around 3% - 10%, and the accuracy error of the correlation is estimated to be about 3%. A list of the uncertainty levels in DPIV/T, as well as the accuracy levels, is given in Table 2.1.

## 2.5 Summary

It is possible using DPIV/T to measure simultaneously both velocity and temperature fields by seeding the flow with the TLC particles. By generating a sheet of white light and capturing the images on to a 3-CCD video camera, the velocity and temperature of the flow can be deduced from the displacement and the color of the TLC particles, respectively. A comprehensive study of the uncertainties involved in using the micro-encapsulated TLC particles for temperature measurement in water is made, and it is found that there exists a large uncertainty (5% - 20%) in the temperature measurement of individual TLC particles regardless of the temperature calibration method. To reduce the uncertainty (2% - 10%), a process is developed where the temperature at a given location is computed by averaging the temperatures of the particles within a specified sampling window. Finally, the accuracy errors of the mean temperature and mean velocity-temperature correlation ($u_i$'T') using DPIV/T are estimated to be 2% and 3%, respectively.

Table 2.1 Uncertainty levels in DPIV/T

| | Uncertainty of individual particle | Uncertainty using 32x32 pixel sampling window | Error in accuracy |
|---|---|---|---|
| Velocity | N/A | 1% | 1% |
| Temperature | 5% - 20% | 2% - 10% | 2% |
| Velocity-Temperature Correlation | N/A | 3% - 10% | 3% |

# Chapter 3

# Experimental Setup

## 3.1 Experimental Setup

The experiments are conducted in a small water tunnel facility which has a test section of size 15.2 cm wide and 15.2 cm high as shown in Fig. 3.1. The tunnel is operated by a pair of pumps which can run at flow speeds between 3 to 50 cm/s. The temperature of the flow through the test section can be raised by a bank of staggered heating rods in the inlet pipe to the diffuser section of the tunnel and can be lowered by a re-circulating chiller (Neslab RTE-110) at the downstream section of the tunnel. Using a closed-loop temperature controller (Tronac PTC-41), the mean freestream temperature can be maintained to within ±0.02 °C at a flow speed of 5 cm/s or within ±0.01 °C at a flow speed of 40 cm/s.

The test cylinder is an electrically heated rod of diameter 9.53 mm (Watlow Firerod). The electric heating element is protected by an outer sheath which is made from Incoloy™ alloy. A J-type thermocouple, which can give an estimate of the cylinder temperature, is embedded in the core of the cylinder at mid-span. The temperature of the thermocouple is read by a thermocouple thermometer (Omega HH21) which has a temperature resolution of ±0.1 °C. The cylinder is heated by a constant DC voltage power supply (Kepco BOP 50-4M) which maintains a thermal boundary condition of constant integrated heat flux over the surface of the cylinder. The cylinder is mounted horizontally to a transverse oscillating mechanism by two vertical hollow supports at the ends of the cylinder. The hollow supports pass the electrical and thermocouple leads from the cylinder to the power supply and thermocouple thermometer, respectively. The supports are thermally insulated from the cylinder by a layer of RTV. The disturbance to the flow by the supports is minimized by placing them outside of the two flat end plates which have rounded leading edges. The distance between the two end plates is 12.1 cm, and thus the

effective aspect ratio (L/D) of the cylinder is 13. The picture of the entire assembly is shown in Fig. 3.2, and the schematic of the cylinder end condition is shown in Fig. 3.3.

The oscillating mechanism is a 6" cone speaker where the cone is stiffened by a circular thin-aluminum plate. The plate resists deformation of the cone by torsion and keeps the cylinder level with respect to the bottom of the tunnel. The speaker is driven by a feedback amplifier which is fed a sinusoidal signal from a multi-wave generator (HP 3314A). With the cylinder mass, the speaker is capable of generating sinusoidal motion amplitude of 4 mm peak-to-peak from 0 to 10 Hz. The actual displacement of the cylinder is measured by an optical transducer (photo-detector grid) which generates a voltage proportional to the displacement of a beam from a laser diode mounted on the cylinder oscillating mechanism (Fig. 3.4).

### 3.2 Velocity and Temperature Measurements

The freestream velocity measurements are made using a single component Laser Doppler Anemometer (LDA) placed several diameters upstream of the test cylinder. The velocity and temperature measurements in the wake are made using a DPIV/T setup as described in Section 2.4.1. The camera, which is placed approximately 2 m from the test section, images an area of 60 mm wide by 50 mm high at the mid-span of the test section. The flow is seeded with 40 μm diameter thin-walled encapsulated TLC particles (Hallcrest BM40C26W20) which have thermal response time of 4 milliseconds (Dabiri and Gharib, 1991). The response time is much smaller than the expected time scale of the vortex shedding (≈600 milliseconds). The flow is illuminated from the bottom of the test section by a xenon white light sheet of 2 - 3 mm thickness, and the images are digitized to a real-time digital video recorder with 8-bit resolution per RGB channel (24-bit total).

An instantaneous view of the flow with the heated cylinder in place is shown in Fig. 3.5. The coordinate system used in the study is shown in Fig. 3.6, and the derived temperature and velocity fields using DPIV/T are shown in Fig. 3.7. Unfortunately, the shadow cast by the cylinder prevents any gathering of information about the velocity or the temperature above the cylinder, and the immediate area

surrounding the cylinder (shown by the larger white concentric circle outside the cylinder in Fig. 3.7) cannot be imaged due to light blockage by the end of the cylinder nearest to the camera. Because DPIV/T cannot resolve the boundary layer, the technique cannot return any information about the temperature of the cylinder surface. In addition, because DPIV/T uses 32x32 pixel interrogation windows (0.3Dx0.3D), it cannot resolve the thin thermal shear layers. However, the flow does becomes resolved by DPIV/T immediately after the vortices are from by the roll-up of the shear layers at which time the flow scales becomes of the order of the cylinder diameter. A full discussion of the resolution capabilities of DPIV/T is given in Appendix A.

# Chapter 4

# Transport of Heat in the Wake

## 4.1 Introduction

In this chapter, we examine the mechanism of heat transport in the wake of a heated circular cylinder using DPIV/T. We examine the wakes of two cases, the stationary cylinder and the cylinder in forced oscillation. Using the triple decomposition, we examine the role of each heat flux component, the mean, coherent, and incoherent, in the transport of heat in the wake. We also examine the production terms of turbulence and how they relate to the topology of the flow. Finally, we test the validity of the gradient transport model in describing the turbulent heat transport processes in the wake of a heated circular cylinder.

## 4.2 Triple Decomposition

The wake of a circular cylinder is dominated by large-scale coherent structures which are the Karman vortices. To separate the dynamics of the large-scale coherent structures from the incoherent motions, we use the triple decomposition, first introduced by Reynolds and Hussain (1972), where the flow is decomposed into:

$$s = \overline{s} + \widetilde{s} + s_r', \tag{4.1}$$

where $\overline{s}$ (overbar) is the mean component, $\widetilde{s}$ (tilde) is the periodic or coherent component, $s_r'$ (subscript r and prime) is the incoherent or random component of any variable, s. This is in contrast to the standard Reynolds decomposition:

$$s = \overline{s} + s', \tag{4.2}$$

where s' (prime only) is the fluctuation from the mean. This will be called the global fluctuation and is defined as:

$$s' = \widetilde{s} + s_r'. \tag{4.3}$$

The mean, $\bar{s}$, is defined as:

$$\bar{s} = \frac{1}{N}\sum_{n=1}^{N} s_n , \tag{4.4}$$

where N is the total number of samples taken. In the case of a flow which has some periodic motion, such as vortex shedding, the population of N samples can be divided into sub-populations where each sub-population may correspond to a particular phase of the periodic motion. Thus the mean at constant phase, <s>, can be defined as:

$$< s >= \frac{1}{N_i}\sum_{v=1}^{N_i} s_v , \tag{4.5}$$

where $N_i$ is the number of samples at the i'th phase or sub-population. The periodic component, $\tilde{s}$, can be computed from Equation (4.4) and (4.5), where:

$$\tilde{s} = < s > - \bar{s} , \tag{4.6}$$

and by definition, $\bar{\tilde{s}} = 0$, $<s_r'> = 0$, and $\overline{\tilde{s}s_r'} = 0$.

In the context of coherent structures, it is more useful to rewrite Equation (4.1) as:

$$s = <s> + s_r', \tag{4.7}$$

since we will examine incoherent fluctuations with respect to the coherent structures.

### 4.3 Topological Classification

In the present study, we shall encounter critical points in the flow, namely saddles and centers. These critical points in the flow are points in the velocity field where $u_x=u_y=u_z=0$. These points may be the separation points of the boundary layers, centers of vortices, and/or saddle nodes in the flow. The problem we encounter is that the critical points are frame *dependent*. The centers of vortices can only be observed if we move with the convective velocity of the vortices. At any other velocity, the centers will be at a different location. To avoid this ambiguity, we employ the critical point analysis, which is frame *independent*, as introduced by Perry and Fairlie (1974). At each point in the flow, the flow can be classified by its invariants of the velocity gradient tensor, or:

$$P = \mathrm{tr} < \nabla \vec{u} >,$$
$$Q = \det < \nabla \vec{u} >, \tag{4.8}$$
$$R = -\lambda_1 \lambda_2 \lambda_3,$$

where:

$$\lambda_{1,2,3} = \frac{1}{2}(\mathrm{tr} < \nabla \vec{u} > \pm \sqrt{(\mathrm{tr} < \nabla \vec{u} >)^2 - 4 \det < \nabla \vec{u} >}, \tag{4.9}$$

and tr is the trace, and det is the determinant. The invariants are given for the phase averaged velocity gradient tensor which is useful for examining the topology of coherent structures. For an incompressible flow, $P = 0$, since $\mathrm{tr} < \nabla \vec{u} >= 0$, and $R = 0$ for a flow which is nearly two-dimensional, i.e., $\partial/\partial z < > = <u_z> = 0$, as may be expected in the case of the phase averaged velocity field for a two-dimensional body such as a circular cylinder. In such flows, the topology is described only one invariant, $Q$. If $Q<0$, the point in the flow can be classified as being at a region of saddle, or a region where the fluid is being stretched in one direction and compressed in the other. If $Q>0$, the point is at a region of center, or a region where the fluid is rotating. Finally, if $Q=0$, it is at a region of shear, or a region where the fluid is being sheared. These regions are illustrated in Fig. 4.1.

### 4.4 Governing Equations

For a flow which is incompressible, has only a small change in kinetic energy as compared to the change in thermal energy, i.e., small Eckert number ($Ec = \Delta u^2/C_p \Delta T \rightarrow 0$), and has small viscous dissipation ($Ec/Re \rightarrow 0$), the transport of heat or "temperature" is governed by the scalar convection-diffusion equation. For a fluid with constant heat capacity, $C_p$, and thermal conductivity, k, the equation is given by:

$$\frac{\partial T}{\partial t} + u_j \frac{\partial T}{\partial x_j} = -\alpha \frac{\partial}{\partial x_j}(-\frac{\partial T}{\partial x_j}), \tag{4.10}$$

where $\alpha = k/(\rho C_p)$, and $\alpha$ is the heat diffusion coefficient. For a flow which is unsteady or turbulent, we can derive the equation for the mean temperature by decomposing the variables into a mean and fluctuating components:

$$T = \overline{T} + T', \tag{4.11}$$

and

$$u_j = \overline{u}_j + u_j', \tag{4.12}$$

where the overbars and primes are defined as given in Section 4.2. Substituting Equations (4.11) and (4.12) into (4.11):

$$\frac{\partial}{\partial t}(\overline{T} + T') + \frac{\partial}{\partial x_j}((\overline{T} + T')(\overline{u}_j + u_j')) = -\frac{\partial}{\partial x_j}(-\alpha \frac{\partial}{\partial x_j}(\overline{T} + T')). \tag{4.13}$$

By taking the average of equation (4.13):

$$\frac{\partial \overline{T}}{\partial t} + \frac{\overline{\partial T'}}{\partial t} + \frac{\partial}{\partial x_j}(\overline{u}_j \overline{T} + \overline{u}_j \overline{T'} + \overline{u_j' \overline{T}} + \overline{u_j' T'}) = -\frac{\partial}{\partial x_j}(-\alpha \frac{\partial}{\partial x_j}(\overline{T} + \overline{T'})), \tag{4.14}$$

and noting:

$$\frac{\partial}{\partial t}\overline{T} = \overline{T'} = \overline{u}_j \overline{T'} = \overline{u_j' \overline{T}} = 0,$$

the equation for the mean temperature can be expressed as:

$$\overline{u}_j \frac{\partial \overline{T}}{\partial x_j} = -\frac{\partial}{\partial x_j}(\overline{u_j' T'} - \alpha \frac{\partial \overline{T}}{\partial x_j}). \tag{4.15}$$

The "temperature" in the equation is conserved, and has two flux terms, $\overline{u_j' T'}$ and $-\alpha\, \partial/\partial x_j \overline{T}$ which are the mean global turbulent and the molecular heat flux vectors, respectively.

For the mean heat equation at constant phase, substituting T with its triple decomposition into Equation (4.10) and averaging at constant phase leads to:

$$\frac{\partial < T >}{\partial t} + < u_j > \frac{\partial < T >}{\partial x_j} = -\frac{\partial}{\partial x_j}(< u_{r_j}' T_r' > - \alpha \frac{\partial < T >}{\partial x_j}). \tag{4.16}$$

Again, the "temperature" is conserved and has two flux terms, $< u_{r_j}' T_r' >$ and $-\alpha\, \partial/\partial x_j <T>$, which are the phase averaged incoherent and molecular heat flux vectors, respectively.

### 4.5 Experimental Conditions

The Reynolds number based on the freestream velocity, $U_\infty$, the cylinder diameter, D, and the kinematic viscosity at freestream temperature, $\nu$, is 610 for both the stationary and the forced oscillation case. The freestream velocity and temperature are 6.4 cm/s and 25.8 °C, respectively. For the case of the forced

oscillating cylinder, the amplitude, A, and the oscillation frequency of the cylinder, $f_c$, are 0.95 mm and 1.405 Hz, which correspond to A/D=0.1 and $St_c$=0.21, respectively. The Strouhal frequency of cylinder oscillation, $St_c$ is defined as $f_cD/U_\infty$. The frequency chosen, $St_c$=0.21, deliberately coincides with the vortex shedding frequency of the stationary cylinder and is a frequency at which the vortex shedding cycle becomes synchronized with the mechanical oscillation cycle of the cylinder. The motion of the cylinder is a sinusoid, and the maximum transverse velocity achieved is $0.022U_\infty$. The cylinder is electrically heated with a constant power input of 63.8 W for both cases. The temperatures at the core of the cylinder, $T_{tc}$, are 41.5 °C and 39.5 °C for the stationary and the forced oscillation cases, respectively. These values correspond to estimated temperatures at the surface of the cylinder, $T_c$, of 36.8 °C and 34.8 °C, respectively. The method used to estimate the surface of the temperature is given in Section 5.3.

The heating is sufficiently low to consider the temperature as a passive scalar. The effect on the momentum equation is minimized by keeping the ratio $Gr/Re^2$, which measures the ratio of the buoyancy forces as compared to the inertial forces, low at 0.05. The Grashof number is defined as: $Gr = (g\beta(T_c - T_\infty)D^3)/\nu^2$, where $g$ is the acceleration of gravity, and $\beta$ is the coefficient of thermal expansion. An experiment to verify that the heating does not affect the near wake is presented in Appendix D.

### 4.6 Averaging Methodology

The statistics are generated from 1000 pairs of image, corresponding to 1000 instantaneous velocity and temperature fields. The number represents roughly 95 vortex shedding cycles. The phase averaged statistics are generated by equally dividing the vortex shedding cycle into 12 phases. For each phase, roughly 85 independent velocity and temperature fields are used to compute the statistics.

For the forced oscillation case, there is no ambiguity in dividing the vortex shedding cycle since the shedding is synchronized with the mechanical motion of the cylinder. However, there exists an ambiguity in the phase of the vortex shedding cycle for the stationary case since the period of the shedding may vary slightly in

each cycle. This ambiguity was encountered by both Cantwell and Coles (1983) and Matsumura and Antonia (1993) who had to adjust slightly the period of each vortex shedding cycle to compute the phase average correctly. Only the deviations from each period-adjusted vortex shedding cycle were counted as incoherent fluctuations. Following their methodology, we also adjust the period of each vortex shedding cycle in computing the phase average quantities.

To compute the phase average, a reference signal from which the phase of the vortex shedding can be determined is required. Cantwell and Coles (1983) used the signal from a static pressure tap on the surface of the cylinder 65° from the forward stagnation point of the cylinder, while Matsumura and Antonia (1993) used the signal from a hot-wire just outside of the wake. Others have used the lift signal as the reference signal (Karniadakis, 1997), but any clean signal generated by the vortex shedding process may suffice. For this study, the vertical velocity ($u_y$) at the location of maximum $u_y$ fluctuations on the centerline of the wake is used as the reference signal. The maximum $u_y$ fluctuations occur just downstream the region where the vortices roll-up, and the $u_y$ signal there is both clear and large in magnitude. A typical $u_y$ signal is shown in Fig. 4.2. From this signal, the period of each shedding cycle is determined by measuring the time between consecutive zero crossings of the $u_y$ signal, and each period is divided into evenly spaced phases as shown in Fig. 4.3.

## 4.7 Results

### 4.7.1 Mean Results for Stationary Cylinder

The mean velocity field and the profiles of mean $u_x$ and $u_y$ at x/D=1, 2, 3, and 4 are shown in Fig. 4.4, 4.5, and 4.6, respectively. The standard deviations of the mean (SDOM) of the profiles are shown by the light error bars. The SDOM is the uncertainty associated with the unsteady fluctuations of the flow, not the measurement uncertainty of DPIV/T. The length of the wake bubble (saddle node) in the mean velocity field is measured to be x/D=2.4. This length is significantly farther downstream than what is nominally measured, x/D≈1.8 (Noca et al., 1998) at this Reynolds number. The discrepancy is due to the small aspect ratio (L/D=13) of the

cylinder which tends to move the roll-up of the vortices farther downstream, thus increasing the wake bubble length and decreasing the base pressure (Noca et al., 1998; Norberg, 1994). Only when the aspect ratio of the cylinder (L/D) exceeds 50 or so, can the bubble length reach the "nominal" value at this Reynolds number (Noca et al., 1998). As a consequence of small aspect ratio, the shear layers are very long ($x/D \approx 2$) as shown in the time averaged vorticity field in Fig. 4.7.

The mean temperature field and the profiles of temperature at x/D=1, 2, 3, and 4 are shown in Fig. 4.8 and 4.9, respectively. There are several points to note here. Because of the resolution limitation of DPIV/T, the temperatures of the thin shear layers are greatly underestimated at x/D=1. The thickness of the thermal shear layer profile is approximately 0.15D which is smaller in dimension than the 0.3D by 0.3D size of the DPIV/T interrogation windows. The resolution of the shear layer in the velocity field is less of an issue since the lateral extent of the velocity profile is larger or about 0.4D. The estimated scales and the resolution issues are discussed in detail in Appendix A. The asymmetrical temperature profile, i.e., higher temperatures for y/D>0, is observed at all x/D locations and is believed to be caused by an uneven heating of the cylinder at the top and bottom surfaces. The discrepancy cannot be accounted by the SDOM which are shown as light error bars in Fig. 4.9. The asymmetry may be a result of a problem with the accuracy of DPIV/T (Appendix A), but it is believed to be a flow phenomenon since the measurements do not show significant asymmetry in the y-direction as evidenced by the upper and lower freestream having the same temperature. The vorticity profiles in Fig. 4.10 do not show any asymmetry which indicates that the vortices are being shed symmetrically. Therefore, it is believed that the asymmetry in temperature is caused by an uneven heating of the cylinder surface, higher at the top and lower at the bottom. The asymmetry in the temperature profile is observed for every case of experiments, but unfortunately, the uneven heating conjecture could not be verified since the design of the cylinder oscillation assembly prevented the cylinder from being rotated 180°.

The mean global turbulent heat flux, $\overline{u_j'T'}$, is shown in Fig. 4.11. The structure of $\overline{u_j'T'}$ in the near wake is dominated by two large counter-rotating vortex-

like structures (x/D≈2, y/D≈±0.5), symmetric about the wake centerline. These structures are a result of the large entrainment of the cold freestream fluid into the region by the vortices during their roll-up. Farther downstream (x/D>3.5), $\overline{u_j'T'}$ at the outer edges of the wake (y/D≈±0.6) turns from upstream to downstream direction (≈45°) as result of the heat being transported downstream by the hot fluid rotating inside the vortices. The causes of these features are more clearly illustrated in the next section.

### 4.7.2 Phase Averaged Results for Stationary Cylinder

The sequences of phase averaged vorticity and temperature for 12 evenly divided phases are shown in Fig. 4.12(a,b) and 4.13(a,b). The sequence of velocity field in the frame of the vortices is shown in Fig. 4.14(a,b). Because the vortices roll-up from the hot shear layers, the temperature can be as good an indicator of the vortices as the vorticity. From Fig. 4.12 and 4.13, it is immediately apparent that the shear layers are very long (x/D≈2), and the roll-up of the vortices occurs far downstream (x/D≈2). During the roll-up of the vortices, substantial amount of cold fluid from the freestream is entrained by the vortices into the "formation" region as shown during the roll-up of the lower vortex in Phase (c) (Fig. 4.13(a) and 4.14(a)). The cold fluid is mainly entrained from the downstream side of the vortex (x/D=3, y/D=-0.5; Phase (c), Fig 4.13(a)), as observed by Cantwell and Coles (1983). This process is also the "alleyway" as described by Perry et al. (1982) under which the fluid outside of the wake penetrates into the region of stagnant fluid at the base of the cylinder.

The sequences of phase averaged coherent heat flux, $\tilde{u}_j\tilde{T}$, and incoherent heat flux, $<u_{r_j}'T_r'>$, are shown in Fig. 4.15(a,b) and 4.16(a,b). The transport of heat by the coherent heat flux, $\tilde{u}_j\tilde{T}$, is carried out by two large-scale motions of the fluid, the motion of cold fluid from the freestream being entrained into the wake and the motion of the hot fluid rotating inside of the vortices. In Fig. 4.17, both the motion of the cold fluid entering the wake (x/D=2.2, y/D=0.4 and x/D=3.3, y/D=-0.4) and the

vertical motion of the hot fluid inside the vortices (x/D=3.8, y/D=0.8) can be seen carrying large amount of heat laterally out of the wake. The rotating motion of the hot fluid inside the vortices also carries heat downstream (x/D=4.4, y/D=0.5) which is responsible for the global turbulent heat flux vectors having component in the downstream direction (Fig. 4.11).

The maximum magnitude of the incoherent heat flux, $<u_{r_j}' T_r'>$, is roughly one-fifth the maximum magnitude of $\tilde{u}_j \tilde{T}$ at Re=610 and makes only a small contribution to the overall turbulent heat flux. At higher Reynolds numbers, its contribution is expected to be larger (Matsumura and Antonia, 1993). The role of $<u_{r_j}' T_r'>$ is to carry heat away from the vortices. The detachment process of the vortices generates a turbulent exchange of heat between the vortices and the cold fluid being entrained into the wake, and the exchange results in transport of heat out of the vortices on their upstream faces (x/D=2.5, y/D=0; Fig. 4.18). This turbulent exchange continues as the vortices move downstream where the same type of exchange (x/D=4.5, y/D=0.5; Fig. 4.18) begins to occur on the downstream faces of the vortices.

### 4.7.3 Mean Results for Forced Oscillating Cylinder

The mean velocity field is shown in Fig. 4.19 in the frame stationary with respect to the tunnel. The profiles of mean $u_x$ and $u_y$ are shown in Fig. 4.20, and 4.21, respectively, and their SDOM are shown by the light error bars. The length of the mean wake bubble in this case is measured to be x/D=1.3. This is considerably shorter than the length for the stationary case (x/D=2.4) and suggests that the vortices are rolling-up much closer to the cylinder. The shear layers also appear to be very short (x/D≈0.9) as shown in the mean vorticity field in Fig. 4.22.

The mean temperature field and the temperature profiles are shown in Fig. 4.23 and 4.24, respectively. In this case, there is little sign of the shear layer by x/D=1, and the temperature profiles are much lower and wider than the stationary case. The wider profiles in both temperature and velocity (Fig. 4.20) for given x/D

location indicate that the wake is exchanging temperature and momentum more rapidly with the freestream fluid than the wake of a stationary cylinder.

The mean global turbulent heat flux, $\overline{u_j'T'}$, is shown in Fig. 4.25. $\overline{u_j'T'}$ is similar to the stationary case, except that the counter-rotating vortex-like structures are much closer to the cylinder. Again, the structure is due to large entrainment of the cold freestream fluid by the vortices during their roll-up, which may occur close to the cylinder. Farther downstream (x/D>3.5), $\overline{u_j'T'}$ is again observed to turn toward the downstream direction.

### 4.7.4 Phase Averaged Results for Forced Oscillating Cylinder

The sequences of phase averaged vorticity and temperature for 12 evenly divided phases are shown in Fig. 4.26(a,b) and 4.27(a,b). In this case, there is no ambiguity in the phase since the reference signal is the transverse displacement of the cylinder which is synchronized with the vortex shedding cycle. The sequence of velocity field in the frame of the vortices is shown in Fig. 4.28(a,b). As expected, the shear layers are very short (x/D≈0.9), and the vortices roll-up very close to the base of the cylinder (x/D≈1.2). The entrainment process of the freestream into the wake is similar during the roll-up of the vortices, but the rolled-up vortices appear to the be more circular (Fig. 4.26(a,b) and 4.27(a,b)) than those rolled-up from the stationary cylinder (Fig. 4.12(a,b) and 4.13(a,b)).

The sequences of phase averaged coherent heat flux, $\tilde{u}_j\tilde{T}$, and incoherent heat flux, $<u_{r_j}'T_r'>$, are shown in Fig. 4.29(a,b) and 4.30(a,b). The mechanisms of heat transfer by $\tilde{u}_j\tilde{T}$ and $<u_{r_j}'T_r'>$ are very similar to the case of the stationary cylinder. The transport of heat through $\tilde{u}_j\tilde{T}$ is carried out by the motion of the cold fluid being entrained into the wake and the motion of the hot fluid inside the vortices (Fig. 4.31), while heat is transported out of the vortices by $<u_{r_j}'T_r'>$ through turbulent heat exchange between the hot fluid inside the vortices and the entrained cold fluid (Fig. 4.32).

## 4.8 Discussion

### 4.8.1 Transport of Heat in the Wake

To exchange heat effectively with the surrounding fluid, the heat must be transported laterally out of the wake. In the framework of the triple decomposition, heat can be transported by three different heat fluxes, the mean, the coherent, and the incoherent heat flux. To examine separately the role each heat flux plays in transporting heat out of the wake, we rewrite the mean heat equation, Equation (4.15), in conservative form. By separating the global turbulent heat flux into its coherent and incoherent parts, Equation (4.15) becomes:

$$-\frac{\partial}{\partial x_j}(\overline{u}_j\overline{T}+\overline{\tilde{u}_j\tilde{T}}+\overline{u'_{rj}T'_r}-\alpha\frac{\partial\overline{T}}{\partial x_j})=0. \qquad (4.17)$$

$\overline{\tilde{u}_j\tilde{T}}$ and $\overline{u'_{rj}T'_r}$ are computed over one vortex shedding cycle since they are only defined over one period. The quantity inside the parenthesis is the total heat flux, not be confused with the mean heat flux, $\overline{u}_j\overline{T}$, which is only part of the total heat flux.

The mean heat fluxes, $\overline{u}_j\overline{T}$, are shown in Fig. 4.33 and 4.34 for the stationary and forced oscillation cases. In both cases, heat is transported by the mean heat flux mainly in the downstream direction. The role of $\overline{u}_j\overline{T}$ is to bring the heat from the hot shear layers into the wake and transport it down the wake. While $\overline{u}_j\overline{T}$ transports heat into and down the wake, $\overline{u}_j\overline{T}$ does not transport any heat out of the wake since it never acquires a vector component away from the wake centerline. Because the mean wake entrains fluid and thus the vertical velocity component points inward toward the centerline, the heat flux vectors cannot point outward from the centerline and transport heat out of the wake. Therefore, $\overline{u}_j\overline{T}$ can carry heat downstream but not out of the wake.

The mean coherent heat fluxes, $\overline{\tilde{u}_j\tilde{T}}$, are shown in Fig. 4.35 and 4.36 for the stationary and forced oscillation case. $\overline{\tilde{u}_j\tilde{T}}$ is a heat flux which transports heat laterally out of the wake and widens the wake. It plays a major role in transporting

heat out of the mean wake bubble within which hot fluid re-circulates around the base of the cylinder. Heat is transported out of the bubble by the entraining cold fluid during the roll-up of the vortices as discussed in Section 4.7.2 and 4.7.4. Similarly, heat is transported laterally out of the wake through entrainment of cold fluid from the freestream and transport of hot fluid out of the vortices (Fig. 4.17). $\overline{\tilde{u}_j\tilde{T}}$ also plays a minor role in transporting heat down the wake. This is through rotation of hot fluid around the vortices (Fig. 4.17) which produces a component in $\overline{\tilde{u}_j\tilde{T}}$ which points downstream.

The mean incoherent heat fluxes, $\overline{u'_{rj}T'_r}$, are shown in Fig. 4.37 and 4.38 for the stationary and the forced oscillation case. $\overline{u'_{rj}T'_r}$ also transports heat out of the wake and widens the wake, although to a lesser extent. At Re=610, the contribution from $\overline{u'_{rj}T'_r}$ is relatively small, about an order of magnitude smaller than $\overline{\tilde{u}_j\tilde{T}}$. Therefore, the transport of heat out of the wake is accomplished mostly through the large-scale coherent motions and not through the incoherent motions of the wake at this Reynolds number. Somewhat surprisingly, the mean incoherent heat flux, $\overline{u'_{rj}T'_r}$, appears to be larger in both relative magnitude with respect to the coherent heat flux and absolute magnitude for the forced oscillation case as compared to the stationary case. Because the wake is synchronized with the mechanical oscillation, the wake is thought to be more organized in the case of forced oscillations. However, the observed trend is opposite what is commonly believed. Even the incoherent stresses, such as $\langle u'_{rx}u'_{ry}\rangle$ (Fig. 4.47, and 4.48), show the same behavior. It may be speculated that the wake develops a three-dimensional instability or is relaxing to a different wake pattern for the forced oscillating case. The increase in the incoherence is not due to the difference in phase averaging technique, averaging with respect to $u_y$ for the stationary case and cylinder displacement for oscillating case, since averaging with respect to the $u_y$ velocity for the oscillating case produces an identical result. Further experiments are required to determine the cause of this surprising behavior. In any case, it is observed that the incoherent heat flux of a forced oscillating cylinder

plays a larger role in transporting heat out of the wake than that of a stationary cylinder.

In summary, the heat is transported laterally out of the wake by the coherent and incoherent heat fluxes. The overall transport of heat, the total heat flux, which includes the contributions from all three heat fluxes, is shown in Fig. 4.39 and 4.40 for the stationary and the forced oscillation case. There is still the molecular heat flux which is neglected since it is small compared to the turbulent heat fluxes as it is scaled by 1/(RePr), where Pr is the Prandtl number. The molecular heat flux is not negligible at the boundary layers and the shear layers, but both features are not resolved by DPIV/T. The contribution from each heat flux becomes apparent from these figures. The role of the mean heat flux, $\overline{u}_j\overline{T}$, is to first bring the heat from the shear layers into the wake. Then the role of the coherent, $\overline{\tilde{u}_j\tilde{T}}$, and the incoherent heat flux, $\overline{u_{rj}'T_r'}$, is to transport heat out to the outer edge of the wake where the mean heat flux, $\overline{u}_j\overline{T}$, again transports the heat downstream. The combined effect is that the total heat flux vectors point slightly away from the centerline, and the wake is able to effectively transport heat in both lateral and downstream directions as it grows downstream.

### 4.8.2 Production of Turbulence

It has been observed by Cantwell and Coles (1983) that for the near wake (x/D<10) of a circular cylinder, the production of kinetic energy fluctuations occurs in the saddle regions of the phased averaged velocity field. They conjectured that the production of kinetic energy in the saddle regions is universal for turbulent flows. In any turbulent flow, coherent structures must exist to maintain turbulent intensity by generating saddle regions at which the strain rates are large. At these saddle regions, turbulence is generated through a mechanism of three-dimensional vortex stretching. Similar conjectures have been made by Hussain (1981) in shear layers. In this study, similar observations are made at much lower Reynolds number, 610, as compared to 140,000 for Cantwell and Coles (1983). The kinetic energy production at constant phase, defined as:

$$< P_k >= - < u_{ri}' u_{rj}' > \frac{\partial < u_i >}{\partial x_j}, \qquad (4.18)$$

is plotted in Fig. 4.41 and 4.42 at Phase (g) and (f) for the cases of stationary and forced oscillating cylinders, respectively. Using the topological classification described in Section 4.3, the kinetic energy production is found to be large in the regions classified as saddles where the strain rates are large, as shown in Fig. 4.43 and 4.44.

An analogous term, the production of temperature fluctuations, $<P_T>$, is plotted in Fig. 4.45 and 4.46. The production of temperature fluctuations, derived in Appendix B, is defined as:

$$< P_T >= - < u_{rj}' T_r' > \frac{\partial < T >}{\partial x_j}. \qquad (4.19)$$

The figures show that the production of kinetic energy and temperature fluctuations occur at different regions of the flow field. While production of kinetic energy fluctuations occurs in saddle regions, production of temperature fluctuations occurs at the outer edges of the center regions. While the high strain rates at the saddle region can generate fluctuations in kinetic energy possibly through vortex stretching as conjectured by Cantwell and Coles (1983), the high strain rates cannot generate temperature fluctuations, $<P_T>$, because only cold freestream fluid which does not support any temperature gradients or incoherent heat flux is located at the saddle region for this wake. On the other hand, the center regions have strong temperature gradients because they contain almost all of the heat from the cylinder as the vortices have rolled-up from the hot shear layers. The center regions also possess large heat exchange and momentum exchange $<u_{rx}' u_{ry}'>$ (Fig. 4.47 and 4.48). Thus the only regions which have all of the necessary ingredients to produce temperature fluctuations, strong temperature gradients and large incoherent heat flux, are at the outer edges of the center regions. Unlike $<P_k>$ which is almost always positive, $<P_T>$ may have regions of both positive and negative values, all within a single vortex (center region). However, the net value is usually positive.

The fact that $<P_T>$ occurs within the vortices (center regions) suggests that it is has only local influence, i.e., only at the vortices. Since the vortices continually

entrain the surrounding fluid as they grow, the temperature fluctuations generated within the vortices is unlikely to escape. Therefore, the temperature fluctuations may be all produced and dissipated within the vortices. This appears to be the case as the plots of incoherent temperature fluctuations, $\sqrt{< T_r^{'2} >}$, show that the fluctuations mainly occur at the cores of the vortices (Fig. 4.49 and 4.50).

### 4.8.3 Examination of the Gradient Transport Model in the Wake

For turbulence models in computer simulations such as the Reynolds Averaged Navier-Stokes Simulation (RANS), the unsteady RANS, or the Large Eddy Simulation (LES), the classical assumption is that the turbulent heat flux is related to the mean temperature by a gradient, or:

$$\overline{u_j' T'} = -\alpha_t \frac{\partial \overline{T}}{\partial x_j}, \tag{4.20}$$

where $\alpha_t$ is the turbulent thermal diffusivity coefficient. Equation (4.20) implies that the turbulent heat flux is co-linear with the molecular heat flux if the turbulent thermal diffusivity, $\alpha_t$, is a scalar quantity. The above equation assumes that the quantities are mean quantities, but the same argument can be extended phase averages and spatial averages as in unsteady RANS and LES, respectively.

Equation (4.20) is analogous to classical modeling of the turbulent (Reynolds) stress tensor, $-\overline{u_i' u_j'}$, in the mean momentum equation. In simulations such as the isotropic k-ε RANS (Launder and Spalding, 1974), the turbulent stress tensor is assumed to be proportional to the mean velocity gradient tensor stress by:

$$-\overline{u_i' u_j'} = \nu_t \left( \frac{\partial \overline{u}_i}{\partial x_j} + \frac{\partial \overline{u}_j}{\partial x_i} \right), \tag{4.21}$$

where $\nu_t$ is the turbulent eddy viscosity. In many models, the turbulent thermal diffusivity coefficient is related to the turbulent eddy viscosity by the turbulent Prandtl number, $Pr_t$, which is defined as:

$$Pr_t = \frac{\nu_t}{\alpha_t}.$$

The turbulent Prandtl number is assumed to be of order (1) and is assumed to be ≈1 in most cases. From experimental studies (Franke et al., 1989, Liu et al., 1994) and DNS simulations, it has been demonstrated that the concept eddy viscosity is flawed because the turbulent stress tensor is not proportional to the mean velocity gradient tensor in an actual flow. Since the accuracy of the turbulent eddy viscosity model is called into question, the concept of the turbulent Prandtl number and the turbulent thermal diffusivity coefficient becomes suspect. Therefore, we test the validity of Equation (4.20) by examining whether the molecular and turbulent heat flux vectors are co-linear (parallel to each other) in the wake behind a heated circular cylinder

The mean molecular heat flux and the turbulent heat flux is shown in Fig. 4.51 and Fig 4.52 for the stationary and forced oscillating cylinders, respectively. For the stationary case, the main feature of the molecular heat flux close to the cylinder (x/D<2) is the diffusion of heat out of the shear layers. Because of the spatial resolution limitation of DPIV/T, the molecular heat flux vectors at the shear layer is underestimated. The turbulent heat vectors, while difficult to see in the figure, point upstream. Similar observations have been made by Karniadakis (1997) in DNS simulations. At x/D≈2.5, the turbulent heat flux exhibits a vortex-like structure symmetric about the centerline. The molecular heat flux does not exhibit this feature, and the vectors point nearly vertically away from the wake centerline past x/D>2 as the largest gradients are in the vertical direction due to the temperature difference between the wake and the freestream. The turbulent heat flux vectors nearly point vertically away from the wake centerline at x/D=2.5, but begin to turn towards the downstream direction for x/D>3 from the contribution of the coherent heat flux vectors which point downstream because of the rotation of the hot fluid around the vortices. Similar observations are made of the molecular and turbulent heat flux vectors for the case of the wake of an oscillating cylinder, except that everything occurs much closer to the cylinder as the vortices roll-up immediately behind the cylinder. Even in the mean, the assumption that the molecular and turbulent heat flux vectors are co-linear appears to be invalid.

The phase averaged molecular heat flux, $-\alpha\, \partial/\partial x_j \langle T \rangle$, and the incoherent heat flux, $\langle u_{r_j}' T_r' \rangle$, are shown for Phase (g) and (f) in Fig. 4.53 and 4.54 for the case of

stationary and forced oscillating cylinders, respectively. These are the quantities computed in an unsteady RANS simulation. Again, it is immediately apparent that the two vectors are far from co-linear almost anywhere in the wake. In fact, in the region of the vortices, where the both heat flux vectors are respectively large, the vectors are nearly perpendicular. The molecular heat flux diffuses heat radially out of the hot cores of the vortices, while the incoherent heat flux transports heat in the direction normal to the wake centerline. These results show that scalar transport models of the gradient transport type in unsteady RANS simulations will do poorly in modeling the physical process of turbulent heat transport in the wake of a bluff body.

**4.9 Summary**

In this chapter, we examine the mechanism of heat transport in the wake of a heated circular cylinder using DPIV/T. By decomposing the total heat flux into its mean, coherent, and incoherent heat flux using the triple decomposition, it is observed that the heat is transported down the wake mostly by the mean heat flux and is transported laterally out of the wake by the coherent and the incoherent heat fluxes. The coherent heat flux, which is much larger in magnitude than the incoherent heat flux at Re=610, transports heat out of the wake by processes of entrainment of the cold freestream fluid and lateral movement of the hot fluid inside the vortices.

The production of kinetic energy and temperature fluctuations is found to be at different topological regions of the flow. The kinetic energy fluctuations is found to be produced in the saddle regions as found by previous studies. The temperature fluctuations are found to be produced at the edges of center regions, or at the edges of the vortex cores. Finally, the gradient transport model is found to be poor in describing the turbulent heat transport in the wake of a circular cylinder. The turbulent heat flux vectors is not found to be co-linear with the gradient vectors of the mean or phase averaged temperatures.

# Chapter 5

# Effect of Forced Oscillation on Convection of Heat

## 5.1 Introduction

In this chapter, we examine the effect of transverse forced oscillation on the heat transfer from the surface of a cylinder. It is known that there is a significant increase in the surface heat transfer when a cylinder is forced to oscillate at a frequency corresponding to the vortex shedding frequency of a stationary cylinder. The rise in the surface heat transfer is attributed to the phenomenon of "lock-in" or synchronization of the vortex shedding with the mechanical oscillation of the cylinder. Slightly above the synchronization frequency, it has been observed that the surface heat transfer may increase or decrease depending on the oscillation amplitude (Cheng et al., 1997). However, little is known about what happens to the heat transfer well above the synchronization frequency, and in this chapter, a study of this region is made as well as the region near the synchronization frequency.

## 5.2 Experimental Conditions

The average heat transfer from the surface of a cylinder in forced oscillation is measured for three different Reynolds numbers of 550, 1,100, and 3,500 based on a freestream temperature of 25.8 °C. The cylinder is heated with constant power inputs of 45.5, 58.4, and 90.9 W for Re=550, 1,100, and 3,500, respectively. Again, the ratio $Gr/Re^2$ is kept low enough to not affect the wake structure.

The measurements are made at two amplitudes, A/D=0.1 and 0.2. The range of Strouhal frequency of the cylinder, $St_c$, is from 0 to 0.95 for Re=550 and 1,100. The ranges in physical frequency unit are from 0 to 5.6 Hz for Re=550, and from 0 to 11.4 Hz for Re=1,100. For Re=3,500, the range of $St_c$ is from 0 to 0.35, corresponding to a range in physical frequency from 0 to 13.4 Hz. The maximum

frequency at this Reynolds number is limited by the mechanical driving mechanism which cannot exceed 14 Hz.

### 5.3 Nusselt Number

The Nusselt number, defined as:

$$Nu = \frac{hD}{k},$$

where h is the average convection heat transfer coefficient, and k is the thermal conductivity of the fluid medium, is computed from the estimate of the average surface temperature of the cylinder and the input power. Because the Biot number, defined as:

$$Bi = \frac{hD}{k_C},$$

where $k_c$ is thermal conductivity of the cylinder, is of order unity, the approximation that the temperature at the surface, $T_c$, is the same as the temperature at the core, $T_{tc}$, cannot be made. Therefore, a first order approximation is made to estimate the surface temperature from the core temperature as measured by the embedded thermocouple ($T_{tc}$).

We assume that the temperature varies only in the radial direction and that the cylinder is composed of a uniformly heated inner shell and an unheated outer shell (Fig. 5.1). If we assume uniform material properties, the steady-state temperature distribution in the inner shell is then given by the heat equation in radial coordinates:

$$\frac{\partial^2 T}{\partial r^2} + \frac{1}{r}\frac{\partial T}{\partial r} + \dot{q} = 0 \qquad (R_1 \le r \le R_2) \qquad (5.1)$$

where $\dot{q}$ is the power input per unit volume, or:

$$\dot{q} = \frac{\dot{Q}}{\pi(R_2^2 - R_1^2)L} \qquad (5.2)$$

where $\dot{Q}$ is the total power input, L is the length of the cylinder, $R_1$ is the radius at which the thermocouple is located, and $R_2$ is the outer radius of the inner shell. The steady-state temperature distribution in the outer shell is given simply by:

$$\frac{\partial^2 T}{\partial r^2}+\frac{1}{r}\frac{\partial T}{\partial r}=0, \qquad (R_2 \le r \le R_3). \tag{5.3}$$

The boundary conditions for these equations are:

$$T(R_1)=T_{tc}, \tag{5.4}$$

$$-k_{co}\left.\frac{\partial T}{\partial r}\right|_{r=R3}=h(T_c-T_\infty)=\frac{\dot{Q}}{2\pi R_3 L}, \tag{5.5}$$

where $k_{CO}$ is the thermal conductivity of the outer shell, and $R_3$ is the outer radius of the cylinder. The matching condition is at $R_2$ where the temperatures of the outer and inner shells must be equal. Solving Equations (5.1) and (5.3) with the appropriate boundary conditions, the temperature at the surface, $T_c$, is given by:

$$T_c=T_{tc}-\frac{\dot{Q}}{2\pi L}\left[\frac{1}{k_{CO}}\ln\left(\frac{R_3}{R_2}\right)+\frac{1}{k_{CI}}\left(\frac{1}{2}-\frac{R_2^2}{R_2^2-R_1^2}\ln\left(\frac{R_2}{R_1}\right)\right)\right], \tag{5.6}$$

where $k_{CI}$ is the thermal conductivity of the inner shell. From Equation (5.6) and (5.5), we can compute the convection heat coefficient, where:

$$h=\frac{\dfrac{\dot{Q}}{2\pi R_3 L}}{(T_{tc}-T_\infty)-\dfrac{\dot{Q}}{2\pi L}\left[\dfrac{1}{k_{CO}}\ln\left(\dfrac{R_3}{R_2}\right)+\dfrac{1}{k_{CI}}\left(\dfrac{1}{2}-\dfrac{R_2^2}{R_2^2-R_1^2}\ln\left(\dfrac{R_2}{R_1}\right)\right)\right]}. \tag{5.7}$$

From h, we can then compute the Nusselt number. The values for the constants used in the computation of h is given in Table 5.1. A note is made about the temperature at the surface which is not truly uniform around the circumference of the cylinder. The temperature at the base of the cylinder is higher than that of the forward stagnation point. This is confirmed by intrusive thermocouple measurements at various locations around the surface of the cylinder. However, the gradients are found to be much higher in the radial direction than in the circumferential direction, and therefore the approximation of only radial temperature dependence may be suitable.

### 5.4 Results

The plots of Nusselt number versus oscillation frequency are shown in Fig. 5.2, 5.3, and 5.4 for Reynolds numbers of 550, 1,100, and 3,500, respectively. At every Reynolds number and oscillation amplitude, there exists a peak near $St_c \approx 0.21$.

As previous noted, these peaks are associated with the synchronization of the vortex shedding with the mechanical oscillations. This phenomenon has been observed by many previous researchers starting from Kezios and Prasanna (1966). For each Reynolds number, higher oscillation amplitudes results in higher Nusselt number at this frequency as noted by previous researchers (Kezios and Prasanna, 1966; Cheng et al., 1997).

The locations of all of the peaks appear to be correlated with the amplitude of oscillation, and the heat transfer curves are re-plotted for each amplitude in Fig. 5.5 and 5.6 for A/D=0.1 and 0.2, respectively. In these figures, the Nusselt numbers for each Reynolds number are normalized by their respective stationary values (A/D=0, $St_c$=0 ). The figures show that the locations of the peaks and valleys are nearly coincident for given amplitude, irrespective of the Reynolds number. For A/D=0.1, there is a broad valley from $St_c \approx 0.3$ to $\approx 0.45$, and a broad peak at $St_c \approx 0.6$ with roughly the same height as the peak at $St_c$=0.21. For A/D=0.2, there are valleys at $St_c \approx 0.3$ and 0.4, and two peaks at $St_c \approx 0.35$ and $\approx 0.55$.

**5.5 Discussion**

While it has been well documented that there exists an increase in the Nusselt number at the synchronization frequency ($St_c \approx 0.2$), the increases in the Nusselt number at other frequencies have never been documented in literature. The results of this study show that the Nusselt number does not increase or decrease monotonically past the synchronization frequency ($St_c \approx 0.2$), but has definite peaks and valleys. Without the knowledge of the flow field, it may be conjectured that the peaks in the Nusselt number may be associated with certain modes of the wake. The increase at $St_c \approx 0.6$ for A/D=0.1 may be associated with a mode at three times the natural shedding frequency, whereas the increases seen at $St_c \approx 0.35$ and 0.55 for A/D=0.2 may be associated with modes at twice and three times the natural vortex shedding frequency, respectively. At the higher amplitude (A/D=0.2), the mode frequencies appear to have shifted slightly away from exact multiples of the fundamental synchronization frequency.

The increase in the Nusselt number cannot be simply accounted for by the "effective" velocity of the cylinder due to added velocity from the oscillatory motion of the cylinder. Following Sreenivasan and Ramachandran (1961), the effective velocity, $V_e$, is defined as:

$$V_e = \sqrt{U_\infty^2 + V_v^2}, \tag{5.8}$$

where:

$$V_v = \frac{2\pi f A}{\sqrt{2}}, \tag{5.9}$$

is the RMS velocity of the oscillation. For a stationary cylinder, the MacAdams relation (MacAdams, 1954) predicts the Nusselt number as function of the Reynolds number (100<Re<4000) or the freestream velocity as:

$$Nu \propto Re^{0.475} \propto U_\infty^{0.475}. \tag{5.10}$$

Substituting $V_e$ into Equation (5.7), the Nusselt number as function of oscillation frequency and freestream velocity becomes:

$$Nu(A, f_c, U_\infty) \propto \left(U_\infty^2 + 2\pi^2 f_c^2 A^2\right)^{0.475}. \tag{5.11}$$

This is plotted as the solid curves in Fig. 5.5 and 5.6. It is observed that this relation cannot account for the increase in the Nusselt number for the oscillation frequencies of interest.

The trends in Fig. 5.5 and 5.6 are actually consistent with those observed by Cheng et al. (1997) which are shown in Fig. 1.3. They observed that for A/D=0.138, the Nusselt number decreased and remained low past $St_c \approx 0.2$, while at A/D=0.314, the Nusselt number first decreased then began to increase again. Since they did not measure the Nusselt number beyond 1.5 times the shedding frequency ($St_c \approx 0.30$), they likely observed a decrease associated with a valley from $St_c \approx 0.3$ to $\approx 0.45$ for A/D=0.134, and an increase associated with a peak at $St \approx 0.35$ for A/D=0.314. They attributed the rise at A/D=0.314 past $St \approx 0.3$ to the "turbulence" effect. They did not precisely define what the "turbulence" effect was, although it is inferred from their paper that it is associated with some unsteady (incoherent) motion of the wake or the boundary layer. In the following chapter, we explore the possibility of this and/or

other effects, such as the modes of the wake, by studying the wake in detail using DPIV/T.

### 5.6 Summary

In this chapter, we examine the effect of forced transverse oscillations on the heat transfer from the surface of a circular cylinder. A map is made of the heat transfer versus forced oscillation frequency for oscillation amplitudes, A/D=0.1 and 0.2. It is found that besides the increase in heat transfer at the oscillation frequency corresponding to the unforced vortex shedding frequency, there are other higher frequencies, most likely to be super-harmonics, at which there is a large increase in the heat transfer. In particular, there is a large increase in heat transfer at approximately three times the unforced vortex shedding frequency for A/D=0.1, and there are large increases at approximately two and three times the frequency for A/D=0.2.

Table 5.1 Cylinder parameters.

| Re | Q (W) | $T_\infty$ (°C) | $R_1$ (mm) | $R_2$ (mm) | $R_3$ (mm) | $k_{CI}$ (W/m °C) | $k_{CO}$ (W/m °C) | L (mm) |
|---|---|---|---|---|---|---|---|---|
| 550 | 45.5 | 25.8 | 1.0 | 32.0 | 47.6 | 12 | 12 | 150 |
| 1100 | 58.4 | 25.8 | 1.0 | 32.0 | 47.6 | 12 | 12 | 150 |
| 3500 | 90.9 | 25.8 | 1.0 | 32.0 | 47.6 | 12 | 12 | 150 |

# Chapter 6

# Relationship between Wake Structure and Convection of Heat

## 6.1 Introduction

The phenomenon of "lock-in" or the synchronization of the vortex shedding with the mechanical oscillation has been attributed to the reason behind the increase in the surface heat transfer when a cylinder is forced to oscillate at a frequency corresponding to that of the vortex shedding of a stationary cylinder. Nevertheless, no explanation has been given as to how the synchronization leads to a change in the rate of surface heat transfer from the cylinder. In this chapter, we attempt to identify the link between the structure of the wake and the increase in surface heat transfer at the synchronization frequency and other frequencies as observed in the previous chapter, by studying the wake using DPIV/T.

## 6.2 Experimental Conditions

The experimental conditions are identical to the conditions described in Section 4.4. The Reynolds number is 610, and the freestream temperature is 25.8 °C. The cylinder is heated with a constant power input of 63.8 W for all cases. Wake velocity-temperature field measurements using DPIV/T are made for two different amplitudes (A/D=0.1 and 0.2) at frequencies corresponding to peaks and valleys of the heat transfer versus oscillation frequency curve in Fig. 5.5 and 5.6. A total of nine cases, denoted by Roman numerals I through IX, are studied. The amplitudes, frequencies, and Nusselt numbers of these cases are listed in Table 6.1. For cases I and II, 1000 pairs of images are taken, while 500 pairs of images are taken for all other cases, III through IX.

## 6.3 Results

*Case I:*

This is the reference case of the stationary cylinder. The mean velocity and vorticity fields are shown in Fig. 6.1 and 6.2. The length of the wake bubble in the mean velocity field is measured to be x/D=2.4, and long shear layers (x/D≈2) are observed in the mean vorticity field. The unforced shedding frequency is observed at St=0.21 as shown by the Power Spectral Density (PSD) in Fig. 6.3. The Strouhal frequency, St, is defined as $St = fD/U_\infty$, where f is the frequency. The PSD for this and every other case is computed from the time-trace of $u_y$ (transverse velocity) at the location of maximum $u_y$ fluctuations on the wake centerline. The sequences of the phase averaged vorticity and temperature fields are shown in Fig. 6.4(a,b) and 6.5(a,b). The vorticity contours, which nearly mirror the temperature contours (albeit with different signs at the top and bottom of the cylinder), show that the vortices begin to roll-up at x/D≈2 (Phase (k), Fig. 6.4(b)). As shown by the sequence of the phase averaged close-up velocity field near the base of the cylinder in Fig. 6.6(a,b), there remains a region of stagnant fluid immediately behind the base of the cylinder at every phase of the shedding cycle.

*Case II:*

The cylinder in this case is forced to oscillate at the vortex shedding frequency of the stationary cylinder (St=0.21) with amplitude of A/D=0.1. At this oscillation frequency, $St_c$=0.21, the wake is synchronized with the mechanical oscillations, and corresponds to the peak in the Nusselt number at $St_c$=0.21 in Fig. 5.5. The mean velocity and vorticity fields in Fig. 6.7 and 6.8 show that the wake bubble is much shorter (x/D=1.3), and the shear layers are very short, perhaps extending to x/D≈0.9. The sequences of the phase averaged vorticity, temperature, and velocity fields are shown in Fig. 6.9(a,b), 6.10(a,b), and 6.11(a,b), respectively. The vorticity contours show that the vortices roll-up immediately behind the cylinder at x/D≈1 (Phase (k), Fig. 6.9(b)).

*Case III:*

The cylinder in this case is oscillated at $St_c$=0.34 with A/D=0.1. This corresponds to the valley in the Nusselt number past $St_c \approx 0.25$ in Fig. 5.5. The mean velocity and vorticity fields are shown in Fig. 6.12 and 6.13. The length of the wake bubble has increased to back to x/D=2.4, and the shear layers are once again long. While the cylinder is oscillated at $St_c$=0.34, the PSD (Fig. 6.14) shows that the dominant frequency in the wake is at St=0.20. This suggests that the shedding of the large-scale vortices is unaffected by the cylinder oscillation and remains near the unforced frequency of St=0.21. There is little sign of wake excitation at the frequency of oscillation ($St_c$=0.34) in the PSD. The sequence of the phase averaged vorticity is shown in Fig. 6.15. The sequence of six phases (a-f) corresponds to one oscillation of the cylinder. The vorticity field at each phase looks remarkably like the mean vorticity in Fig. 6.13. This demonstrates that the large-scale vortex shedding is unaffected by the cylinder oscillation, and this behavior has been documented by Ongoren and Rockwell (1988) for the cases of a cylinder oscillated at frequencies above the unforced vortex shedding frequency with small amplitudes (A/D<0.2). By phase averaging with respect to $u_y$ (same technique as case I), the large-scale vortex shedding cycle can be recovered as shown in Fig. 6.16, 6.17, and 6.18 for the vorticity, temperature and velocity fields, respectively. Like Case I, there always remains a region of stagnant fluid in the vicinity of the base of the cylinder.

*Case IV:*

The cylinder in this case is oscillated at $St_c$=0.58 with A/D=0.1. This corresponds to the broad peak in the Nusselt number at $St_c \approx 0.6$ in Fig. 5.5. The mean velocity and vorticity fields are shown in Fig. 6.19 and 6.20. The most immediate features of this wake are the extremely short wake bubble ($x/D \approx 1$) and the short shear layers ($x/D \approx 0.6$). The PSD in Fig. 6.21 shows that there are two dominant frequencies, St=0.20 and St=0.58. Since St=0.58 is nearly three times St=0.20, it suggests a coupling between the vortex shedding process and cylinder oscillations. Indeed, a vortex shedding cycle is recovered by phase averaging with respect to one-third of the forced oscillation frequency of the cylinder, and the results are shown in

Fig. 6.22(a-c), 6.23(a-c), and 6.24(a-c) for the vorticity, temperature and velocity fields, respectively. The wake pattern has undergone period tripling with respect to the cylinder oscillation period. Starting from Phase (a) in Fig. 6.22(a) where the lower vortex is beginning to roll-up (x/D=1, y/D=-0.6), it takes two cylinder oscillations for this vortex to shed from the cylinder as shown in Phase (l) in Fig. 6.22(b). Immediately following this vortex, a smaller vortex of the same sign rolls-up behind the primary vortex (Phase (o), Fig. 6.22(c)) and sheds in one cylinder oscillation (Phase (r), Fig. 6.22(c)).

*Case V:*

The cylinder is oscillated at $St_c$=0.21 and A/D=0.2. This is again the case of the wake being synchronized with the mechanical oscillation, corresponding to the first major peak in Fig. 5.6. The mean velocity and vorticity fields in Fig. 6.25 and 6.26 show that the wake bubble and the shear layers are short at x/D=1.5 and x/D=1.0, respectively. The sequences of the phase averaged vorticity, temperature, and velocity fields are shown in Fig. 6.27, 6.28, and 6.29, respectively. The vorticity contours again show that the vortices roll-up immediately behind the cylinder at x/D≈1 (Phase (a), Fig. 6.27), and the region of stagnant fluid normally near the base of the cylinder has been replaced by a region of energetic fluid (Phase (a), Fig. 6.29).

*Case VI:*

The cylinder is oscillated at $St_c$=0.30 with A/D=0.2 which corresponds to a valley in the Nusselt number at $St_c$≈0.23 in Fig. 5.6. The mean velocity and vorticity fields are shown in Fig. 6.30 and 6.31. The length of the wake bubble and the shear layers have increased to x/D=1.9 and x/D≈1.2, respectively. The PSD shows that the large-scale vortex shedding has moved to St=0.19 as shown in Fig. 6.32. There appears to be a small peak at St=0.30, corresponding to the cylinder oscillation frequency. Nevertheless, no synchronized wake pattern could be observed by phase averaging with respect to this frequency or any of the sub-frequencies (1/1.5, 1/2, 1/3). The vortex shedding cycle can be recovered once again by phase averaging with respect to $u_y$, and the vorticity, temperature, and velocity fields are shown in Fig.

6.33, 6.34, and 6.35, respectively. The vortices may come close to the base of the cylinder (Phase (f), Fig. 6.33) at times, but remain farther away than the previous case of wake synchronization (Phase (a), Fig. 6.27).

*Case VII:*

The cylinder is oscillated at $St_c$=0.37 with A/D=0.2. This corresponds to the peak in the Nusselt number at $St_c \approx 0.35$ in Fig. 5.6. The mean velocity and vorticity fields, which show that the wake has a very short wake bubble and shear layers, x/D=1.2 and x/D≈0.8, respectively, are shown in Fig. 6.36 and 6.37. The PSD in Fig. 6.38 shows that there are two dominant frequencies, St=0.19 and St=0.37. By phase averaging with respect to one-half of the cylinder oscillation frequency ($St_c$=0.37), a vortex shedding cycle is recovered as shown in Fig. 6.39(a,b), 6.40(a,b), and 6.41(a,b) for the vorticity, temperature and velocity fields, respectively. The wake pattern has undergone period doubling with respect to the cylinder oscillation period. Starting from Phase (c) in Fig. 6.39(a) where the lower vortex is beginning to roll-up (x/D=1, y/D=-0.7), one cycle is completed before this vortex is shed as shown in Phase (i) of Fig. 6.39(b). Following this vortex is a slightly smaller vortex of the same sign which rolls-up in another cylinder oscillation (Phase (a), Fig. 6.39(a)). The two vortices then appear to merge downstream (x/D≈4) as shown in Phase (f) of Fig. 6.39(a). Again, the first vortex is observed to roll-up very close to the cylinder.

*Case VIII:*

The cylinder is oscillating at $St_c$=0.42 with A/D=0.2 which corresponds to a valley in the Nusselt number at $St_c \approx 0.40$ in Fig. 5.6. The mean velocity and vorticity fields are shown in Fig. 6.42 and 6.43. The length of the wake bubble and the shear layers have increased to x/D=2.1 and x/D≈1.2, respectively. The PSD shows that the large-scale vortex shedding frequency has moved to St=0.21 as shown in Fig. 6.44. This frequency corresponds to one-half of the oscillation frequency, and the phase average results with respect to one-half the oscillation frequency show that, like the previous case, the wake pattern has undergone period doubling with respect to the cylinder oscillation period. The vorticity, temperature, and velocity fields are shown

in Fig. 6.45(a,b), 6.46(a,b), and 6.47(a,b). The vortex formation process is similar to the previous case (Case VII), having two pairs of like-sign vortices shed in two cylinder oscillations. One difference is that the vortices seem to merge much faster ($x/D \approx 2.5$) as shown in Phase (c) of Fig. 6.45(a). Another important difference is that the vortices roll-up much farther downstream with perhaps the closest approach occurring at Phase (f) of Fig. 6.45(a), in comparison to Phase (e) of Fig. 6.39(a) of the previous case.

*Case IX:*

Finally, this is the case of the cylinder being oscillated at $St_c=0.51$ with $A/D=0.2$. This corresponds to the peak in the Nusselt number at $St_c \approx 0.5$ in Fig. 5.6. The mean velocity and vorticity fields are shown in Fig. 6.48 and 6.49. The wake has extremely a short wake bubble ($x/D \approx 0.75$) and shear layers ($x/D \approx 0.5$). The PSD in Fig. 6.50 shows that the cylinder oscillation and the vortex shedding cycle have become synchronized, as evidenced by the two peaks at frequencies of $St=0.17$ and $St=0.51$. The wake pattern appears to be very similar to Case IV, or the case of wake period tripling with $A/D=0.1$, and the vorticity, temperature, and velocity fields are shown in Fig. 6.51(a-c), 6.52(a-c), and 6.53(a-c), respectively. Again, a large primary vortex is shed in two cylinder oscillations, and a smaller vortex of like-sign is shed on the third oscillation. The primary vortex again rolls-up very close to the cylinder as observed in Phase (h) of Fig. 6.51(b).

## 6.4 Discussion

### 6.4.1 Roll-up Distance versus Heat Transfer

The most immediate observation to from these results is the connection between the distance at which the vortices roll-up and the surface heat transfer. The length of the wake bubble in the mean velocity field is a good measure of the downstream distance at which vortices roll-up. For all of the high heat transfer cases, Case II, IV, V, VII, and IX, the length of the wake bubble is observed to be short,

$x/D<1.5$. For all of the the low heat transfer cases, Case I, III, VI, and VIII, the length is observed to be long, $x/D>1.9$.

The reason behind the increased heat transfer when the vortices roll-up close to the cylinder is that the vortices are able scrub away the hot fluid at the base of the cylinder. In the case of a stationary cylinder, there is a region of stagnant fluid just behind the cylinder which does not convect any heat away from the base of the cylinder. This region of stagnant fluid behind the cylinder (extending out to $x/D\approx2$) can be seen by the temperature and velocity fields of Case I, and III (Fig. 6.4(a-b), 6.5(a-b) for Case I; Fig. 6.16, 6.17 for Case III). In the high heat transfer cases, this region is non-existent as shown in temperature and velocity fields for Case II (Fig. 6.10(a-b), 6.11(a-b)). While the local Nusselt number is not measured in the study and thus cannot verify the increase in the heat transfer at the base of the cylinder, it is strongly believed that the heat transfer does increase at the base when the vortices roll-up close to the cylinder and are able to scrub away the normally stagnant and non-heat convecting fluid behind the cylinder. As evidence, Fig. 6.54 shows the closest approach that a vortex makes during its roll-up in Case I. The vortex is sufficiently far away that the fluid near the base of the cylinder remains stagnant and does not carry away any heat. Fig. 6.55 shows the closest approach that a vortex makes during its roll-up in Case II. The vortex is close enough to induce flow around the base of the cylinder and carry away heat from the base. The overall heat transfer, therefore increases when the heat transfer rate at the normally low region at the base of the cylinder (Eckert and Soehngen, 1952) is increased.

Karanth et al. (1994) have computed the local Nusselt number around a forced oscillating circular cylinder at the synchronization frequency at $Re=200$ for $A/D=0.25$ using a computational study, but they observed little change in surface heat transfer distribution from that of the stationary cylinder. However, their results are far from conclusive since they only observed 1.2% increase in the overall heat transfer which can be completely accounted for by using the "effective" velocity correction of Equation (5.11). In other words, their heat transfer computations may have only picked up contribution of the simple increase in velocity of the cylinder.

It is tempting to correlate blindly the length wake bubble with the rate of surface heat transfer. However, the heat transfer cannot be a simple function of the wake bubble length because the length can grow or shrink as function of only the Reynolds number. It has been observed that the length of the wake bubble, or the "formation length" of the vortices, increases for roughly 200<Re<1500 (Bloor, 1964). For a cylinder with "high" aspect ratio (L/D>50), the length of the wake bubble increases from x/D=1.6 to 2.2 (≈40% increase) from Reynolds number 500 to 1000 for a stationary cylinder (Noca et al., 1998). The Nusselt number may also increase in this span of Reynolds number by ≈40% (MacAdams, 1954). Since the trends are opposite to those of the forced oscillating cylinder (increase in wake bubble length results in decreased heat transfer), the Reynolds number, not the wake bubble length, must be the essential parameter in determining the heat transfer from a stationary cylinder. When the cylinder is in forced oscillation, the wake bubble length, not the "effective" Reynolds number or freestream velocity (Equation 5.11), appears to be the essential parameter in correlating the heat transfer. Realizing these effects, we present a plot of the trend between the wake bubble length and Nusselt number at Re=610 in Fig. 6.56.

The increase in heat transfer may be also correlated with the increase in the vorticity flux through a surface normal to the wake centerline as shown in Fig. 6.57. The measured vorticity flux is the amount of vorticity passing through a surface below the wake centerline at x/D=0.8, i.e., the location of the lower shear layer. The most likely reason why the Nusselt number correlates so well with the vorticity flux is that the amount of vorticity a shear layer contains may have direct influence the formation length, i.e., length of the mean wake bubble. It is observed that the larger the amount of vorticity flux, the shorter the length of the bubble. This is consistent with the "free-streamline" or "cavity" theory (Roskho, 1993) which predicts that the bubble length will decrease if the vorticity flux is increased. Hence, a shorter bubble length implies more closely rolled-up vortices which are more effective in transporting away the non-heat convecting fluid at the base of the cylinder. The correlation between the vorticity flux and the length of the mean wake bubble is shown in Fig. 6.58.

The heat transfer from the surface of the cylinder does not correlate well with the total amount of circulation shed by the vortices as shown in Fig. 6.59. This is not surprising since the top and bottom vortices shed vorticity of opposite signs. Because the vorticity from the top and bottom may cancel each other during the formation of the vortices, the circulation may be a poor indicator of the total vorticity injected into the shear layers by the cylinder top and bottom. Thus the vorticity injected into the shear layers must be measured directly.

### 6.4.2 Structure of the Wake

The observation of a short wake bubble length, or a roll-up of the vortices close to the cylinder, always coincides with the synchronization of the wake with some integer fraction ($1/n$, $n$=1,2,3) of the mechanical oscillation frequency. Regardless of the oscillation frequency, the frequency of the large-scale vortex shedding remains near St=0.2 (Ongoren and Rockwell, 1988). When the frequency of oscillation approaches some multiples of the large-scale vortex shedding frequency, the wake pattern becomes synchronized with the cylinder oscillation, and this may result in the roll-up of the vortices very close to the cylinder. In cases II and V, the wake is synchronized with the mechanical oscillation frequency since the wake and oscillation frequencies match. For other frequencies which are multiples of the large-scale vortex shedding frequencies, period doubling (case VII) and period tripling (cases IV and IX) are observed with respect to the cylinder oscillation period. This phenomenon of period doubling and tripling has been observed by Ongoren and Rockwell (1988) by flow visualization in water (hydrogen bubble technique) for cylinders of various shapes. For a wedge shaped cylinder, they observed the formation of one small vortex per side (top and bottom) for each oscillation of the cylinder when the oscillation frequency was an integer multiple, $n$, of the large-scale vortex shedding frequency. The $n$ distinct vortices merged downstream to form the large-scale vortices which then shed at a much lower frequency ($1/n$ of the oscillation frequency). The merging process is shown in Fig. 1.2. Similar observations are made in this study, except that merging appears to occur much closer the cylinder, especially for Case IV and IX (i.e., $n$=3). Ongoren and Rockwell (1988) observed

that oscillating the cylinder three times the natural shedding frequency generated three distinct vortices per side, of which the first two merged some distance ($x/D \approx 2.5$, where D is the side length of a 60° wedge) downstream followed by a merger of the third vortex with the first two at $x/D \approx 4$. In this study (circular cylinder as opposed to a wedge), three distinct vortices are not observed. Instead, one large vortex is generated in two cylinder oscillation, and a second smaller vortex is generated which does not appear to merge with the larger vortex in the near wake (Fig. 6.17(a-c), 6.53(a-c)). The circulation of the vortices in each of the cases is presented in Table 6.2.

The synchronization of the wake with the cylinder oscillation is not a sufficient condition to cause the vortices to roll-up close to the cylinder, hence, high heat transfer. For case VII, the wake pattern is synchronized with the one-half the cylinder oscillation frequency. However, the vortices roll-up far downstream and does not appear to effectively scrub away the stagnant fluid at the base of the cylinder (Fig. 6.49(a,b)).

Finally, the oscillation frequencies corresponding to the peaks in the heat transfer rate seem to shift as function of oscillation amplitude. For A/D=0.2, the oscillation frequencies corresponding to the maximum heat transfer rates seem to shift lower than the multiples of the vortex shedding frequency of the unforced cylinder (Fig. 5.6). For smaller amplitude (A/D=0.1), the maximum heat transfer rate seem to nearly coincide with the multiples of the vortex shedding frequency of the unforced cylinder. Oddly, no peak in the heat transfer rate is observed for A/D=0.1 at twice the large-scale vortex shedding frequency. While the results from Case III do not show any synchronization of the wake pattern with the oscillation frequency, the oscillation frequency may be too low ($St_c=0.34$). It is likely that the wake achieves synchronization at $St_c \approx 0.4$ but probably fails to generate a pattern where the vortices roll-up close to the cylinder. Analogously, the heat transfer does not increase for oscillations frequencies corresponding to four or five times the large-scale vortex shedding frequency. The reason for why the wake has certain preferred frequencies at which the vortices are allowed to roll-up close to the cylinder is unknown at this time.

### 6.4.3 Discrepancies

The increases in heat transfer (20% - 40% from the stationary value) are somewhat higher than observed by other researchers. A review of the previous measurements shows that there exists a wide scatter in the measured heat transfer at the wake synchronization frequency ($St_c \approx 0.2$). Experimentally, Kezios and Prasanna (1966) measured increase of 20% for A/D=0.075 at Re=5,500, while Cheng et al. (1997) measured increase of 10% for A/D=0.138 at Re=1,000. There may be several reasons for these discrepancies. First, the present experiments are conducted in water instead of air as was the case for the other measurements. Second, each study used a different technique of computing the Nusselt number. Kezios and Prasanna (1966) used thermocouples on the surface of a cylinder which was heated continuously, and the Nusselt number was estimated from the continuous power input and the average surface temperature. Cheng et al. (1997) used thermocouples embedded within a cylinder which was first heated then allowed to cool by convection. The Nusselt number was computed indirectly by measuring the cooling rate of the cylinder. In this study, the cylinder is continuously heated, but the Nusselt number is computed using an *estimate* of the surface temperature from a thermocouple embedded in the cylinder core and the power input. It can be argued that the method of Kezios and Prasanna (1966) is the most accurate since it is the most direct measure of the Nusselt number. The results of this study are closer to those of Kezio and Prasanna (1966) than Cheng et al. (1997), but the issue is far from resolved. Since the original goal of the study was to study the wake using DPIV/T, the cylinder used in this study was never designed for accurate temperature measurements at the surface. Therefore, the computed Nusselt numbers in this study may not be accurate. However, the trends in the heat transfer rate, i.e., Nusselt number, observed in this study are believed to be completely accurate.

One other issue which must be addressed is the cylinder aspect ratio (L/D). It has been observed that decreasing the aspect ratio increases the wake bubble length; hence, the distance at which the vortices roll-up (Norberg, 1994; Noca et al., 1998). Since the distance at which vortices roll-up plays an important role in the surface heat transfer when the cylinder is oscillated, the aspect ratio may be an important

parameter in determining the relative increase in the heat transfer between a stationary and oscillated cylinder. Review of the aspect ratios used in previous studies show a range of rather low values, from L/D=3 of Saxena and Laird (1978), L/D=10.7 of Kezios and Prasanna (1966), L/D=16 of Cheng et al. (1997), to L/D=17.5 for Sreenivasan and Ramachandran (1961). The end boundary conditions of these experiments have not been well documented. Therefore, the measurements from these studies, as well as the present study, may not be truly representative of heat transfer from an "infinitely long" circular cylinder which may be achieved only when L/D>50 (200<Re<1,000) and L/D>200 for Re>1,000 (Norberg, 1994). The parameters and results of each study are shown in Table 6.3.

### 6.4.4 "Turbulence" Effect

In conclusion, we address the "turbulence" effect as described by Cheng et al. (1997) who attributed it to the rise in heat transfer at A/D=0.314 past $St_c \approx 0.3$ (Fig. 1.3). The "turbulence" effect, as it turns out, appears to be an organized pattern in the wake associated with the synchronization of the wake with the cylinder oscillation through processes of period doubling and tripling. The increase in the heat transfer is believed to be the result of vortices rolling-up closer to the cylinder and scrubbing away the stagnant fluid at the base of the cylinder for selected oscillation frequencies. There may be indeed an effect from incoherent or "turbulent" motions in the wake as suggested by the Nusselt number never quite returning to the value of the stationary cylinder (Fig. 5.5-5.6), but the large increases observed at particular frequencies are the result of coherent or synchronized motion of the wake with respect to the cylinder oscillation.

## 6.5 Summary

In this chapter, a close inspection of the flow field using DPIV/T reveals that the increase in the heat transfer from a forced oscillating cylinder is associated with the distance at which vortices roll-up behind the cylinder. When the vortices roll-up close to the cylinder, the heat transfer is increased. It is observed that the vortices roll-up close to the cylinder when the vorticity flux into the wake becomes large,

consistent with the "free-streamline" theory. The increase is believed to be a result of the removal of the stagnant and low heat convecting fluid at the base of the cylinder when the vortices approach close to the cylinder. It is observed that the close roll-up of the vortices coincides with the synchronization of the wake with the mechanical oscillation of the cylinder through period doubling and/or tripling of the wake pattern with respect to the cylinder oscillation period. However, the synchronization of the wake with the mechanical oscillation is not found to be a sufficient condition to cause a large increase in the surface heat transfer. Only when the wake is synchronized and the vortices roll-up close to the cylinder, is there a large increase in surface heat transfer. Finally, the large increases in the heat transfer appear to be the result of coherent motions of the wake, not "turbulent" or incoherent motions.

Table 6.1 Experimental parameters

| Case | A/D | $St_c$ | Freq. (Hz) | $T_c$ | $\overline{Nu}$ |
|---|---|---|---|---|---|
| I | 0.0 | 0.00 | 0.000 | 36.8 | 21.2 |
| II | 0.1 | 0.21 | 1.405 | 34.8 | 25.9 |
| III | 0.1 | 0.34 | 2.300 | 36.3 | 22.2 |
| IV | 0.1 | 0.58 | 3.900 | 34.6 | 26.5 |
| V | 0.2 | 0.21 | 1.405 | 34.2 | 27.7 |
| VI | 0.2 | 0.30 | 2.000 | 35.3 | 24.6 |
| VII | 0.2 | 0.37 | 2.500 | 34.2 | 27.7 |
| VIII | 0.2 | 0.42 | 2.800 | 35.5 | 24.1 |
| IX | 0.2 | 0.51 | 3.400 | 33.8 | 29.2 |

Table 6.2 Circulation ($\Gamma/DU_\infty$) and vorticity flux ($u_x\omega/U_\infty^2$) of vortices

| Case | $\Gamma$ upper primary vortex | $\Gamma$ upper 2ndary vortex | Total $\Gamma$ upper vortices | $\Gamma$ lower primary vortex | $\Gamma$ lower 2ndary vortex | Total $\Gamma$ lower vortices | $u_x\omega$ lower shear layer |
|---|---|---|---|---|---|---|---|
| I | N/A | N/A | -2.6 | N/A | N/A | 2.7 | 0.98 |
| II | N/A | N/A | -2.5 | N/A | N/A | 2.5 | 1.08 |
| III | N/A | N/A | -2.5 | N/A | N/A | 2.5 | 0.96 |
| IV | -2.3 | -0.7 | -3.0 | 2.2 | 1.0 | 3.2 | 1.13 |
| V | N/A | N/A | -2.4 | N/A | N/A | 2.6 | 1.07 |
| VI | N/A | N/A | -2.6 | N/A | N/A | 2.6 | 0.98 |
| VII | -2.5 | -0.4 | -2.9 | 2.1 | 0.9 | 3.0 | 1.14 |
| VIII | N/A | N/A | -2.1 | N/A | N/A | 2.4 | 0.99 |
| IX | -2.5 | -1.1 | -3.6 | 2.4 | 1.2 | 3.6 | 1.12 |

Table 6.3 Parameters from different studies.

| Authors | Re | Medium | A/D | Max. $Nu/Nu_o$ | $T_c$-$T_\infty$ | L/D |
|---|---|---|---|---|---|---|
| Sreenivasan and Ramachandran (1961) | 5,000-25,000 | Air | 0.43-3.7 | ≈1.0 | ≈75 °C | 18 |
| Kezios and Prasanna (1966) | 5,500-14,000 | Air | 0.02-0.075 | ≈1.2 | ≈85 °C | 11 |
| Saxena and Laird (1978) | 3,500 | Water | 0.89-1.99 | ≈1.6 | ≈9 °C | 3 |
| Cheng et al. (1997) | 200-1000 | Air | 0.14-0.63 | ≈1.3 | ≈65 °C | 16 |
| Present Study | 550-3500 | Water | 0.1-0.2 | ≈1.6 | ≈10 °C | 13 |

# Chapter 7

# Conclusions and Recommendations

## 7.1 Conclusions

An experimental investigation was carried out on the heat transport processes of a heated circular cylinder. An improved DPIV/T technique was developed and used to study the process of turbulent heat transport in the wake of a heated circular cylinder at Reynolds number 610. In addition, a study of the heat transfer from the surface and the wake structure of a cylinder undergoing forced oscillation was made.

The conclusions from the studies are:

1) The velocity and temperature fields of turbulent flows can be measured using an enhanced technique of DPIV/T. The uncertainty in the temperature measurements of DPIV/T can be reduced to 2% - 10% by averaging the temperatures of individual TLC particles within a 32x32 pixel window. The accuracy errors of DPIV/T are 1% and 2% for the velocity and temperature measurements, respectively.

2) In the near wake of a heated cylinder, the heat released by the cylinder is transported downstream mainly by the mean heat flux. The heat is transported laterally out of the wake by the coherent and incoherent heat fluxes. The coherent heat flux, which is much larger than the incoherent heat flux at Re=610, transports heat by entrainment of the cold freestream fluid into the wake and vertical motion of the hot fluid inside the vortices out of the wake. The incoherent heat flux transports heat out the vortices and the wake through a turbulent interaction between the hot fluid inside vortices and the cold fluid entrained into the wake.

3) Productions of kinetic energy and temperature fluctuations occur at different topological regions of the flow. The kinetic energy fluctuations are produced in the saddle regions where strain rates are large. The temperature fluctuations are produced at the outer edges of center regions, i.e., at the edges of the vortex cores.

4) The gradient transport model is poor in describing the turbulent heat transport in the near wake of a heated circular cylinder. The turbulent heat flux vectors are

not co-linear with the gradient vectors of mean temperature, especially at or near the vortices where most of the heat transport occurs.

5) There are large increases in the heat transfer from the surface of a cylinder in forced oscillation at frequencies corresponding to roughly the integer multiples of the large-scale vortex shedding frequency (St≈0.2). Specifically, there are large increases at one and three times the large-scale vortex shedding frequency for A/D=0.1, and there are increases at one, two, and three times the large-scale vortex shedding frequency for A/D=0.2.

6) The wake becomes synchronized with the mechanical oscillation of the cylinder at frequencies corresponding to integer multiples of the large-scale vortex shedding frequency (St≈0.2). The wake synchronizes with the cylinder oscillation by undergoing period doubling and tripling with respect to the cylinder oscillation period for frequencies two and three times the large-scale vortex shedding frequency, respectively.

7) The large increases in the heat transfer from the surface of a forced oscillating cylinder can be correlated with the observation of vortices rolling-up close the base of the cylinder. The increase in heat transfer is believed to be result of energetic fluid of the vortices scrubbing away the normally stagnant and poor heat convecting fluid which normally resides at the base of the cylinder.

### 7.2 Recommendations

There are still some unresolved issues surrounding the technique of DPIV/T and the mechanisms of heat transport from a heated cylinder. The issues which need to be addressed in the future are:

1) The spatial resolution of DPIV/T must be improved for study of turbulent flows. The current resolution can resolve only the largest scales of the flow. The most obvious solution may be to reduce the sampling window size from 32x32 to 16x16 pixels but may result in an unacceptable increase in the measurement uncertainty. The uncertainty must be fully characterized before 16x16 pixel windows can be employed. Another possible solution is to use a higher resolution camera. A 32x32 pixel window size in the image may still be employed while the physical window size is reduced.

2) Why is the incoherent heat flux larger for the forced oscillating cylinder than the stationary cylinder? It is observed that the incoherent heat flux is larger for the forced oscillating cylinder even at the synchronization frequency where the wake pattern is thought to be more coherent. What is the cause of the incoherence?

3) How does the aspect ratio affect the surface heat transfer from a stationary cylinder? It is known that the aspect ratio can change the downstream distance at which the vortices roll-up. Since the heat transfer rate of a forced oscillating cylinder is strongly correlated with the distance at which the vortices roll-up, how does the changes in the roll-up distance associated with changes in the aspect ratio affect the heat transfer?

4) Why do the vortices roll-up close to the cylinder at the forced oscillation frequency of three times the large-scale vortex shedding frequency, but not at two times for A/D=0.1? A related issue is why the vortices do not roll-up close at four or five times the large-scale vortex shedding frequency for either A/D=0.1 and 0.2.

5) What happens to the heat transfer rate beyond five times the large-scale vortex shedding frequency? The heat transfer rate appears to reach a minimum at five times the large-scale vortex shedding frequency for each case of Reynolds number and oscillation amplitude. However, heat transfer rate computed using "effective" velocity is beginning to rise rapidly at this frequency. Does the heat transfer rate computed using the "effective" velocity ever overtake the actual measured heat transfer? Are there more maxima in the heat transfer at higher oscillation frequencies?

# Appendix A

# Resolvable Scales Using DPIV/T

The current implementation of DPIV/T sacrifices spatial resolution for better temperature precision. Because DPIV/T uses a rather large sampling window, 0.3D by 0.3D, where D is the diameter of the cylinder, it is important to know what scales are resolved and not resolved by this technique in the wake of a heated circular cylinder. The large-scale dynamics are well captured by DPIV/T since the local integral scale, $l$, becomes larger than D once the vortices are formed. However, prior to the roll-up of the vortices, the scale of the shear layers, which are laminar at Re=610, is relatively small. Thus to check if the shear layers are resolved, we conservatively estimate the thickness of the shear layers from the Blasius solution of a free shear layer with the upper stream velocity at $U_\infty$ and lower stream velocity at zero. The visual thickness of the velocity profile of the shear layer at one diameter downstream is estimated as:

$$\delta_U = \delta_{U=0.99} - \delta_{U=0.01} \approx 0.4D.$$

The temperature diffuses at a slower rate, $Pr^{-1/2}$, and its profile thickness is:

$$\delta_T \approx 0.15D,$$

for Pr=6 (water). Therefore, DPIV/T does not resolve the temperature profile of the shear layers with a sampling window size of 0.3D by 0.3D, and the heat flux at the shear layer may be greatly underestimated. This is evident in Fig. A.1 which is a plot of the total heat flux (sum of mean and turbulent heat flux) in the streamwise direction at several downstream locations. The heat flux is shown for the case of a stationary cylinder, which has shear layers extending out to $x/D \approx 2$. Because the temperature of the shear layers is under-resolved, the peaks at $y/D = \pm 0.6$ for $x/D=1$ corresponding to the heat flux at the shear layers are neither sharp or tall, and the total heat flux (integral of the curve) at this downstream location is much smaller as compared to locations farther downstream (x/D=2,3,4).

Once the shear layers roll-up into the vortices, the local integral scale, $l$, becomes the order of D, but other scales are introduced as the flow becomes turbulent. A scale which is important is the Taylor microscale. This is the scale at which mixing (local, not molecular) is expected to begin (Miller, 1991). The Taylor microscale, $\lambda_M$, can be estimated by:

$$\frac{\lambda_M}{l} = \left(\frac{15}{A}\right)^{1/2} \mathrm{Re}_l^{-1/2},$$

where A is an undetermined constant of order (1). The Taylor microscale is not truly applicable at Re=610 since the turbulence is weak and not isotropic. Nevertheless, it is a rough estimate of the mixing scale and is estimated to be:

$$\lambda_M \approx 0.15l.$$

At the initial roll-up of the vortex, $l$ is ≈D, so the "Taylor" microscale may not be fully resolved. However, farther downstream, $l$ quickly becomes much larger than D ($l$/D > 2), and the "Taylor" scale should be resolved.

The Taylor microscale is the scale of the momentum, and the analogous scale for the temperature, or the temperature microscale, $\lambda_T$, is estimated to be:

$$\lambda_T \approx 0.05l,$$

from the relation:

$$\frac{\lambda_T}{\lambda_M} = C\,\mathrm{Pr}^{-1/2},$$

where C is an undetermined constant of order (1). The temperature microscale is more difficult to resolve and is resolved only when the vortex move well downstream (x/D > 4) where $l$/D>3.

While DPIV/T may have trouble resolving the smaller scales in the flow, the most energetic scales associated with velocity and temperature fluctuations are expected to at the largest scale, or $l$. A crude test whether DPIV/T is capturing all of the energy associated with velocity and temperature fluctuations is to compute the total heat flux using DPIV/T for various downstream locations. The total heat flux can be measured using a wake survey method described in Appendix C, and the results for a stationary cylinder with heat input of 63.8 W are shown in Fig. A.2. The total heat flux should be ideally equal to the total heat released by the cylinder if the

mean heat flux, $\overline{u}_x \overline{T}$, and the turbulent heat flux, $\overline{u_x' T'}$, are well resolved and computed accurately.

For x/D < 2, the computed heat release by the cylinder is well below 63.8 W, and this is because DPIV/T is unable to resolve the thin shear layers and capture all of the heat flux in the wake. Once the shear layers roll-up into the vortices (x/D≈2), DPIV/T is able to capture most if not all of the heat flux in the wake. For x/D>2, the computed heat release becomes equal to or greater than the actual heat released by the cylinder. This discrepancy cannot be fully accounted for by the SDOM (Standard Deviation Of Mean) which is shown by the error bars. There are a couple of explanations for this discrepancy. One explanation is that the flow is not two-dimensional as assumed in computing the heat release of the cylinder (Appendix C). If the cylinder or the wake has any spanwise variation in the heat flux, the computed heat release will be inaccurate since heat flux measurements from only one mid-span plane are used for the computation. The other explanation is that the temperature measurements of DPIV/T are not accurate. SDOM does not return any information about the accuracy of the measurements, and therefore cannot estimate the uncertainty due to the accuracy error of DPIV/T. In Chapter 2, the accuracy error of the temperature from DPIV/T measurements was estimated to be 2%. In actual temperature units, this corresponds to accuracy error of ±0.05 °C for a temperature span of 2.5 °C. The method of computing heat release using a wake survey of the heat flux turns out to be extremely sensitive to temperature uncertainty because the mean temperature in the wake is very low. While the instantaneous temperature and the temperature fluctuations are large due to the formation of hot vortices, the mean temperature of the wake is very low. In fact, an accuracy error of ±0.02 °C, which is half of the estimated accuracy error of DPIV/T, may account completely for the observed discrepancy. Therefore, the overestimation of the heat release by the cylinder is probably a combination of the inaccuracy of DPIV/T and a spanwise variation in the heat release by the cylinder. In conclusion, it is likely that DPIV/T is capturing most of the energetic scales of the velocity and temperature fluctuations in the wake once the shear layers roll-up into the vortices.

# Appendix B

# Production of Temperature Fluctuations

The equation for the temperature fluctuations is derived by first substituting $T = \overline{T} + T'$ and $u_j = \overline{u}_j + u_j'$ into the heat equation (Equation B.1) and subtracting the mean (Equation B.2) to obtain Equation (B.3):

$$\frac{\partial}{\partial t}(\overline{T} + T') + (\overline{u}_j + u_j')\frac{\partial}{\partial x_j}(\overline{T} + T') = \alpha\frac{\partial^2}{\partial x_j^2}(\overline{T} + T'). \tag{B.1}$$

$$-\frac{\partial \overline{T}}{\partial t} + \overline{u}_j\frac{\partial \overline{T}}{\partial x_j} + \frac{\partial}{\partial x_j}(\overline{u_j'T'}) = \alpha\frac{\partial^2 \overline{T}}{\partial x_j^2}. \tag{B.2}$$

$$\frac{\partial T'}{\partial t} + u_j'\frac{\partial \overline{T}}{\partial x_j} + u_j'\frac{\partial T'}{\partial x_j} + \overline{u}_j\frac{\partial T'}{\partial x_j} - \frac{\partial}{\partial x_j}(\overline{u_j'T'}) = \alpha\frac{\partial^2 T'}{\partial x_j^2}. \tag{B.3}$$

Multiplying Equation (B.3) by T' and taking the time average, we obtain:

$$\overline{T'\left(\frac{\partial T'}{\partial t} + u_j'\frac{\partial \overline{T}}{\partial x_j} + u_j'\frac{\partial T'}{\partial x_j} + \overline{u}_j\frac{\partial T'}{\partial x_j} - \frac{\partial}{\partial x_j}(\overline{u_j'T'}) = \alpha\frac{\partial^2 T'}{\partial x_j^2}\right)}. \tag{B.4}$$

We note that:

$$\overline{T'\frac{\partial T'}{\partial t}} = \frac{\partial}{\partial t}(\frac{1}{2}\overline{T'^2}) = 0. \tag{B.5}$$

$$\overline{T'u_j'\frac{\partial \overline{T}}{\partial x_j}} = \overline{u_j'T'}\frac{\partial \overline{T}}{\partial x_j}. \tag{B.6}$$

$$\overline{T'u_j'\frac{\partial T'}{\partial x_j}} = \frac{\partial}{\partial x_j}(\frac{1}{2}\overline{u_jT'^2}) - \frac{1}{2}\overline{T'^2\frac{\partial u_j'}{\partial x_j}} = \frac{\partial}{\partial x_j}(\frac{1}{2}\overline{u_j'T'^2}). \tag{B.7}$$

$$\overline{T'\overline{u}_j\frac{\partial T'}{\partial x_j}} = \overline{u}_j\frac{\partial}{\partial x_j}(\frac{1}{2}\overline{T'^2}). \tag{B.8}$$

$$-\overline{T'\frac{\partial}{\partial x_j}(\overline{u_j'T'})} = -\overline{T'}\frac{\partial}{\partial x_j}(\overline{u_j'T'}) = 0. \tag{B.9}$$

$$\overline{T'\alpha\frac{\partial^2 T'}{\partial x_j^2}} = \alpha\left(\frac{\partial^2}{\partial x_j^2}\left(\frac{1}{2}\overline{T'^2}\right) - \overline{\frac{\partial T'}{\partial x_j}\frac{\partial T'}{\partial x_j}}\right). \tag{B.10}$$

Finally, we arrive at the equation for the production of temperature fluctuations:

$$\overline{u}_j\frac{\partial}{\partial x_j}\left(\frac{1}{2}\overline{T'^2}\right) = -\frac{1}{2}\frac{\partial}{\partial x_j}\left(\overline{u_j'T'^2} - \alpha\frac{\partial}{\partial x_j}\overline{T'^2}\right) - \overline{u_j'T'}\frac{\partial\overline{T}}{\partial x_j} - \alpha\left(\overline{\frac{\partial T'}{\partial x_j}\frac{\partial T'}{\partial x_j}}\right). \tag{B.11}$$

The divergence terms,

$$-\frac{1}{2}\frac{\partial}{\partial x_j}\left(\overline{u_j'T'^2} - \alpha\frac{\partial}{\partial x_j}\overline{T'^2}\right), \tag{B.12}$$

are simply transport terms and do not contribute to the generation of temperature fluctuations. The change in temperature fluctuation is determined by the gradient production term,

$$-\overline{u_j'T'}\frac{\partial\overline{T}}{\partial x_j}, \tag{B.13}$$

and the molecular dissipation term,

$$-\alpha\left(\overline{\frac{\partial T'}{\partial x_j}\frac{\partial T'}{\partial x_j}}\right). \tag{B.14}$$

Since molecular dissipation is always positive, turbulent temperature fluctuation can be generated only by the gradient production term (Equation B.13).

For the phase average temperature fluctuations, the production equation becomes:

$$\frac{1}{2}\left(\frac{\partial}{\partial t}\langle T_r''^2\rangle + \langle u_j\rangle\frac{\partial}{\partial x_j}\langle T_r''^2\rangle\right) = \tag{B.15}$$

$$-\frac{1}{2}\frac{\partial}{\partial x_j}\left(\langle u_r'T_r'\rangle - \alpha\frac{\partial}{\partial x_j}\langle T_r''^2\rangle\right) - \langle u_r'T_r'\rangle\frac{\partial\langle T\rangle}{\partial x_j} - \alpha\left\langle\frac{\partial T_r'}{\partial x_j}\frac{\partial T_r'}{\partial x_j}\right\rangle.$$

Again, we note that temperature fluctuations can be only generated by the gradient production term:

$$-\langle u_r'T_r'\rangle\frac{\partial\langle T\rangle}{\partial x_j}. \tag{B.16}$$

# Appendix C

# Control Volume Analysis of Heat Release

The drag of a body can be computed using a control volume balance of momentum. Similarly, the heat release of a body can be computed using a control volume balance of energy. The energy or the heat balance within a control volume can be derived starting from the differential form of the mean heat equation. The mean heat equation for an incompressible fluid with constant k and $C_p$ is:

$$\rho C_p\left[\bar{u}_j\frac{\partial\bar{T}}{\partial x_j}+\frac{\partial}{\partial x_j}(\overline{u_j'T'}-k\frac{\partial\bar{T}}{\partial x_j})\right]=q, \qquad (C.1)$$

where q is the heat source per unit mass. The equation assumes that Ec→0 and Ec/Re→0, or the change of energy is mainly due to change in temperature, and the viscous dissipation is negligible. Using continuity and integrating Equation (C.1) over a fixed volume, we arrive at:

$$\rho C_p\iiint\left[\frac{\partial}{\partial x_j}(\bar{u}_j\bar{T}+\overline{u_j'T'}-k\frac{\partial\bar{T}}{\partial x_j})\right]dV=\iiint q\,dV. \qquad (C.2)$$

The volume integral on the left side of Equation (C.2) can be converted into a surface integral using the Divergence Theorem to give:

$$\rho C_p\iint\left[(\bar{u}_j\bar{T}+\overline{u_j'T'}-k\frac{\partial\bar{T}}{\partial x_j})\bullet\vec{n}\right]dS=Q. \qquad (C.3)$$

The volume integral of the heat source term has been replaced by Q which is the total heat release within the control volume. For a flow with uniform properties along the z-direction, we can write the heat balance per unit length as:

$$\rho C_p L\int\left[(\bar{u}_j\bar{T}+\overline{u_j'T'}-k\frac{\partial\bar{T}}{\partial x_j})\bullet\vec{n}\right]d\ell=Q, \qquad (C.4)$$

where L is the length in z-direction.

For the case of a heated circular cylinder, we can choose a stationary control volume as shown in Fig. C.1. The contour integral around the control volume can be broken up into four integrals, $I_1$, $I_2$, $I_3$, and $I_4$. The upstream integral, $I_1$, becomes:

$$I_1 = -\rho C_p L \int_0^H U_\infty T_\infty dy, \tag{C.5}$$

since far upstream, the velocity and temperature is uniform at freestream conditions. The downstream integral, $I_4$, becomes:

$$I_4 = \rho C_p L \int_0^H \left[ \overline{u}_x \overline{T} + \overline{u_x' T'} - k \frac{\partial \overline{T}}{\partial x} \right] dy. \tag{C.6}$$

The two side integrals:

$$I_2 = I_3 = \rho C_p L \int_0^R \left[ \overline{u}_y \overline{T} + \overline{u_y' T'} - k \frac{\partial \overline{T}}{\partial y} \right] dx, \tag{C.7}$$

can be computed by assuming that far from the body, the temperature is uniform, or:

$$I_2 + I_3 = 2\rho C_p \int_0^R \overline{u}_y T_\infty dx = \dot{m} C_p L T_\infty, \tag{C.8}$$

and the mass flux out of the control volume, $\dot{m}$, is:

$$\dot{m} = \rho \int_0^H (\overline{u}_x - U_\infty) dy. \tag{C.9}$$

Collecting terms and simplifying, the heat release of the cylinder, Q, can be computed by:

$$\rho C_p L \int_0^H \left[ \overline{u}_x (\overline{T} - T_\infty) + \overline{u_x' T'} - k \frac{\partial \overline{T}}{\partial x} \right] dy = Q. \tag{C.10}$$

Thus using a similar method to a wake velocity survey for the computation of its drag, the heat release of a cylinder can be computed by a wake survey of the velocity and the temperature, i.e., the heat flux.

# Appendix D

# Effect of Heating on the Wake

The ratio of the Grashof number versus the square of the Reynolds number, $Gr/Re^2$, determines the relative magnitudes of the buoyancy forces versus the inertial forces in the momentum equation. Therefore, to avoid changes in the near wake flow structure, the ratio $Gr/Re^2$ must be minimized.

In all the experiments described within the thesis, the ratio $Gr/Re^2$ was kept under 0.05. While this value is low, an experiment is conducted to verify that the heating does not affect the flow structure of the near wake. The velocity field of the near wake of a circular cylinder is measured with and without heating to determine if any changes to the flow occurs. The ratio $Gr/Re^2$ is chosen to be 0.1, a value much higher than those used during the actual set of heat transport experiments.

The changes in the wake structure can determined by a comparison of the mean two velocity fields of the heated and unheated cylinder which are shown in Fig. D.1 and D.2, respectively. In both cases, the closure points of the wake bubble are measured to be x/D=2.5, and no significant difference is observed. The slight upward tilting of the wake in both cases is not due to buoyancy, but due to the slight tilt of the camera. The changes in the dynamic structure of the wake can determined by a comparison of the velocity fluctuations which are shown in Fig. D.3 through D.6. The locations and the magnitudes of the contours of these quantities are all within the experimental uncertainty. It is therefore concluded that the effect of heating had negligible effect on the mean and the dynamic structure of the near wake of a circular cylinder.

# References

Bearman, P. W., 1969, On vortex shedding from a circular cylinder in the critical Reynolds number regime, *Journal of Fluid Mechanics*, **37**, pp. 577-586

Behle, M., Schulz, K., Leiner W., Fiebig, M., 1996, Color-based image processing to measure local temperature distributions by wide-band liquid Crystal thermography, *Applied Scientific Research*, **56**, pp. 113-143

Bloor, S., 1964, The transition to turbulence in the wake of a circular cylinder, *Journal of Fluid Mechanics*, **19**, pp. 290-304

Camci, C., Kim, K., Hippensteele, S. A., 1992, A new hue capturing technique for the quantitative interpretation of liquid crystal images used in convective heat transfer studies, *Journal of Turbomachinery*, **114**, pp. 765-775

Cantwell, B., Coles, D., 1983, An experimental study of entrainment and transport in the turbulent near wake of a circular cylinder, *Journal of Fluid Mechanics*, **136**, pp. 321-374

Cheng C. H., Chen, H. N., Aung, W., 1997, Experimental study of the effect of transverse oscillation on convection heat transfer from a circular cylinder, *Journal of Heat Transfer*, **119**, pp. 474-482

Cheng C. H., Hong J. L., 1997, Numerical prediction of lock-on effect on convective heat transfer from a transversely oscillating circular cylinder, *Int. Journal of Heat Mass Transfer*, **40**, pp. 1825-1834

Dabiri, D., Gharib, M., 1991, Digital particle image thermometry: The method and implementation, *Experiments in Fluids*, **11**, pp. 77-86

Dimotakis, P.E., 1991, Turbulent free shear layer mixing and combustion, *Progress in Astronautics and Aeronautics*, **137**, pp. 265-340

Eckert, E. R. G., Soehngen, E., 1952, Distribution of heat transfer coefficients around circular cylinder in crossflow at Reynolds numbers from 20 to 500, *Transactions of the ASME*, **74**, pp. 343-347

Farina, D. J., Hacker, J. M., Moffat, R. J., Eaton, J. K., 1994, Illuminant invariant calibration of thermochromic liquid crystals, *Experimental Thermal and Fluid Science*, **9**, pp. 1-12

Feragson, J. L., 1968, Liquid crystals in nondestructive testing, *Applied Optics*, **7**, pp. 1729-1737

Franke, R., Rodi, W., Schonung, B., 1989, Analysis of experimental vortex-shedding data with respect to turbulence modeling, *Proceedings of 7th Symposium on Turbulent Shear Flows, Stanford University*, pp. 24.4.1-24.4.5

Fureby, C., Tabor, G., Weller, H. G., Gosman, A. D., 1997, A comparative study of subgrid scale models in homogeneous isotropic turbulence, *Physics of Fluids*, **9**, pp. 1416-1429

Hay, J. L., Hollingsworth, D. K., 1996, A comparison of trichromic Systems for use in the calibration of polymer-dispersed thermochromic liquid crystals, *Experimental Thermal and Fluid Science*, **12**, pp. 1-12

Hiller, W. J., Koch, ST., Kowalewski, T. A., Stella, F., 1993, Onset of natural convection in a cube, *International Journal of Heat Mass Transfer*, **36**, pp. 3251-3263

Huang, H., 1997, Private communications, GALCIT, California Institute of Technology

Karanth D., Rankin, G. W., Sridhar, K., 1994, A finite difference calculation of forced convective heat transfer from an oscillating cylinder, *Int. Journal of Heat Mass Transfer*, **37**, pp. 1619-1630

Karniadakis, G. E., 1997, Private Communication, Brown University

Karniadakis, G. E., Brown, G. L., 1995, Vorticity transport in modeling three-dimensional unsteady shear flows, *Physics of Fluids*, **7**, pp. 688-690

Kezios, S. P., Prasanna, K. V., 1966, Effect of vibration on heat transfer from a cylinder in normal flow, *ASME Paper* No. 66-WA/HT-43

Kimura, I., Kuroe, Y., Ozawa, M., 1993, Application of neural networks to quantitative flow visualization, *Journal of Flow Visualization and Image Processing*, **1**, pp. 261-269.

Launder, B. E., Spalding, D. B., 1974, The numerical computation of turbulent flows, *Computational Methods in Applied Mechanical Engineering*, **3**, pp. 269-289

Liu, S., Meneveau, C., Katz, J., 1994, On the properties of similarity subgrid-scale models as deduced from measurements in a turbulent jet, *Journal of Fluid Mechanics*, **275**, pp. 83-119

Martinelli, R. C., Boelter, L. M. K., 1938, The effect of vibration on heat transfer by free convection from a horizontal cylinder, *Proceedings of 5th International Congress of Applied Mechanics*, p. 578

Matsumura, M., Antonia, R. A., 1993, Momentum and heat transport in the turbulent intermediate wake of a circular cylinder, *Journal of Fluid Mechanics*, **250**, pp. 651-668

McAdams, W. H., 1954, *Heat Transmission*, McGraw-Hill, New York, p. 260

Miller, P. L., 1991, Mixing in high schmidt number turbulent jets, *Ph.D. thesis*, California Institute of Technology

Noca, F., Park, H. G., Gharib, M., 1998, Vortex formation length of a circular cylinder (300 < Re < 4,000) using DPIV, *Proceedings of ASME Fluids Engineering Division Summer Meeting*, Paper FEDSM98-5149

Norberg, C., 1994, An experimental investigation of the flow around a circular cylinder: Influence of aspect ratio, *Journal of Fluid Mechanics*, **275**, pp. 258-287.

Ongoren, A., Rockwell, D., 1988, Flow structure from an oscillating cylinder Part 1. Mechanisms of phase shift and recovery in the near wake, *Journal of Fluid Mechanics*, **191**, pp. 197-223

Parsley, M., 1991, *The Hallcrest Handbook of Thermochromic Liquid Crystal Technology*, Hallcrest, Glenview, IL

Perry, A. E., Chong, M. S., Lim, T. T., 1982, The vortex-shedding process behind two-dimensional bluff bodies, *Journal of Fluid Mechanics*, **116**, pp. 77-90

Perry, A. E., Fairlie, B. D., 1974, Critical points in flow patterns, *Advances in Geophysics*, **18B**, pp. 299-315

Reynolds, W. C., Hussain, A. K. M. F., 1972, The mechanism of an organized wave in turbulent shear flow. Part 3. Theoretical models and comparisons with experiments, *Journal of Fluid Mechanics*, **54**, pp. 263-288

Roshko, A., 1992, Instability and turbulence in Sshear flows, Theoretical and Applied Mechanics, Elsevier Science Publishers B.V.

Roshko, A., 1993, Perspectives on bluff body aerodynamics, *Journal of Wind Engineering and Industrial Aerodynamics*, **49**, pp. 79-100

Saxena, U. C., Laird, A. D. K., 1978, Heat transfer from a cylinder oscillating in a cross-flow, *Transactions of the ASME*, **100**, pp. 684-689

Smagorinsky, J., 1963, General circulation experiments with the primitive equations, *Monthly Weather Review*, **93**, pp. 99-165

Sreenivasan, K., Ramachandran, A., 1961, Effect of vibration on heat transfer from a horizontal cylinder to a normal air stream, *Int. Journal of Heat Mass Transfer*, **3**, pp. 60-67

Taneda, S., 1956, Experimental investigation of the wakes behind cylinders and plates at low Reynolds numbers, *Journal of Physical Society of Japan*, **11**, p. 302

Tennekes, H., Lumley, J. L., 1972, *A first course in turbulence*, The MIT Press, Cambridge, Massachusetts

Willert, C. E., Gharib, M., 1991, Digital particle image velocimetry, *Experiments in Fluids*, **10**, pp. 181-193

Williamson, C. H. K, 1988, The existence of two stages in the transition to three dimensionality of a cylinder wake, *Physics of Fluids*, **31**, p. 3165

Williamson, C. H. K., Roshko, A., 1988, Vortex formation in the wake of an oscillating cylinder, *Journal of Fluids and Structures*, **2**, pp. 355-381

# FIGURES

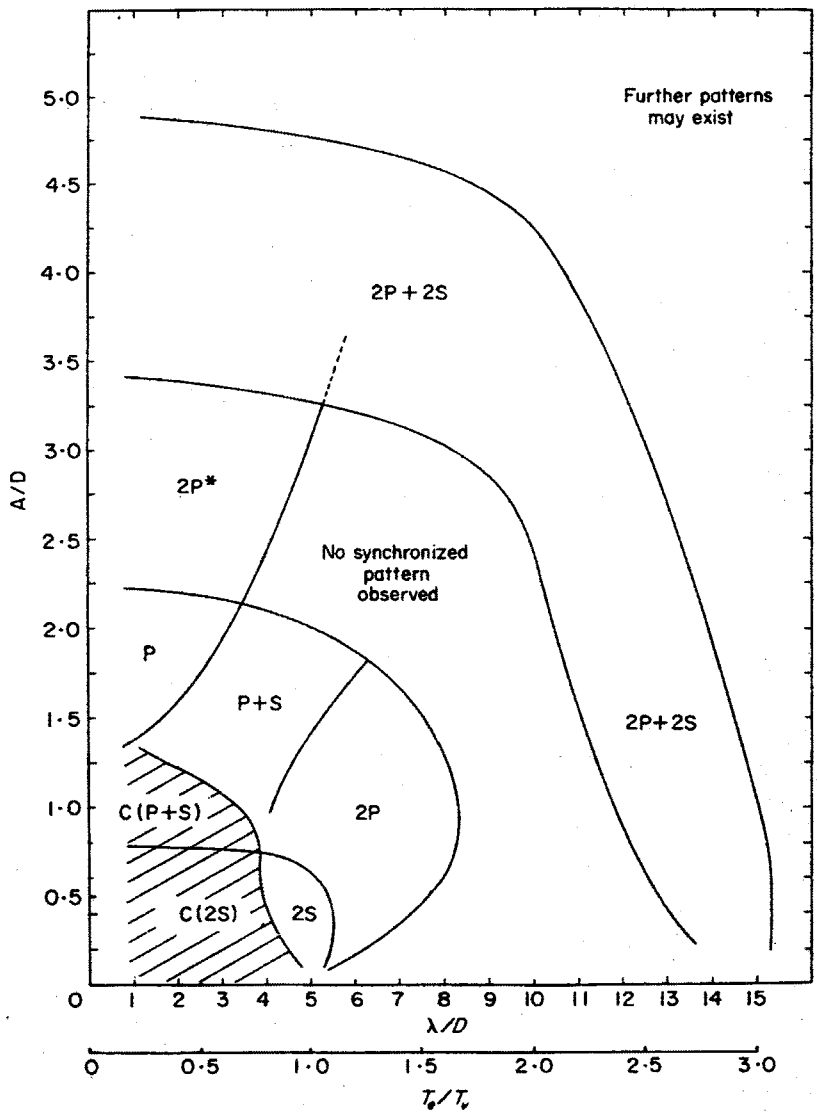


Figure 1.1(a). Map of vortex synchronization regions as function of A/D and $T_e/T_v$ for a forced oscillating cylinder. $T_e$ and $T_v$ are the cylinder oscillation and the vortex shedding frequency of a stationary cylinder, respectively. From Williamson and Roshko (1988).

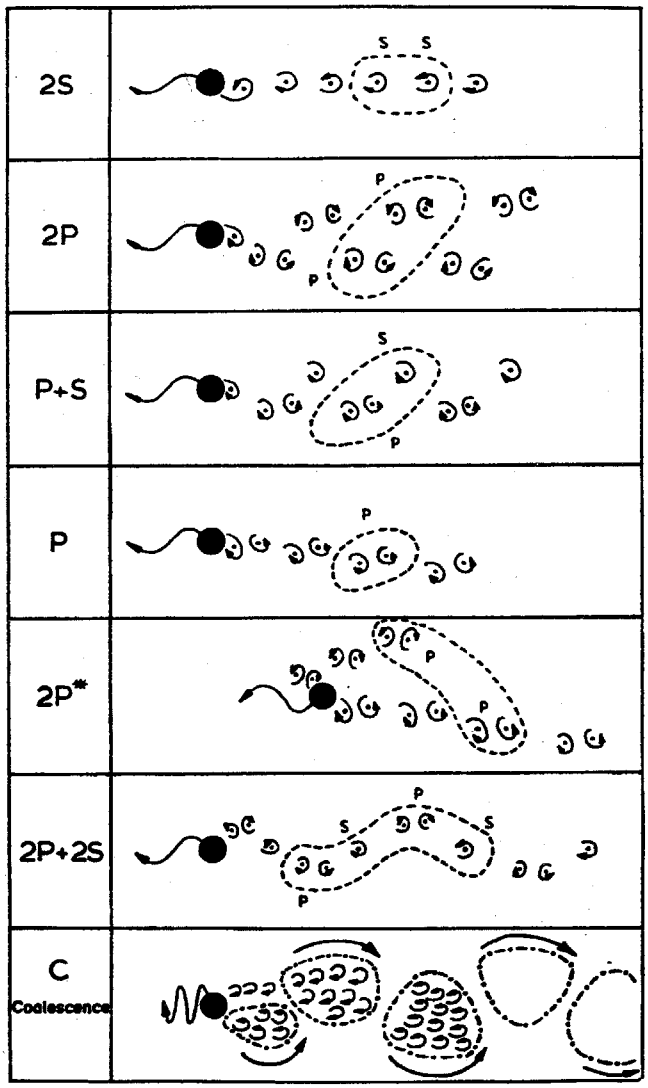


Figure 1.1(b). Sketches of the vortex shedding patterns in the map shown in (a). "P" and "S" stand for vortex pair and a single vortex. The dashed lines encircle the vortices shed in one complete cycle. From Williamson and Roshko (1988).

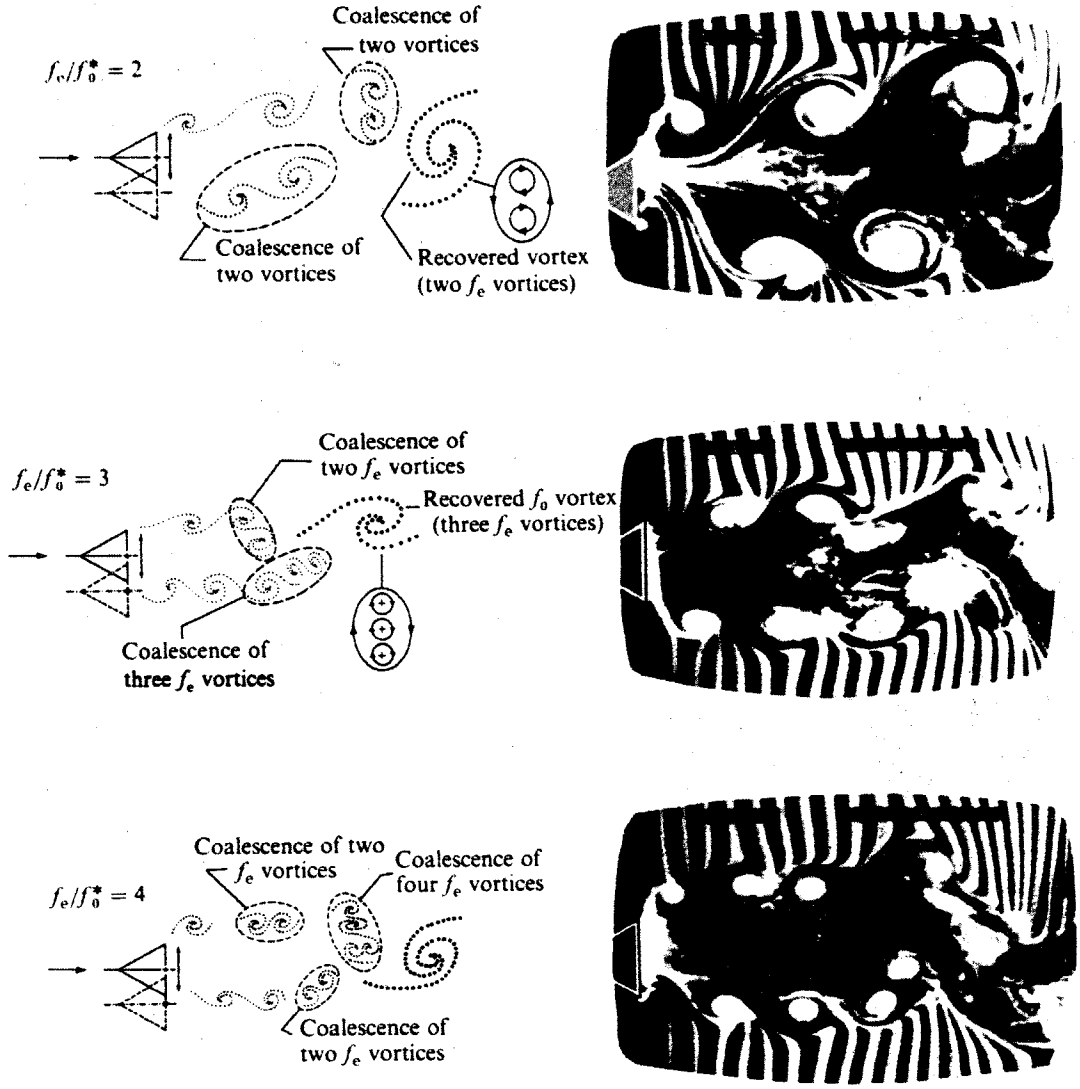


Figure 1.2. Schematics and photos showing vortex merging process for cylinder oscillation frequencies which are integer multiples of the large-scale vortex shedding frequency ($f_e/f_o^*$). From Ongoren and Rockwell (1988).

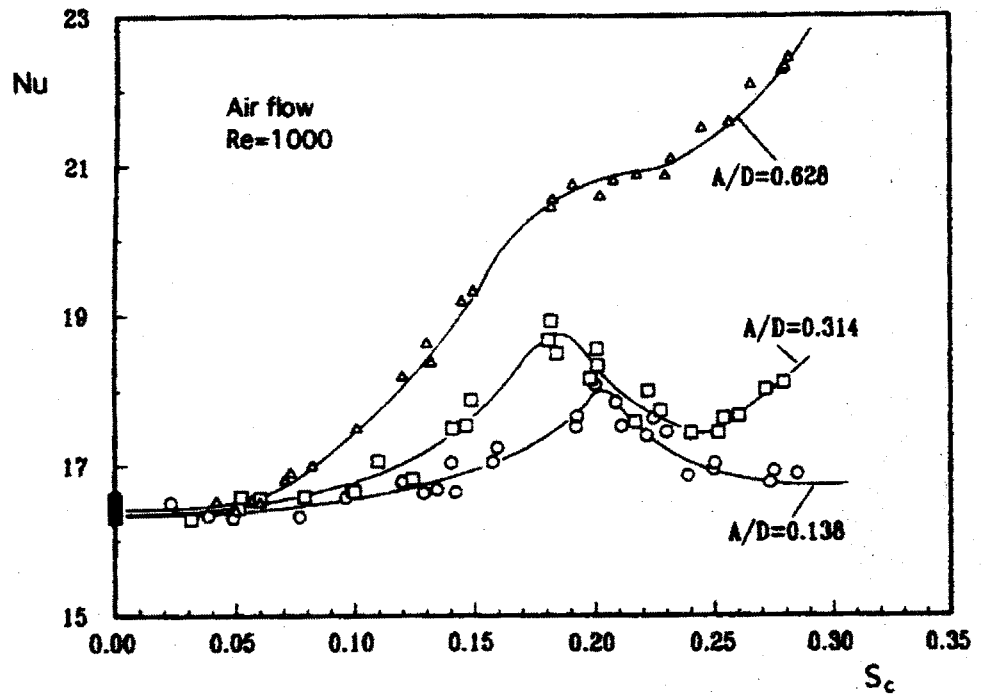


Figure 1.3. Variation of Nusselt number as function of forced oscillation frequency and amplitude of a circular cylinder at Re=1000. $S_c$ is defined as $f_cD/U_\infty$, where $f_c$ is the oscillation frequency of the cylinder. From Cheng et al. (1997).

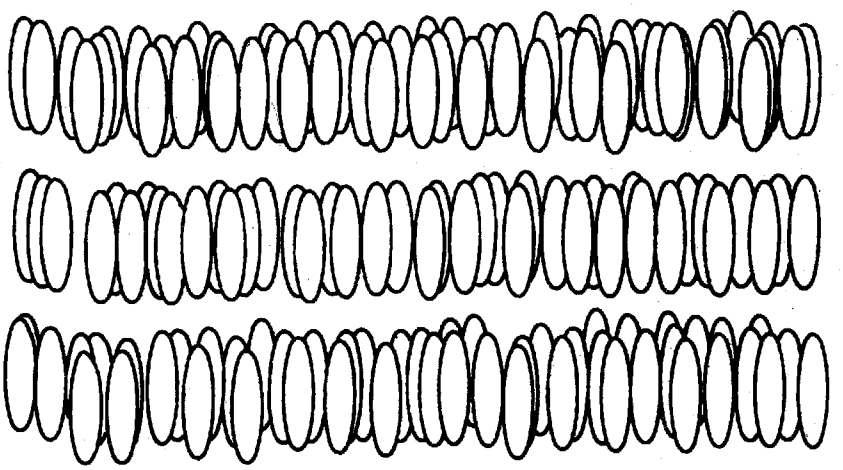

Figure 2.1(a) Orientation of TLC molecules in smetic phase. From Parsley (1991).

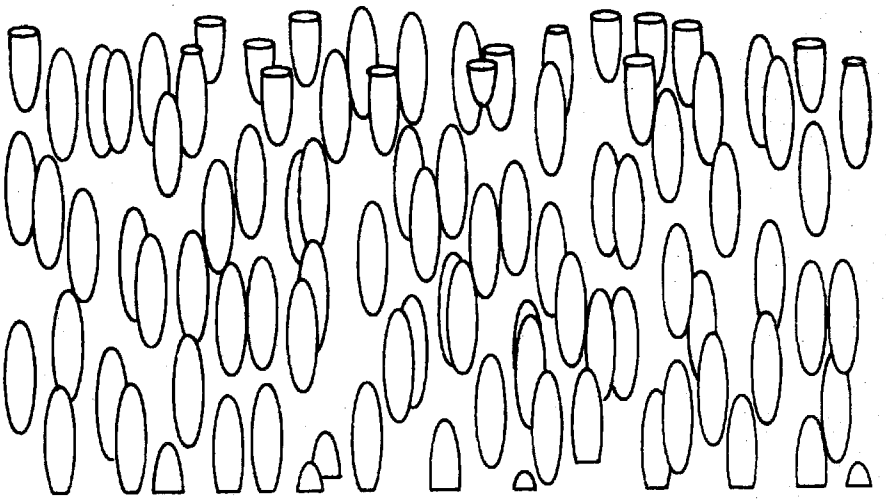

Figure 2.1(b) Orientation of TLC molecules in nematic phase. From Parsley (1991).

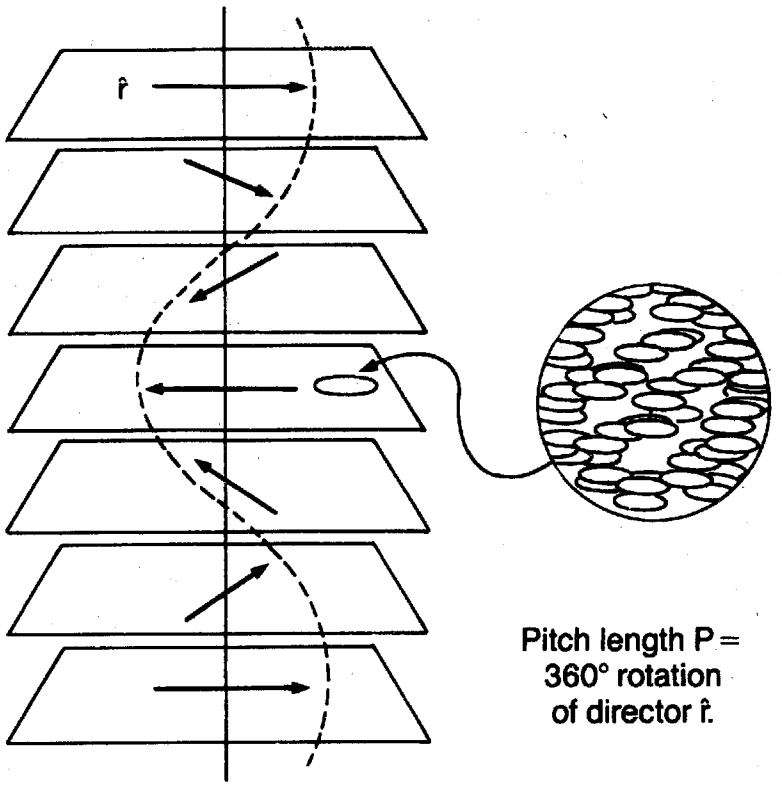


Figure 2.2 Helical structure of TLC molecules. From Parsley (1991).

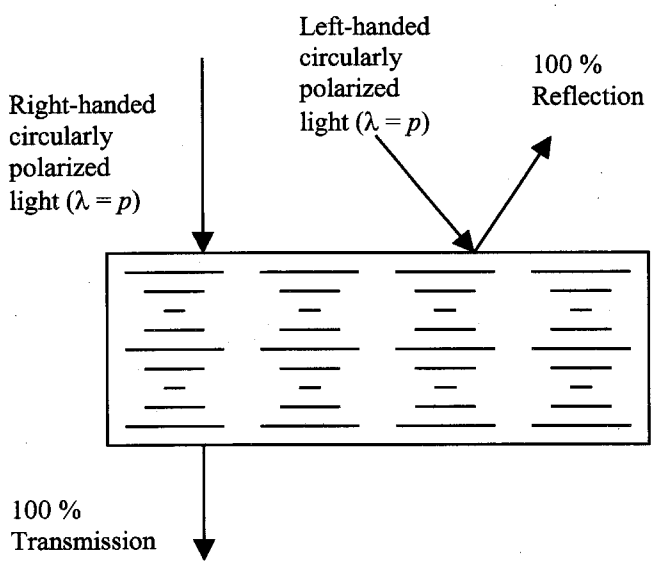


Figure 2.3 Transmission and reflectance characteristics of TLC molecules. From Parsley (1991).

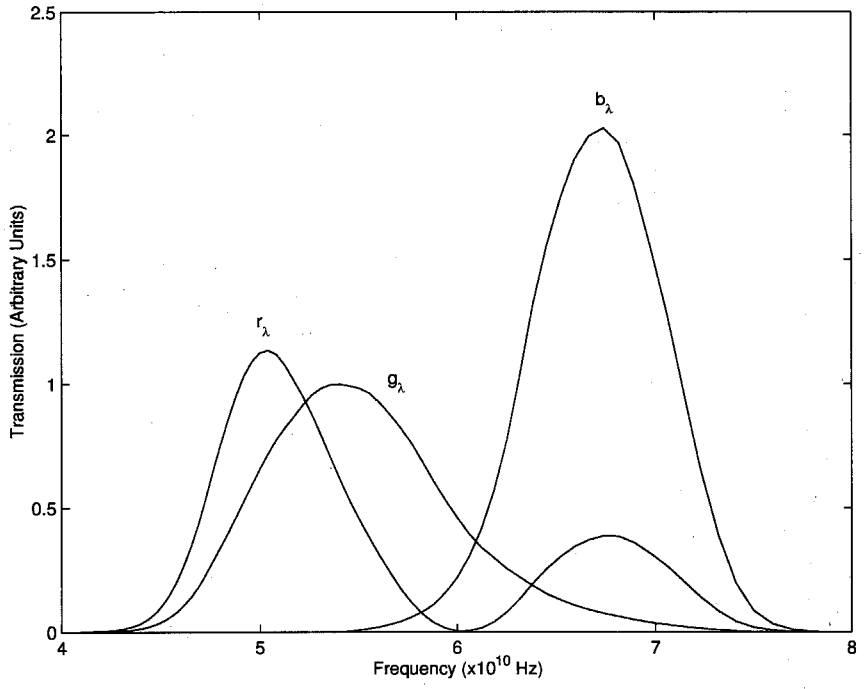


Figure 2.4 Transmission curves of NTSC color filters.

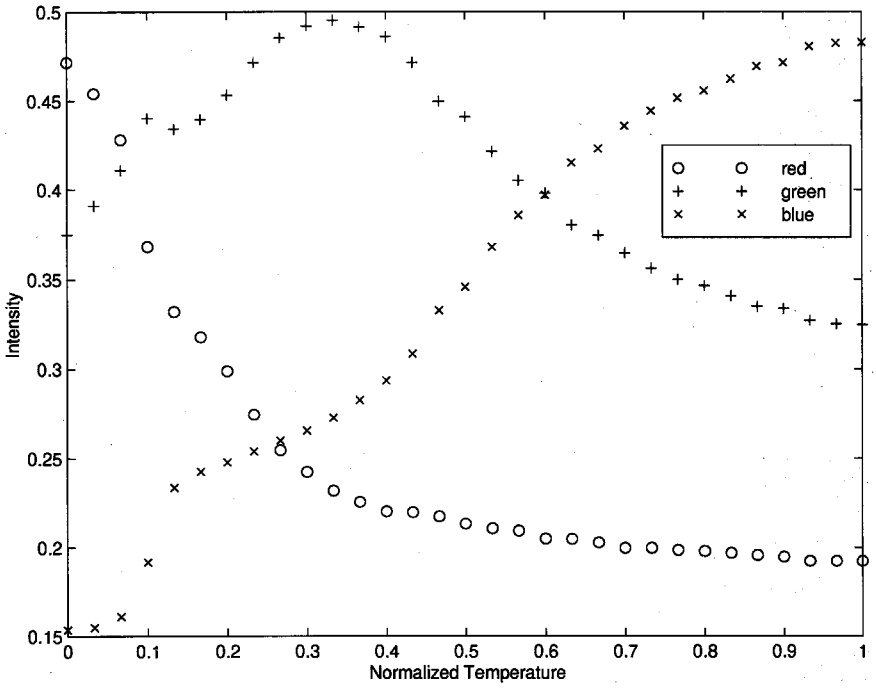


Figure 2.5 Typical curves of r, g, and b channels as function of temperature for TLC particles. The temperature is normalized by $(T - T_{min})/(T_{max} - T_{min})$, where $T_{min}$ and $T_{max}$ are the minimum and maximum temperatures in the range of TLC particles, respectively.

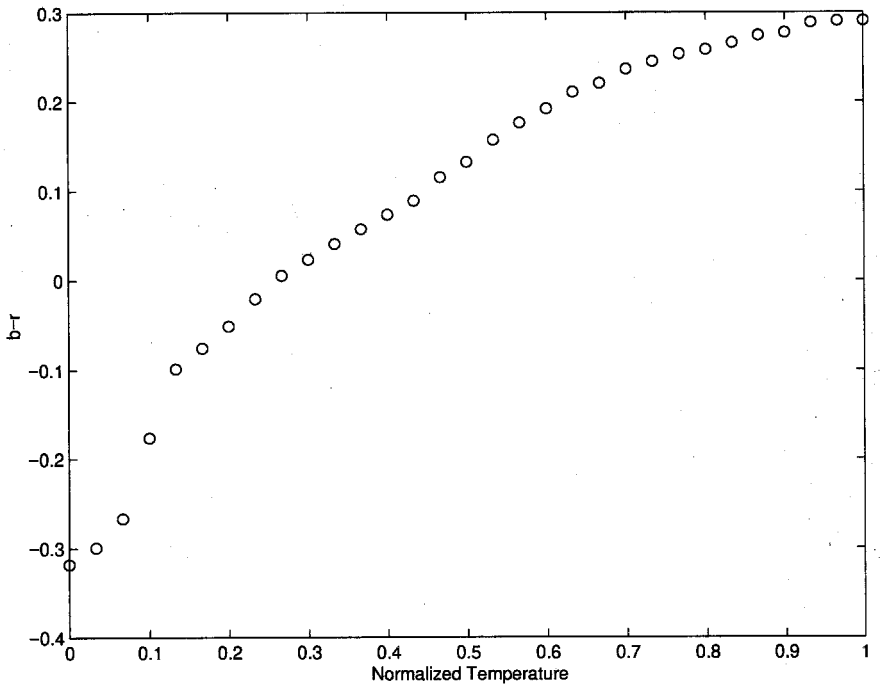


Figure 2.6 Curve of (b – r) derived from the r g b curves in Fig. 2.5.

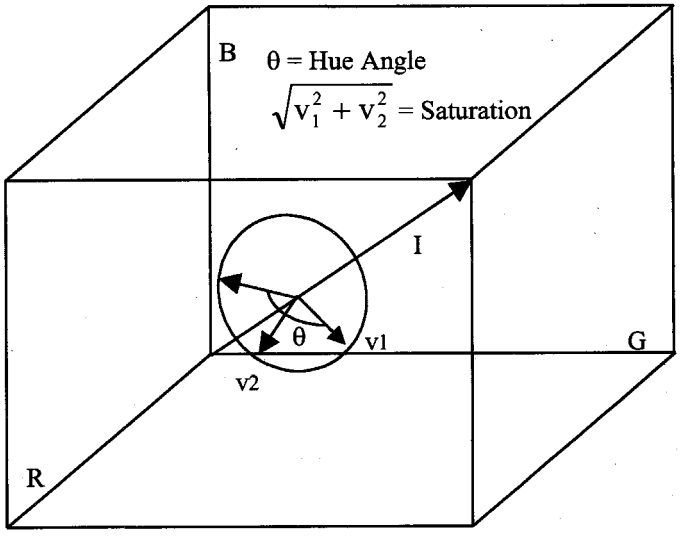


Figure 2.7 H S I color space in relation to R G B color space.

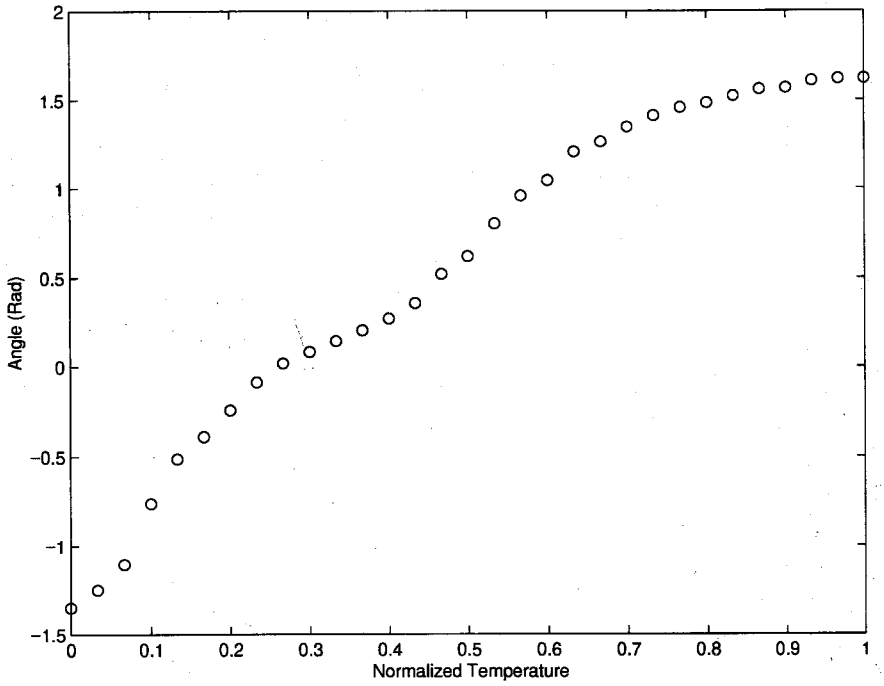


Figure 2.8 Hue as function of temperature generated from r g b curves in Fig. 2.5.

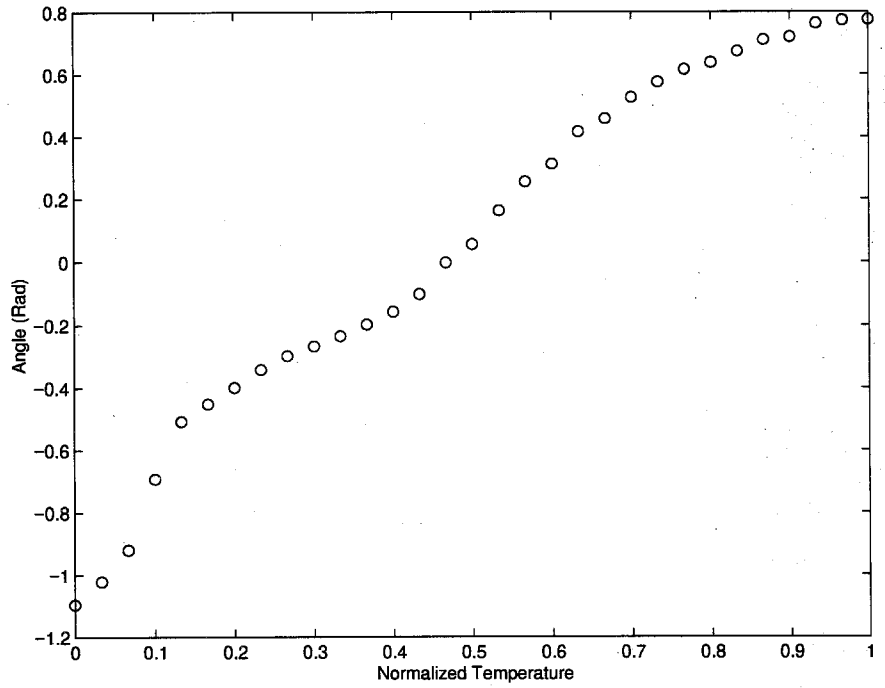


Figure 2.9 Hue as defined by Farina et al. (1994) as function of temperature generated from r g b curves of Fig 2.5

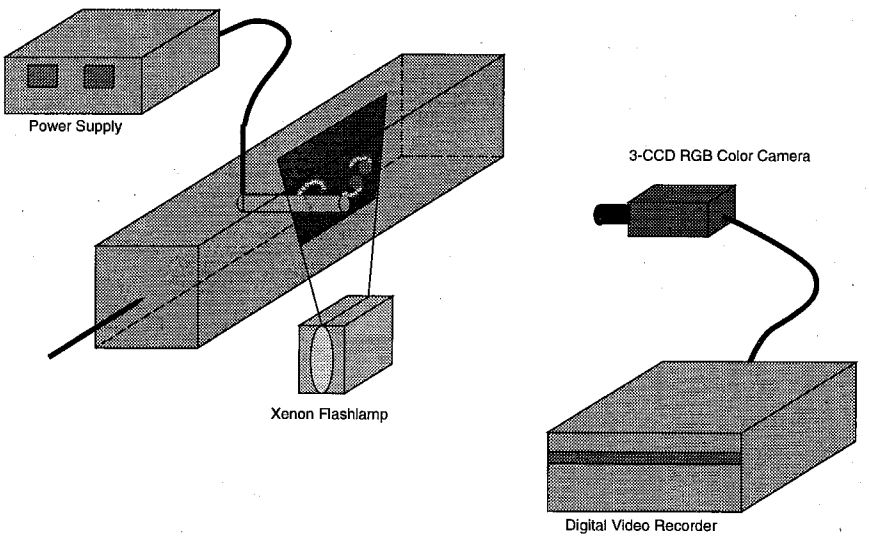


Figure 2.10 DPIV/T experimental setup.

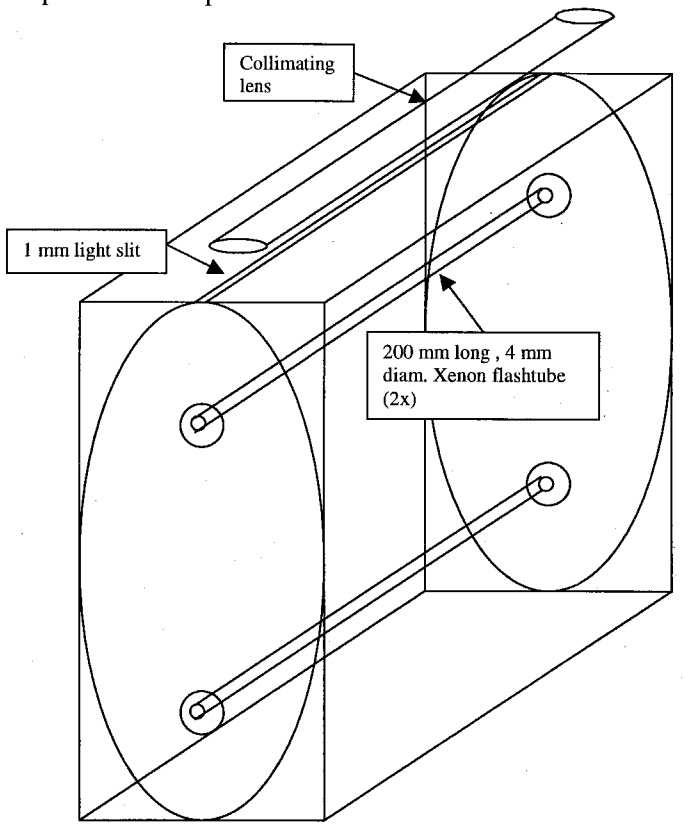


Figure 2.11 Elliptical xenon light reflector assembly.

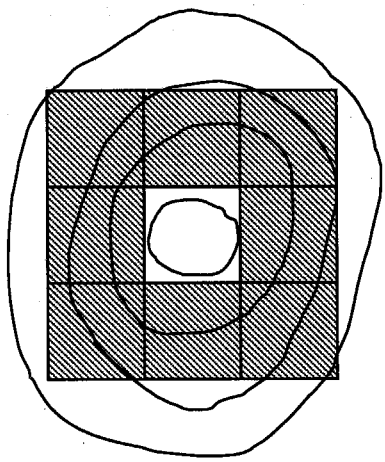

Figure 2.12 Eight nearest neighboring pixels surrounding the centroid pixel.

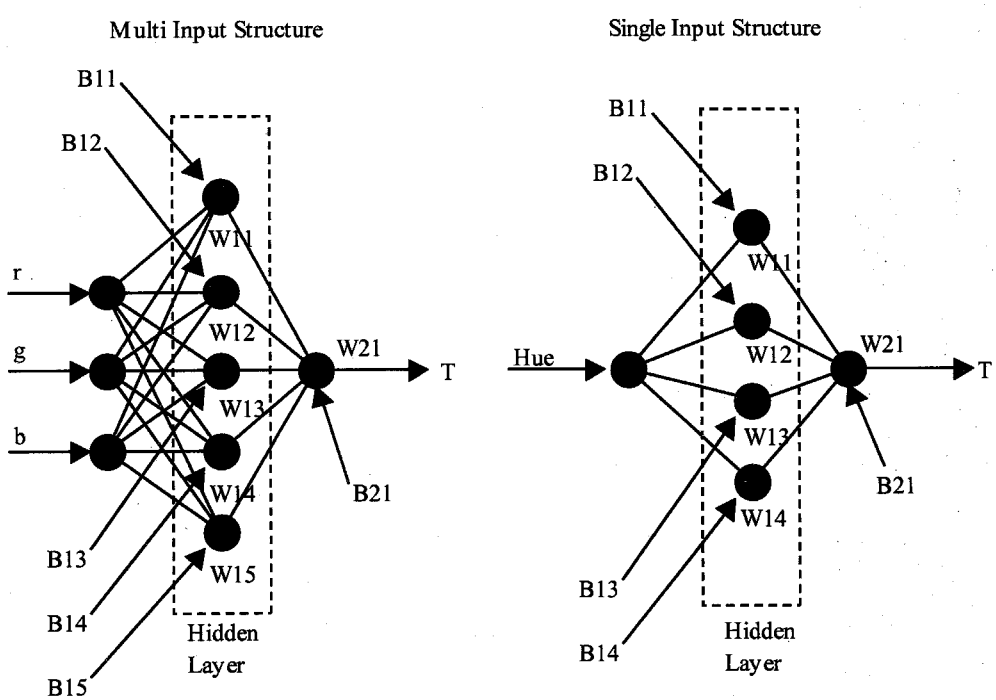


Figure 2.13 Neural network configuration.

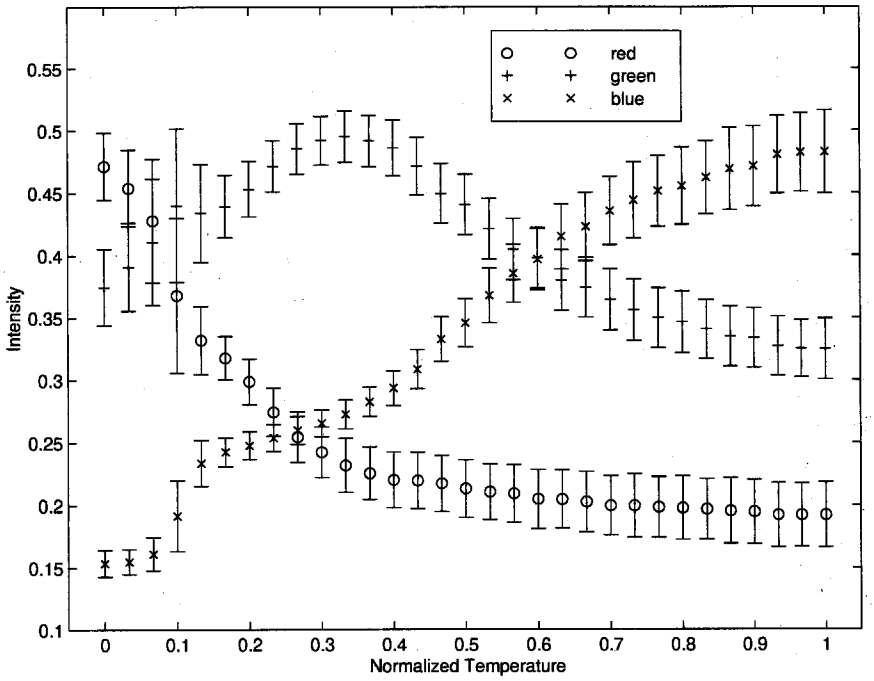


Figure 2.14 Scatter in r g b as function of temperature.

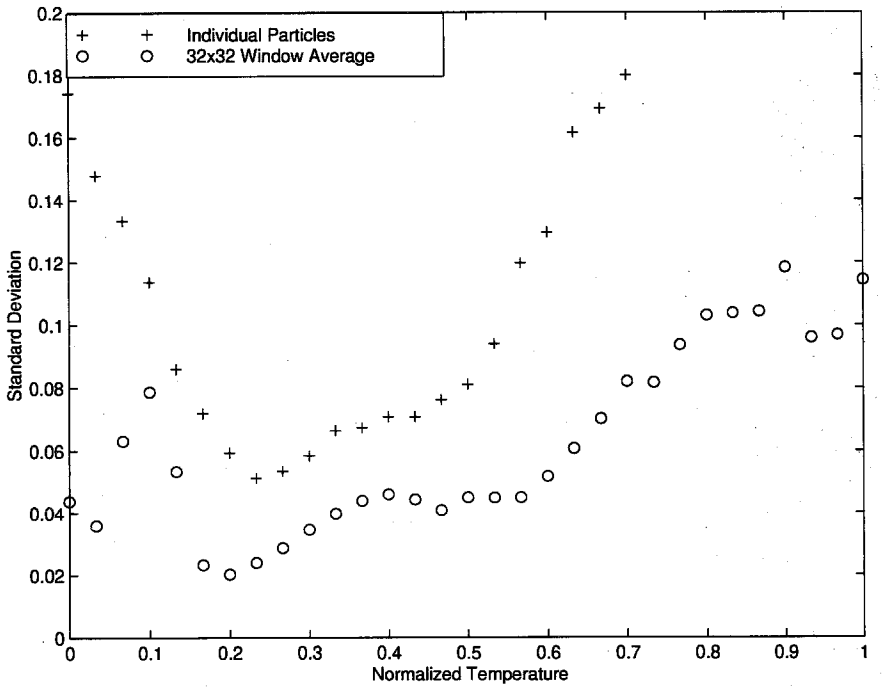


Figure 2.15 Uncertainty in the computed temperature using calibration curves of r g b.

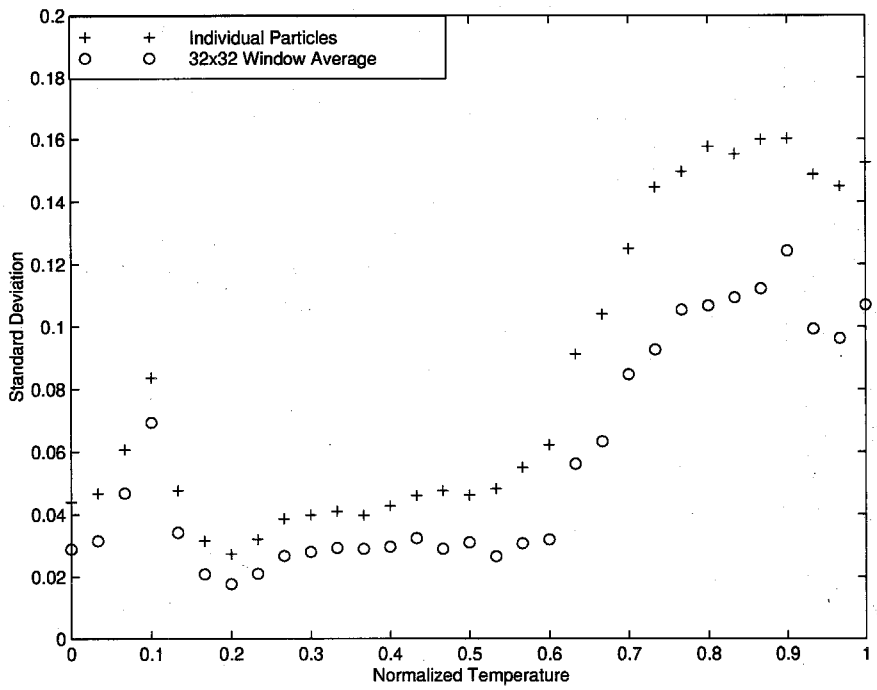


Figure 2.16 Uncertainty in the computed temperature using calibration curve of standard hue.

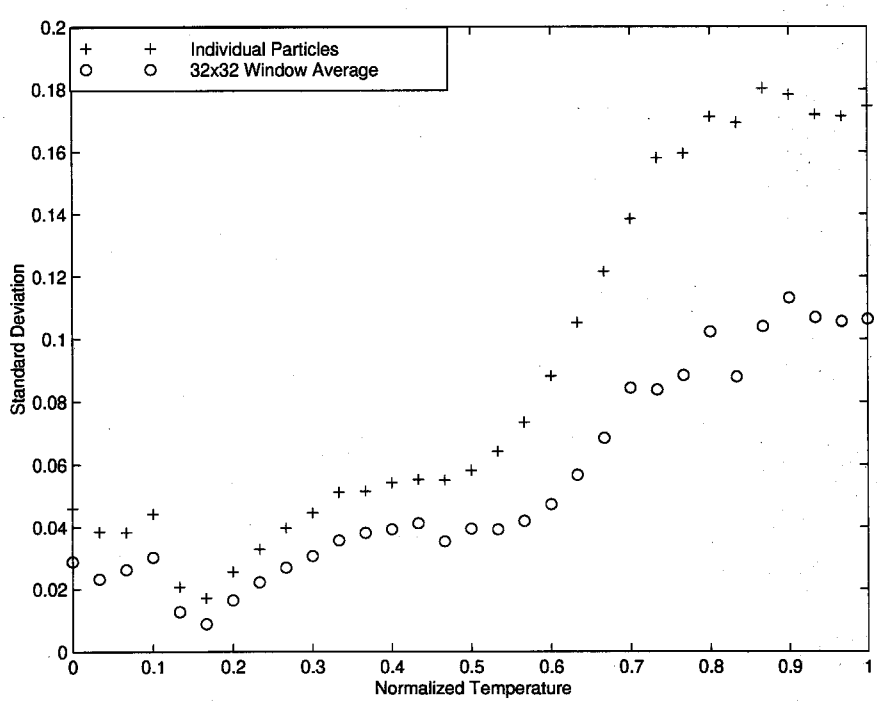


Figure 2.17 Uncertainty in the computed temperature using calibration curve of (b – r).

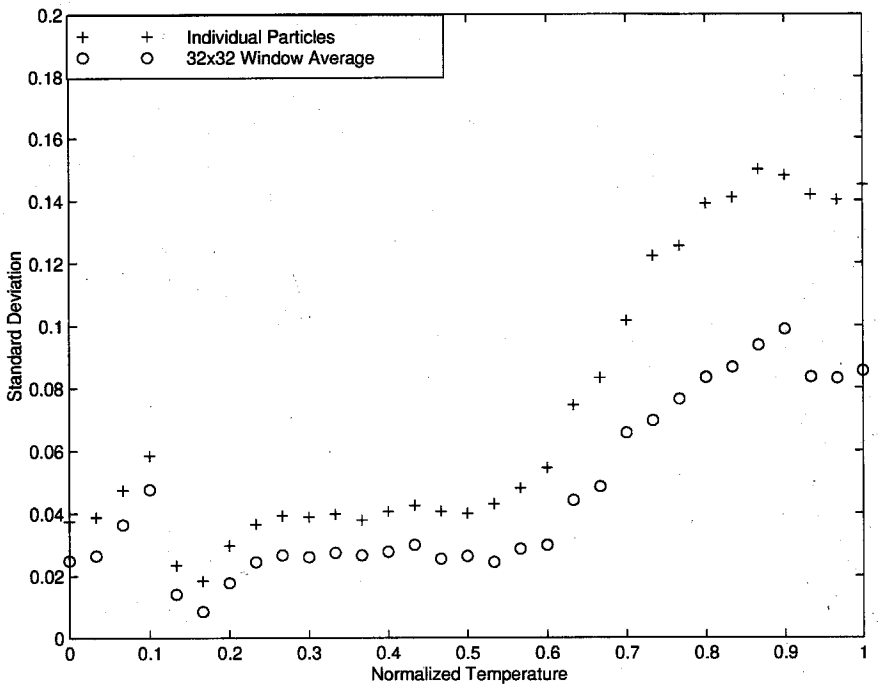


Figure 2.18 Uncertainty in the computed temperature using calibration curve of hue defined by Farina et al. (1994).

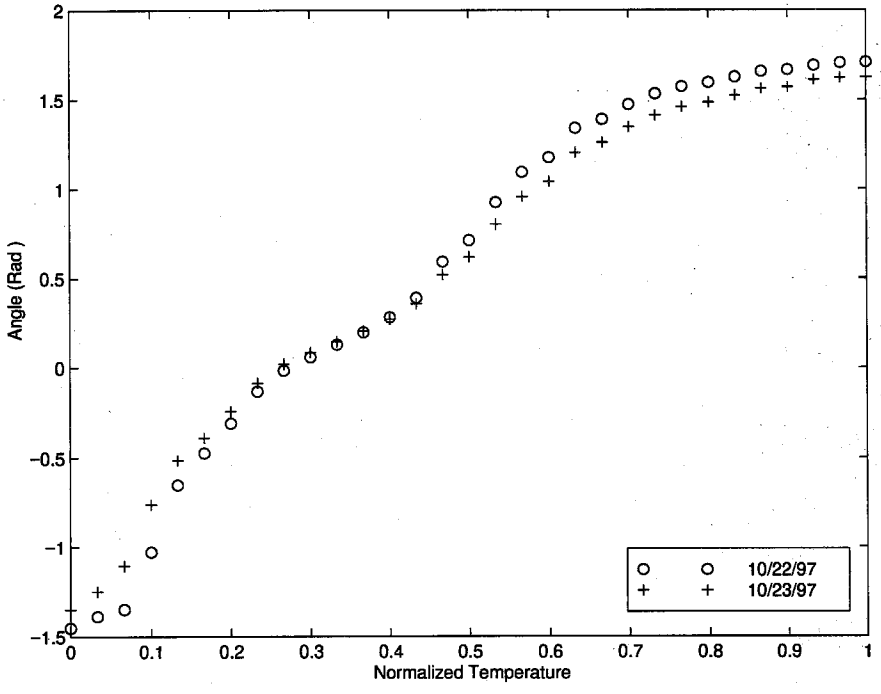


Figure 2.19 Shift in the calibration curve (standard hue) after one day of exposure to water.

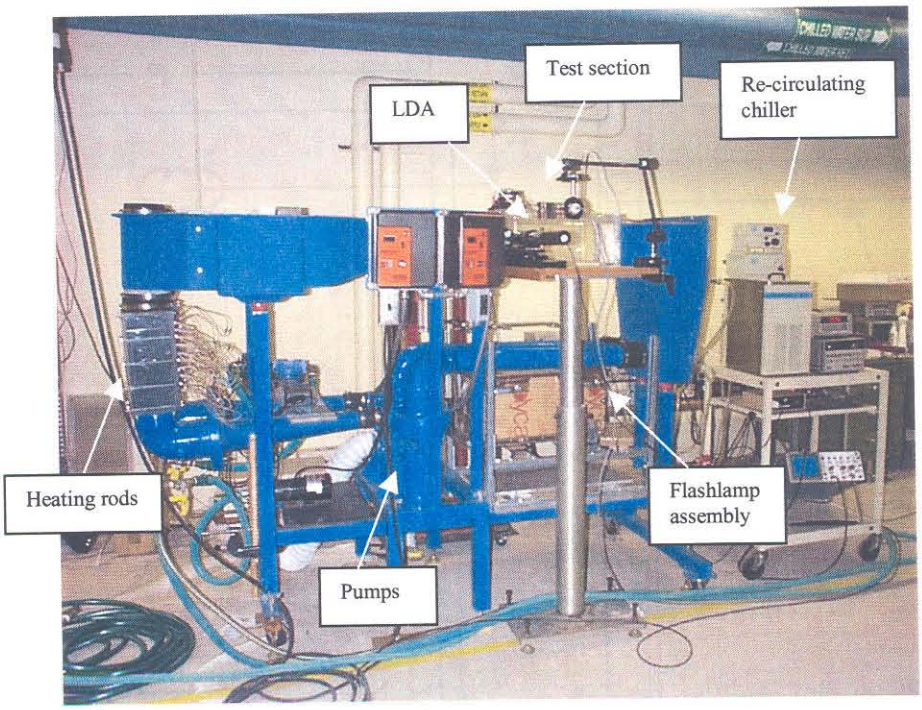


Figure 3.1 Water tunnel facility

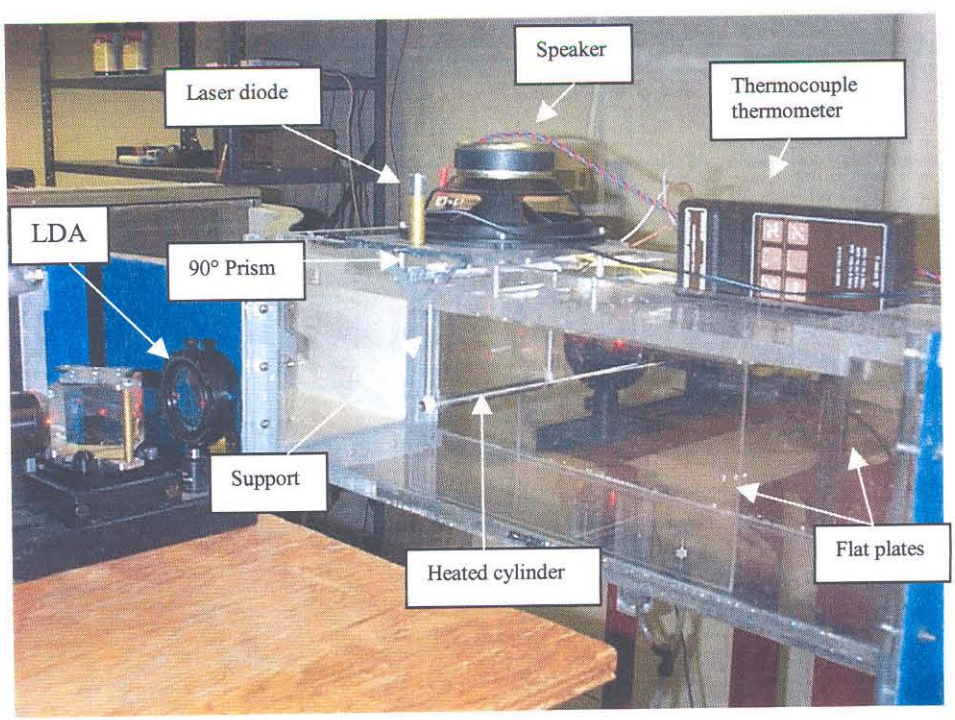


Figure 3.2 Oscillating cylinder assembly.

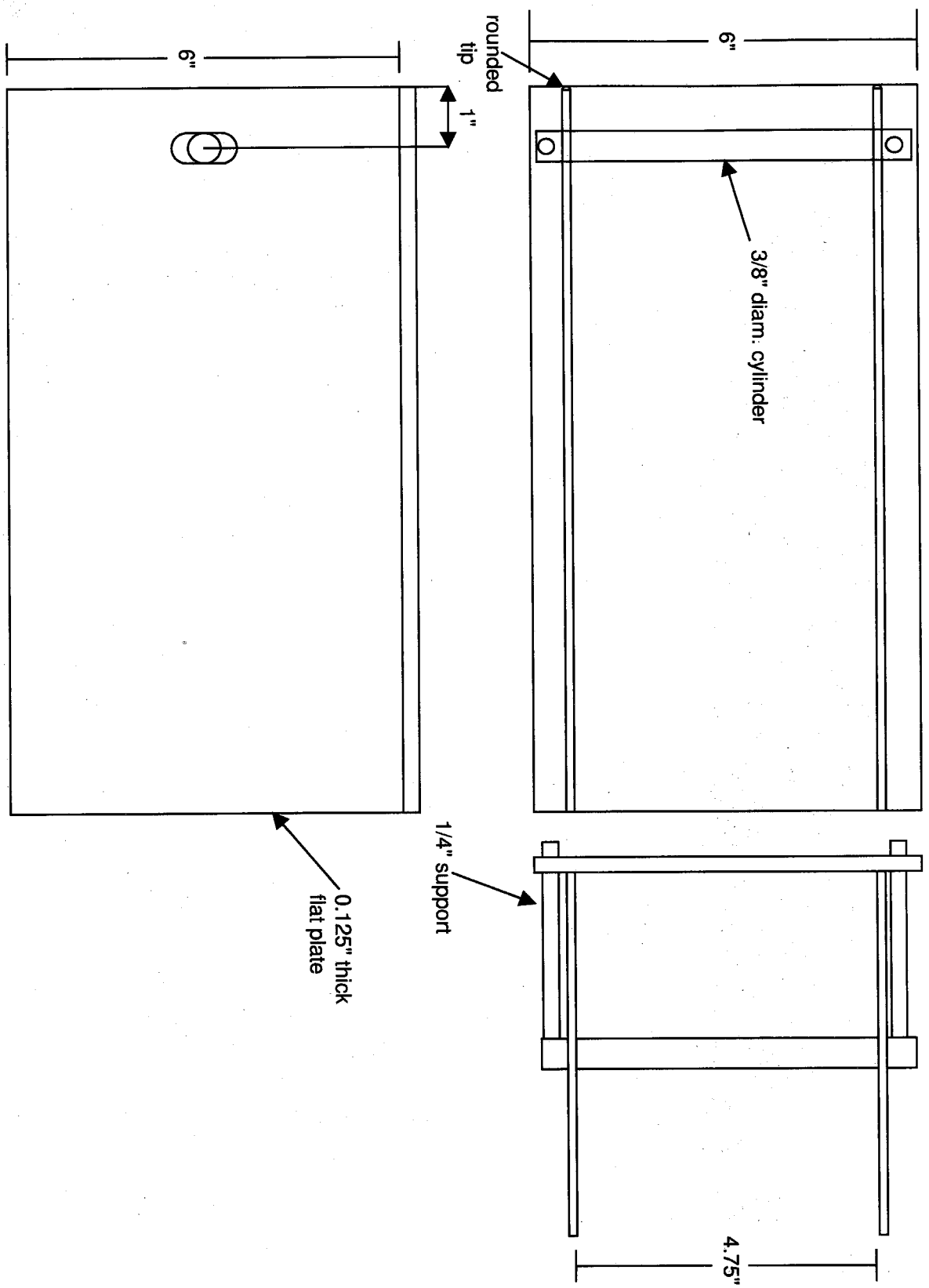


Figure 3.3 Schematic of the cylinder, flat plates, and supports.

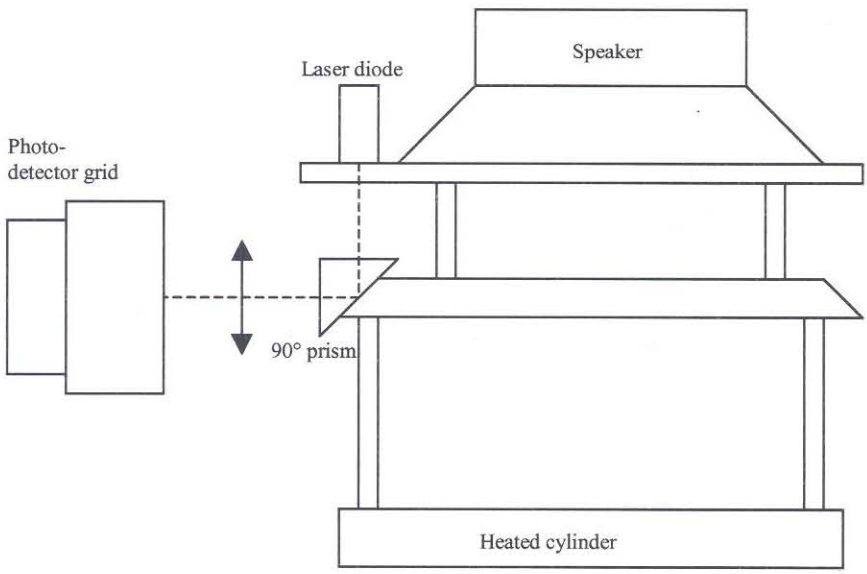


Figure 3.4 Schematic of the displacement measurement system using laser diode and optical transducer. The beam from the diode is reflected 90° by a right angle prism to an optical photo-detector grid.

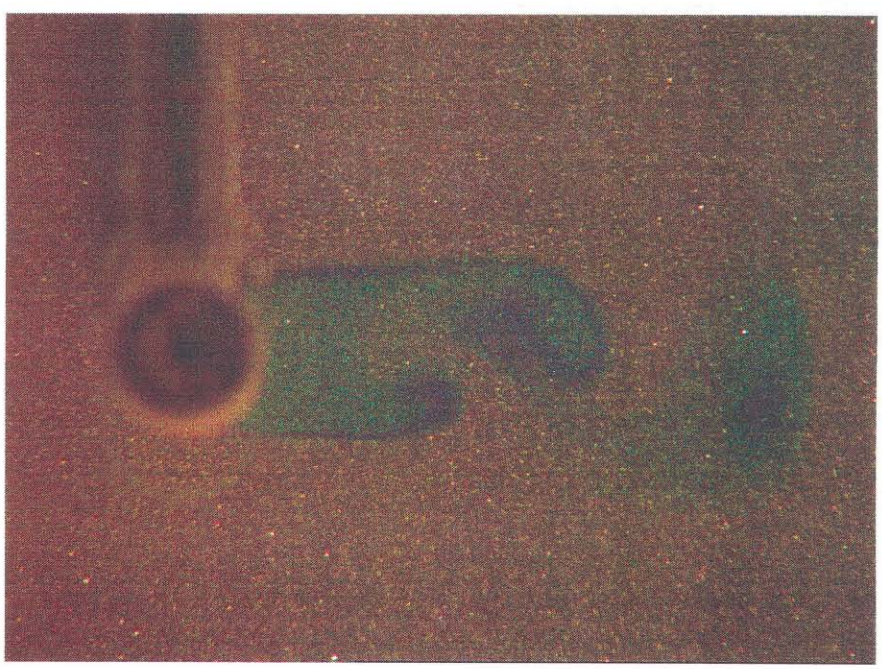

Figure 3.5 Instantaneous view of the flow behind a heated circular cylinder.

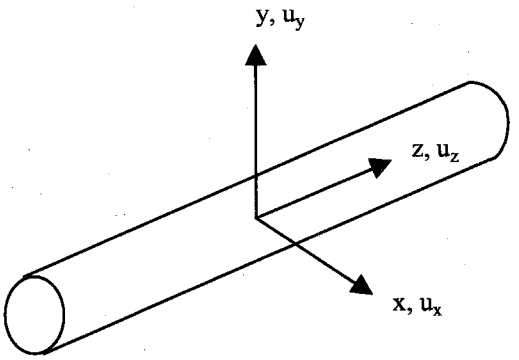


Figure 3.6 Cylinder coordinate system.

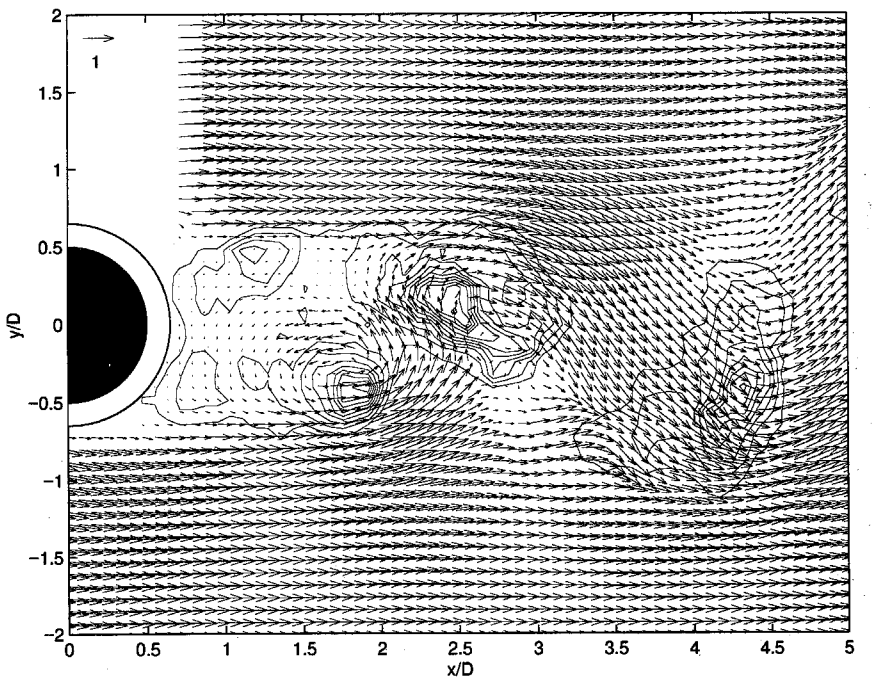


Figure 3.7 Velocity and Temperature fields computed using DPIV/T from image in Fig. 3.5.

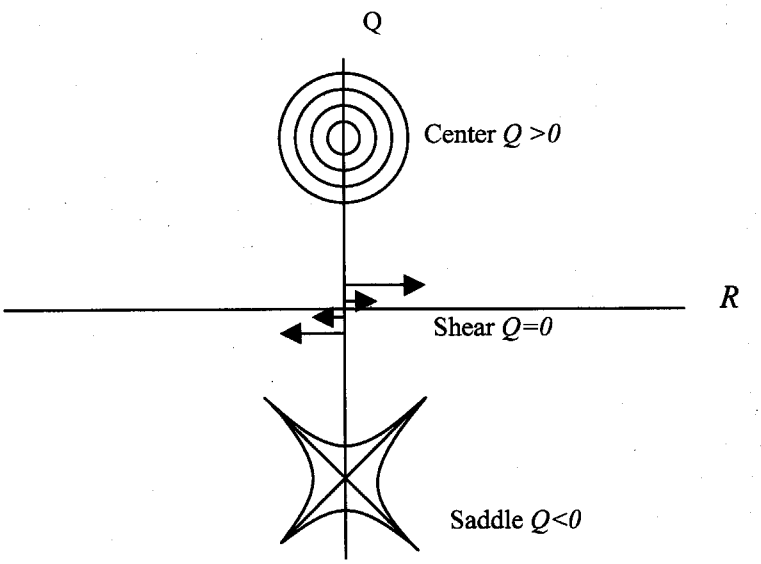


Figure 4.1 Topological classifications of the flow.

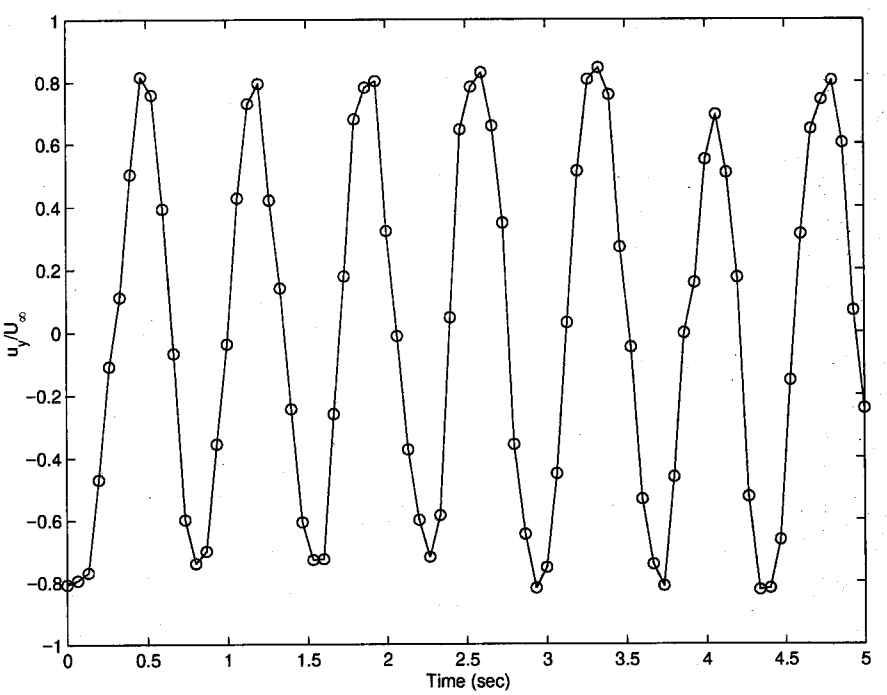


Figure 4.2 $u_y$ signal at location of maximum $u_y$ fluctuations.

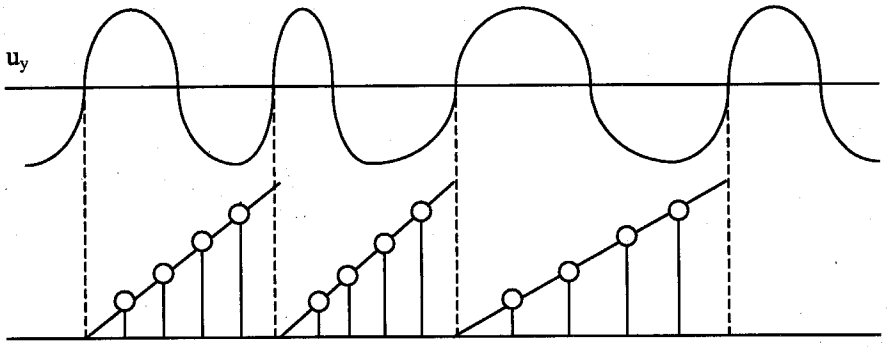


Figure 4.3 Determination of phase within each vortex shedding cycle. The phase is re-locked at each cycle of vortex shedding by locating the zero crossing of $u_y$ because the period of each vortex shedding cycle may vary slightly (exaggerated in figure).

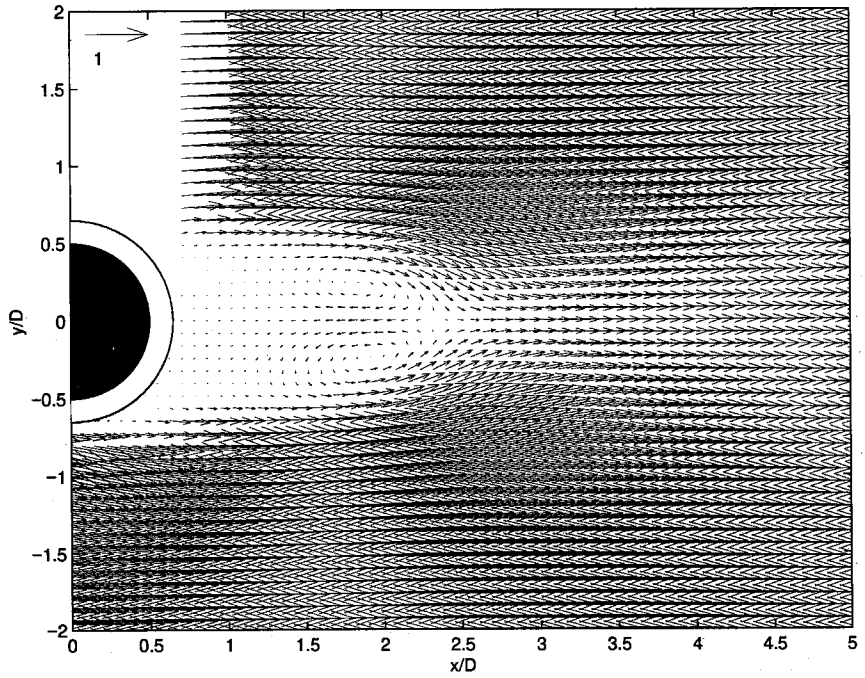


Figure 4.4 Mean velocity field of stationary cylinder at Re=610 (Normalization: u/ $U_\infty$).

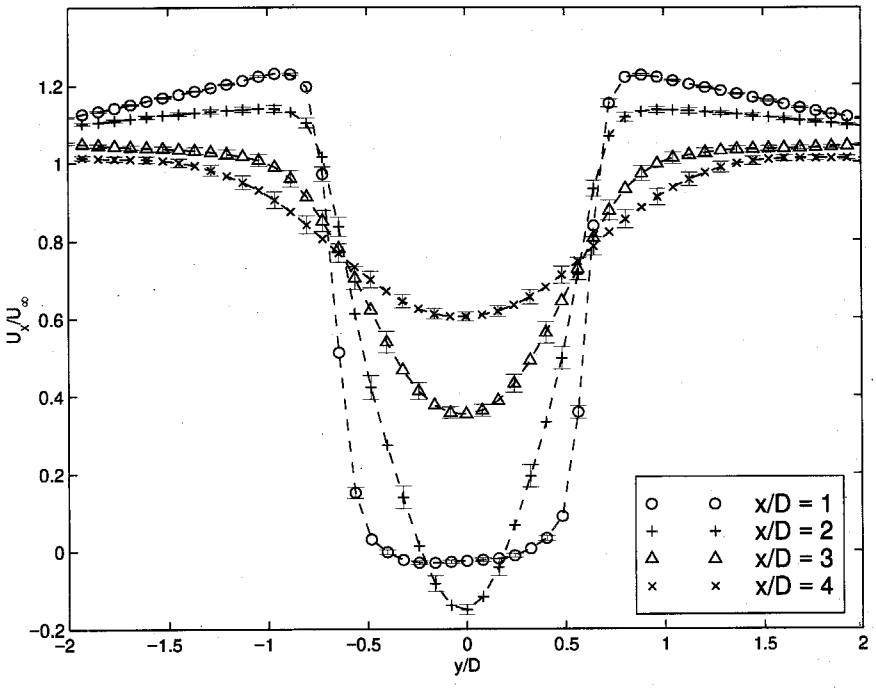


Figure 4.5 Profiles of mean $u_x$ at various downstream stations at Re=610. The light error bars indicate the standard deviations of the mean.

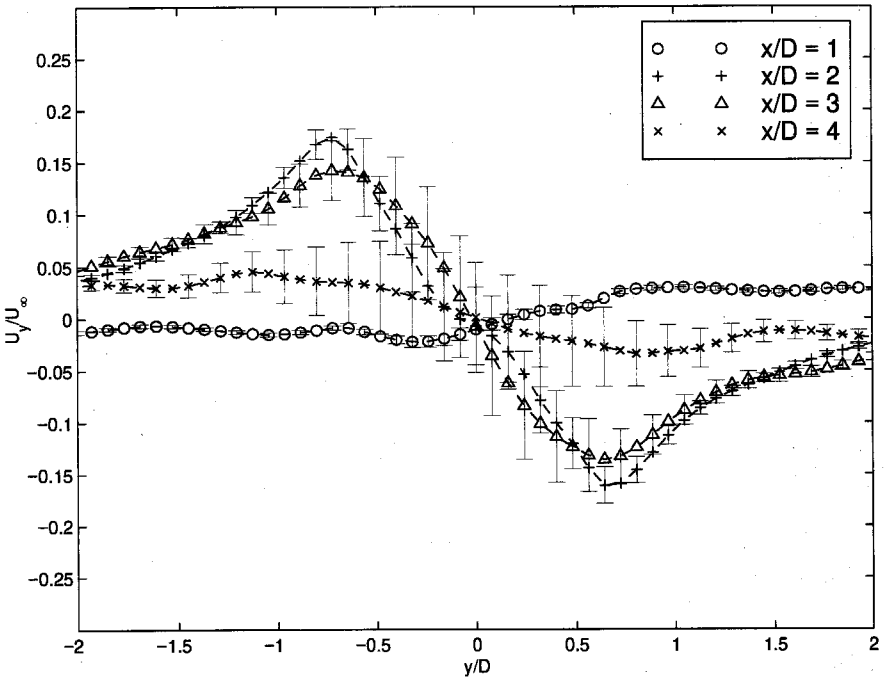


Figure 4.6 Profiles of mean $u_y$ at various downstream locations at Re=610. The light error bars indicate the standard deviation of the mean.

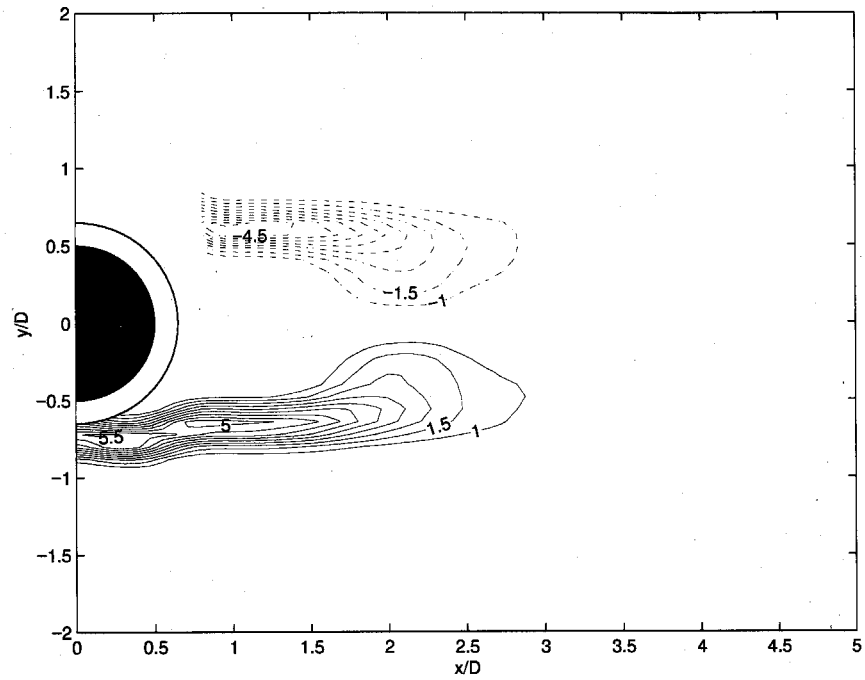


Figure 4.7 Mean vorticity field of stationary cylinder at Re=610 (Normalization: $\omega_z D/U_\infty$). Dashed lines represent negative values.

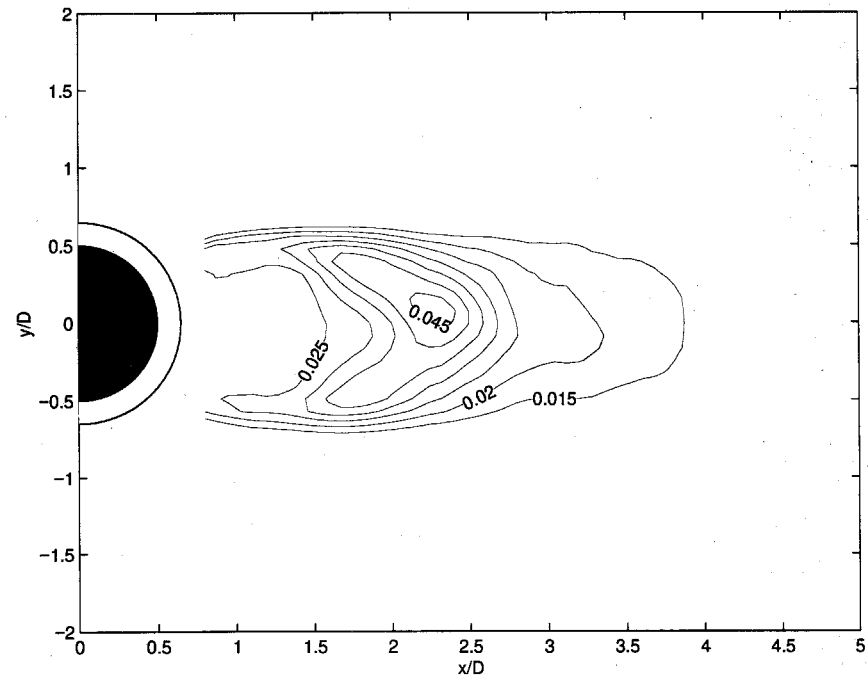


Figure 4.8 Mean temperature field of stationary cylinder at Re=610.
(Normalization: $(T - T_\infty)/(T_c - T_\infty)$).

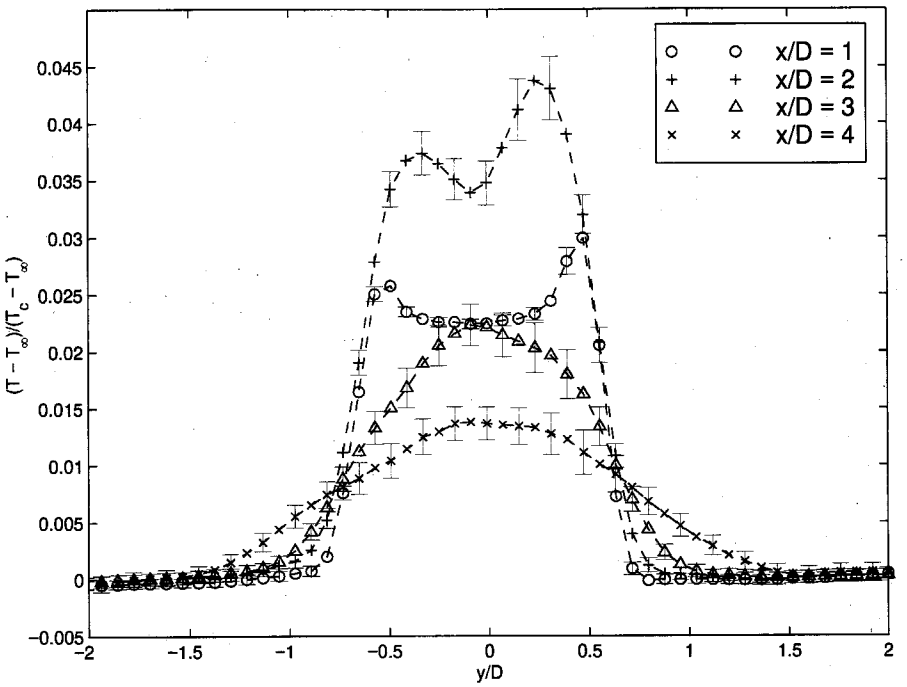


Figure 4.9 Temperature profiles at various downstream locations at Re=610. The light error bars indicate standard deviation of the mean.

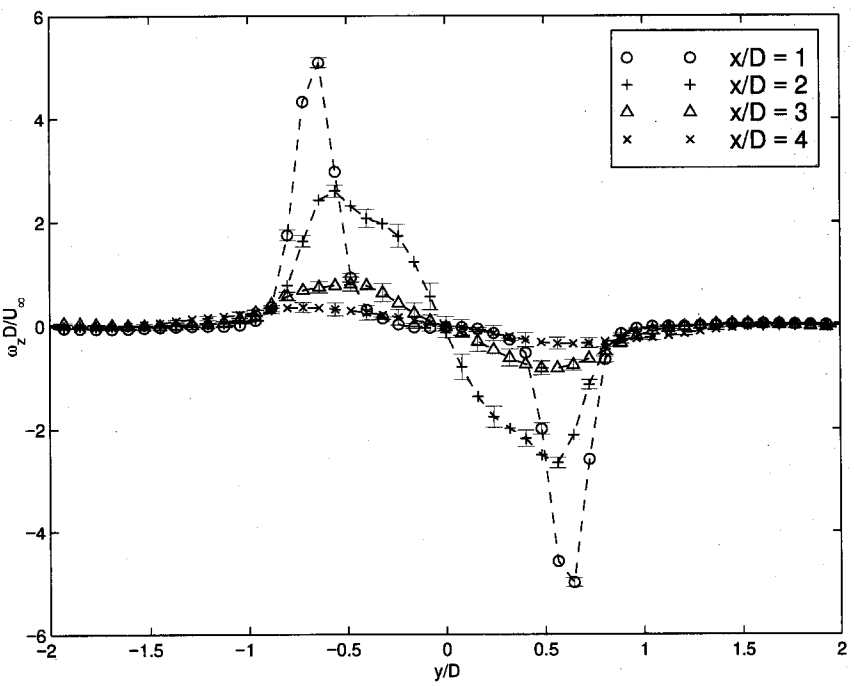


Figure 4.10 Vorticity profiles at various downstream locations at Re=610. The light error bars indicate standard deviation of the mean.

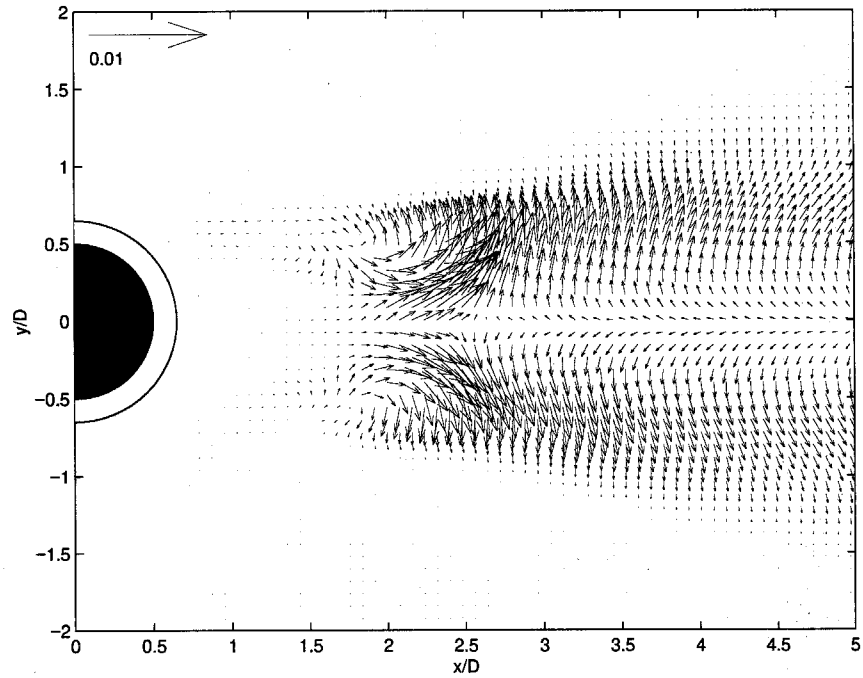


Figure 4.11 Mean global turbulent heat flux of stationary cylinder at Re=610 (Normalization: $u_j'T'/U_\infty(T_c-T_\infty)$).

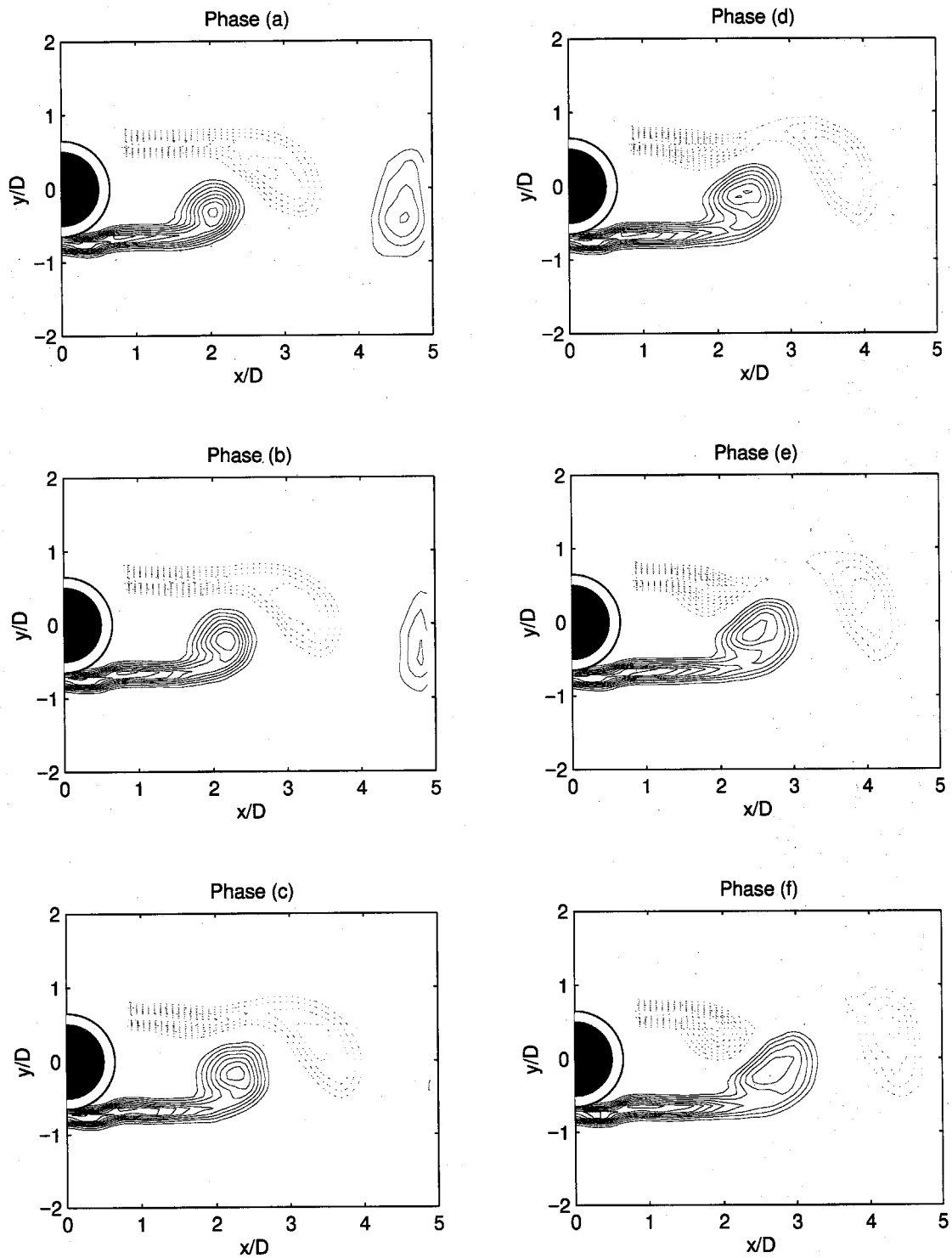


Figure 4.12(a) Sequence of phase averaged vorticity field for stationary cylinder at Re=610 ($|\langle\omega_z\rangle D/U_\infty|>1.0$, contour increment 0.5). The value of the reference phase velocity ($u_y$ at location of maximum fluctuations) corresponding to each letter is shown in Fig. 4.55.

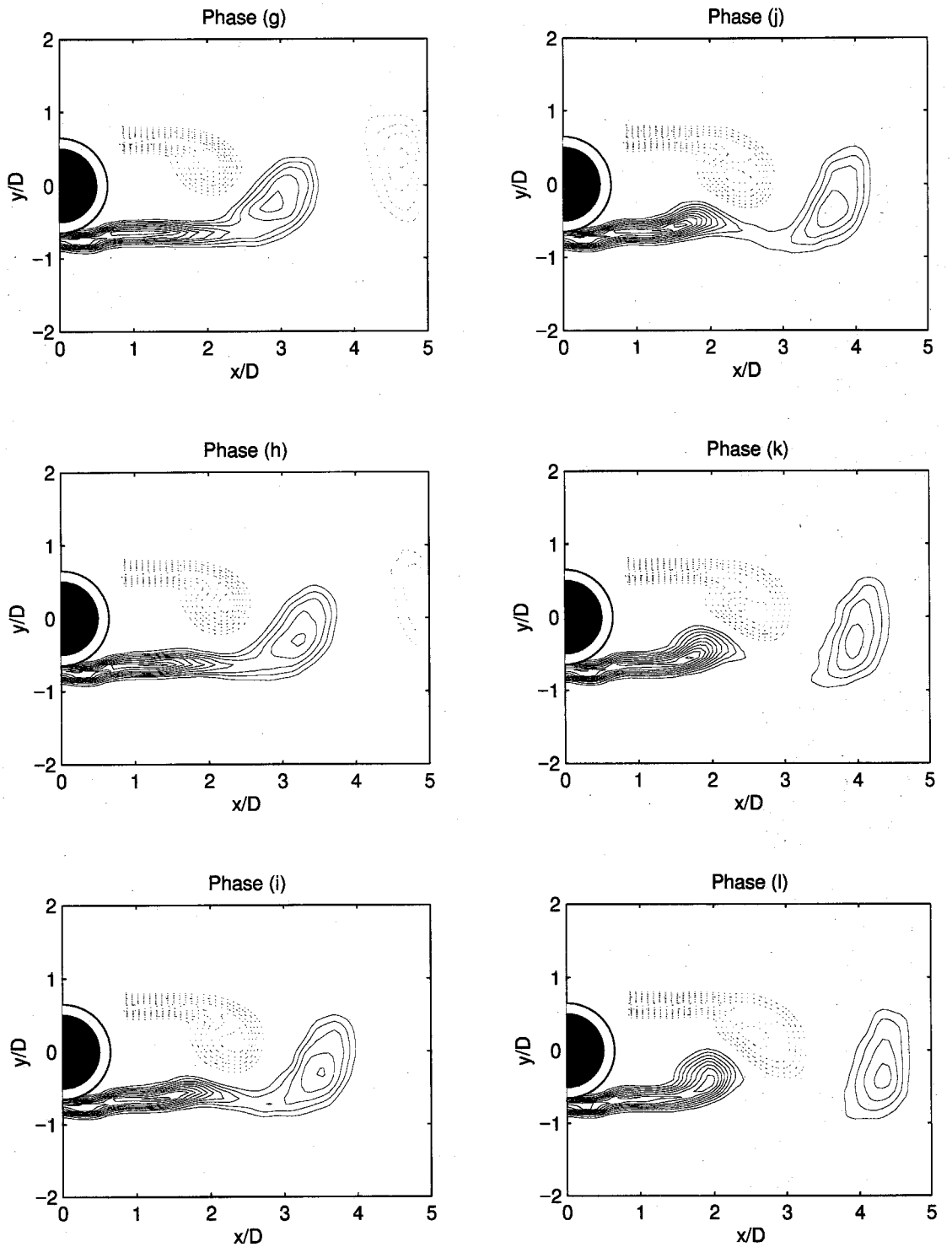


Figure 4.12(b) Sequence of phase averaged vorticity field for stationary cylinder at Re=610 ($|<\omega_z>D/U_\infty|>1.0$, contour increment 0.5). The value of the reference phase velocity ($u_y$ at location of maximum fluctuations) corresponding to each letter is shown in Fig. 4.55.

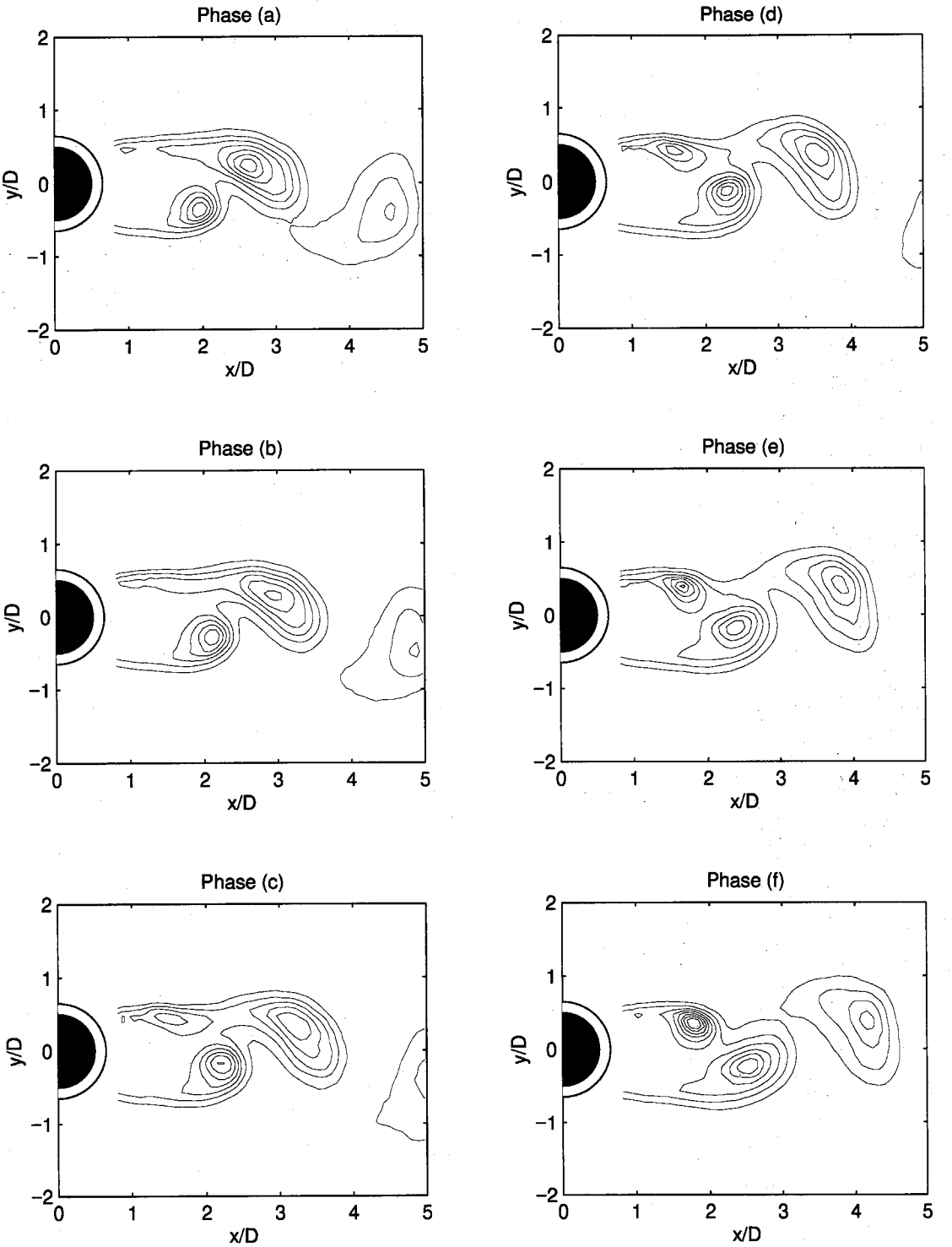


Figure 4.13(a) Sequence of phase averaged temperature field for stationary cylinder at Re=610 ($(<T> - T_\infty)/(T_c - T_\infty)>0.01$, contour increment 0.01). The value of the reference phase velocity ($u_y$ at location of maximum fluctuations) corresponding to each letter is shown in Fig. 4.55.

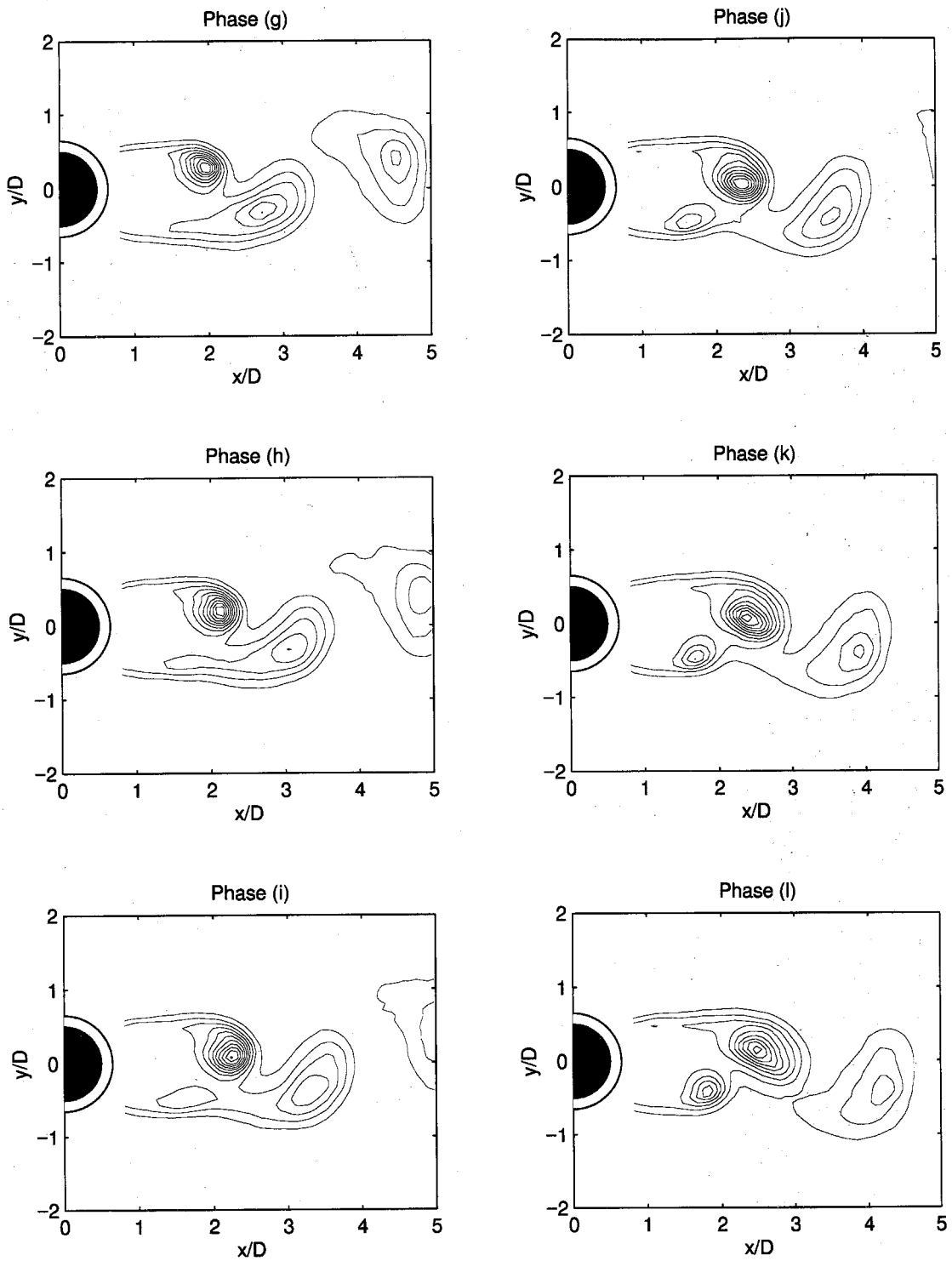


Figure 4.13(b) Sequence of phase averaged temperature field for stationary cylinder at Re=610 ($(<T> - T_\infty)/(T_c - T_\infty)>0.01$, contour increment 0.01). The value of the reference phase velocity ($u_y$ at location of maximum fluctuations) corresponding to each letter is shown in Fig. 4.55.

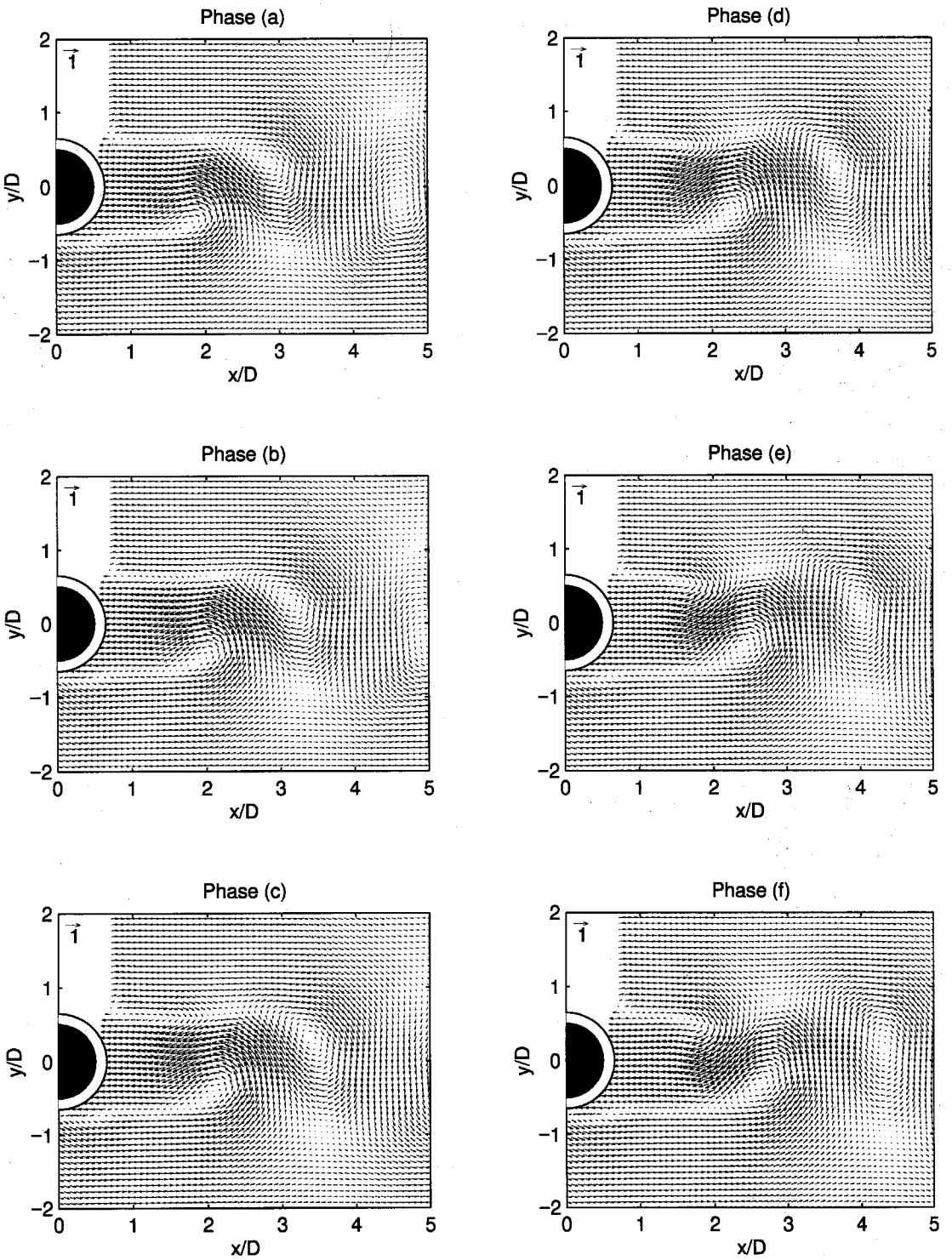


Figure 4.14(a) Sequence of phase averaged velocity field in the frame of the vortices for stationary cylinder at Re=610 ($\langle u \rangle / U_\infty$). The value of the reference phase velocity ($u_y$ at location of maximum fluctuations) corresponding to each letter is shown in Fig. 4.55.

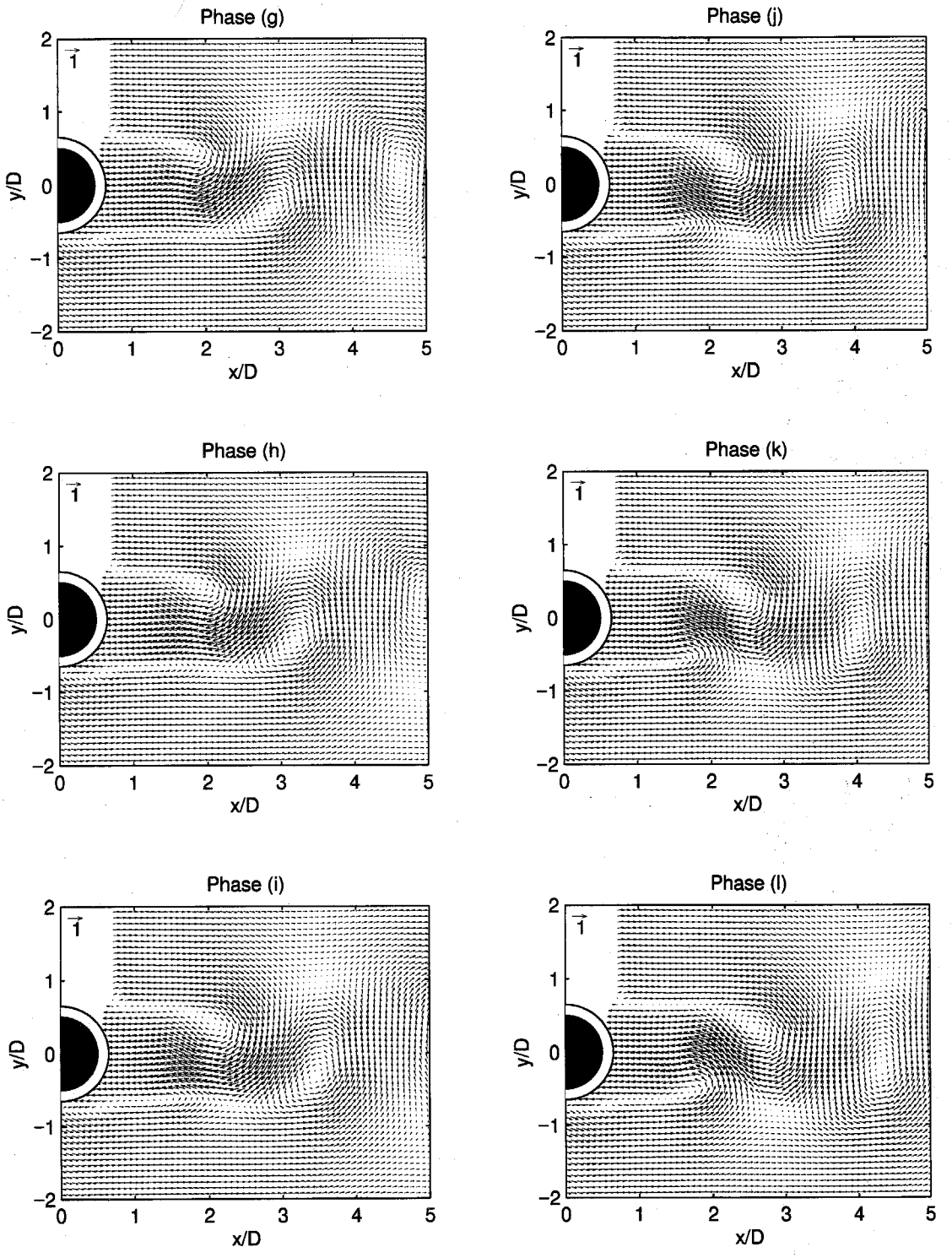


Figure 4.14(b) Sequence of phase averaged velocity field in the frame of the vortices for stationary cylinder at Re=610 ($\langle u \rangle / U_\infty$). The value of the reference phase velocity ($u_y$ at location of maximum fluctuations) corresponding to each letter is shown in Fig. 4.55.

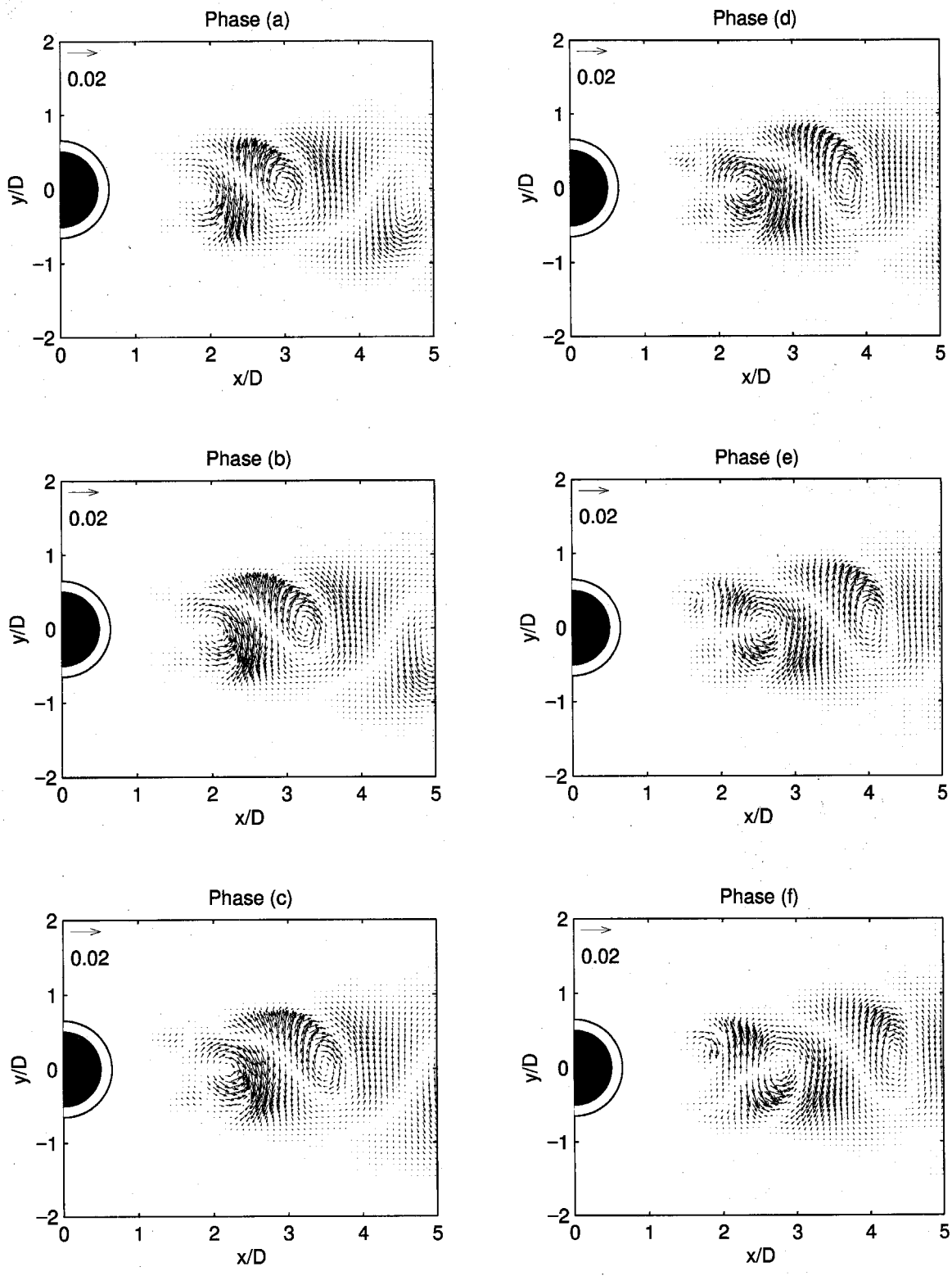


Figure 4.15(a) Sequence of phase averaged coherent heat flux for stationary cylinder at Re=610 (Normalization: $u_j'T'/U_\infty(T_c-T_\infty)$). The value of the reference phase velocity ($u_y$ at location of maximum fluctuations) corresponding to each letter is shown in Fig. 4.55.

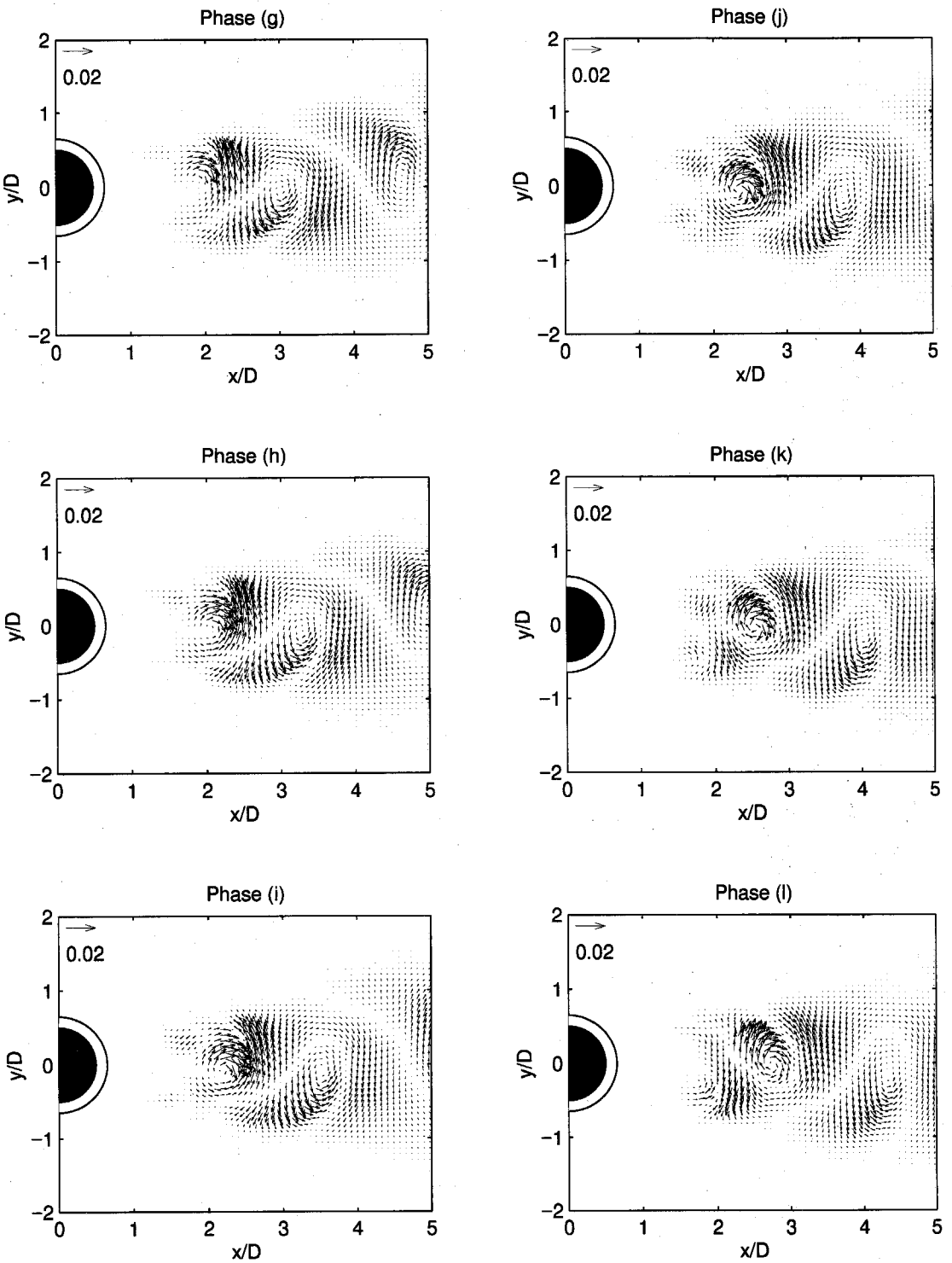


Figure 4.15(b) Sequence of phase averaged coherent heat flux for stationary cylinder at Re=610 (Normalization: $u_j'T'/U_\infty(T_c-T_\infty)$). The value of the reference phase velocity ($u_y$ at location of maximum fluctuations) corresponding to each letter is shown in Fig. 4.55.

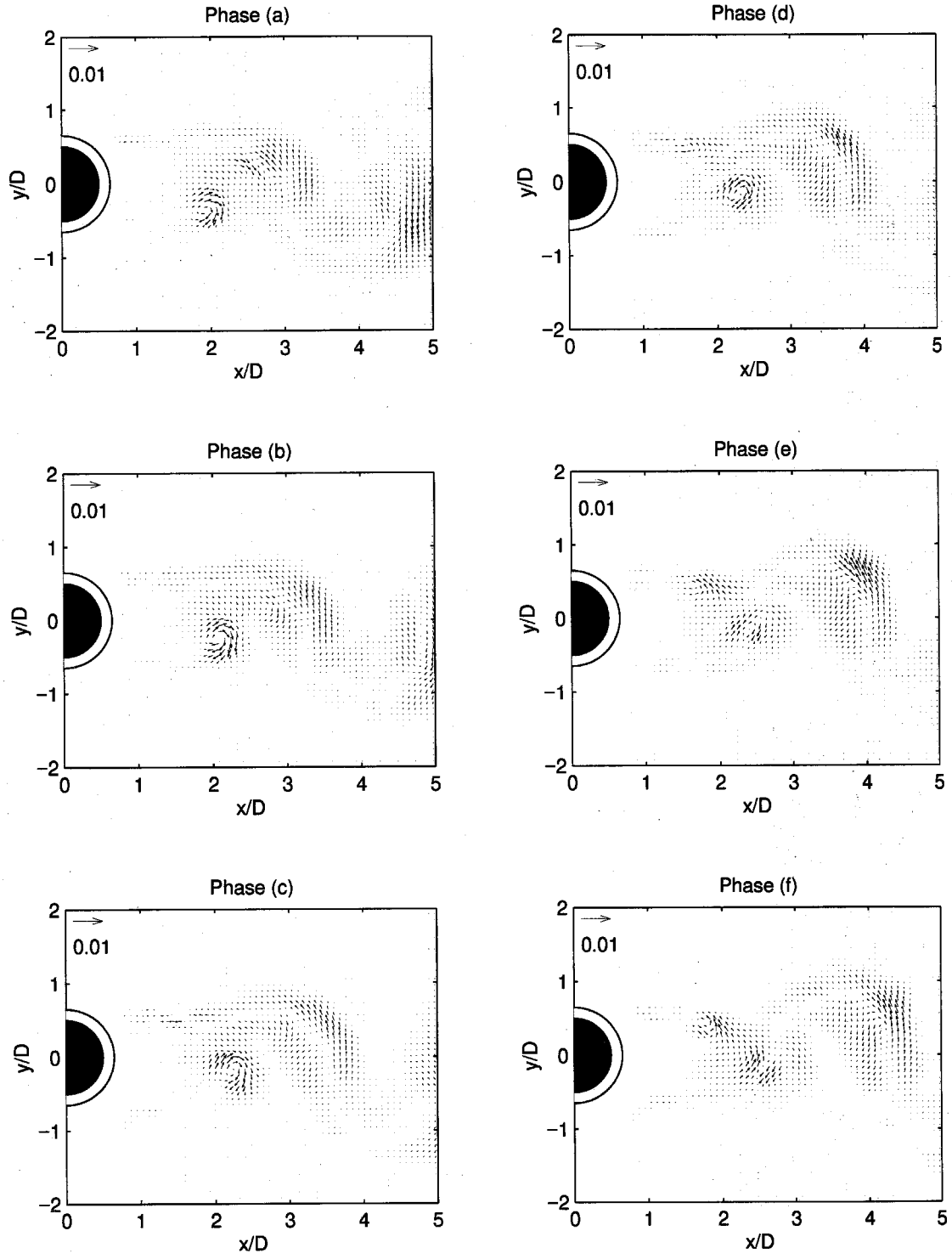


Figure 4.16(a) Sequence of phase averaged incoherent heat flux for stationary cylinder at Re=610 ($\langle u_{ri}'T_r'\rangle/U_\infty(T_c-T_\infty)$). The value of the reference phase velocity ($u_y$ at location of maximum fluctuations) corresponding to each letter is shown in Fig. 4.55.

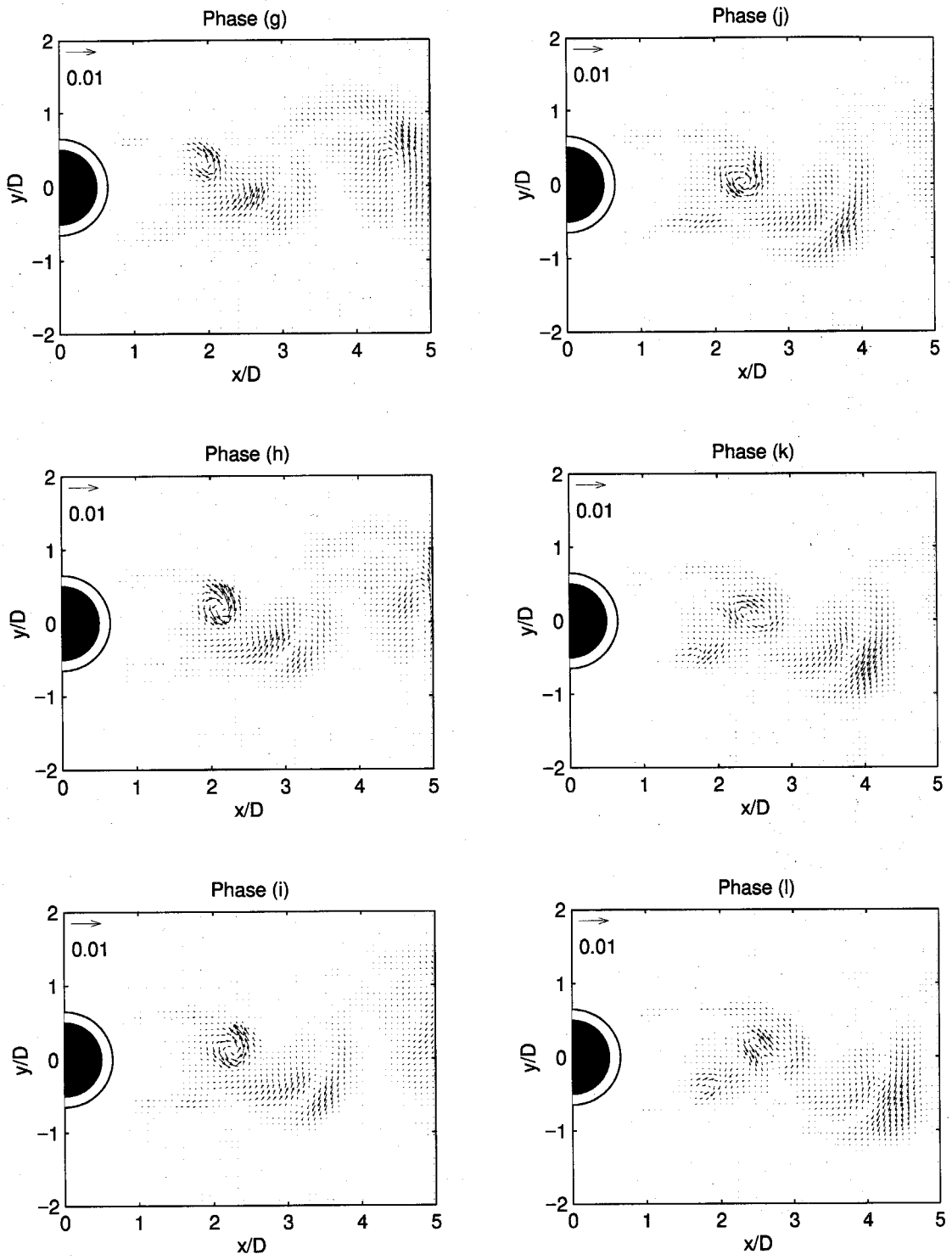


Figure 4.16(b) Sequence of phase averaged incoherent heat flux for stationary cylinder at Re=610 ($\langle u_{ri}'T_r'\rangle/U_\infty(T_c-T_\infty)$). The value of the reference phase velocity ($u_y$ at location of maximum fluctuations) corresponding to each letter is shown in Fig. 4.55.

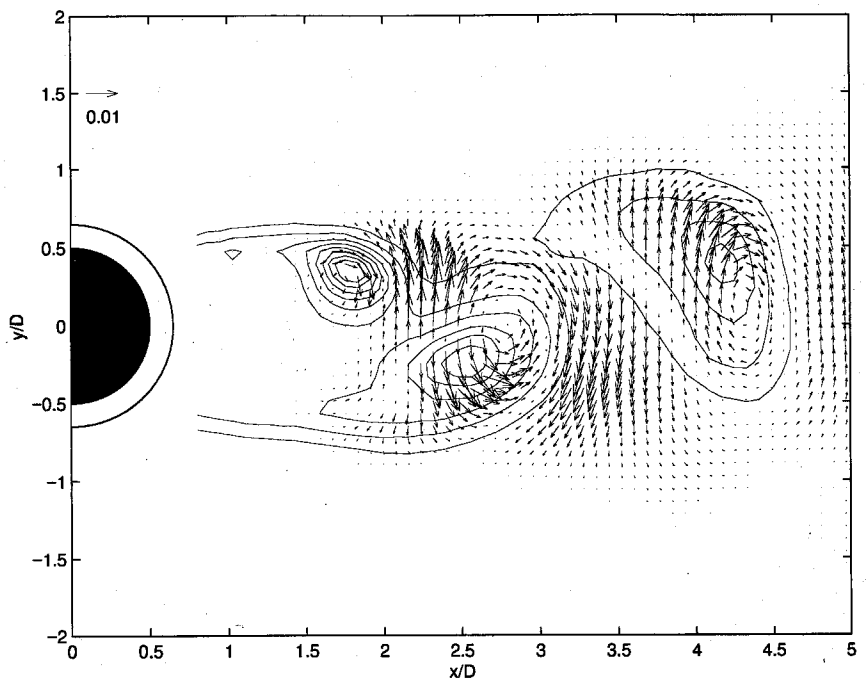


Figure 4.17 Transport of heat out of the wake by the coherent heat flux at Phase (f). The solid lines are contours of temperature.

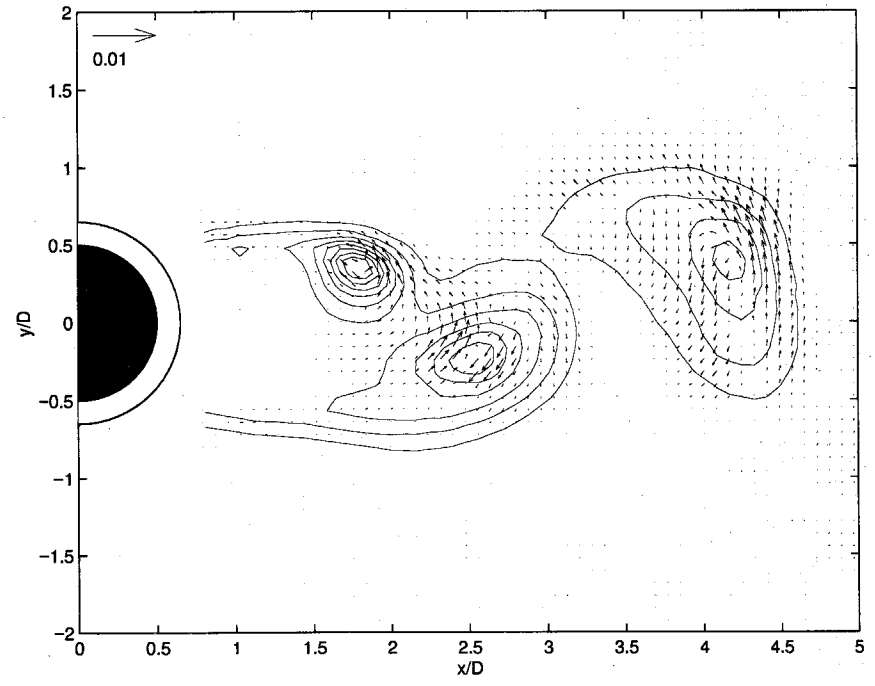


Figure 4.18 Transport of heat out of the vortices and the wake by the incoherent heat flux at Phase (f). The solid lines are contours of temperature.

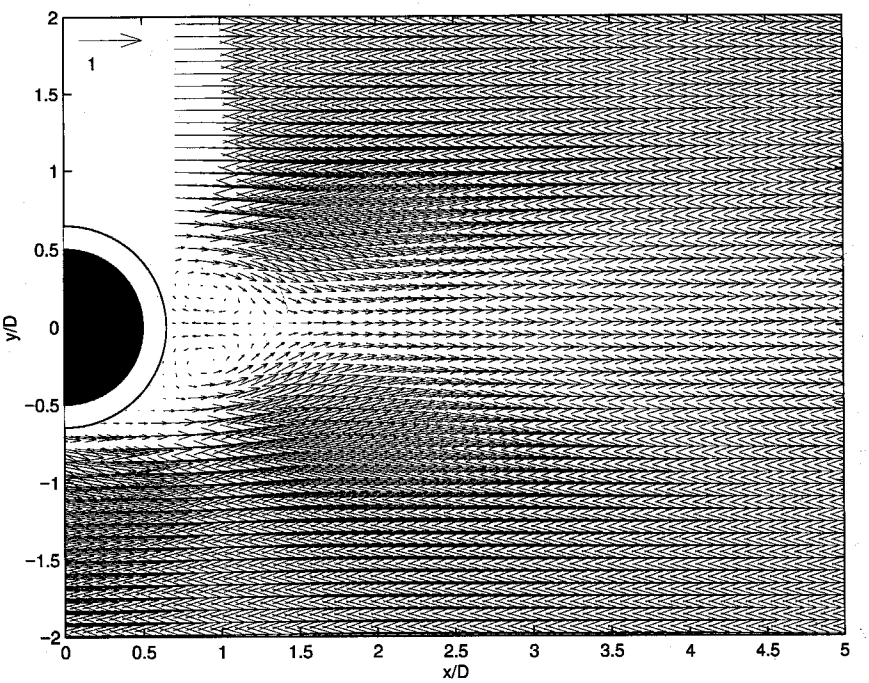


Figure 4.19 Mean velocity field of forced oscillating cylinder at $St_c$=0.21, A/D=0.1.

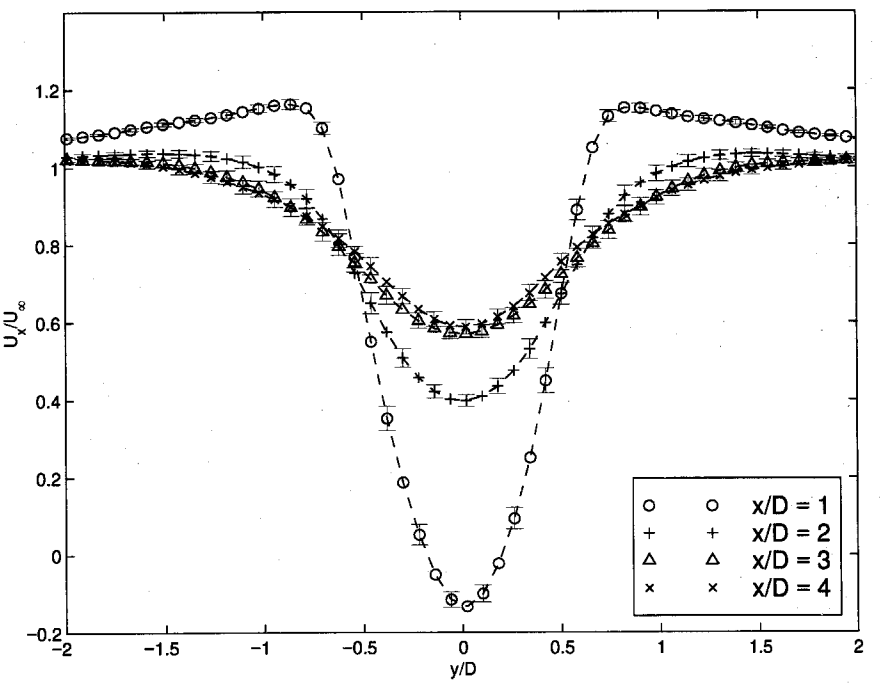


Figure 4.20 Profiles of mean $u_x$ at various downstream stations for forced oscillating cylinder at $St_c$=0.21, A/D=0.1. The light error bars indicate the standard deviations of the mean.

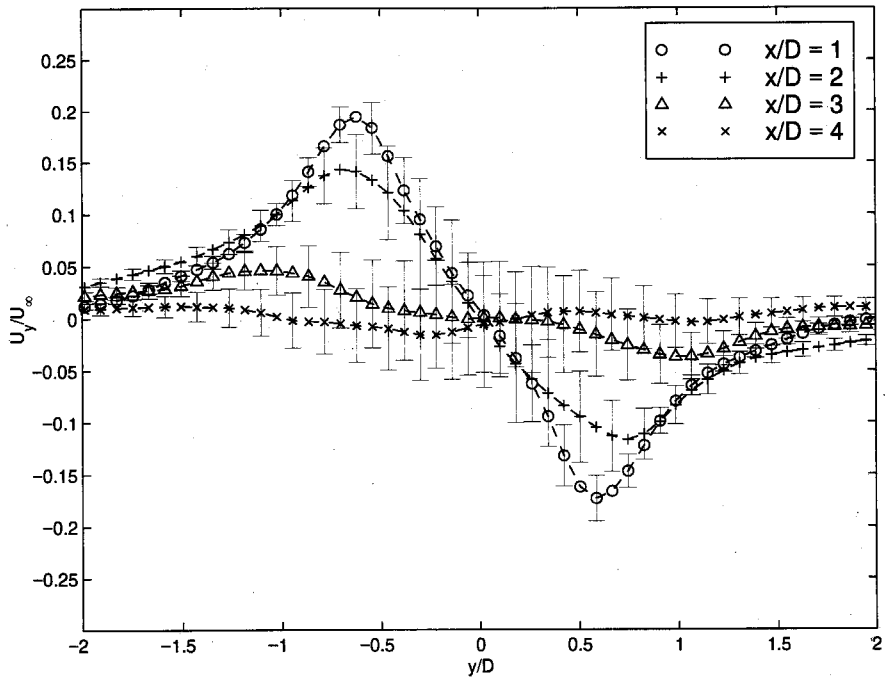


Figure 4.21 Profiles of mean $u_y$ at various downstream stations for forced oscillating cylinder at $St_c$=0.21, A/D=0.1. The light error bars indicate the standard deviations of the mean.

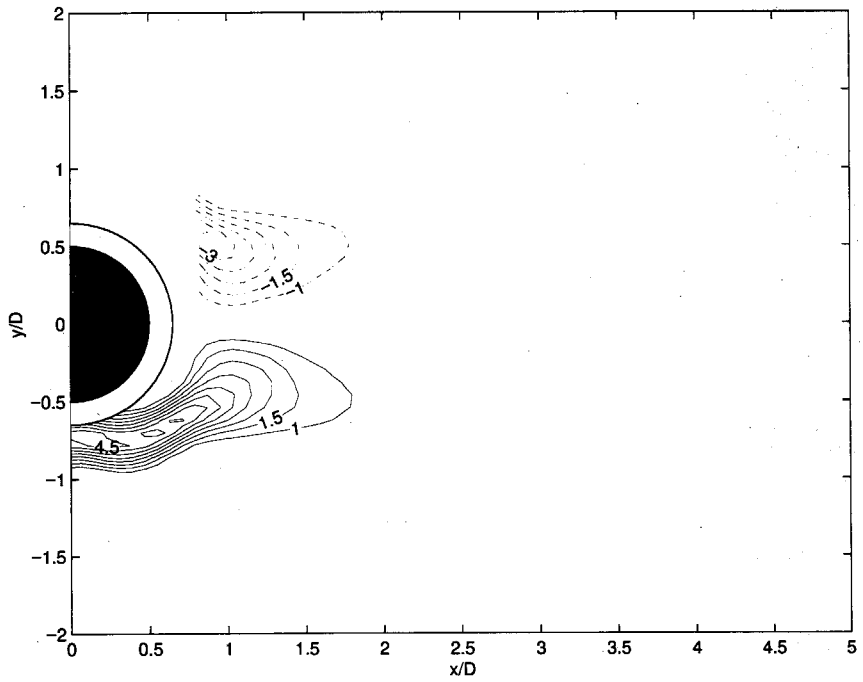


Figure 4.22 Mean vorticity field for forced oscillating cylinder at $St_c$=0.21, A/D=0.1.

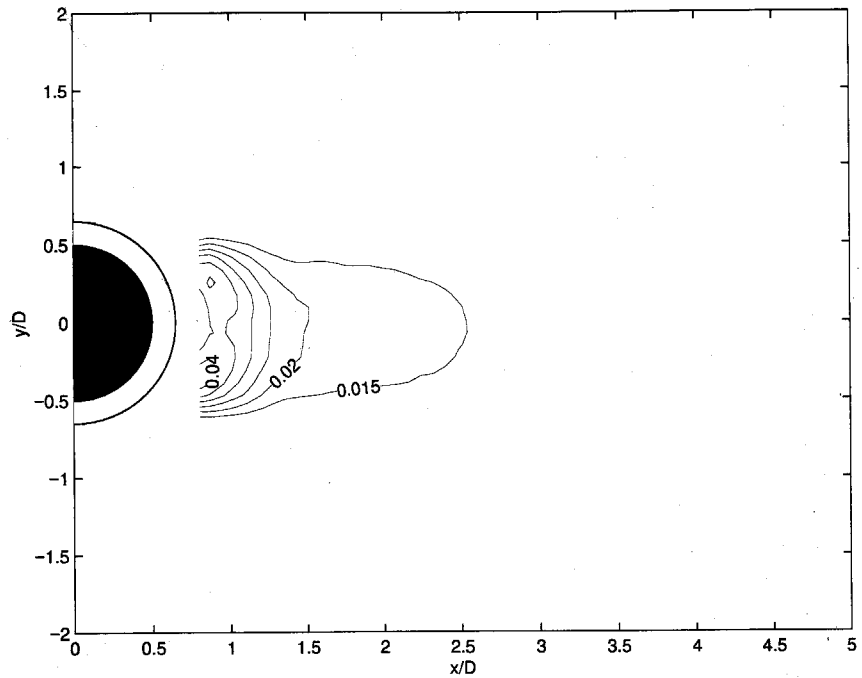


Figure 4.23 Mean temperature field for forced oscillating cylinder at $St_c$=0.21, A/D=0.1.

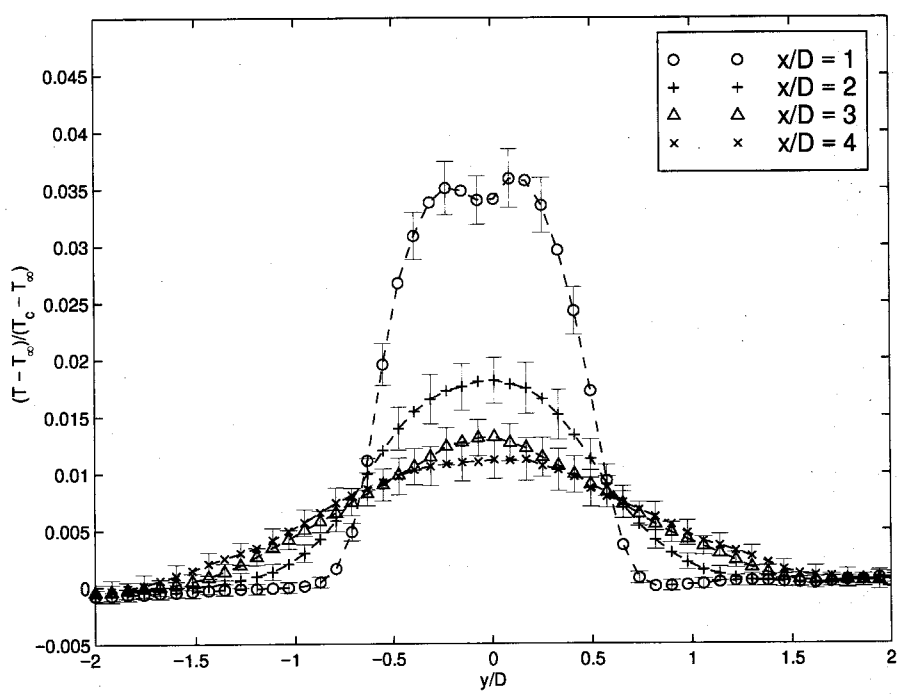


Figure 4.24 Profiles of mean temperature at various downstream stations for forced oscillating cylinder at $St_c$=0.21, A/D=0.1. The light error bars indicate the standard deviations of the mean.

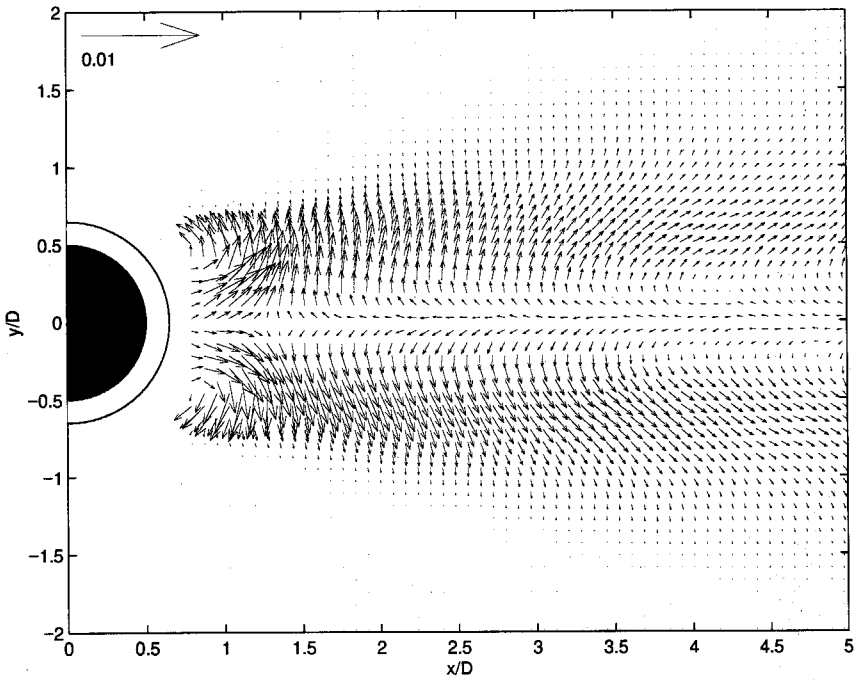


Figure 4.25 Mean global turbulent heat flux for forced oscillating cylinder at $St_c$=0.21, A/D=0.1.

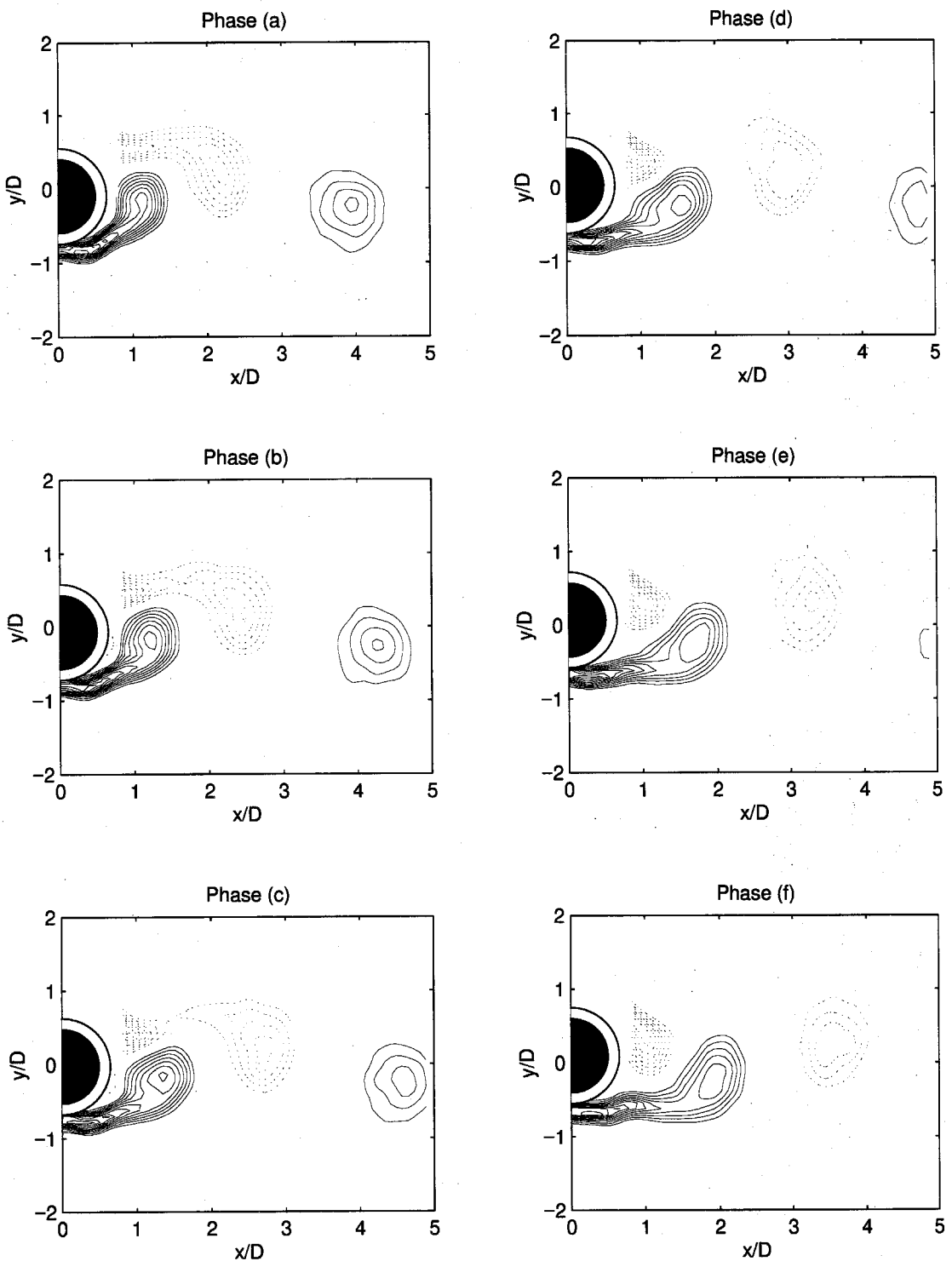


Figure 4.26(a) Sequence of phase averaged vorticity field for forced oscillating cylinder at $St_c$=0.21, A/D=0.1 ($|<\omega_z>D/U_\infty|>1.0$, contour increment 0.5). The y-displacement of the cylinder corresponding to each letter is shown in Fig. 4.55.

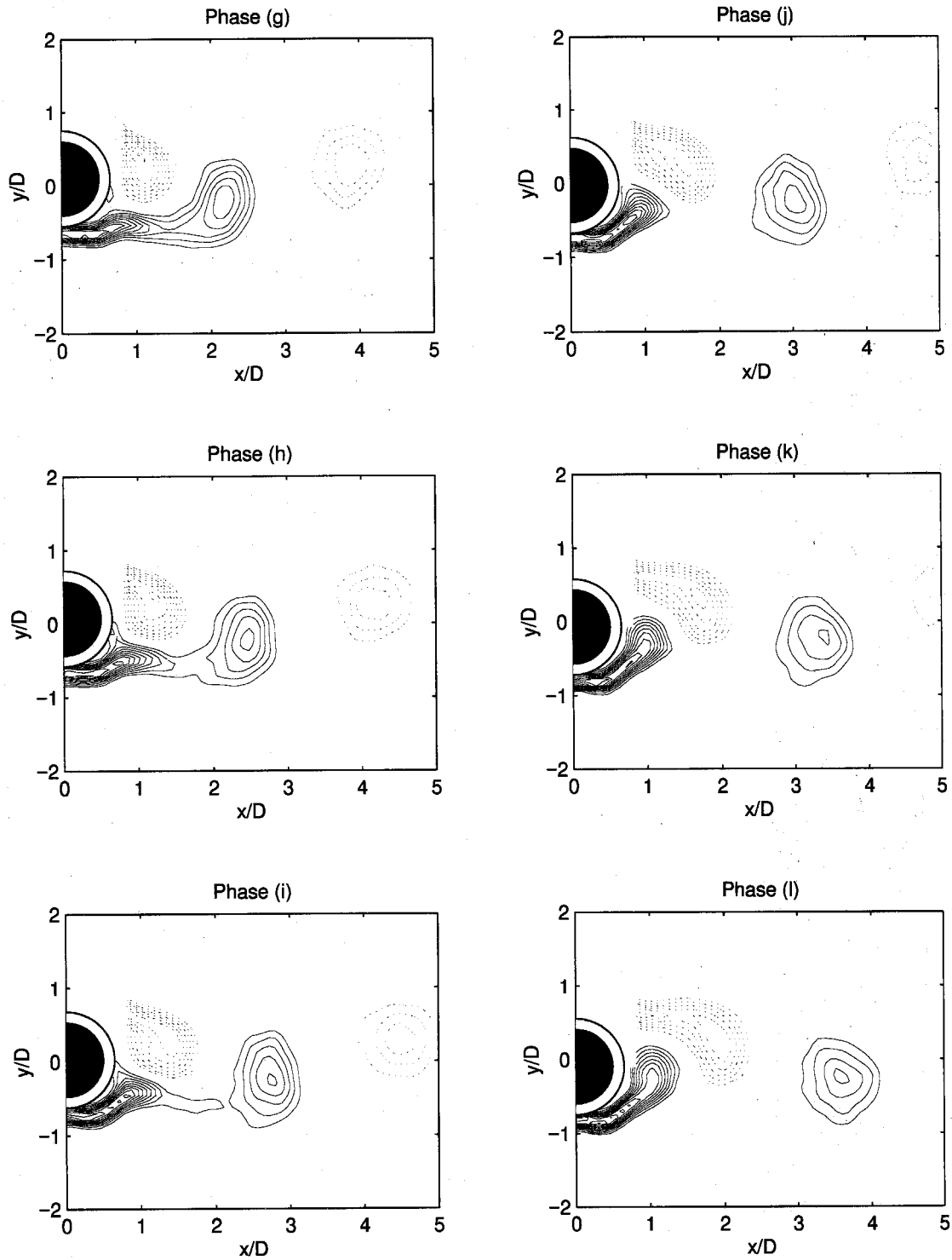


Figure 4.26(b) Sequence of phase averaged vorticity field for forced oscillating cylinder at $St_c$=0.21, A/D=0.1 ($|<\omega_z>D/U_\infty|>1.0$, contour increment 0.5). The y-displacement of the cylinder corresponding to each letter is shown in Fig. 4.55.

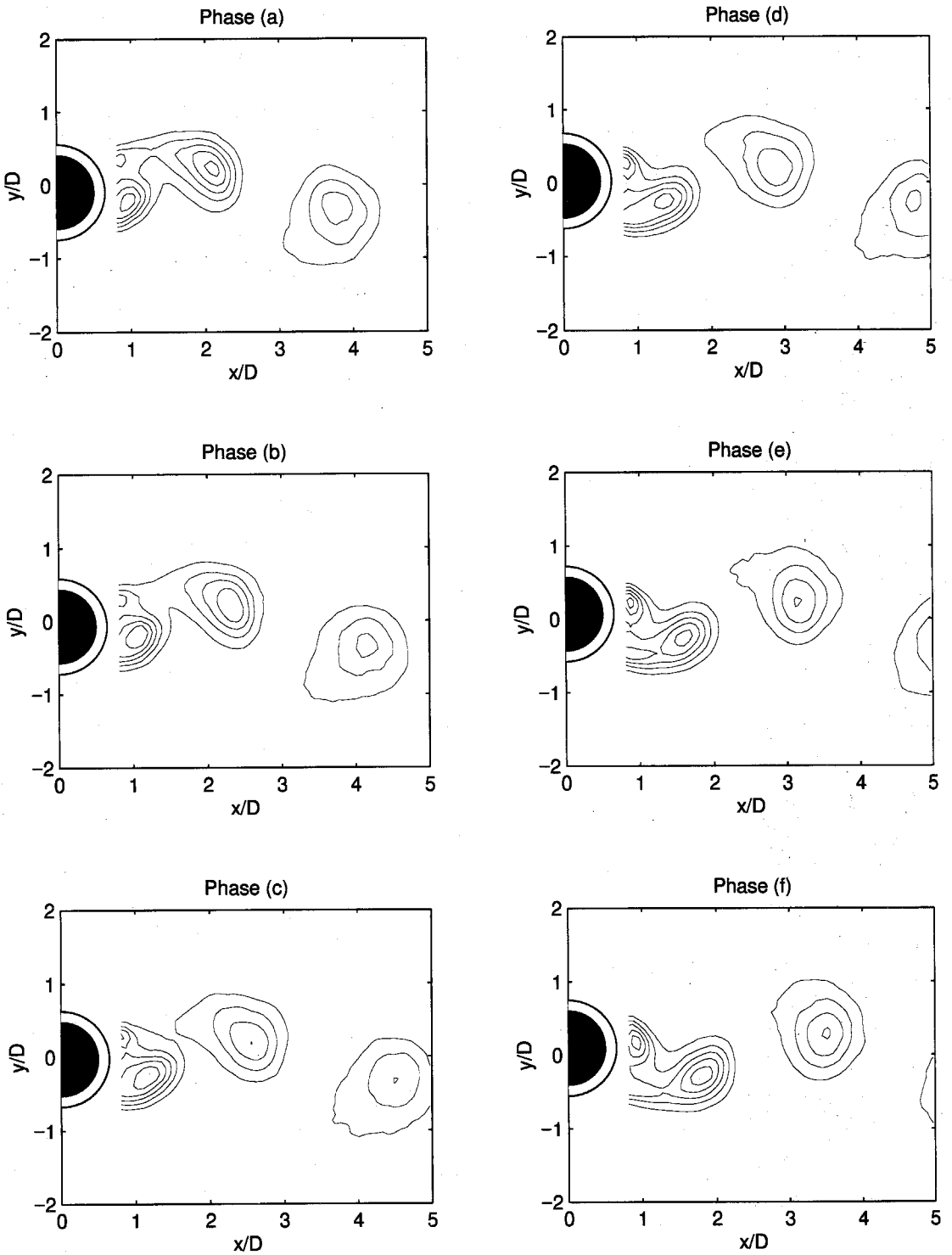


Figure 4.27(a) Sequence of phase averaged temperature field for forced oscillating cylinder at $St_c$=0.21, A/D=0.1 ($(<T> - T_\infty)/(T_c - T_\infty)$>0.01, contour increment 0.01). The y-displacement of the cylinder corresponding to each letter is shown in Fig. 4.55.

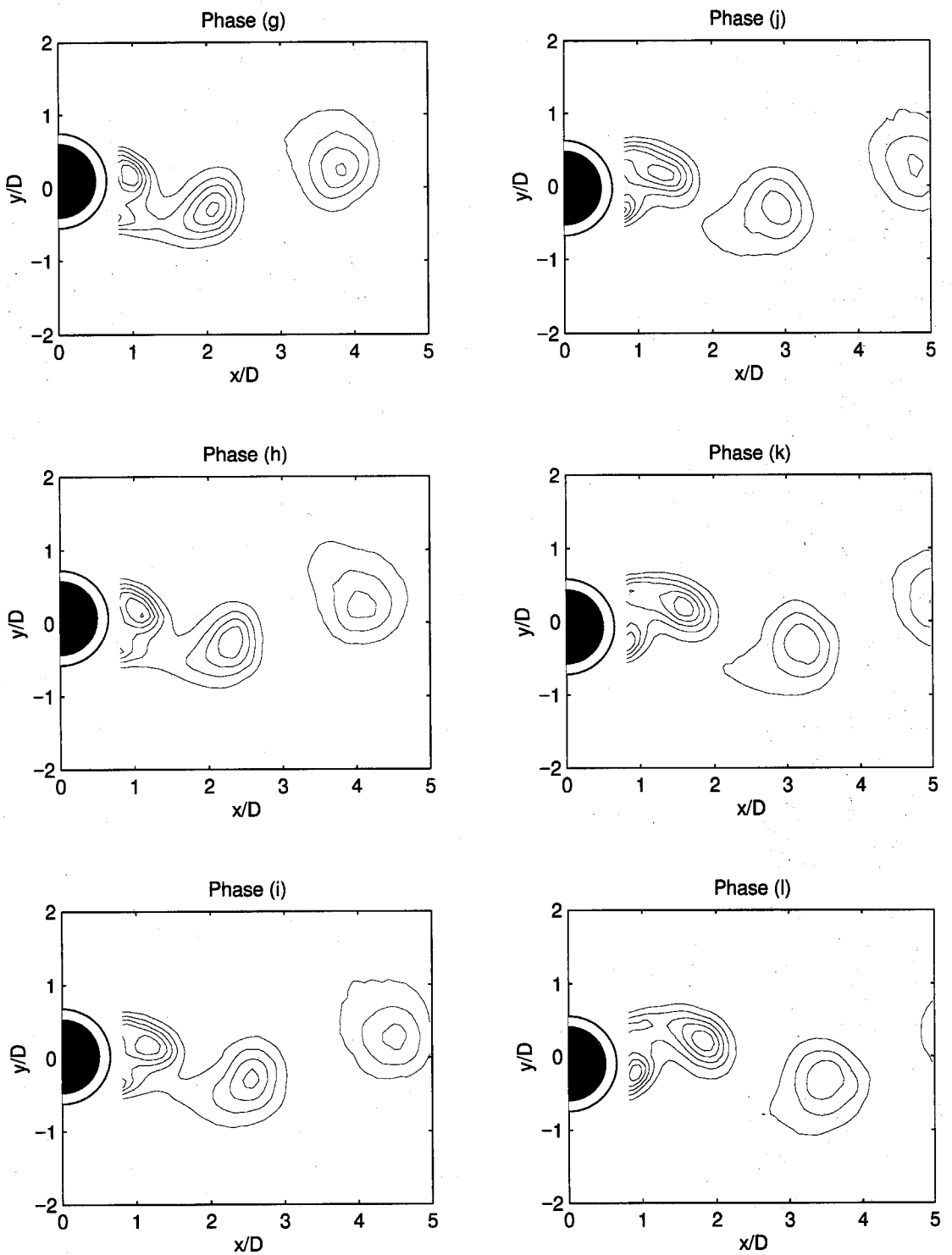


Figure 4.27(b) Sequence of phase averaged temperature field for forced oscillating cylinder at $St_c$=0.21, A/D=0.1 ((<T> - $T_\infty$)/($T_c$ - $T_\infty$)>0.01, contour increment 0.01). The y-displacement of the cylinder corresponding to each letter is shown in Fig. 4.55.

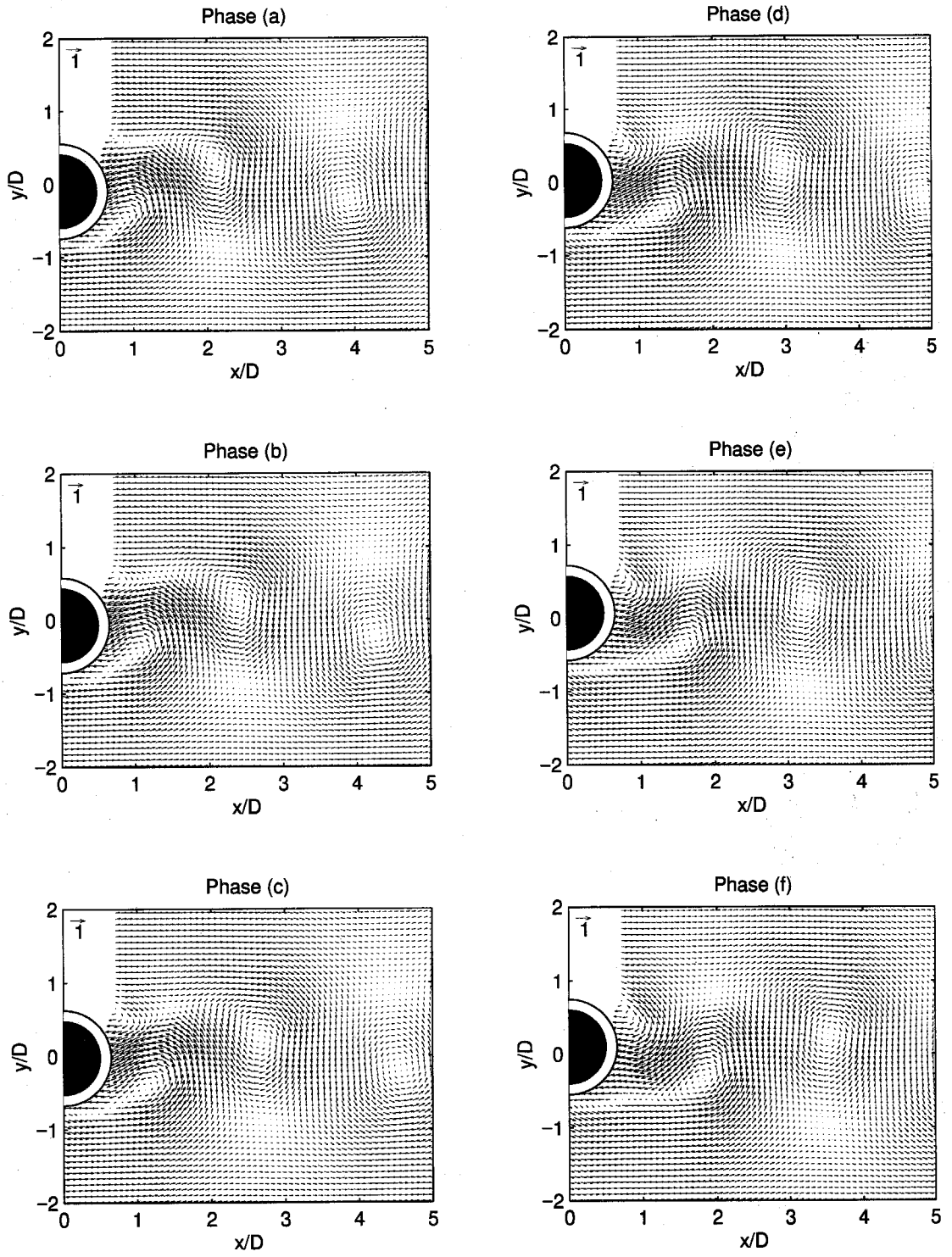


Figure 4.28(a) Sequence of phase averaged velocity field in frame of the vortices ($u_x/U_\infty$=0.7) for forced oscillating cylinder at $St_c$=0.21, A/D=0.1. The y-displacement of the cylinder corresponding to each letter is shown in Fig. 4.55.

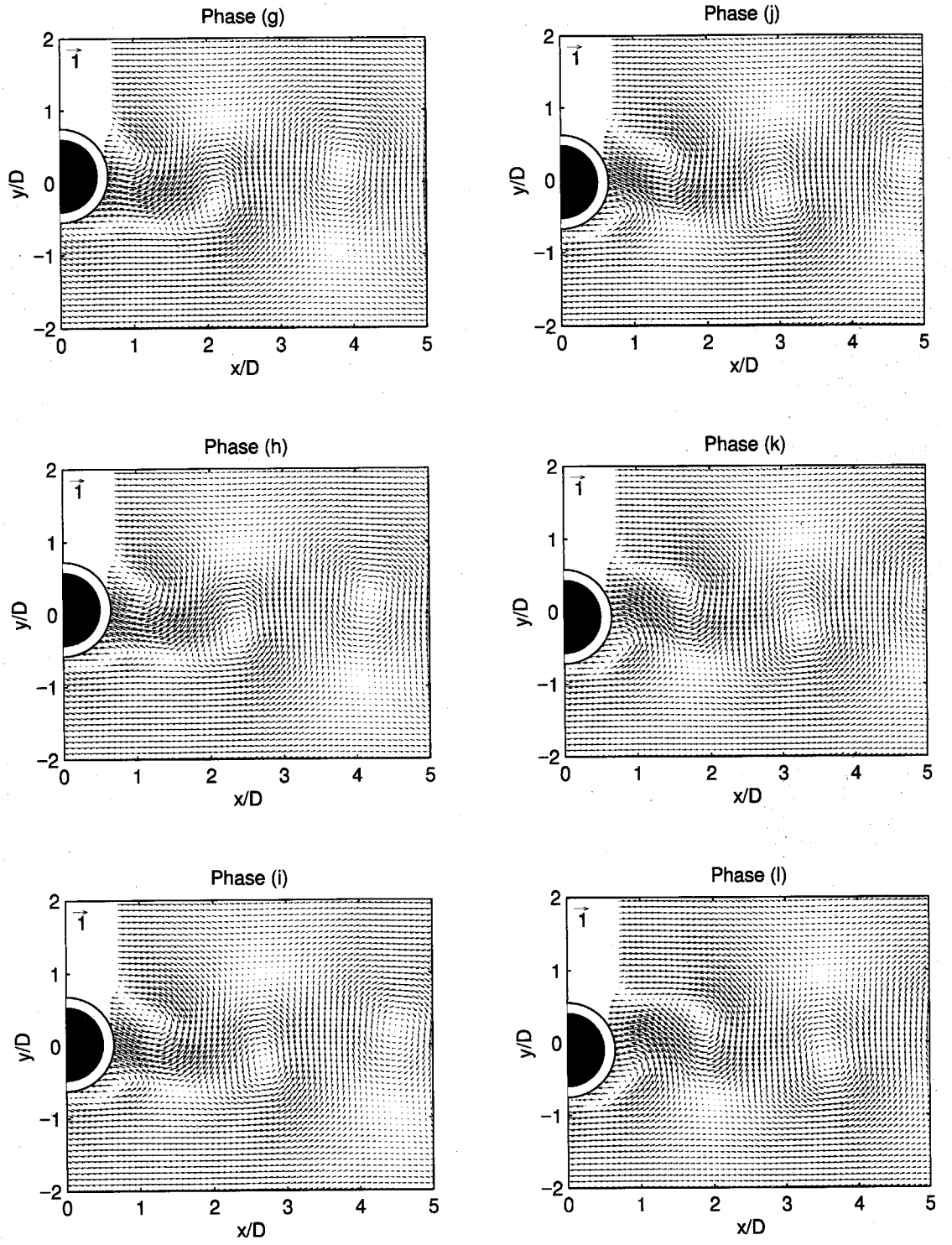


Figure 4.28(b) Sequence of phase averaged velocity field in frame of the vortices ($u_x/U_\infty$=0.7) for forced oscillating cylinder at $St_c$=0.21, A/D=0.1. The y-displacement of the cylinder corresponding to each letter is shown in Fig. 4.55.

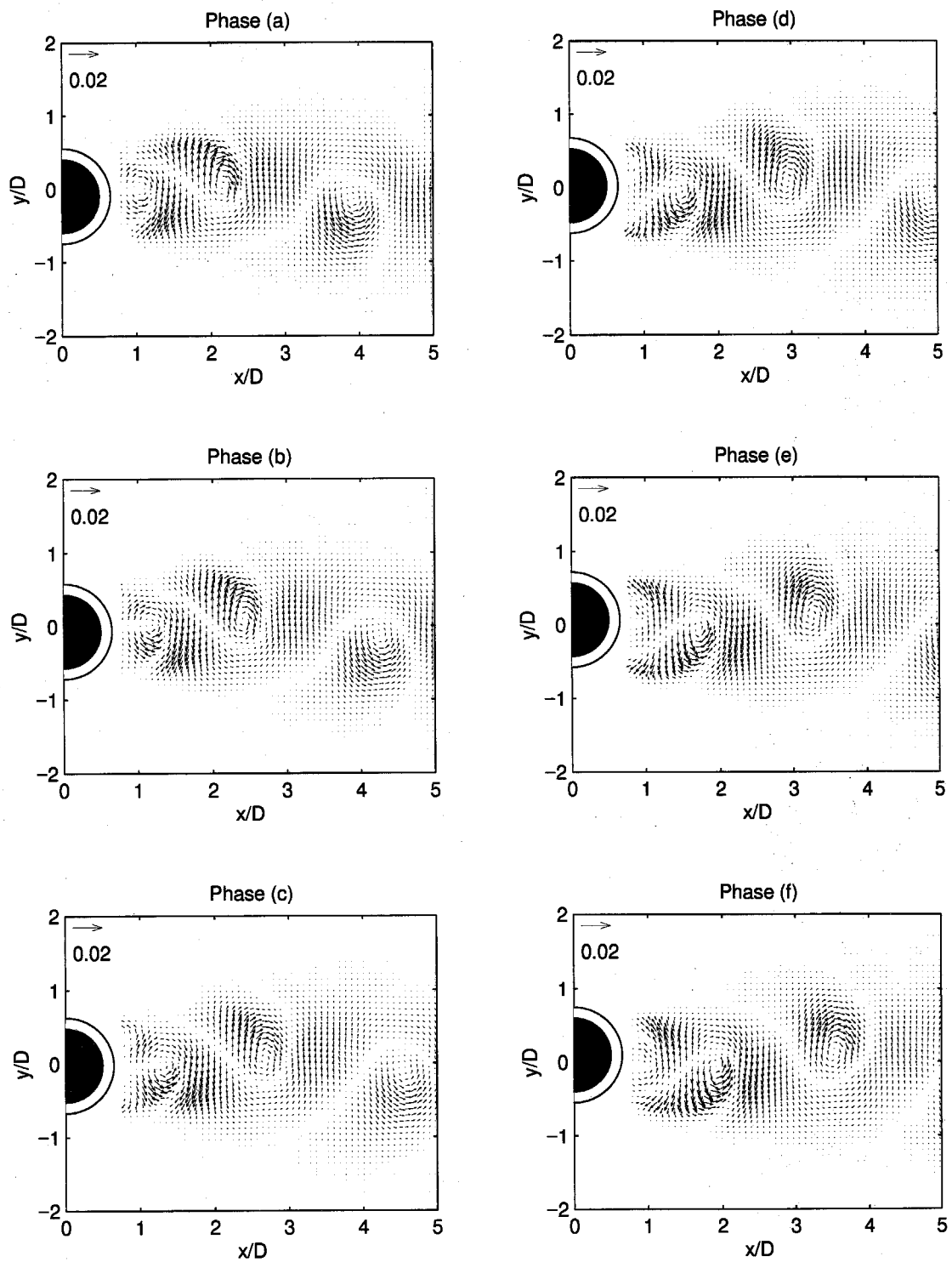


Figure 4.29(a) Sequence of phase averaged coherent heat flux for forced oscillating cylinder at $St_c$=0.21, A/D=0.1. The y-displacement of the cylinder corresponding to each letter is shown in Fig. 4.55.

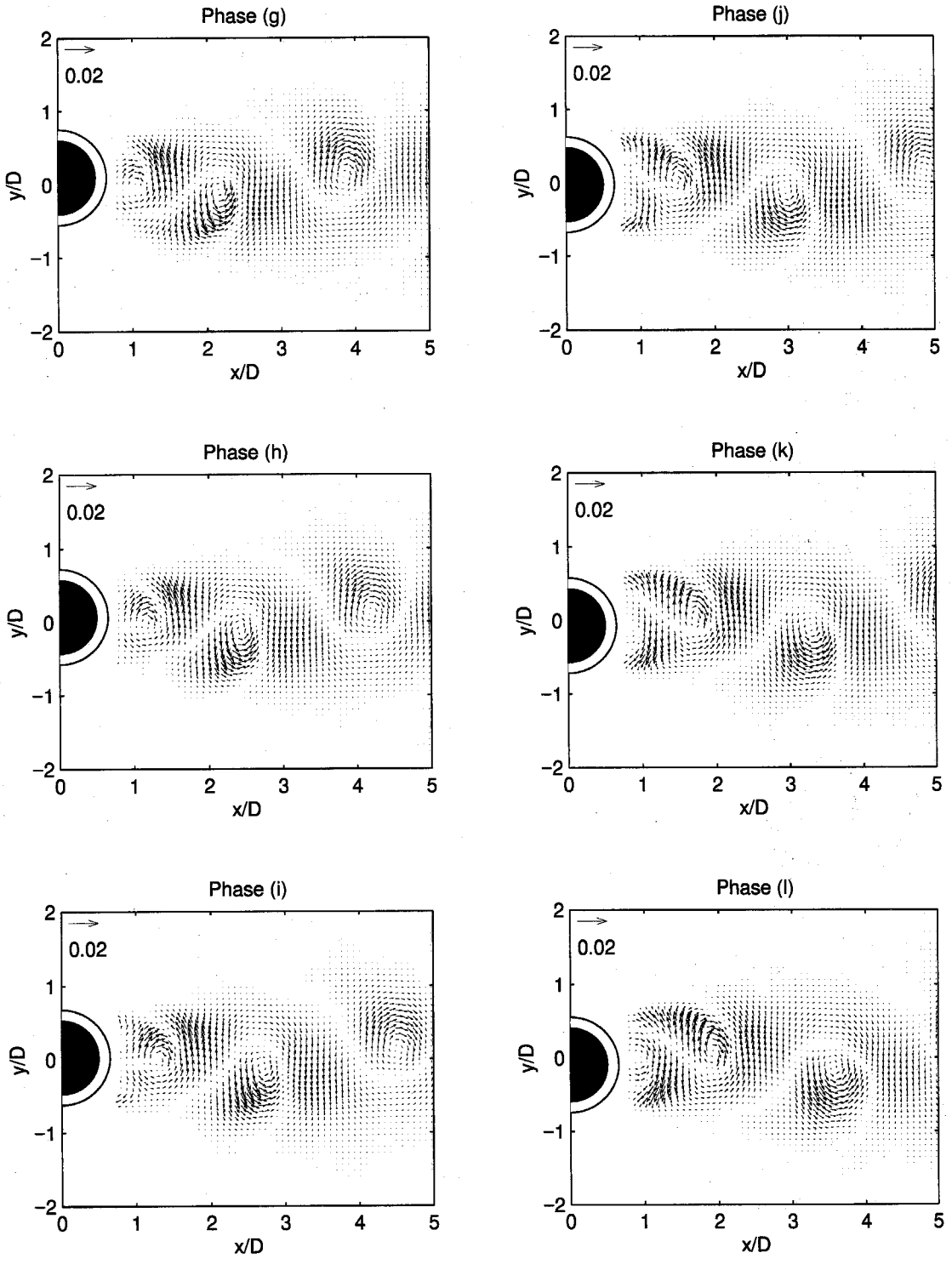


Figure 4.29(b) Sequence of phase averaged coherent heat flux for forced oscillating cylinder at $St_c$=0.21, A/D=0.1. The y-displacement of the cylinder corresponding to each letter is shown in Fig. 4.55.

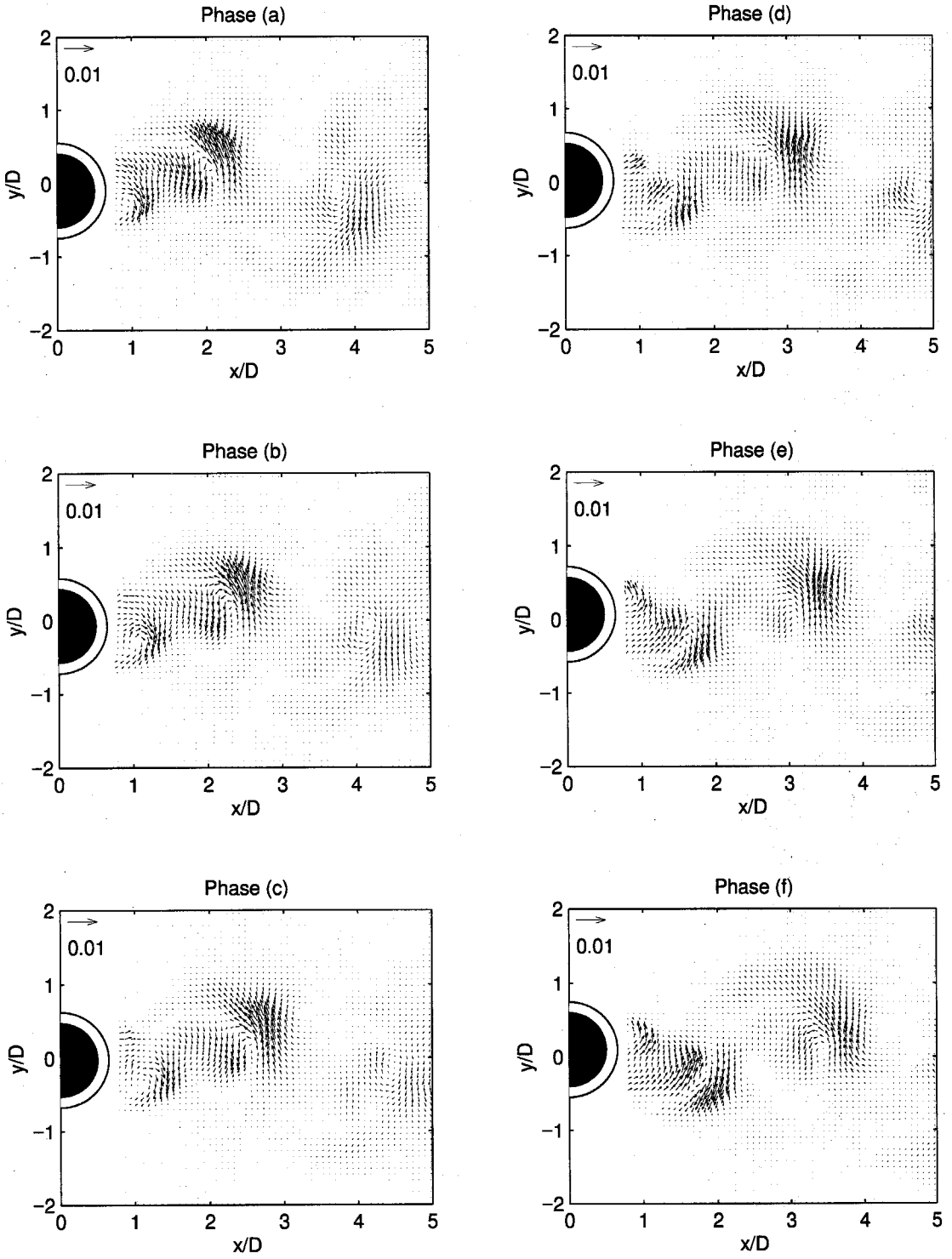


Figure 4.30(a) Sequence of phase averaged incoherent heat flux for forced oscillating cylinder at $St_c$=0.21, A/D=0.1. The y-displacement of the cylinder corresponding to each letter is shown in Fig. 4.55.

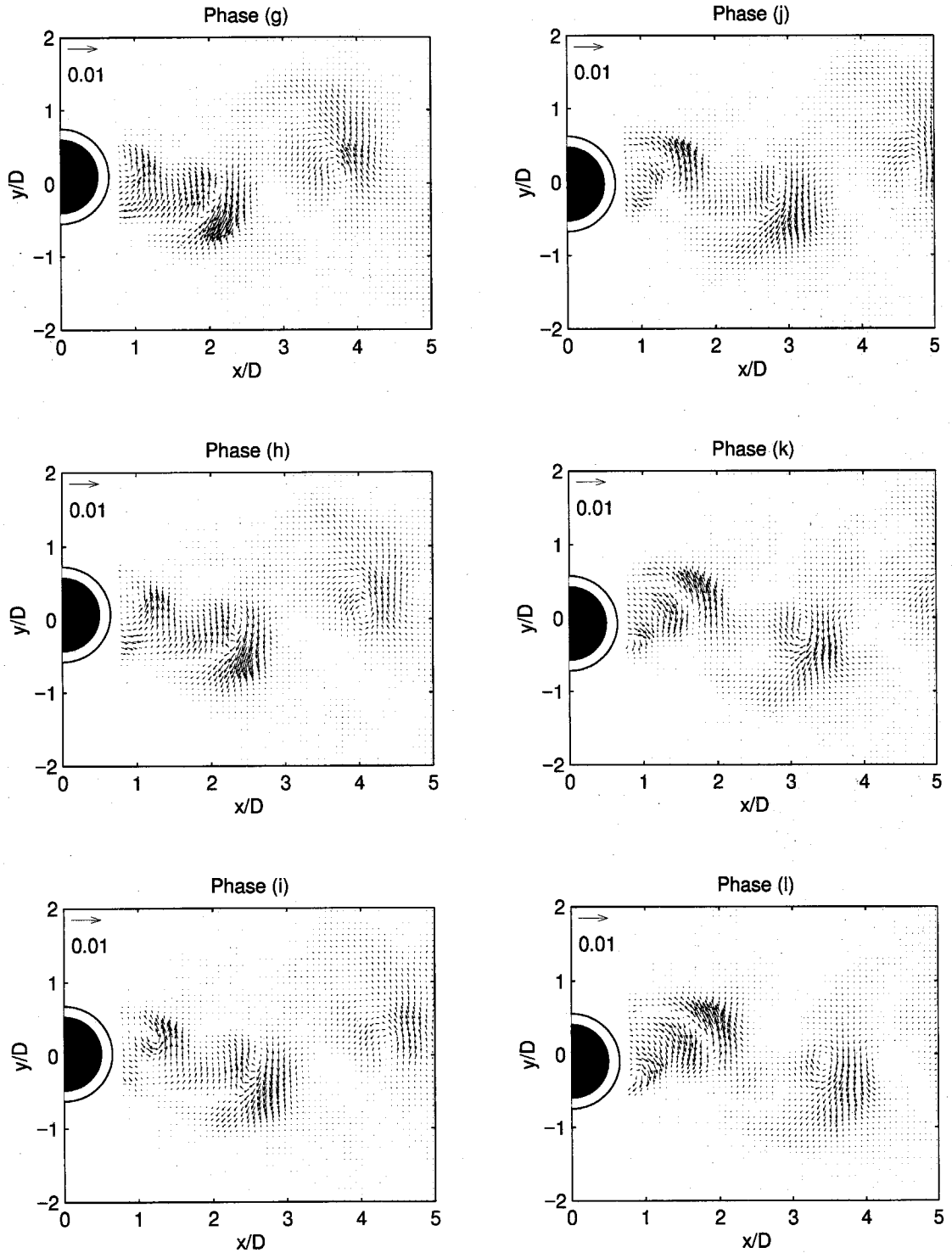


Figure 4.30(b) Sequence of phase averaged incoherent heat flux for forced oscillating cylinder at $St_c$=0.21, A/D=0.1. The y-displacement of the cylinder corresponding to each letter is shown in Fig. 4.55.

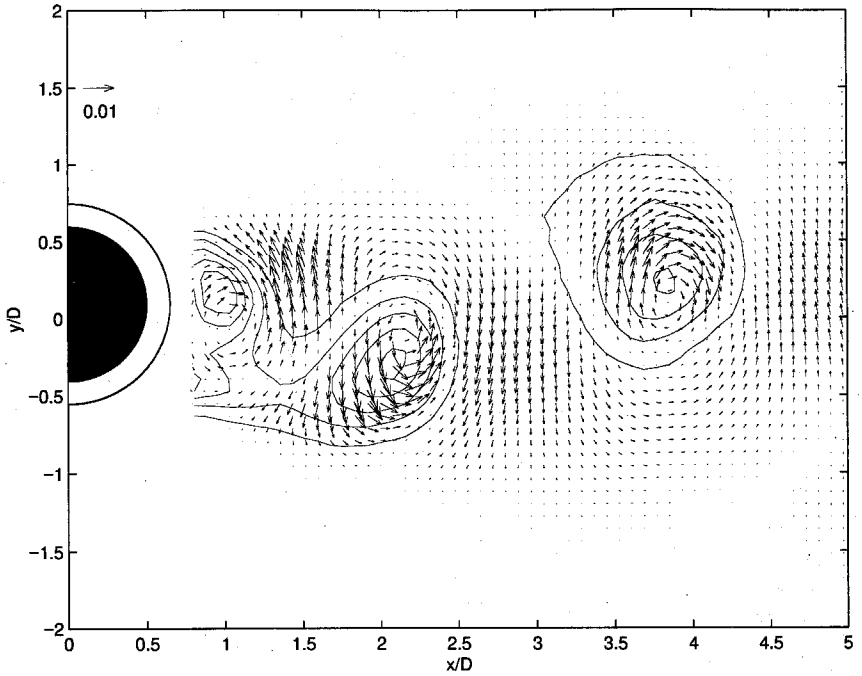


Figure 4.31 Transport of heat out of the wake by the coherent heat flux at Phase (g). The solid lines are contours of temperature.

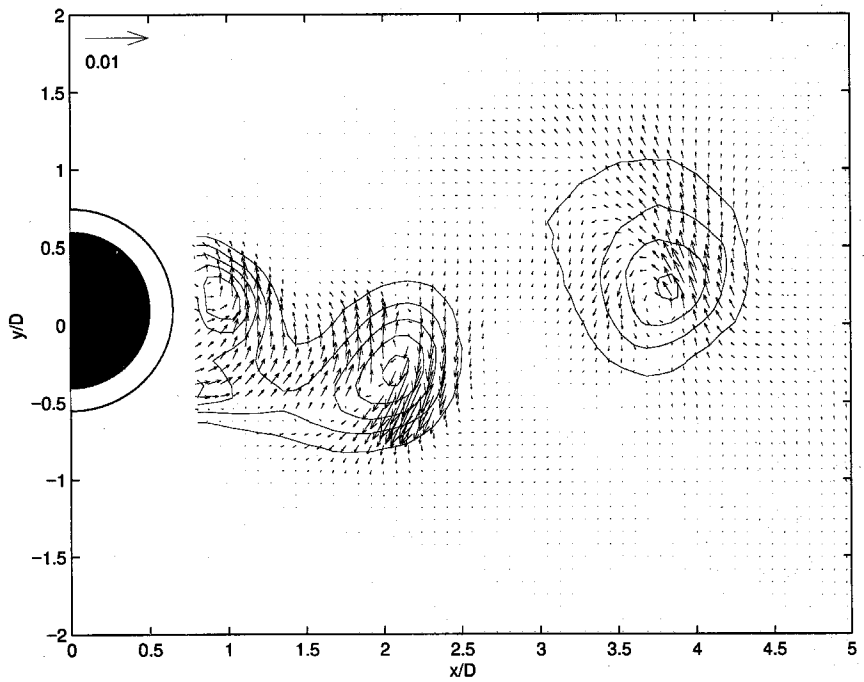


Figure 4.32 Transport of heat out of the vortices and the wake by the incoherent heat flux at Phase (g). The solid lines are contours of temperature.

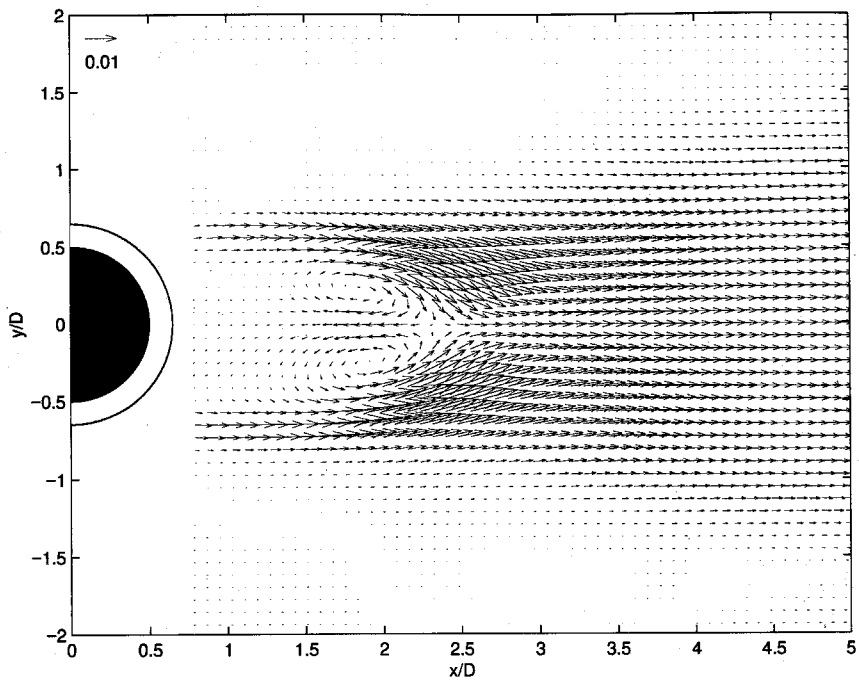


Figure 4.33 Mean heat flux for stationary cylinder at Re=610.

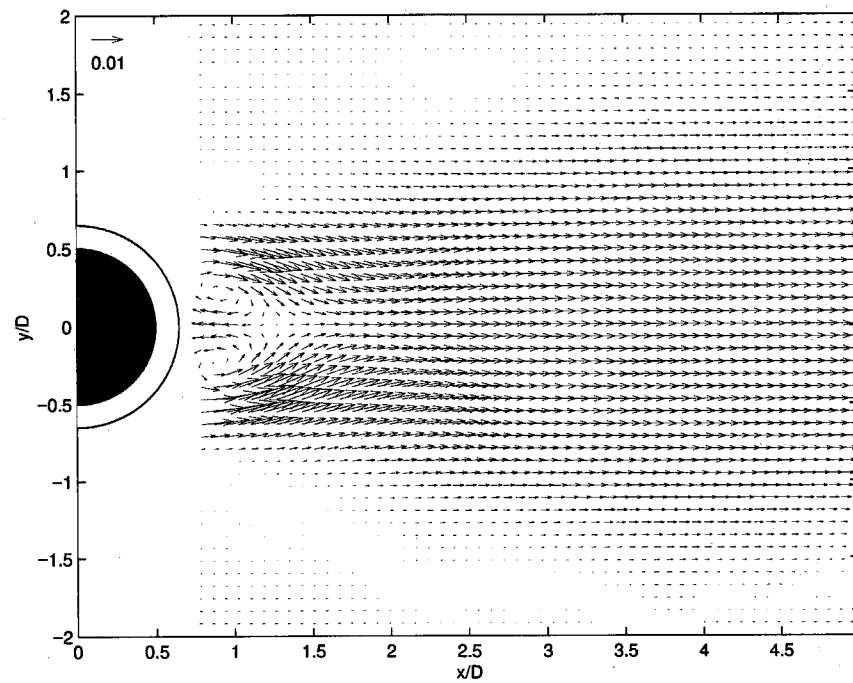


Figure 4.34 Mean heat flux for forced oscillating cylinder at $St_c$=0.21, A/D=0.1.

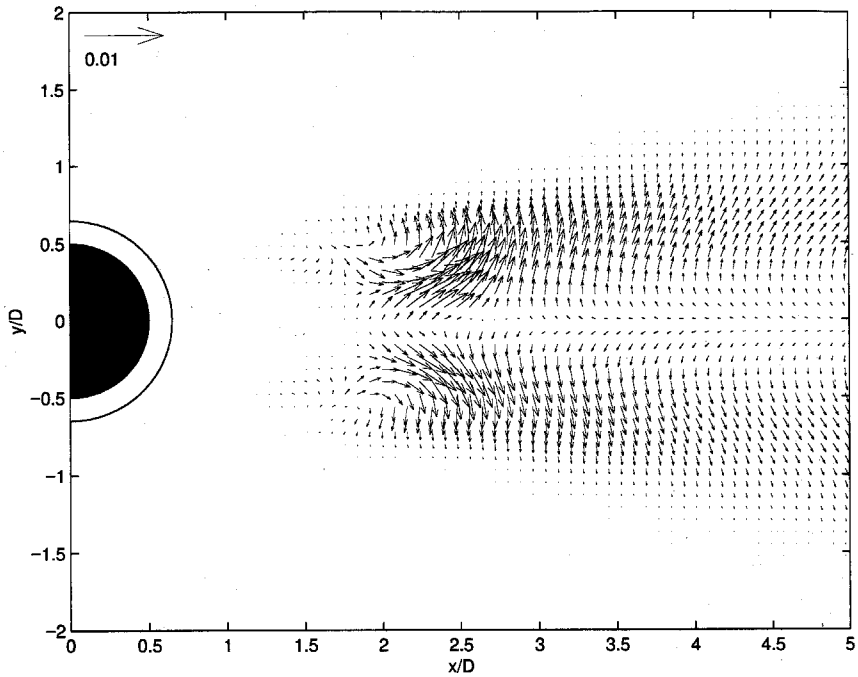


Figure 4.35 Mean coherent heat flux for stationary cylinder at Re=610.

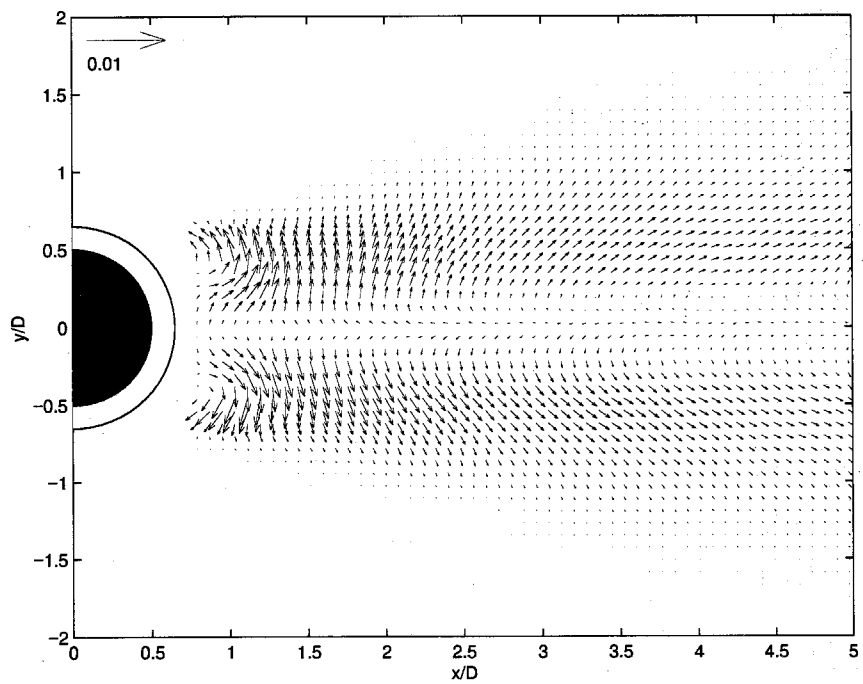


Figure 4.36 Mean coherent heat flux for forced oscillating cylinder at $St_c$=0.21, A/D=0.1.

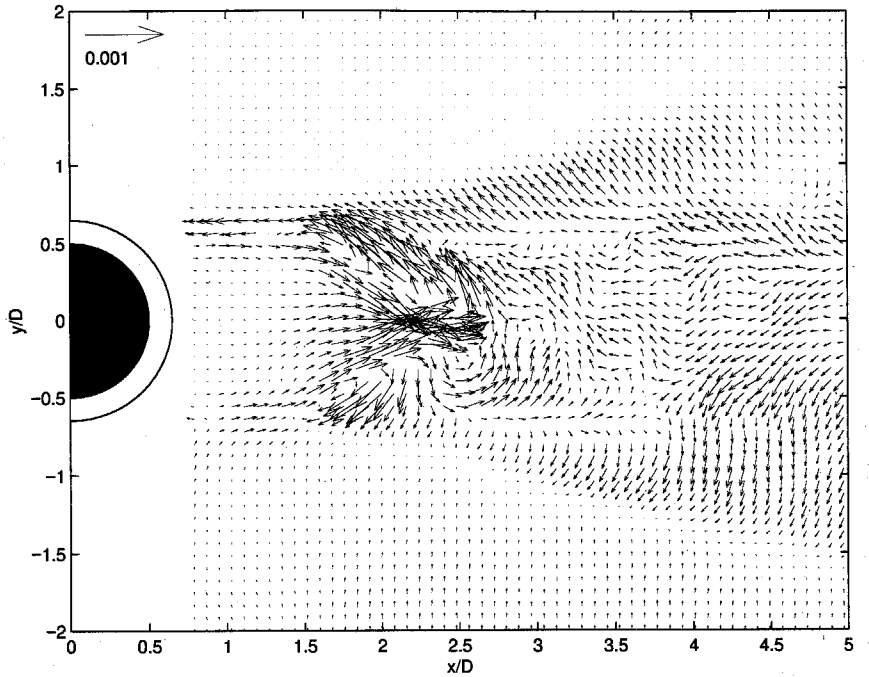


Figure 4.37 Mean incoherent heat flux for stationary cylinder at Re=610.

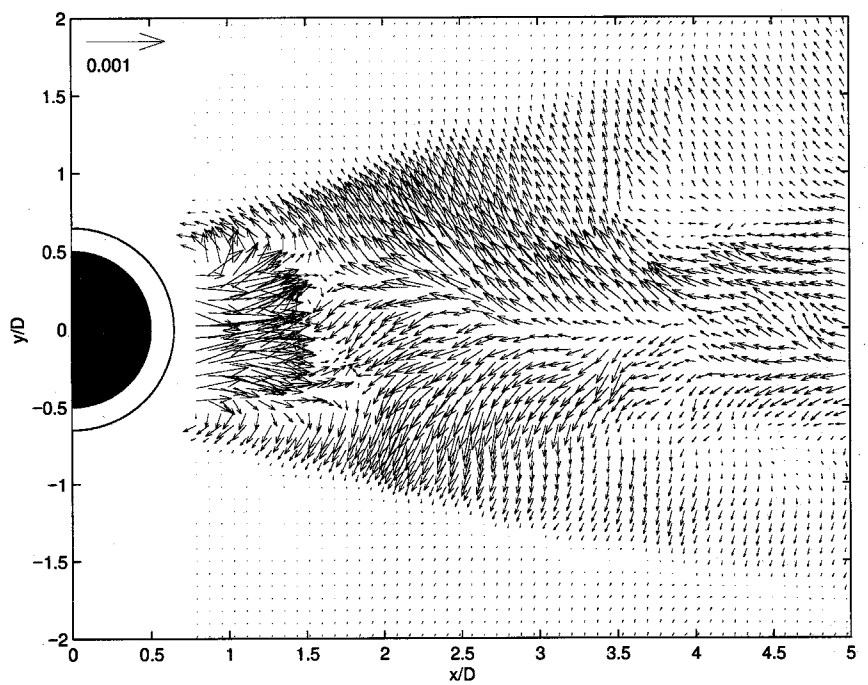


Figure 4.38 Mean incoherent heat flux for forced oscillating cylinder at $St_e$=0.21, A/D=0.1.

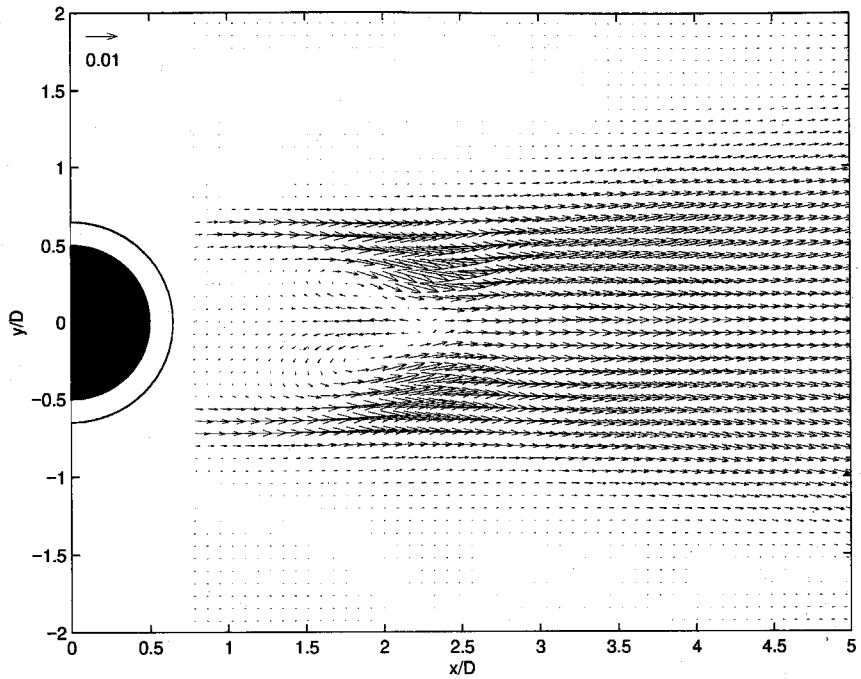


Figure 4.39 Mean total heat flux for stationary cylinder at Re=610.

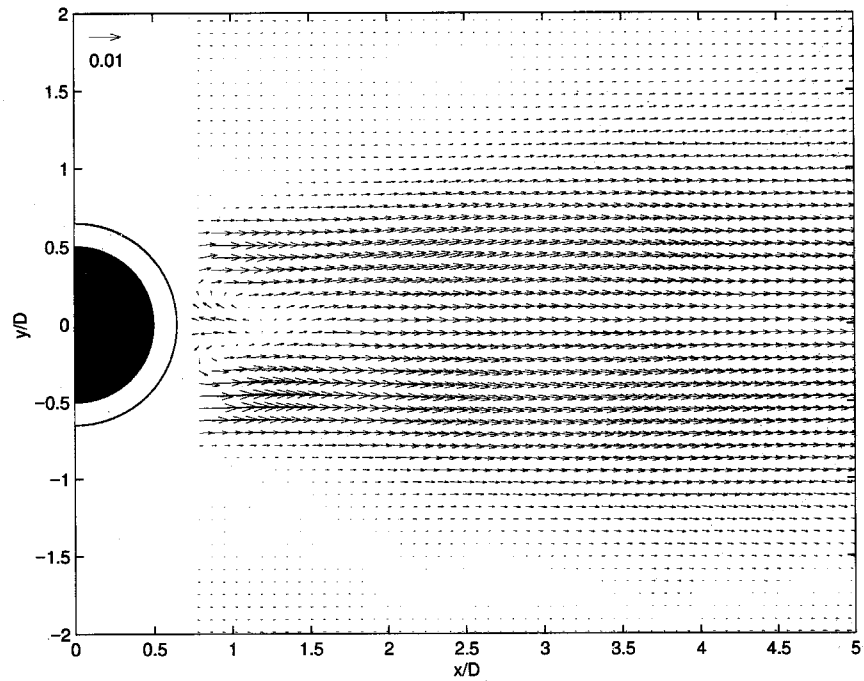


Figure 4.40 Mean total heat flux for forced oscillating cylinder at $St_c$=0.21, A/D=0.1.

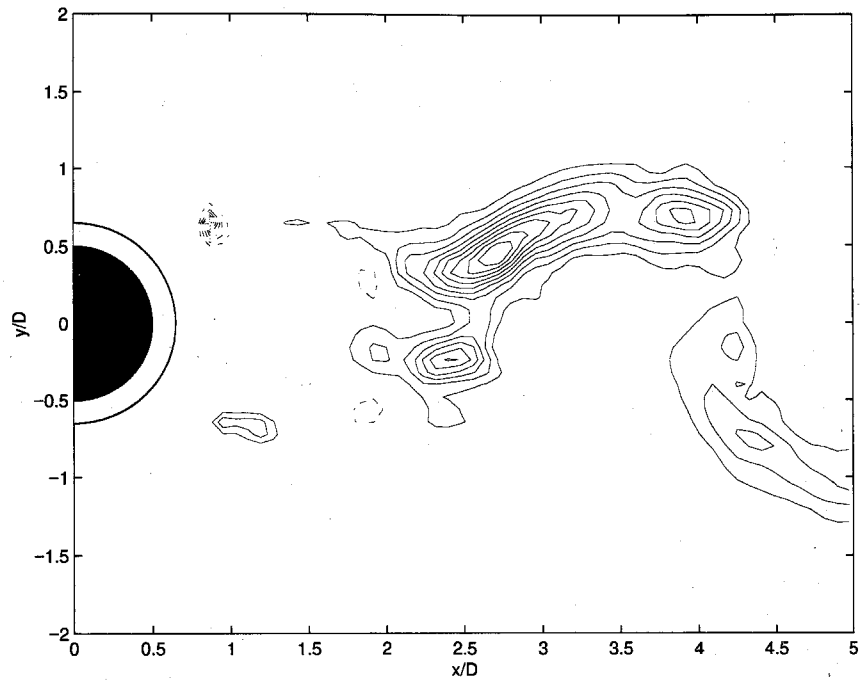


Figure 4.41 Production of kinetic energy fluctuations for stationary cylinder at Phase (f). Solid lines correspond to region of positive production and dashed lines, negative production.

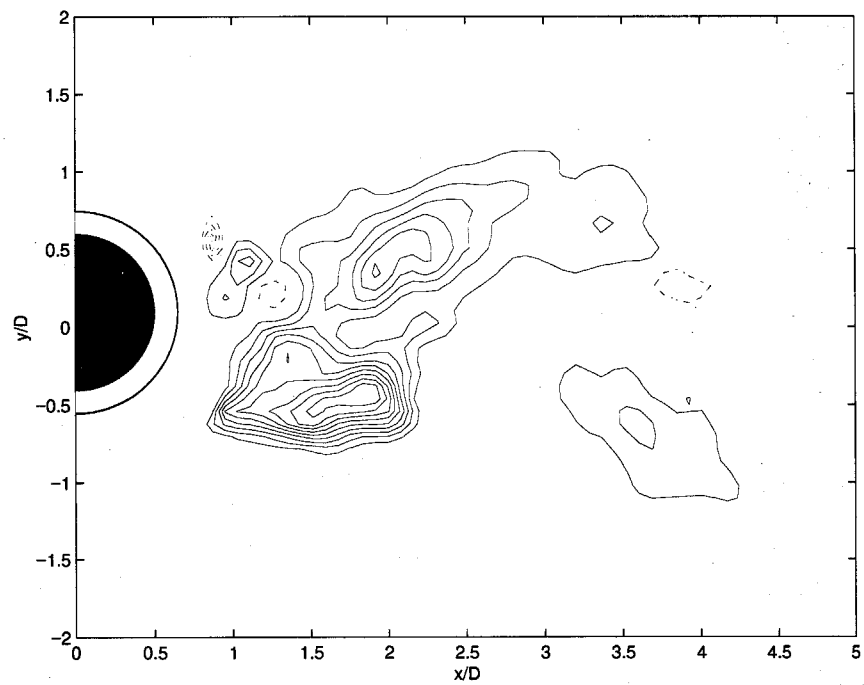


Figure 4.42 Production of kinetic energy fluctuations for forced oscillating cylinder at $St_c$=0.21, A/D=0.1, Phase (g). Solid lines correspond to region of positive production and dashed lines, negative production.

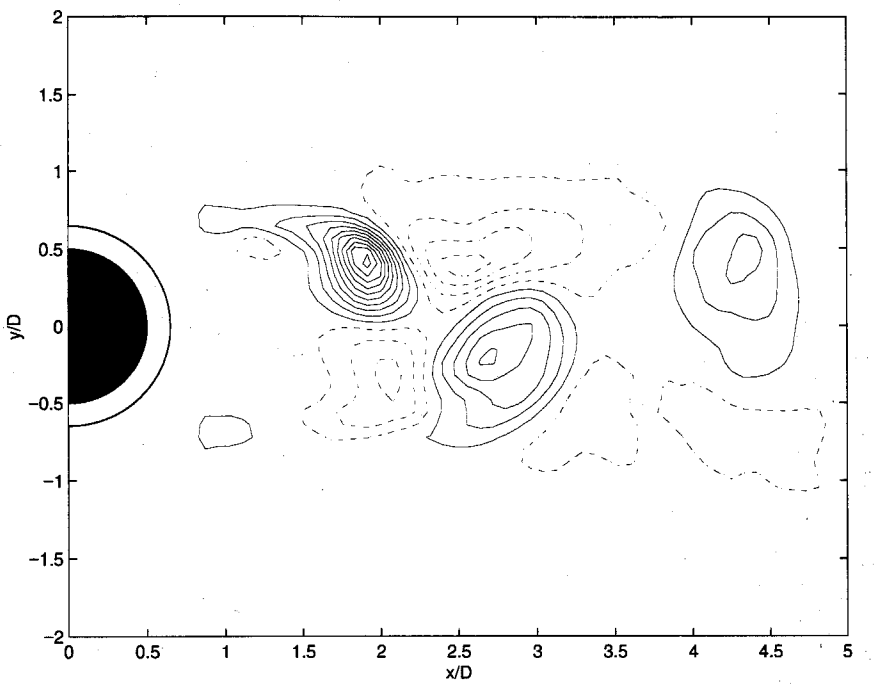


Figure 4.43 Topology of the phase averaged flow for stationary cylinder at Phase (f). The dashed lines correspond to Q<0, or saddle regions, and the solid lines correspond to Q>0, or center regions.

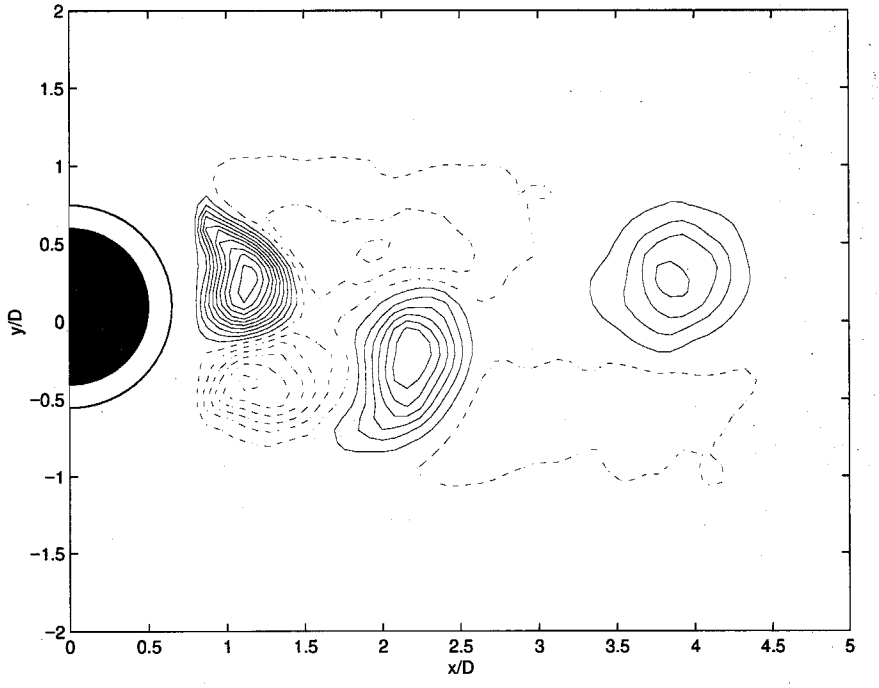


Figure 4.44 Topology of the phase averaged flow for forced oscillating cylinder at $St_c$=0.21, A/D=0.1, Phase (g). The dashed lines correspond to Q<0, or saddle regions, and the solid lines correspond to Q>0, or center regions.

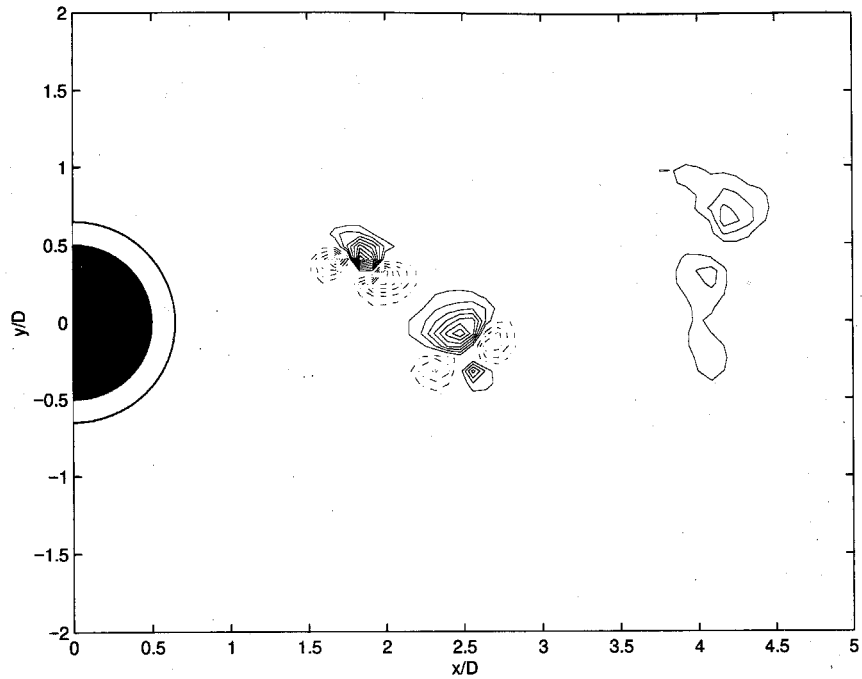


Figure 4.45 Production of temperature fluctuations for stationary cylinder at Phase (f). Solid lines correspond to region of positive production and dashed lines, negative production.

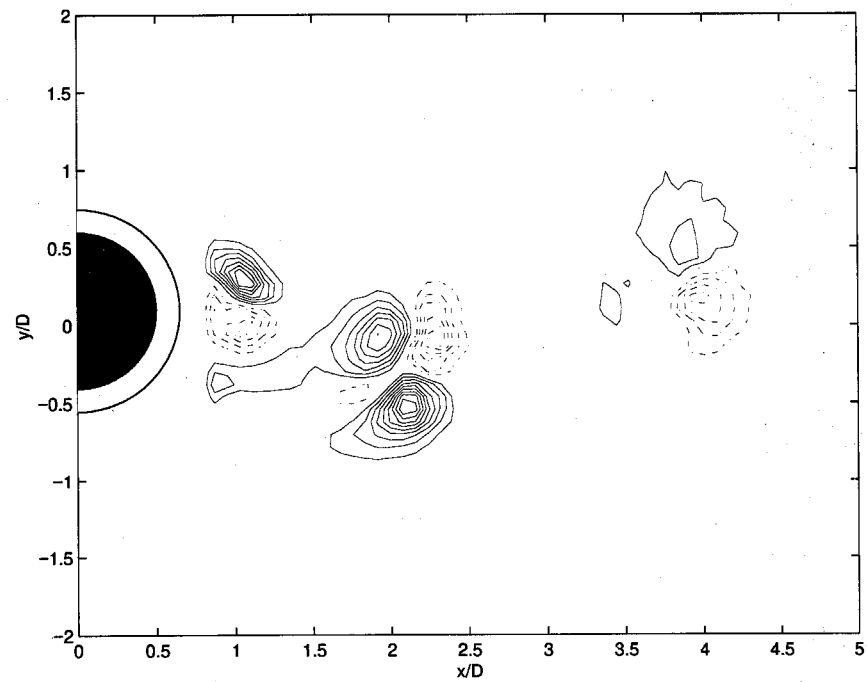


Figure 4.46 Production of temperature fluctuations for forced oscillating cylinder at $St_c$=0.21, A/D=0.1, Phase (g). Solid lines correspond to region of positive production and dashed lines, negative production.

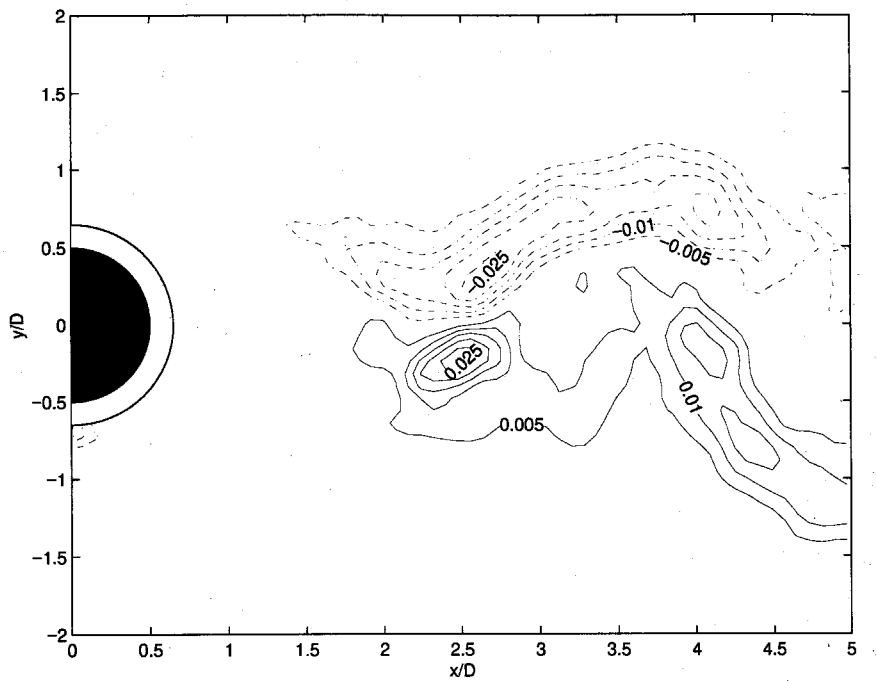


Figure 4.47 Incoherent shear stress $\langle u_{rx}' u_{ry}' \rangle / U_\infty^2$ for stationary cylinder at Phase (f).

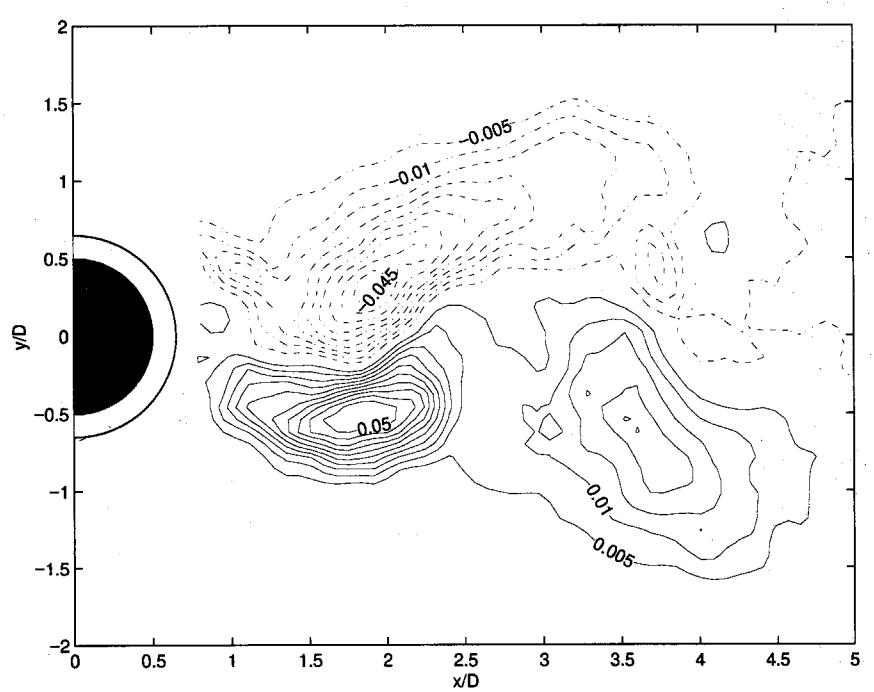


Figure 4.48 Incoherent shear stress $\langle u_{rx}' u_{ry}' \rangle / U_\infty^2$ for forced oscillating cylinder at $St_c$=0.21, A/D=0.1, Phase (g).

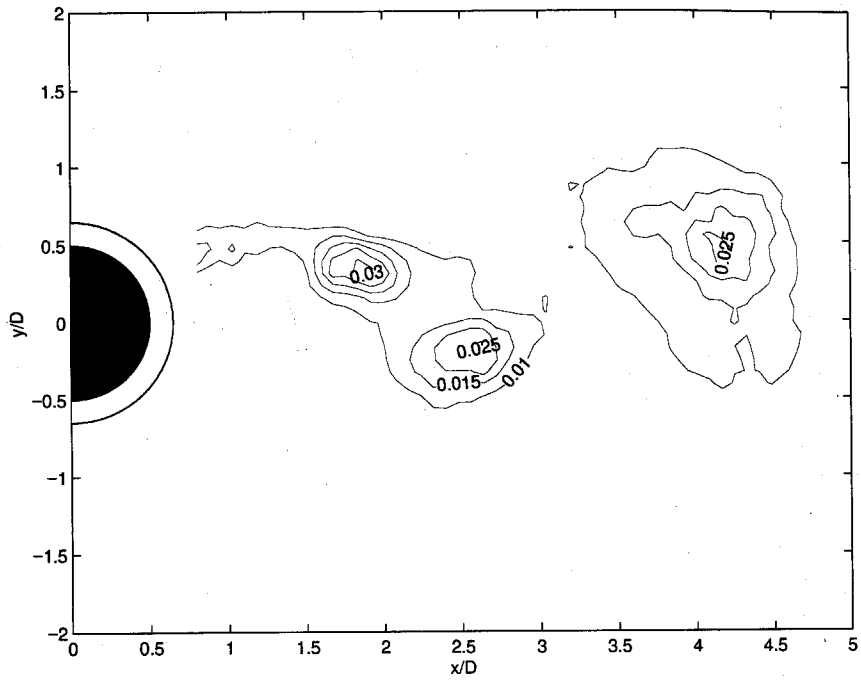


Figure 4.49 RMS of temperature for stationary cylinder at Phase (f).

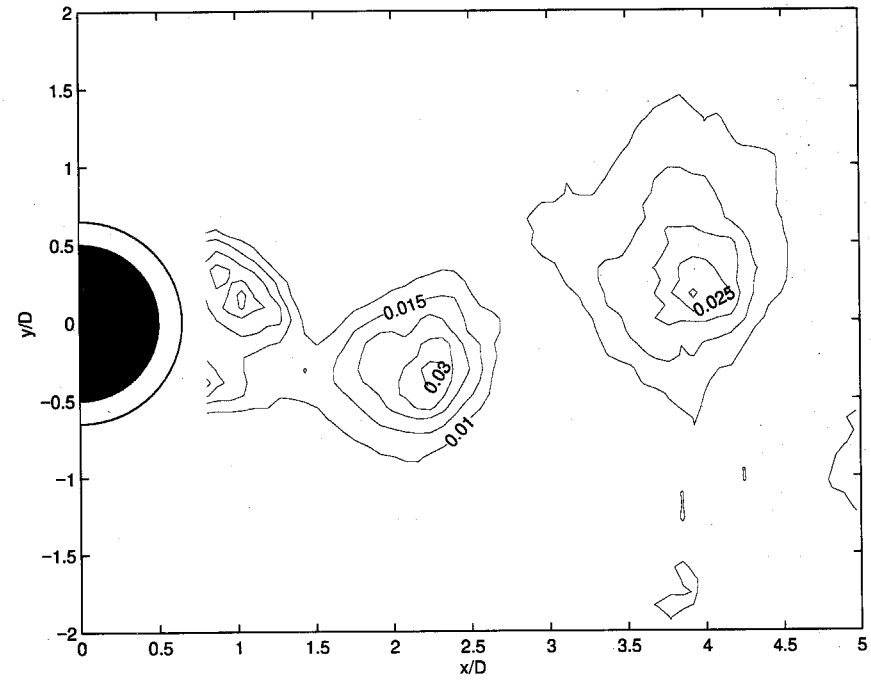


Figure 4.50 RMS of temperature for forced oscillating cylinder at $St_e$=0.21, A/D=0.1, Phase (g).

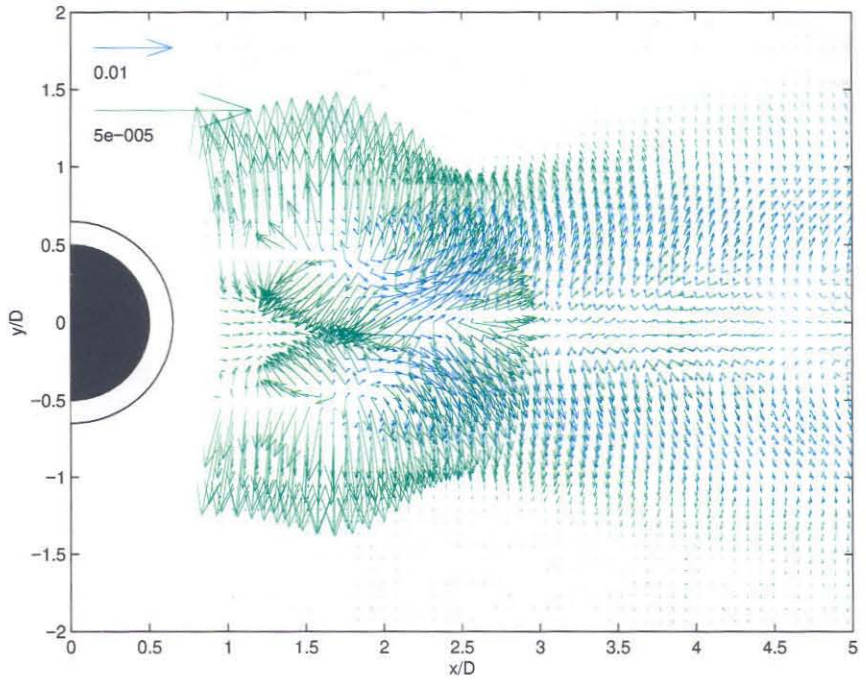


Figure 4.51 Comparision of the direction of mean molecular (green vectors) and mean global turbulent heat flux vectors (blue vectors) in the wake of a stationary cylinder at Re=610. The molecular heat flux is normalized by (-∇T D/ ($T_c$ - $T_\infty$)RePr).

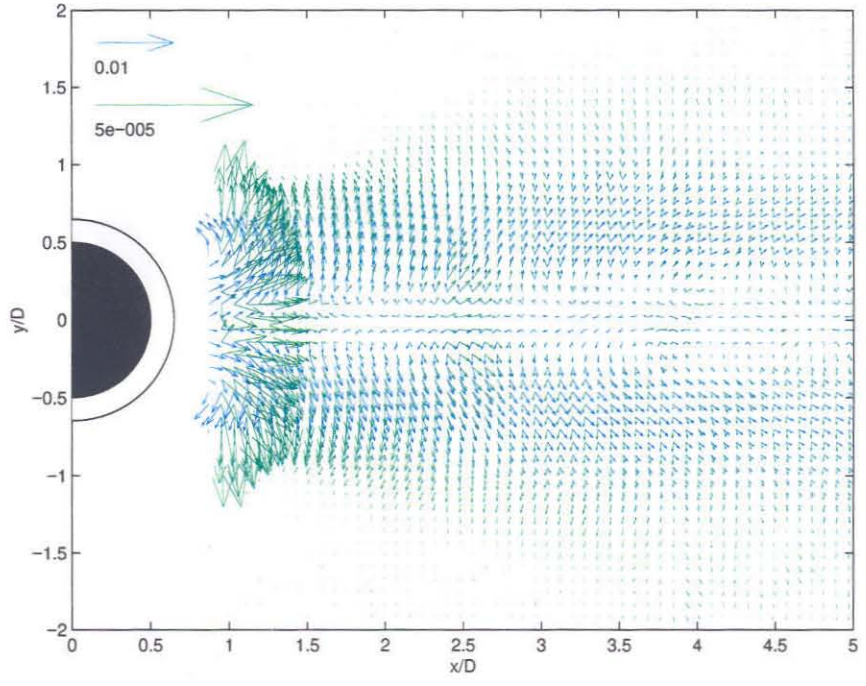


Figure 4.52 Comparision of the direction of mean molecular (green vectors) and mean global turbulent heat flux vectors (blue vectors) in the wake of a forced oscillating cylinder at $St_c$=0.21, A/D=0.1. The molecular heat flux is normalized by (-∇T D/ ($T_c$ - $T_\infty$)RePr).

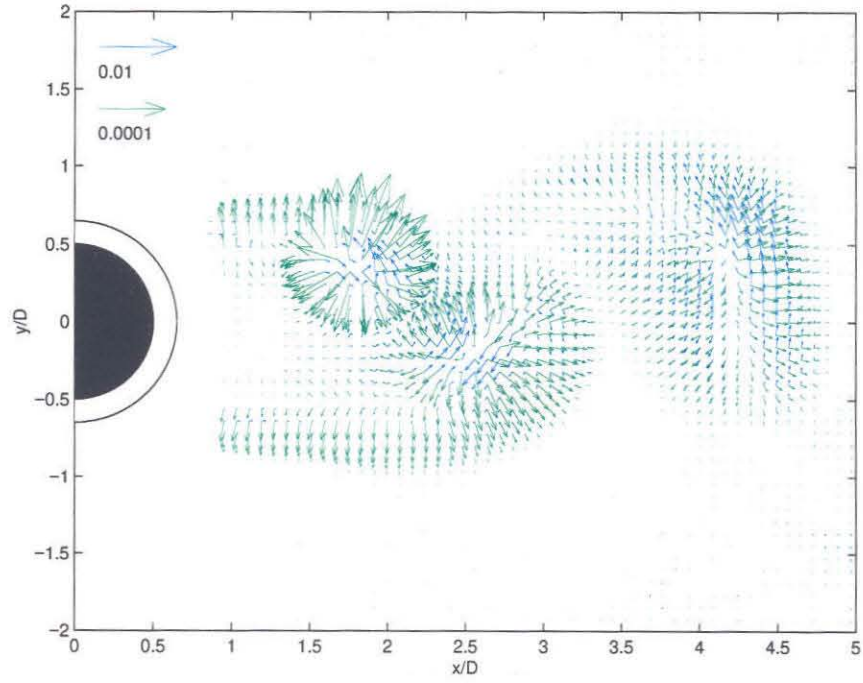


Figure 4.53 Comparision of the direction of the phase averaged molecular (green vectors) and incoherent heat flux vectors (blue vectors) in the wake of a stationary cylinder at Phase (f).

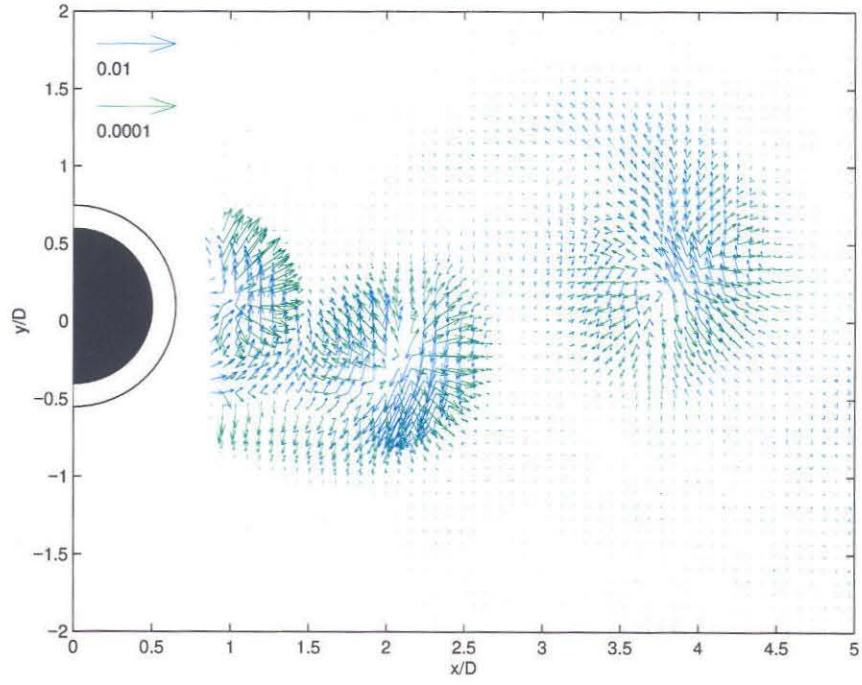


Figure 4.54 Comparision of the direction of the phase averaged molecular (green vectors) and incoherent heat flux vectors (blue vectors) in the wake of a forced oscillating cylinder at $St_c$=0.21, A/D=0.1, Phase (g).

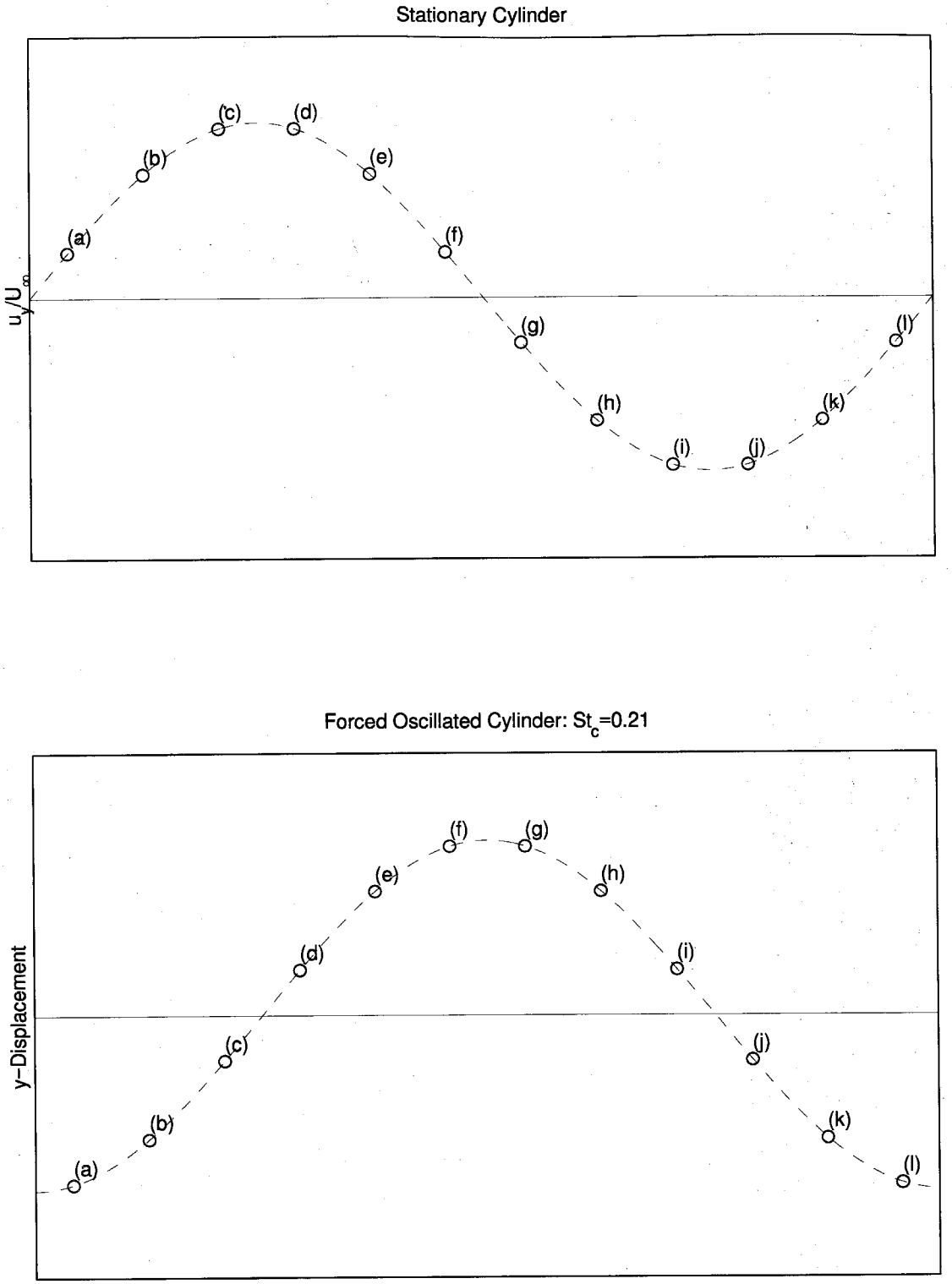


Figure 4.55 $u_y$ value and cylinder displacement corresponding to each letter of phase for stationary (top) and forced oscillating (bottom) cylinder, respectively.

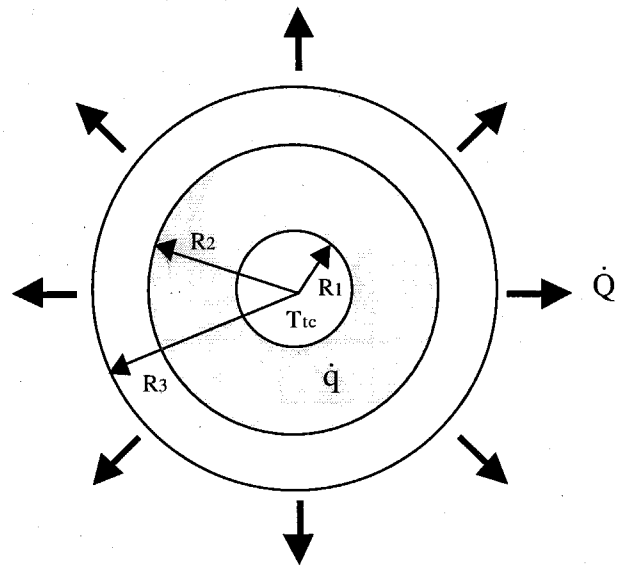


Figure 5.1 Layout of the cylinder.

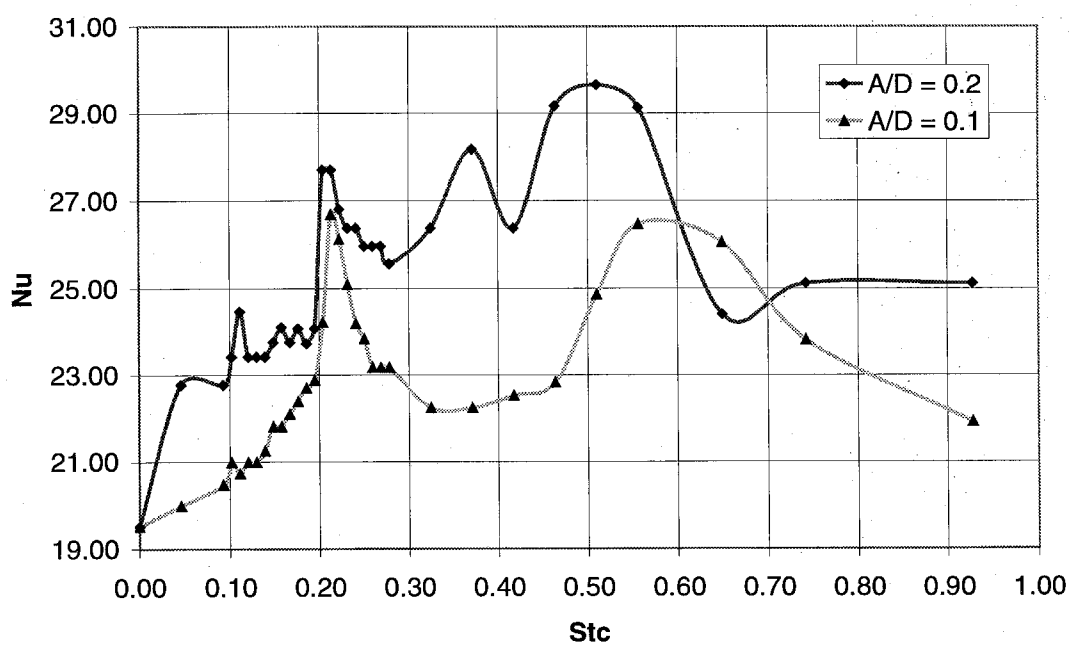


Figure 5.2 Surface heat transfer versus cylinder oscillation frequency for Re=550.

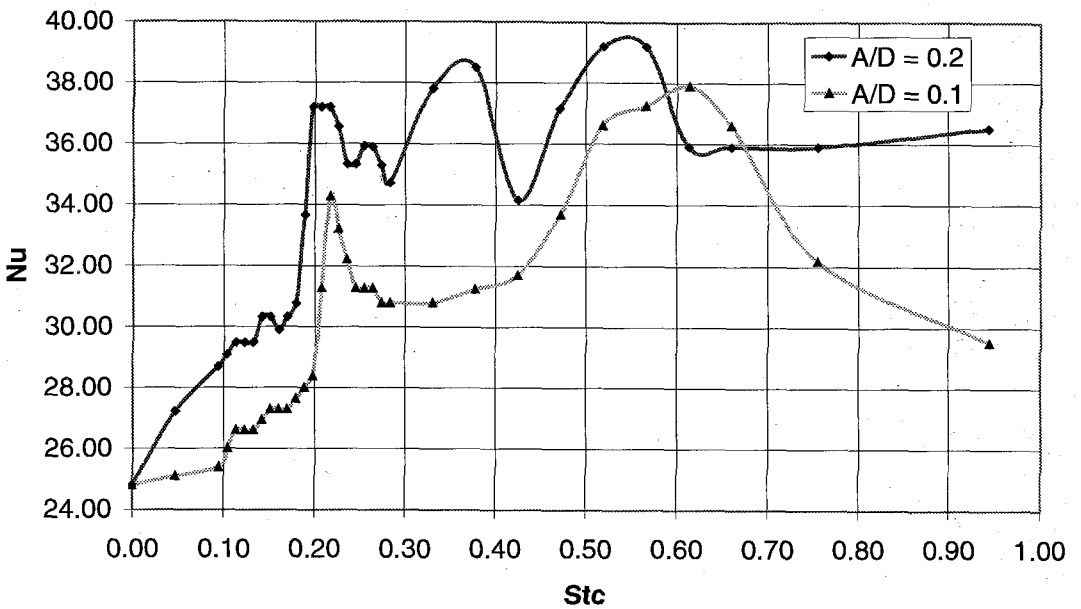


Figure 5.3 Surface heat transfer versus cylinder oscillation frequency for Re=1100.

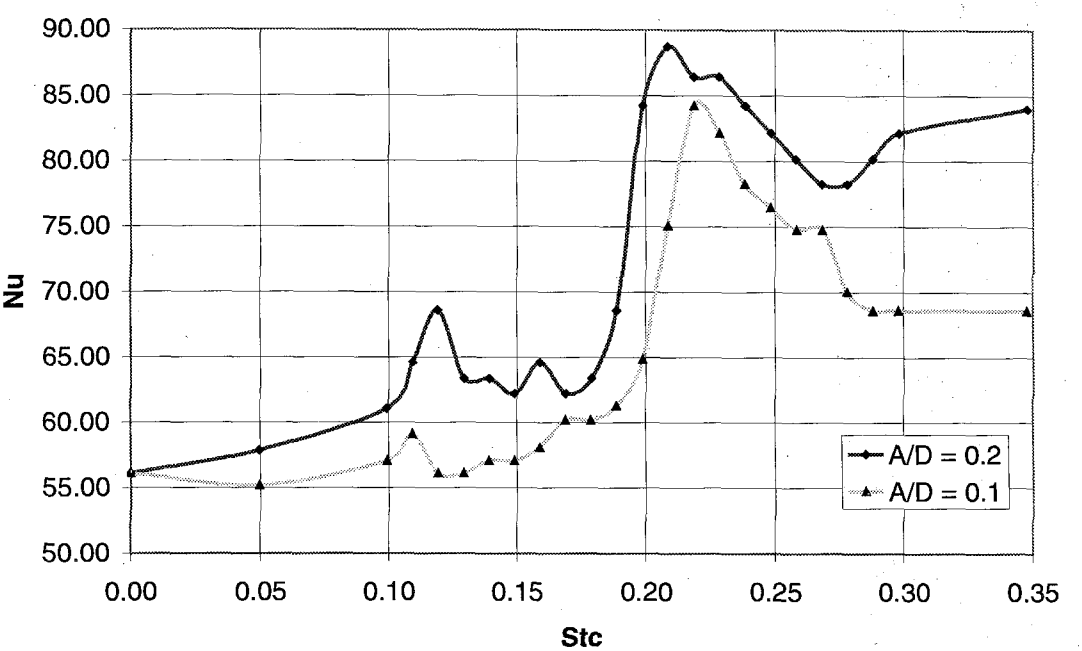


Figure 5.4 Surface heat transfer versus cylinder oscillation frequency for Re=3500.

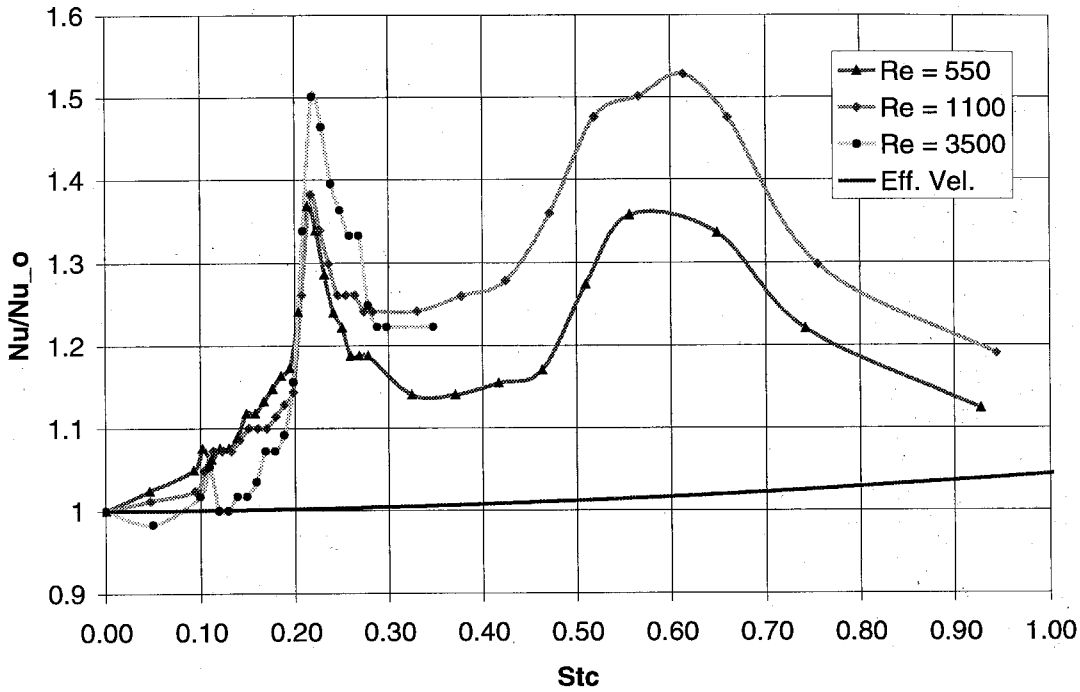


Figure 5.5 Normalized surface heat transfer as function of oscillation frequency for A/D=0.1.

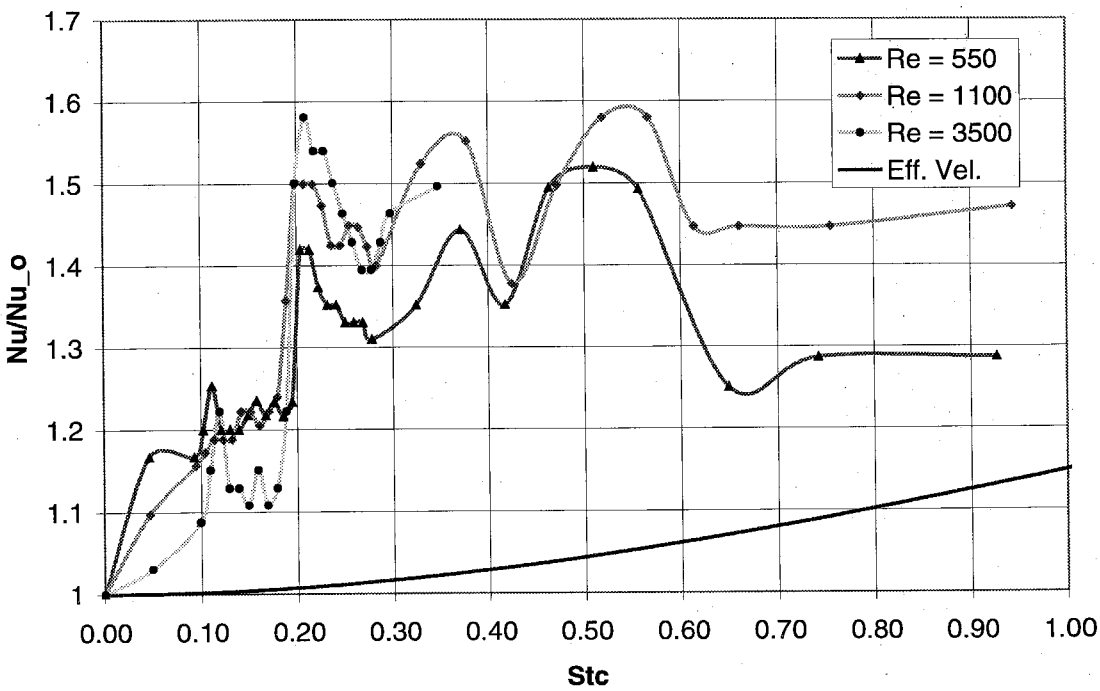


Figure 5.6 Normalized surface heat transfer as function of oscillation frequency for A/D=0.2.

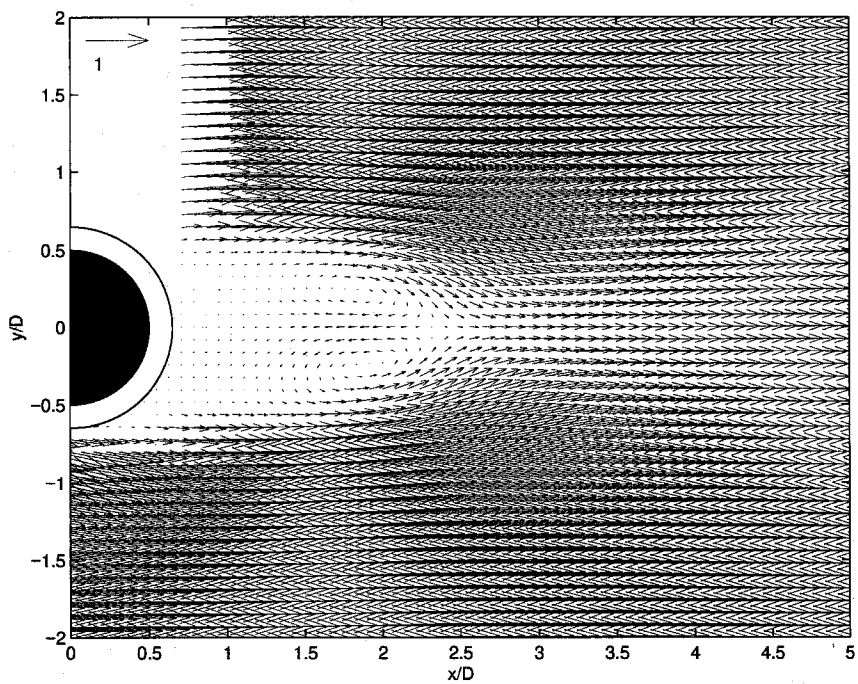


Figure 6.1 Mean velocity field of stationary cylinder (Case I).

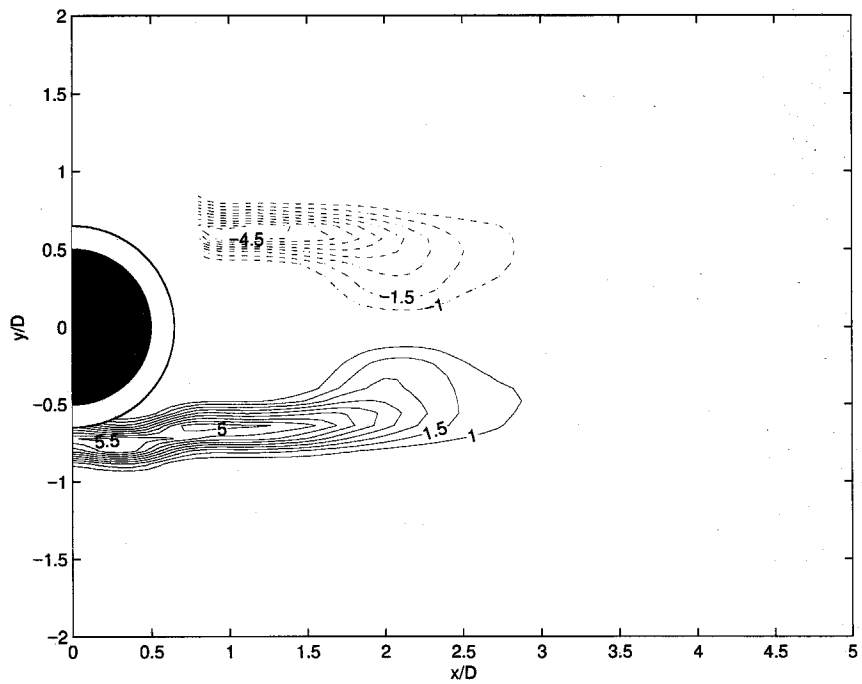


Figure 6.2 Mean vorticity field of stationary cylinder (Case I).

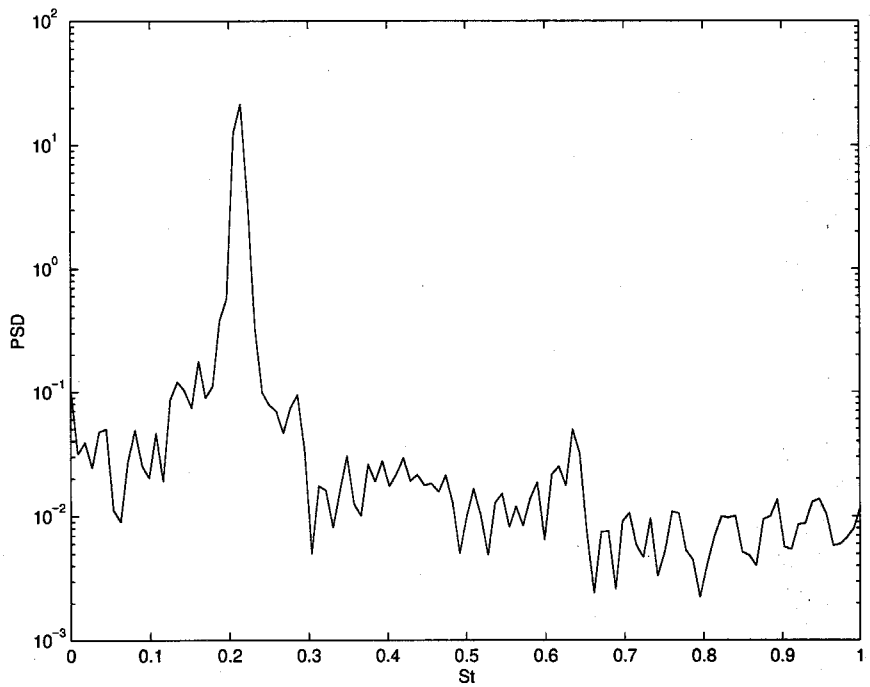


Figure 6.3 PSD of $u_y$ at location of maximum $u_y$ fluctuations on the wake centerline for stationary cylinder (Case I).

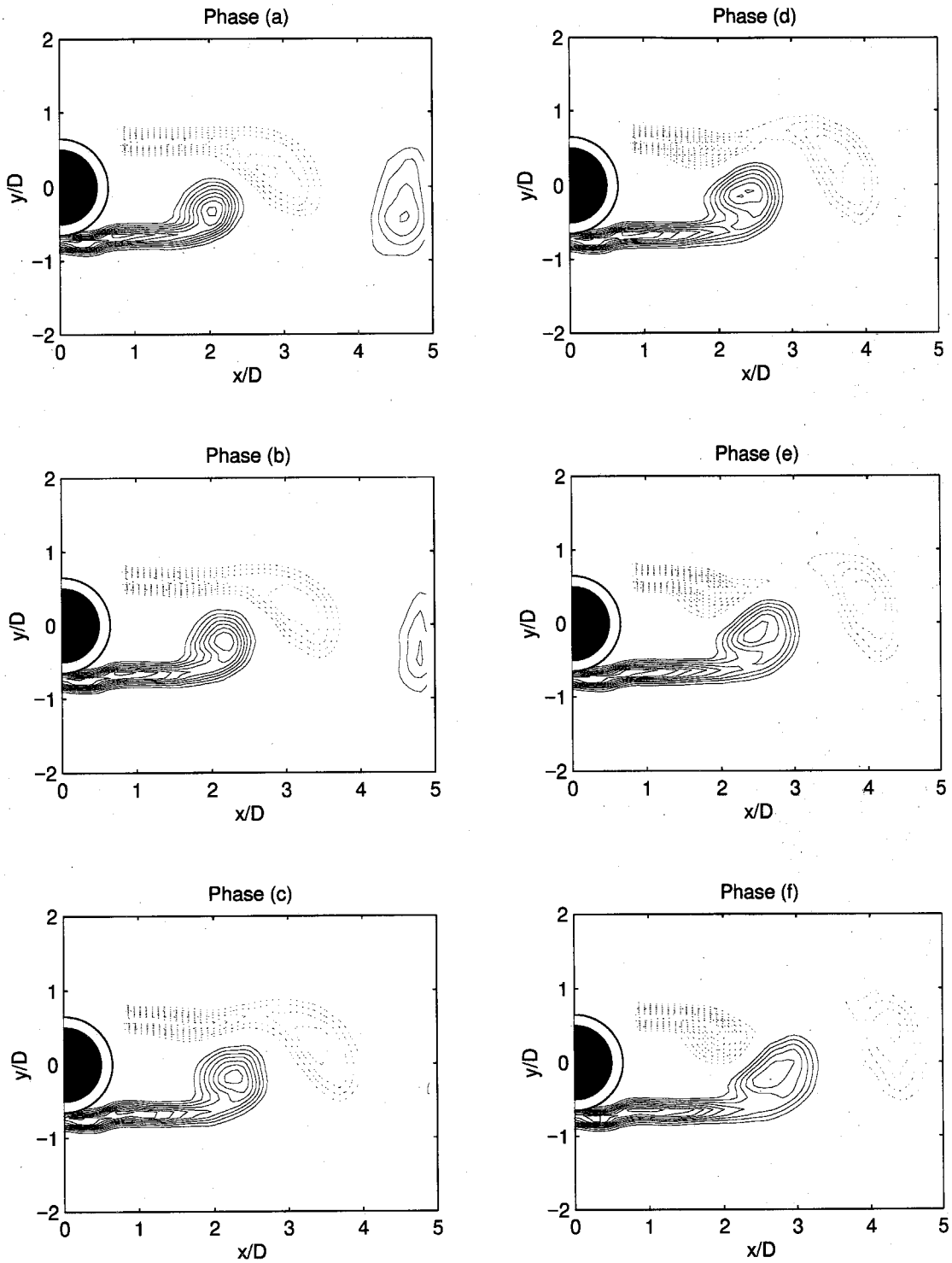


Figure 6.4(a) Sequence of phase averaged vorticity field for stationary cylinder (Case I). ($|<\omega_z>D/U_\infty|>1.0$, contour increment 0.5) The value of the reference phase velocity ($u_y$ at location of maximum fluctuations) corresponding to each letter is shown in Fig. 6.60.

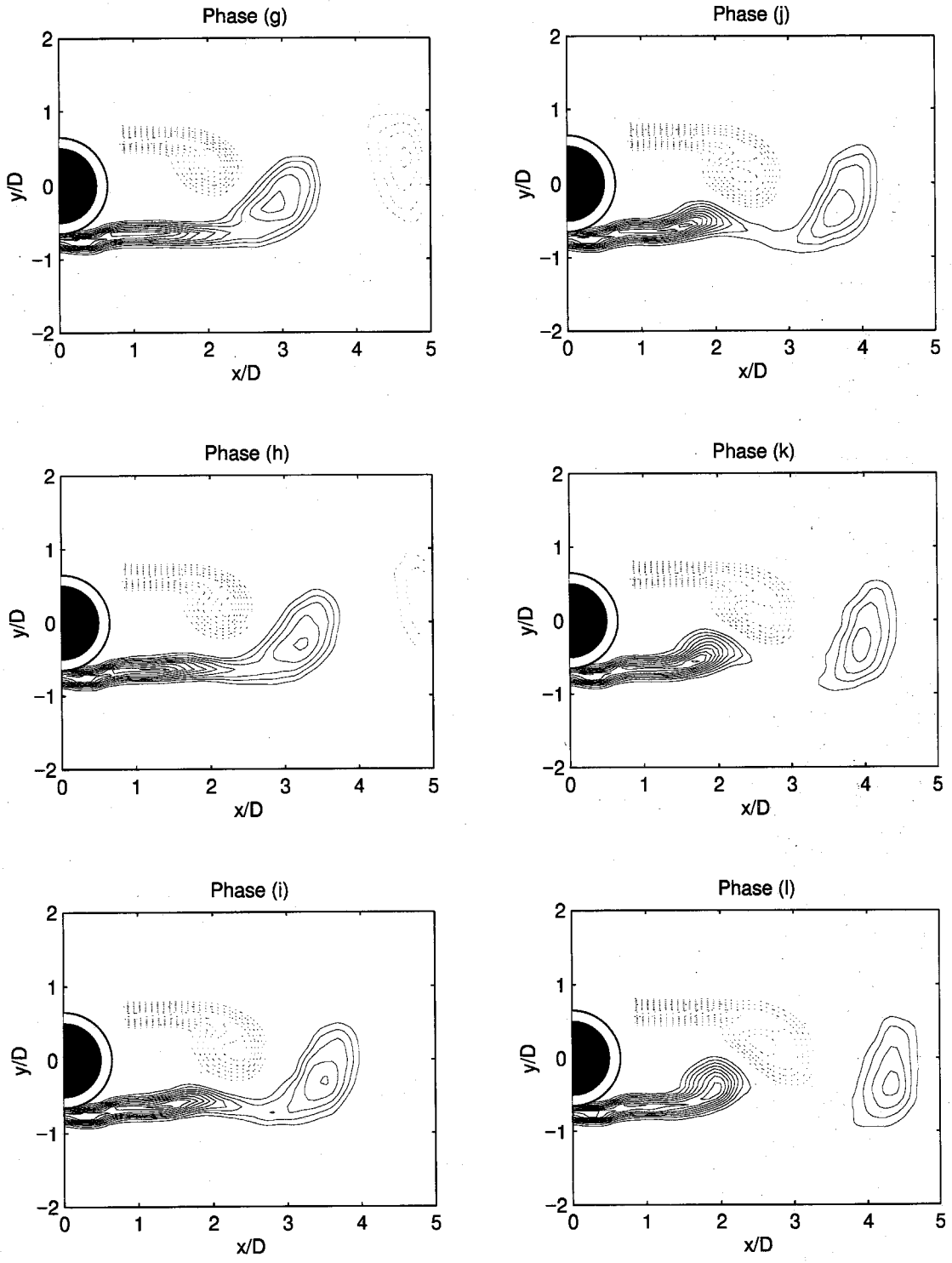


Figure 6.4(b) Sequence of phase averaged vorticity field for stationary cylinder (Case I). ($|<\omega_z>D/U_\infty|>1.0$, contour increment 0.5) The value of the reference phase velocity ($u_y$ at location of maximum fluctuations) corresponding to each letter is shown in Fig. 6.60.

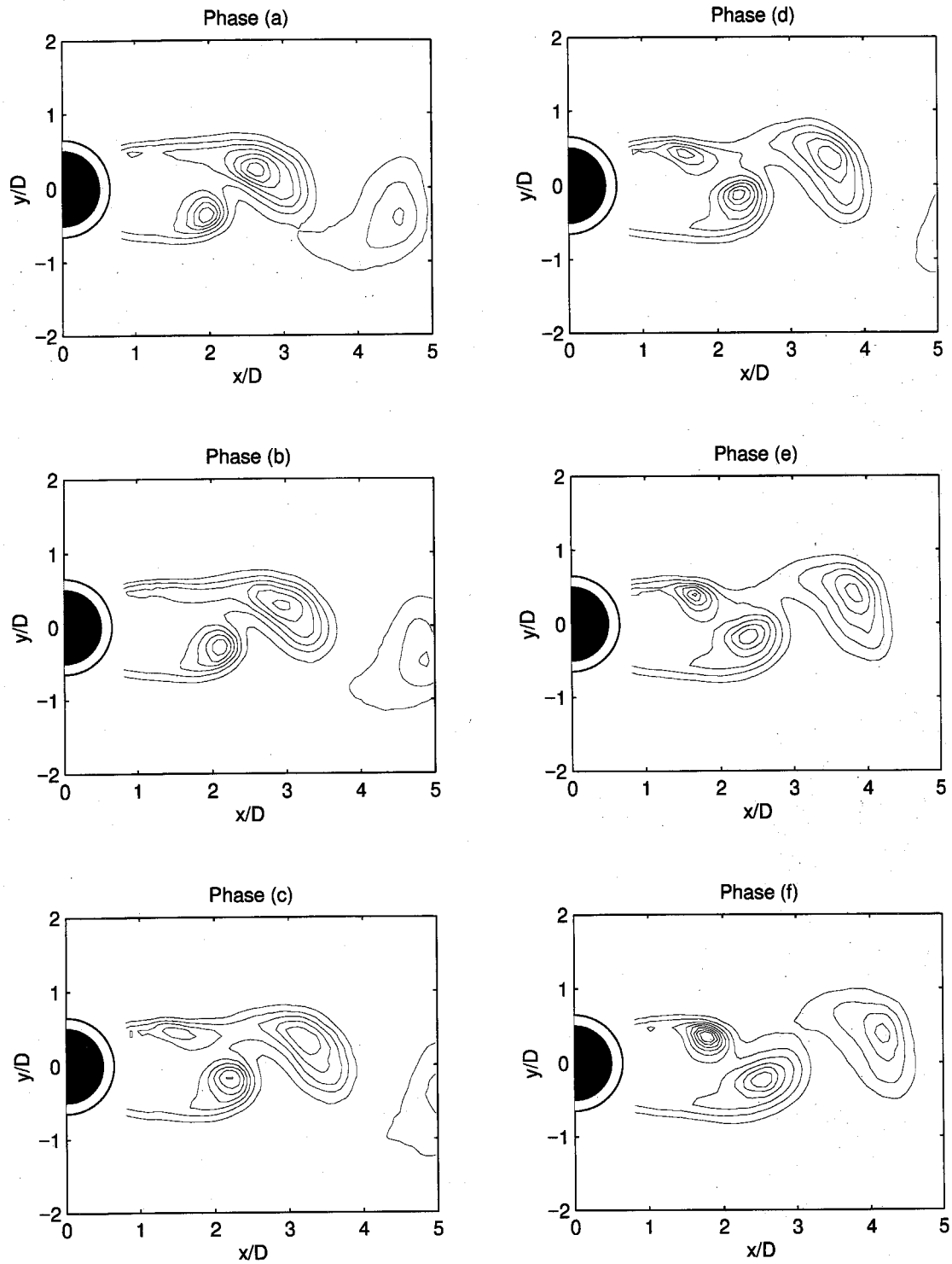


Figure 6.5(a) Sequence of phase averaged temperature field for stationary cylinder (Case I). $((\langle T \rangle - T_\infty)/(T_c - T_\infty) > 0.01$, contour increment 0.01) The value of the reference phase velocity ($u_y$ at location of maximum fluctuations) corresponding to each letter is shown in Fig. 6.60.

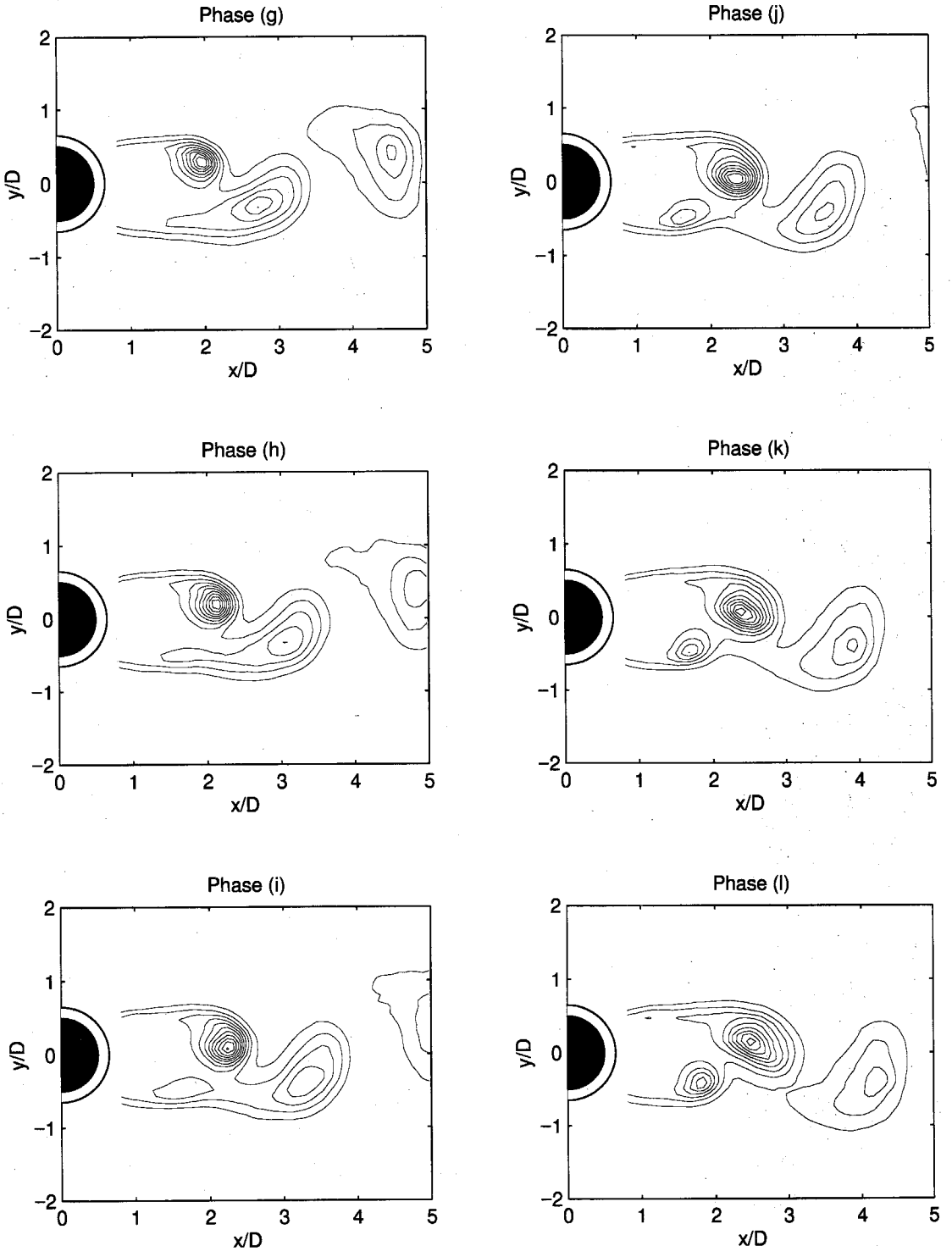


Figure 6.5(b) Sequence of phase averaged temperature field for stationary cylinder (Case I). $((\langle T \rangle - T_\infty)/(T_c - T_\infty) > 0.01$, contour increment 0.01) The value of the reference phase velocity ($u_y$ at location of maximum fluctuations) corresponding to each letter is shown in Fig. 6.60.

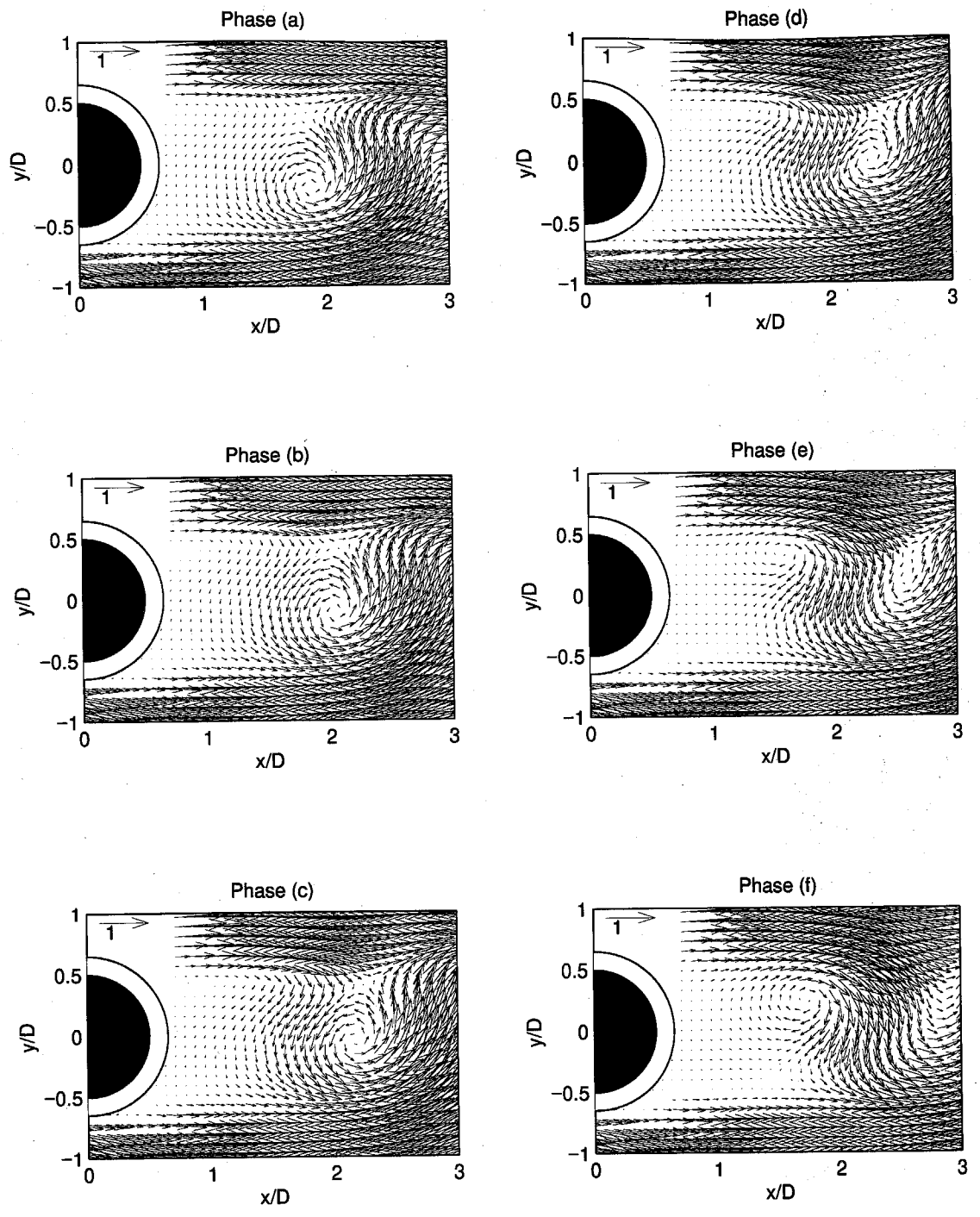


Figure 6.6(a) Sequence of phase averaged velocity field for stationary cylinder (Case I). The value of the reference phase velocity ($u_y$ at location of maximum fluctuations) corresponding to each letter is shown in Fig. 6.60.

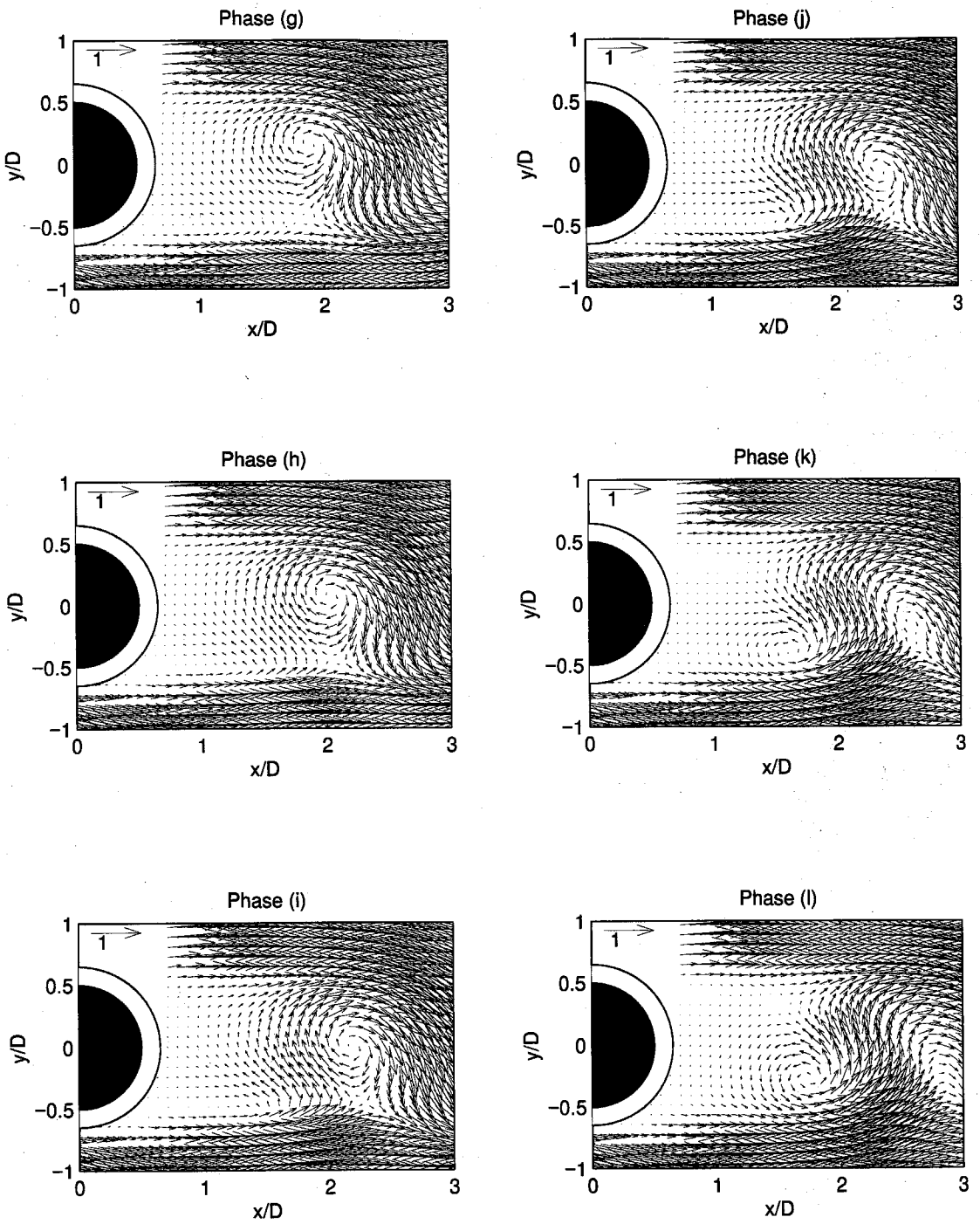


Figure 6.6(b) Sequence of phase averaged velocity field for stationary cylinder (Case I). The value of the reference phase velocity ($u_y$ at location of maximum fluctuations) corresponding to each letter is shown in Fig. 6.60.

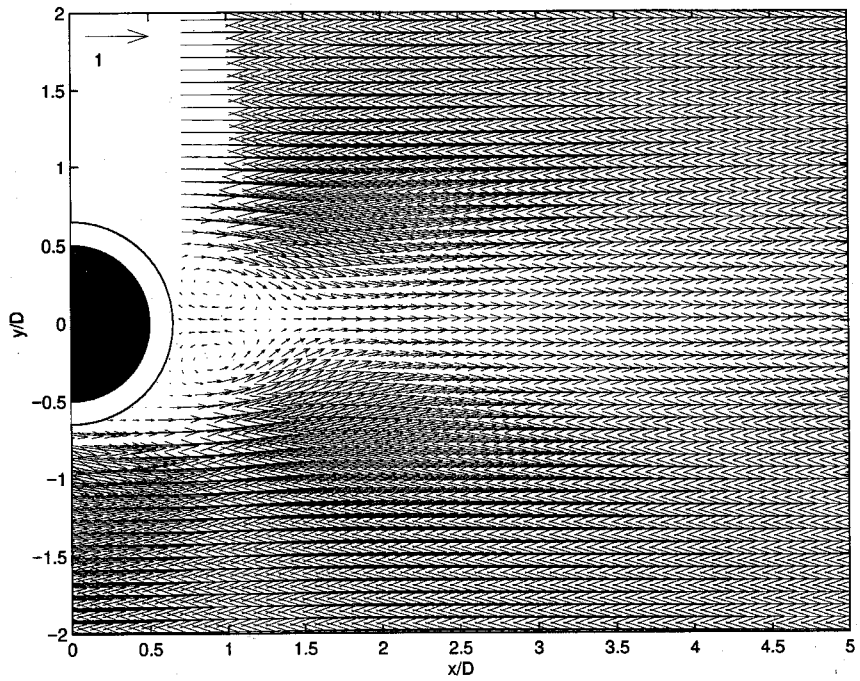


Figure 6.7 Mean velocity field of forced oscillating cylinder at $St_c$=0.21, A/D=0.1 (Case II).

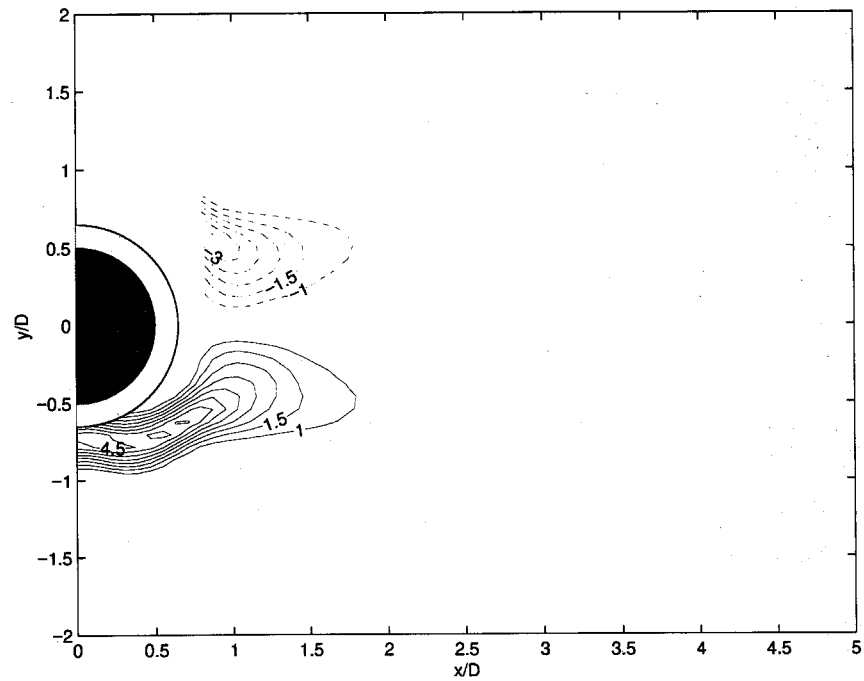


Figure 6.8 Mean vorticity field of forced oscillating cylinder at $St_c$=0.21, A/D=0.1 (Case II).

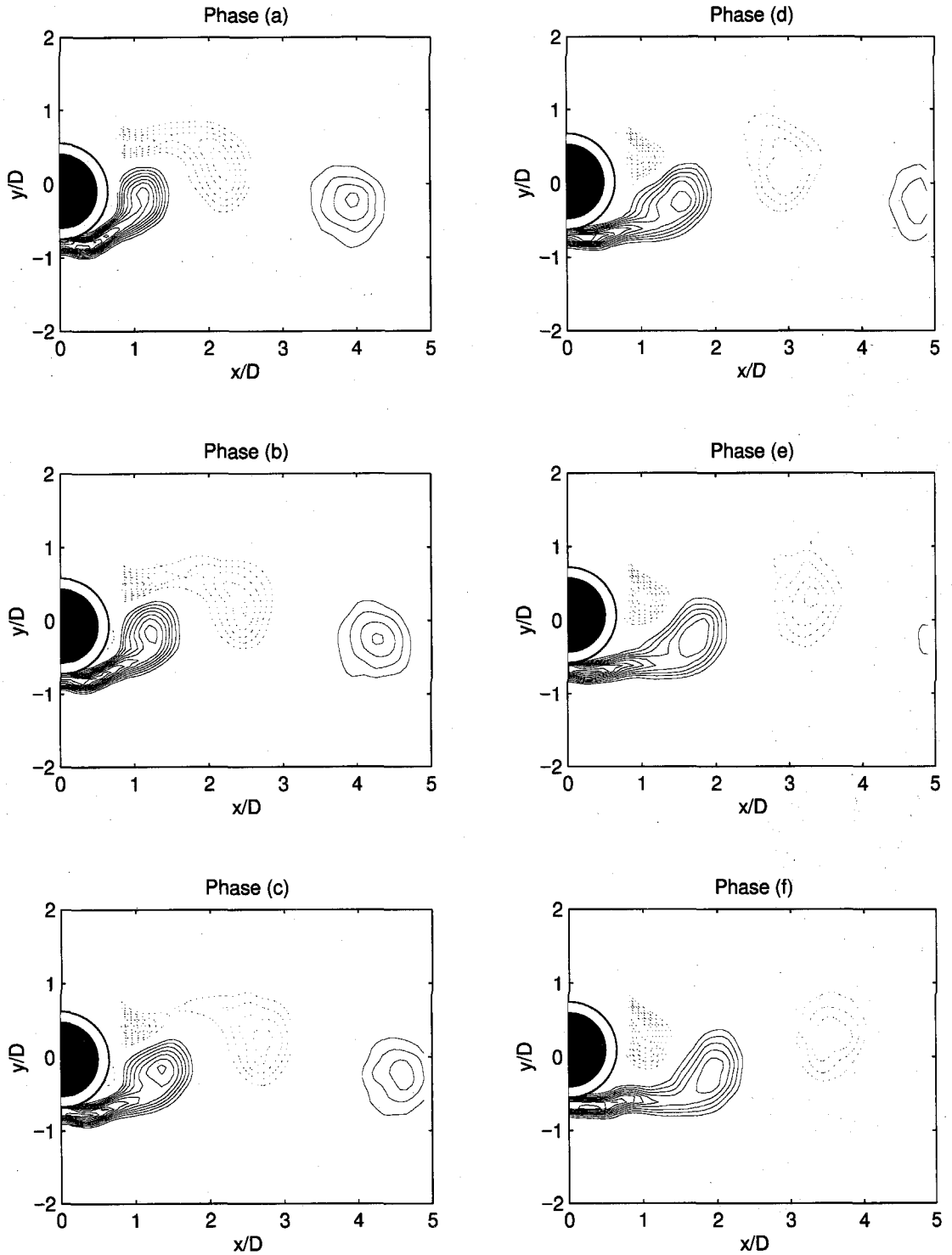


Figure 6.9(a) Sequence of phase averaged vorticity field for forced oscillating cylinder at $St_c$=0.21, A/D=0.1 (Case II). ($|<\omega_z>D/U_\infty|>1.0$, contour increment 0.5) The y-displacement of the cylinder corresponding to each letter is shown in Fig. 6.60.

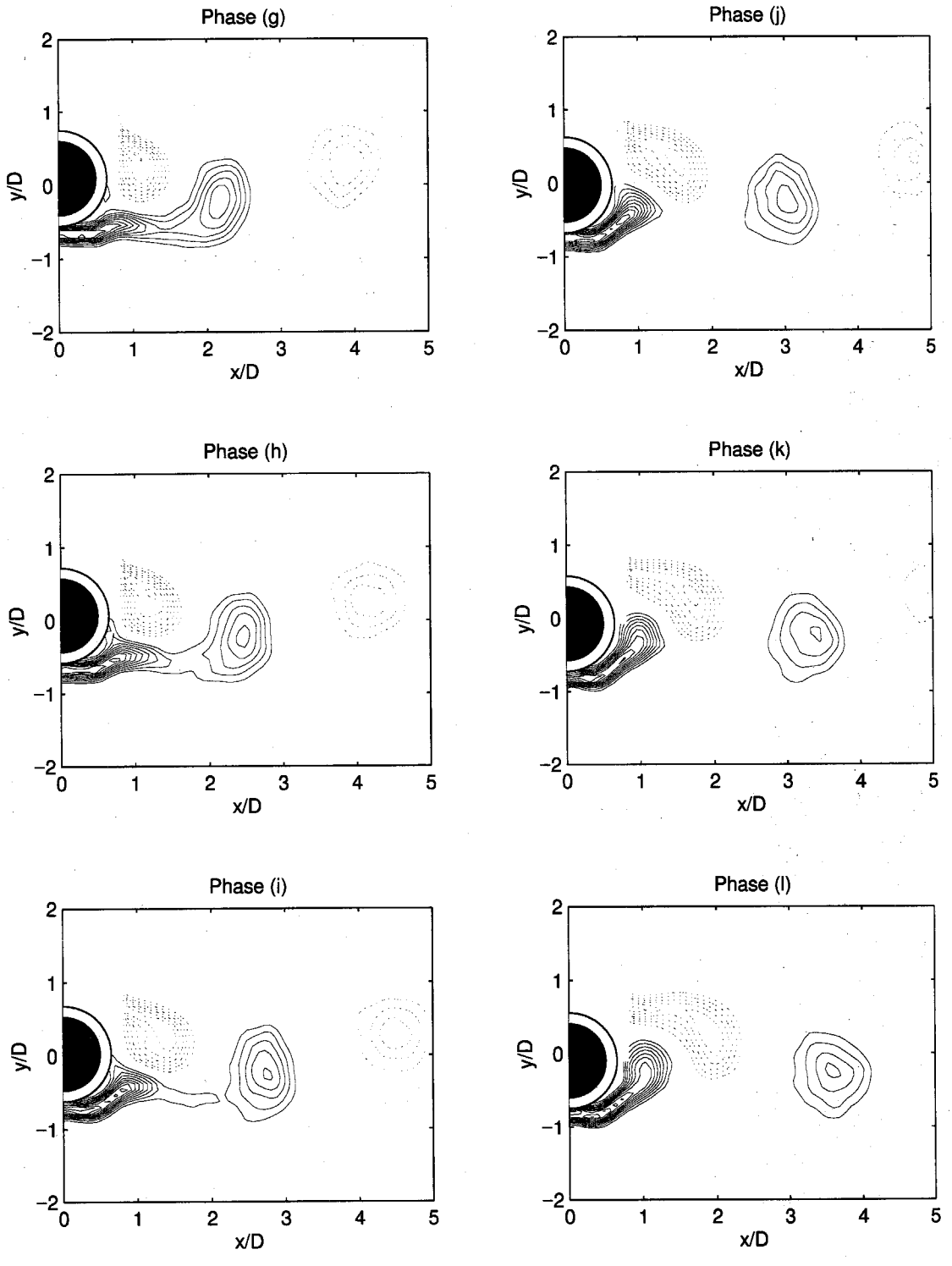


Figure 6.9(b) Sequence of phase averaged vorticity field for forced oscillating cylinder at $St_c$=0.21, A/D=0.1 (Case II). ($|<\omega_z>D/U_\infty|>1.0$, contour increment 0.5) The y-displacement of the cylinder corresponding to each letter is shown in Fig. 6.60.

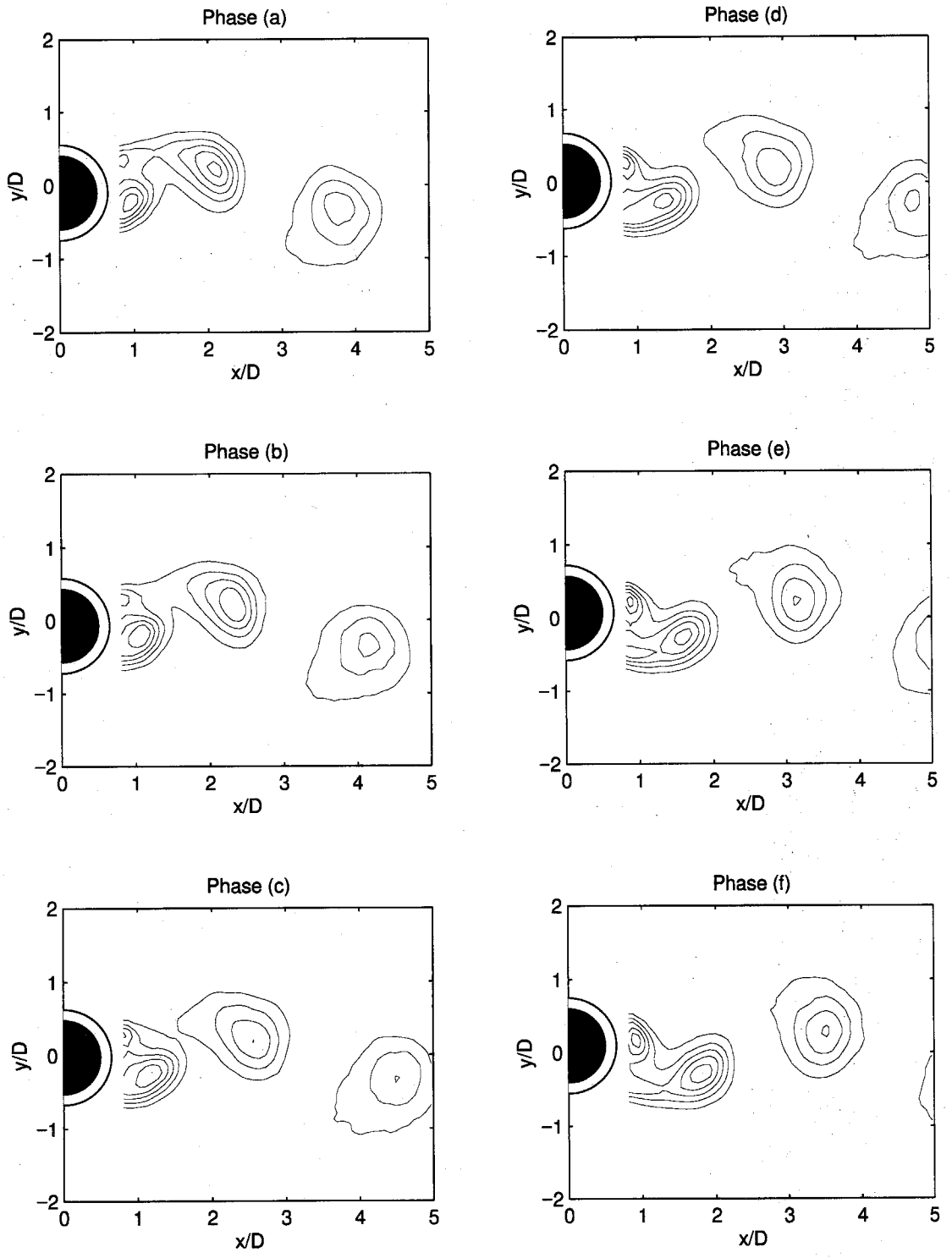


Figure 6.10(a) Sequence of phase averaged temperature field for forced oscillating cylinder at $St_c$=0.21, A/D=0.1 (Case II). ((<T> - $T_\infty$)/($T_c$ - $T_\infty$)>0.01, contour increment 0.01) The y-displacement of the cylinder corresponding to each letter is shown in Fig. 6.60.

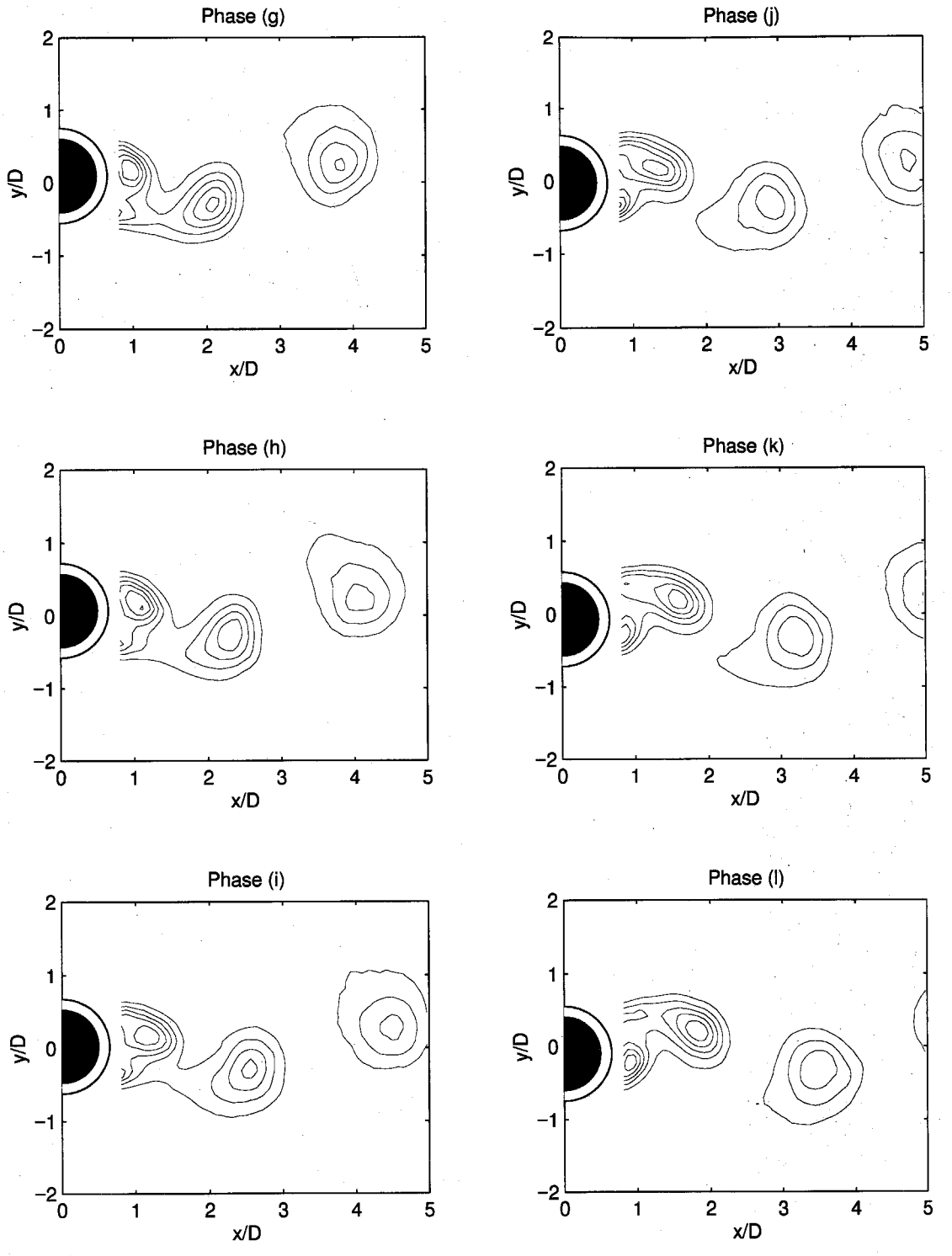


Figure 6.10(b) Sequence of phase averaged temperature field for forced oscillating cylinder at $St_c$=0.21, A/D=0.1 (Case II). ((<T> - $T_\infty$)/($T_c$ - $T_\infty$)>0.01, contour increment 0.01) The y-displacement of the cylinder corresponding to each letter is shown in Fig. 6.60.

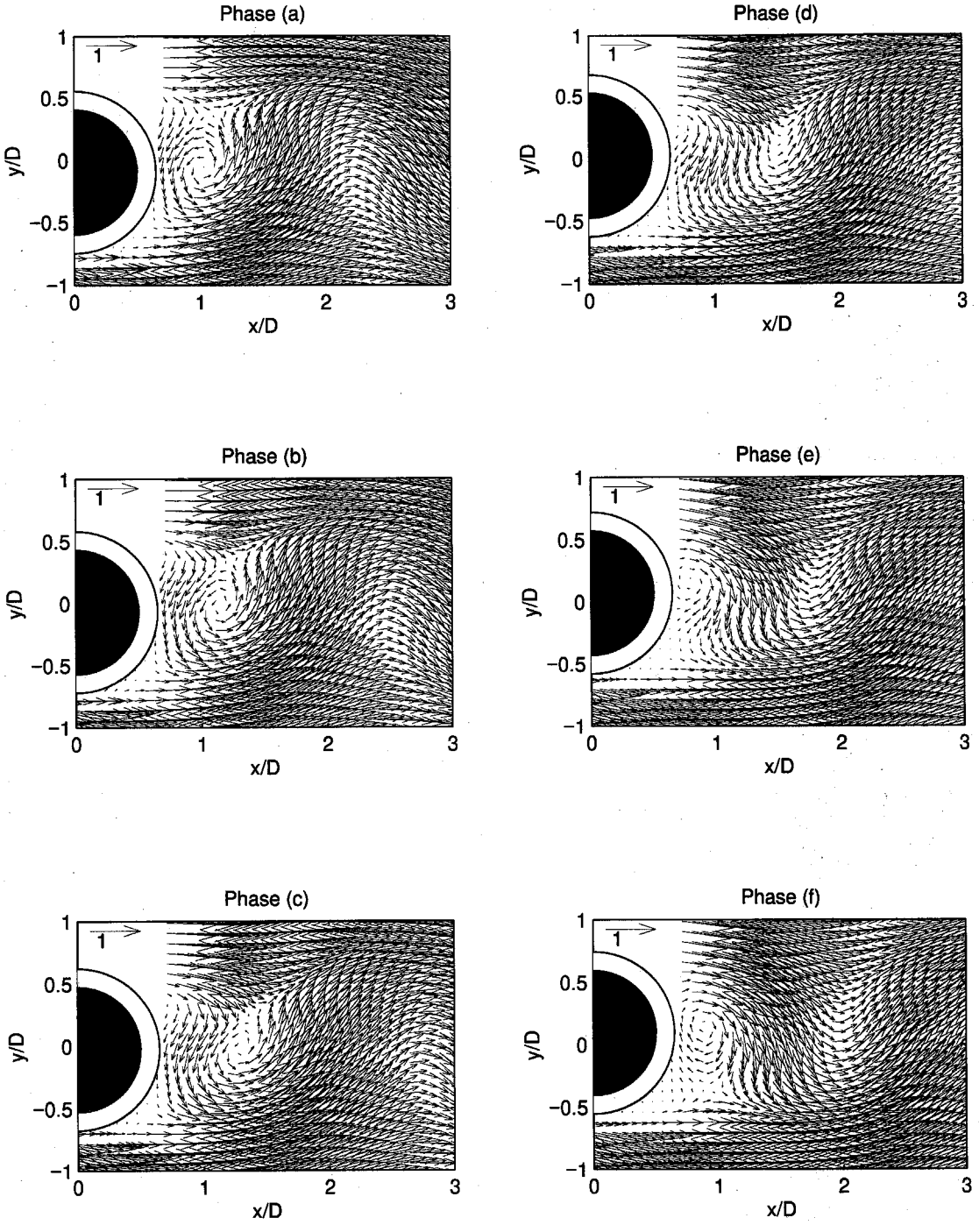


Figure 6.11(a) Sequence of phase averaged velocity field for forced oscillating cylinder at $St_c$=0.21, A/D=0.1 (Case II). The y-displacement of the cylinder corresponding to each letter is shown in Fig. 6.60.

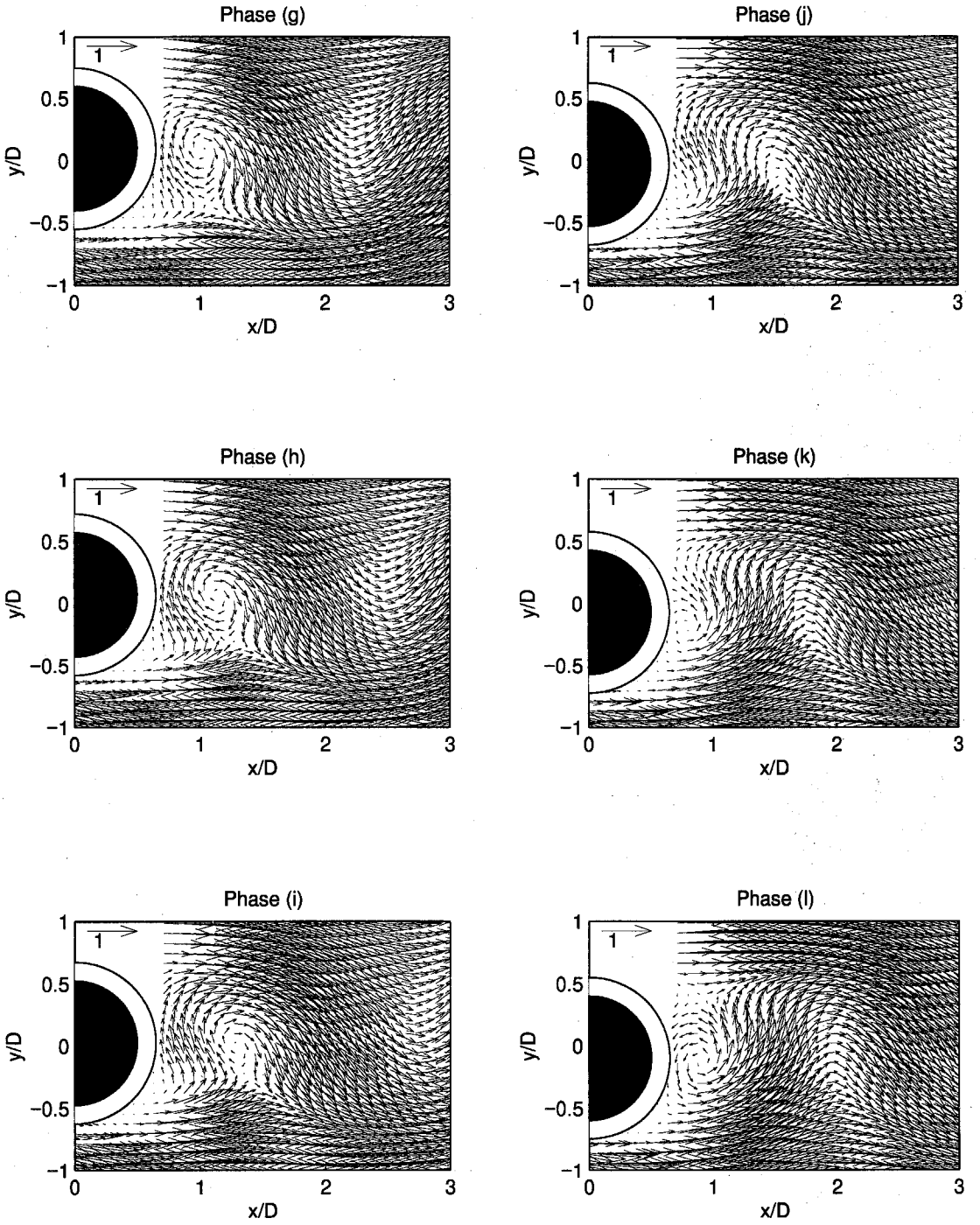


Figure 6.11(b) Sequence of phase averaged velocity field for forced oscillating cylinder at $St_c$=0.21, A/D=0.1 (Case II). The y-displacement of the cylinder corresponding to each letter is shown in Fig. 6.60.

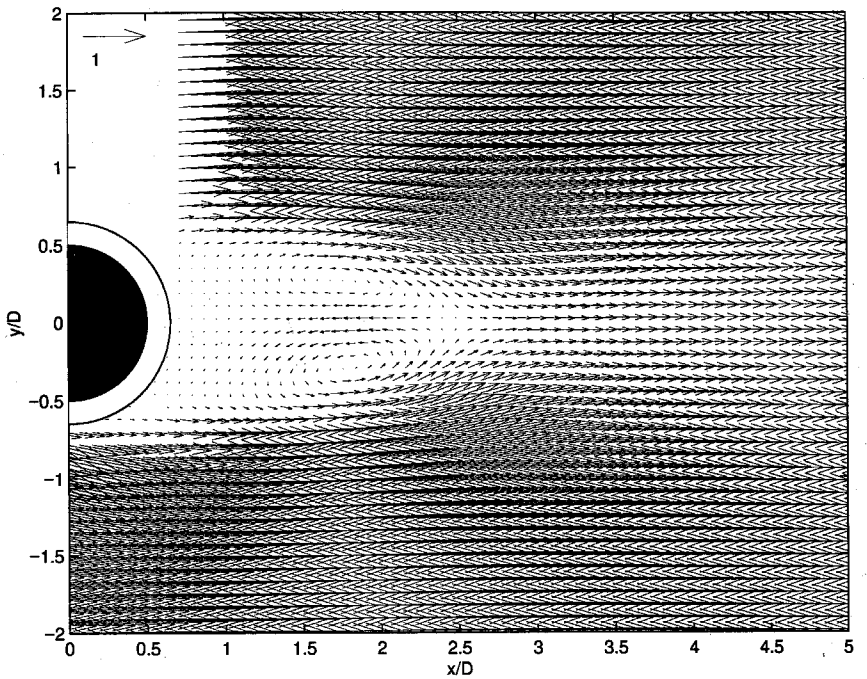


Figure 6.12 Mean velocity field of forced oscillating cylinder at $St_c$=0.34, A/D=0.1 (Case III).

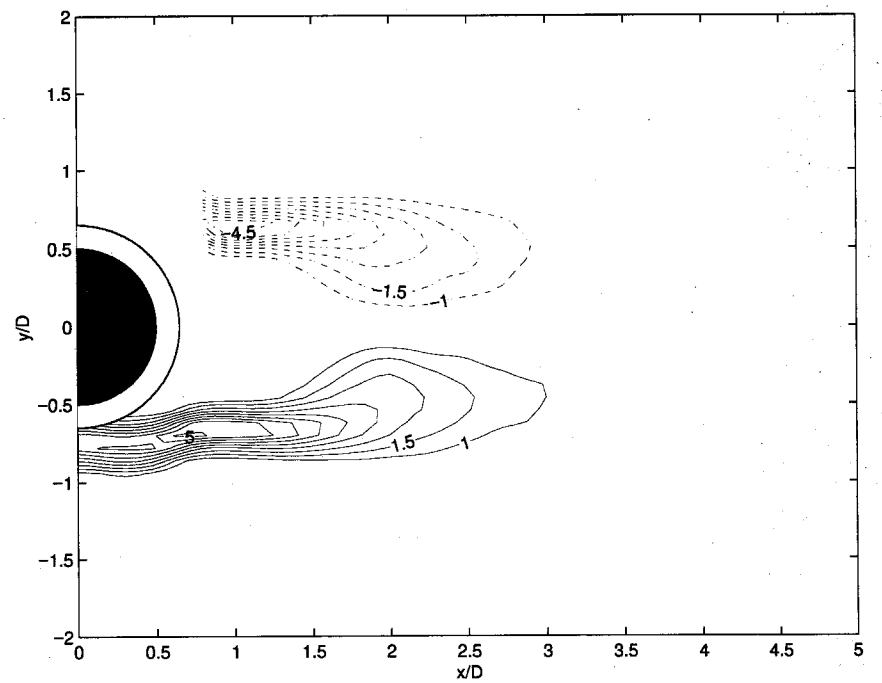


Figure 6.13 Mean vorticity field of forced oscillating cylinder at $St_c$=0.34, A/D=0.1 (Case III).

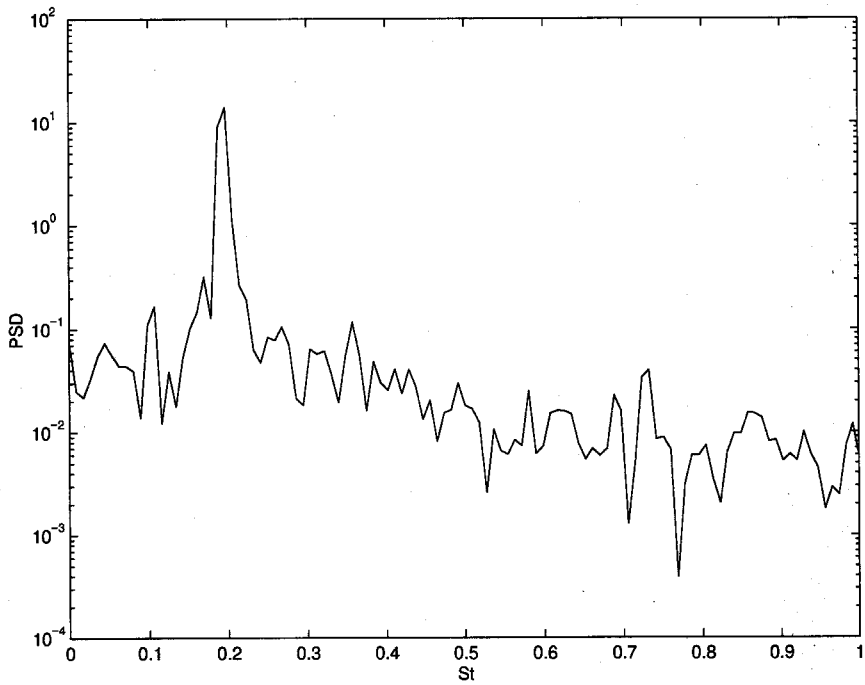


Figure 6.14 PSD of $u_y$ at location of maximum $u_y$ fluctuations on the wake centerline for forced oscillating cylinder at $St_c$=0.34, A/D=0.1 (Case III).

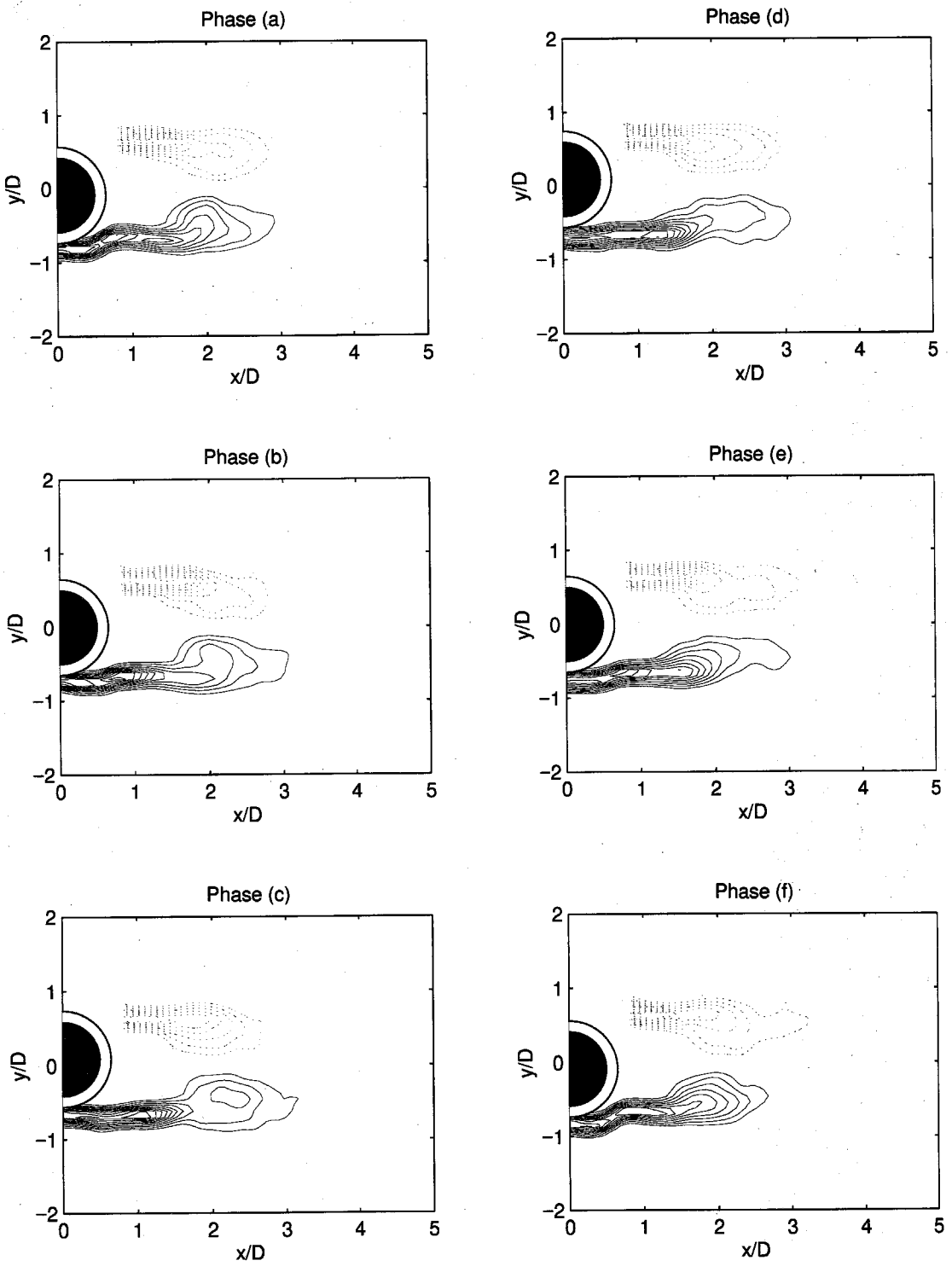


Figure 6.15 Sequence of phase averaged vorticity field for forced oscillating cylinder at $St_c$=0.34, A/D=0.1 (Case III). ($|<\omega_z>D/U_\infty|>1.0$, contour increment 0.5) The phase averaging is done respect to the cylinder oscillation frequency. The y-displacement of the cylinder corresponding to each letter is shown in Fig. 6.60.

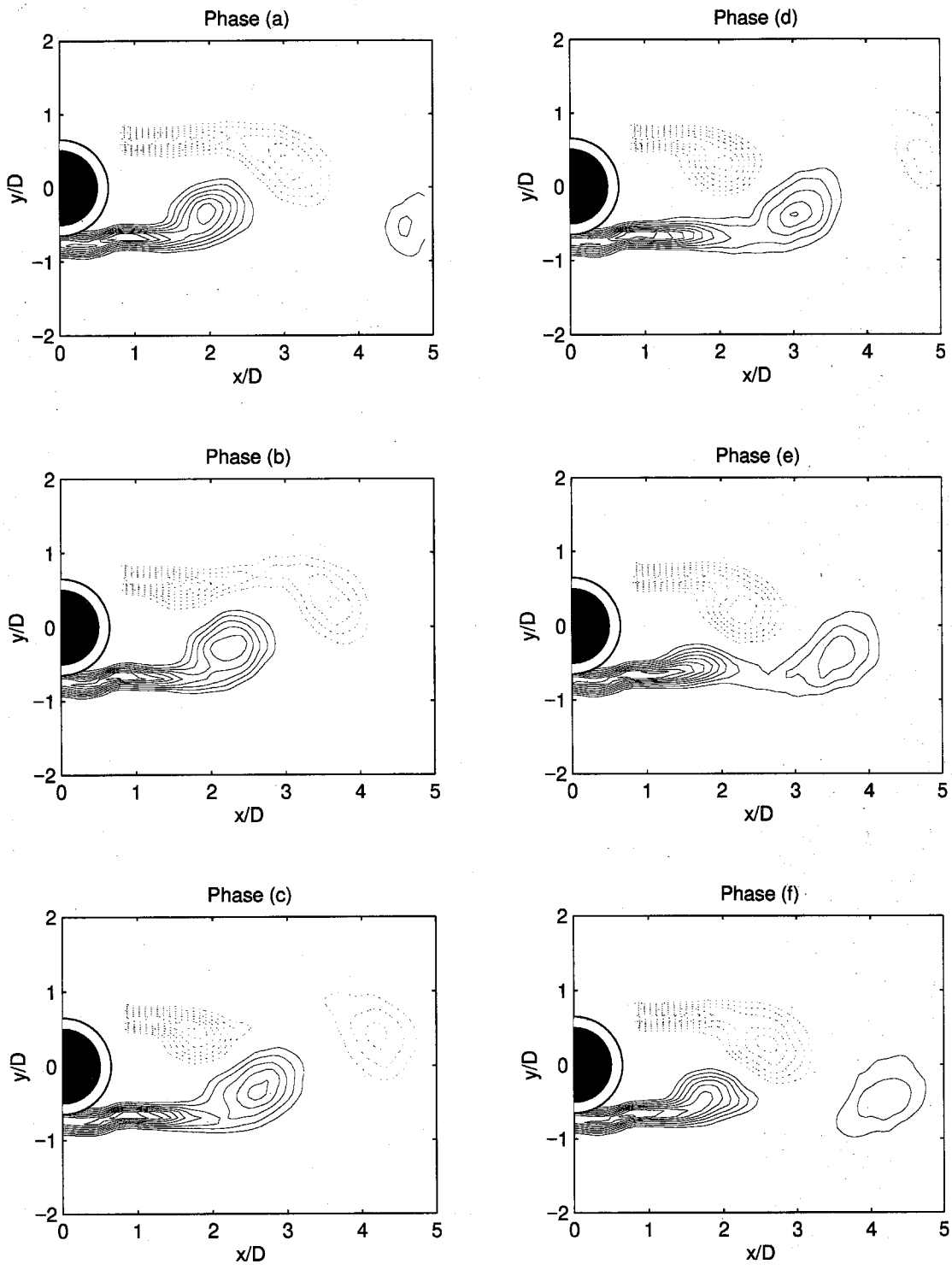


Figure 6.16 Sequence of phase averaged vorticity field for forced oscillating cylinder at $St_c$=0.34, A/D=0.1 (Case III). ($|<\omega_z>D/U_\infty|>1.0$, contour increment 0.5) The phase averaging is done respect to $u_y$ at location of maximum $u_y$ fluctuations on the wake centerline. The value of the reference phase velocity ($u_y$ at location of maximum fluctuations) corresponding to each letter is shown in Fig. 6.60.

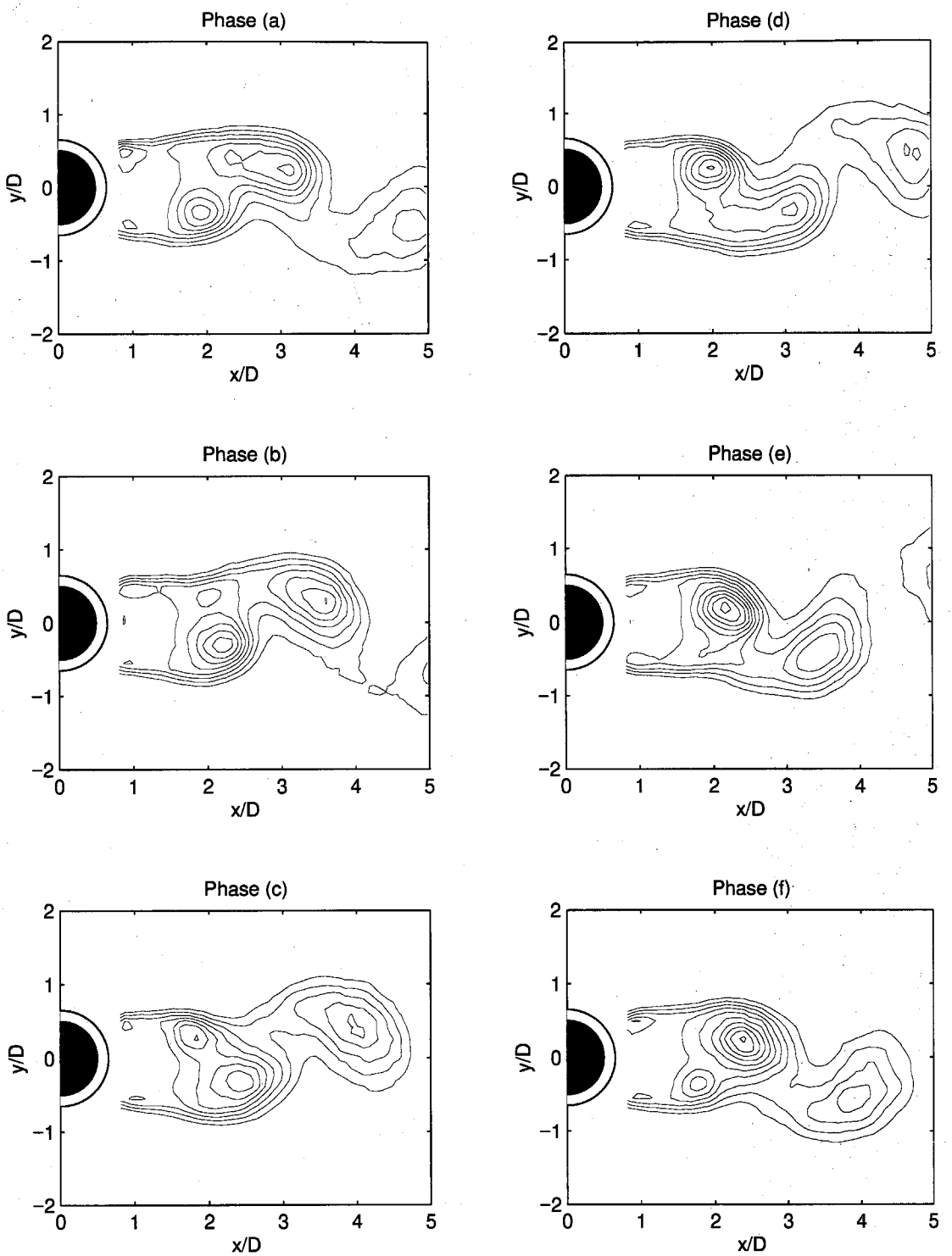


Figure 6.17 Sequence of phase averaged temperature field for forced oscillating cylinder at $St_c$=0.34, A/D=0.1 (Case III). ((<T> - $T_\infty$)/($T_c$ - $T_\infty$)>0.01, contour increment 0.005) The phase averaging is done respect to $u_y$ at location of maximum $u_y$ fluctuations on the wake centerline. The value of the reference phase velocity ($u_y$ at location of maximum fluctuations) corresponding to each letter is shown in Fig. 6.60.

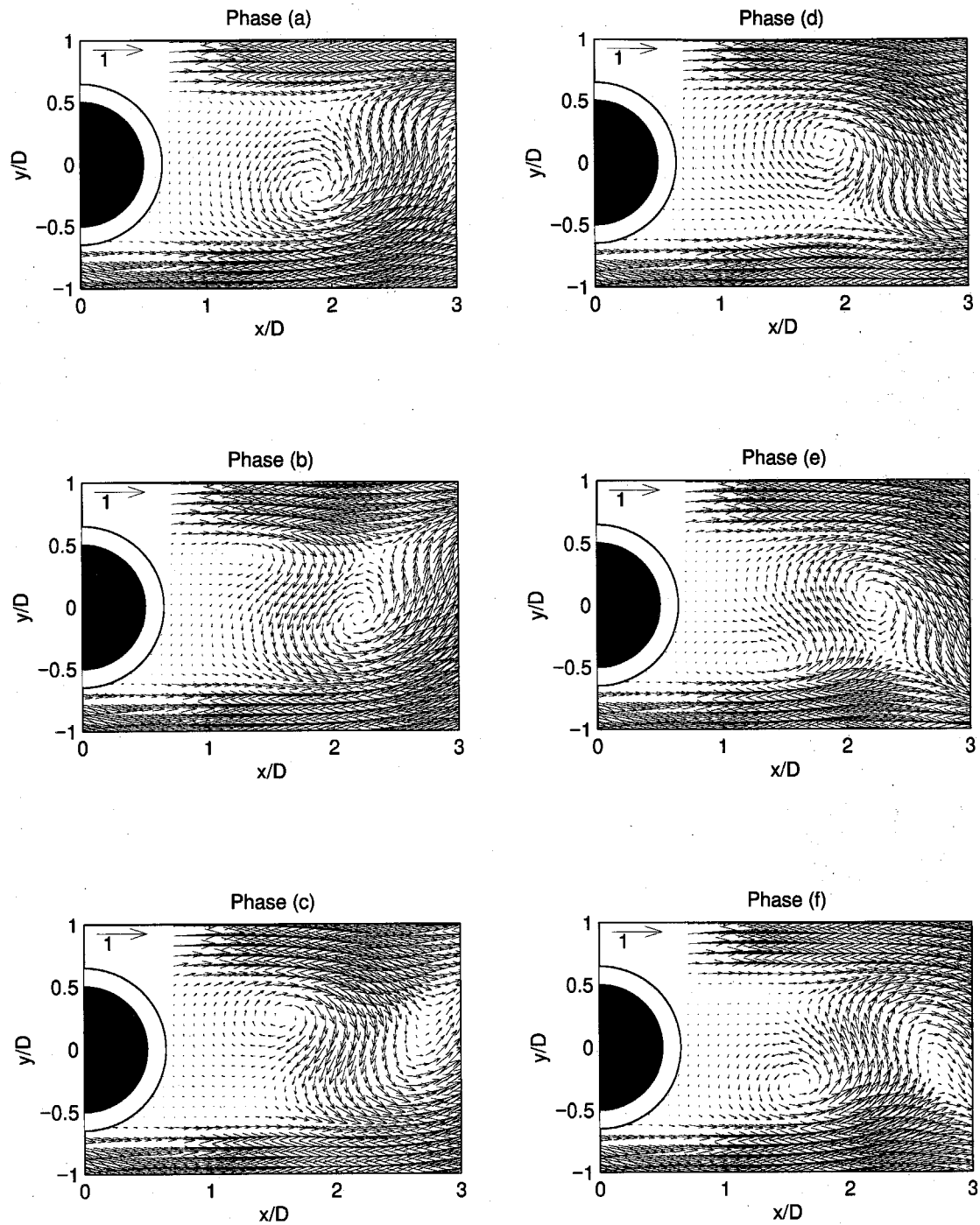


Figure 6.18 Sequence of phase averaged velocity field for forced oscillating cylinder at $St_c$=0.34, A/D=0.1 (Case III). The phase averaging is done respect to $u_y$ at location of maximum $u_y$ fluctuations on the wake centerline. The value of the reference phase velocity ($u_y$ at location of maximum fluctuations) corresponding to each letter is shown in Fig. 6.60.

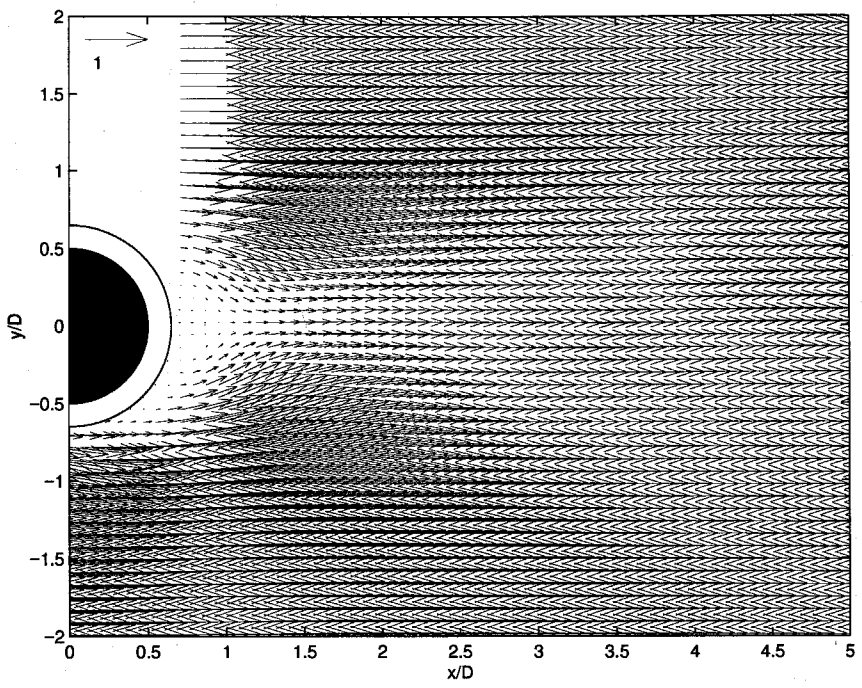


Figure 6.19 Mean velocity field of forced oscillating cylinder at $St_c$=0.58, A/D=0.1 (Case IV).

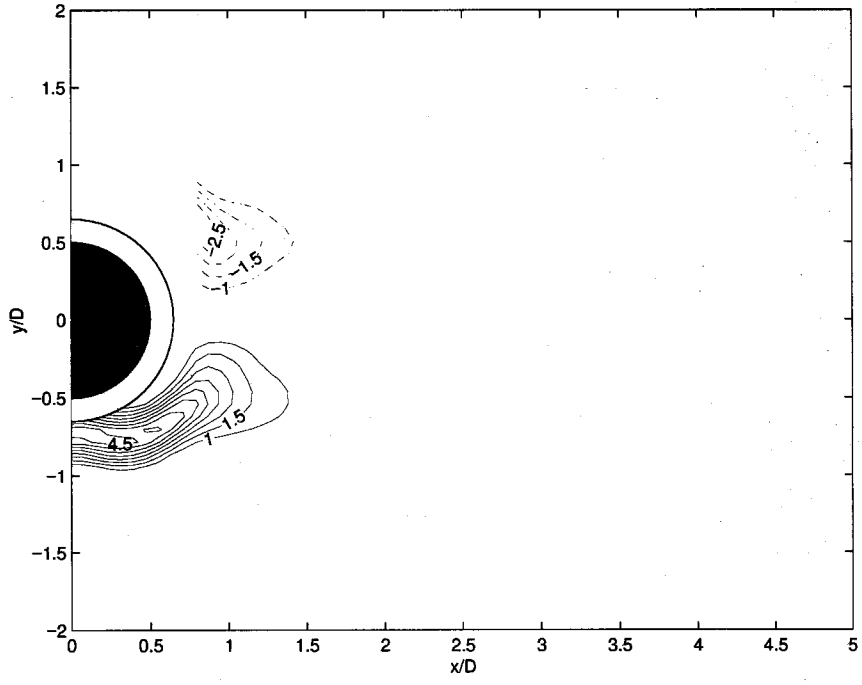


Figure 6.20 Mean vorticity field of forced oscillating cylinder at $St_c$=0.58, A/D=0.1 (Case IV).

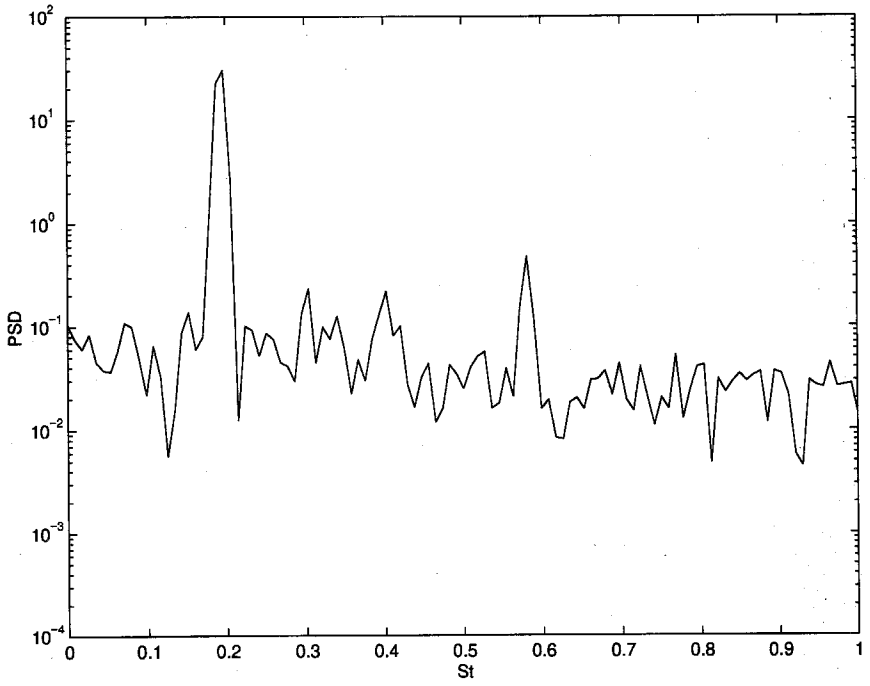


Figure 6.21 PSD of $u_y$ at location of maximum $u_y$ fluctuations on the wake centerline for forced oscillating cylinder at $St_c$=0.58, A/D=0.1 (Case IV).

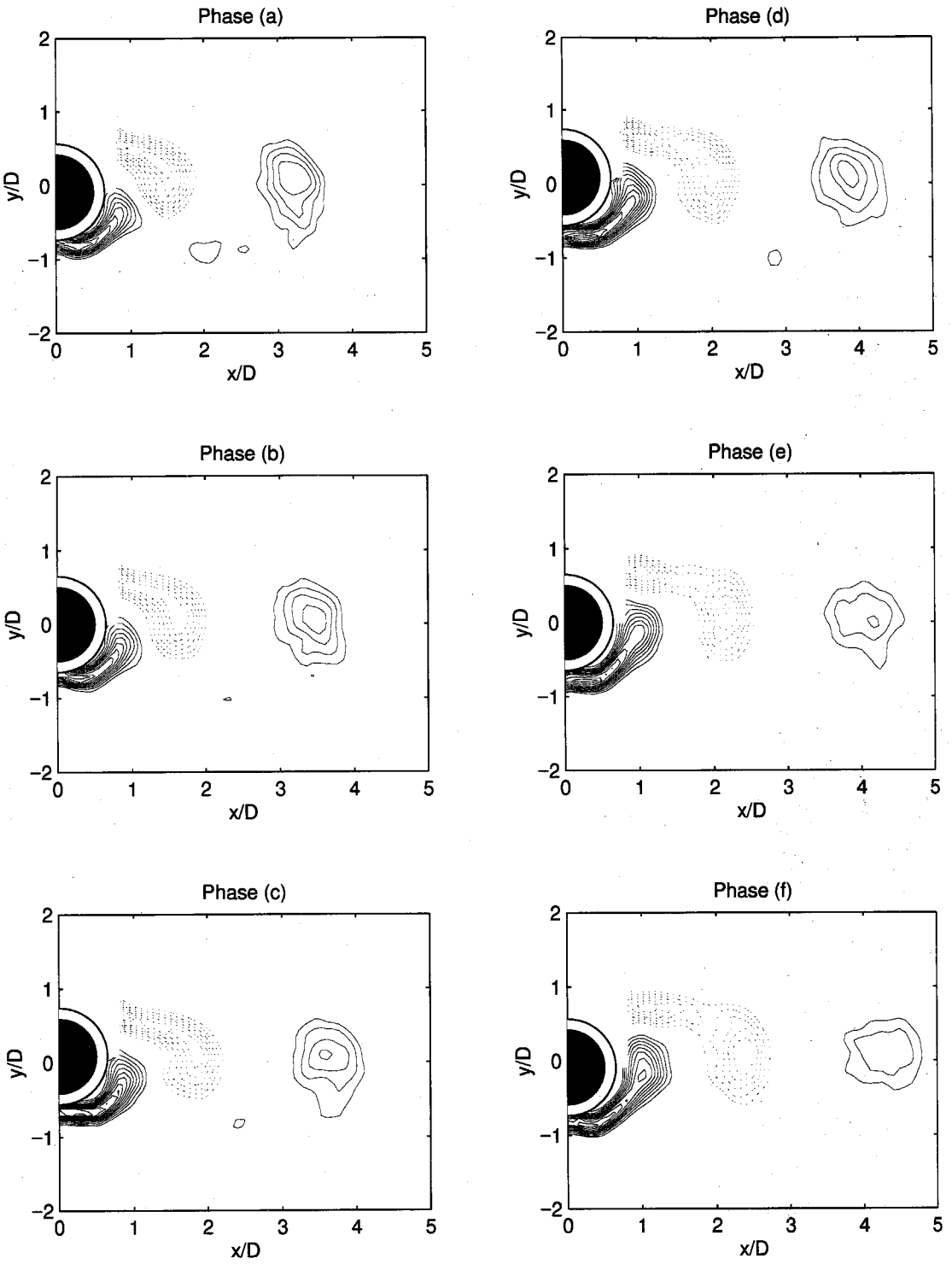


Figure 6.22(a) Sequence of phase averaged vorticity field for forced oscillating cylinder at $St_c$=0.58, A/D=0.1 (Case IV). ($|<\omega_z>D/U_\infty|>1.0$, contour increment 0.5) The y-displacement of the cylinder corresponding to each letter is shown in Fig. 6.60.

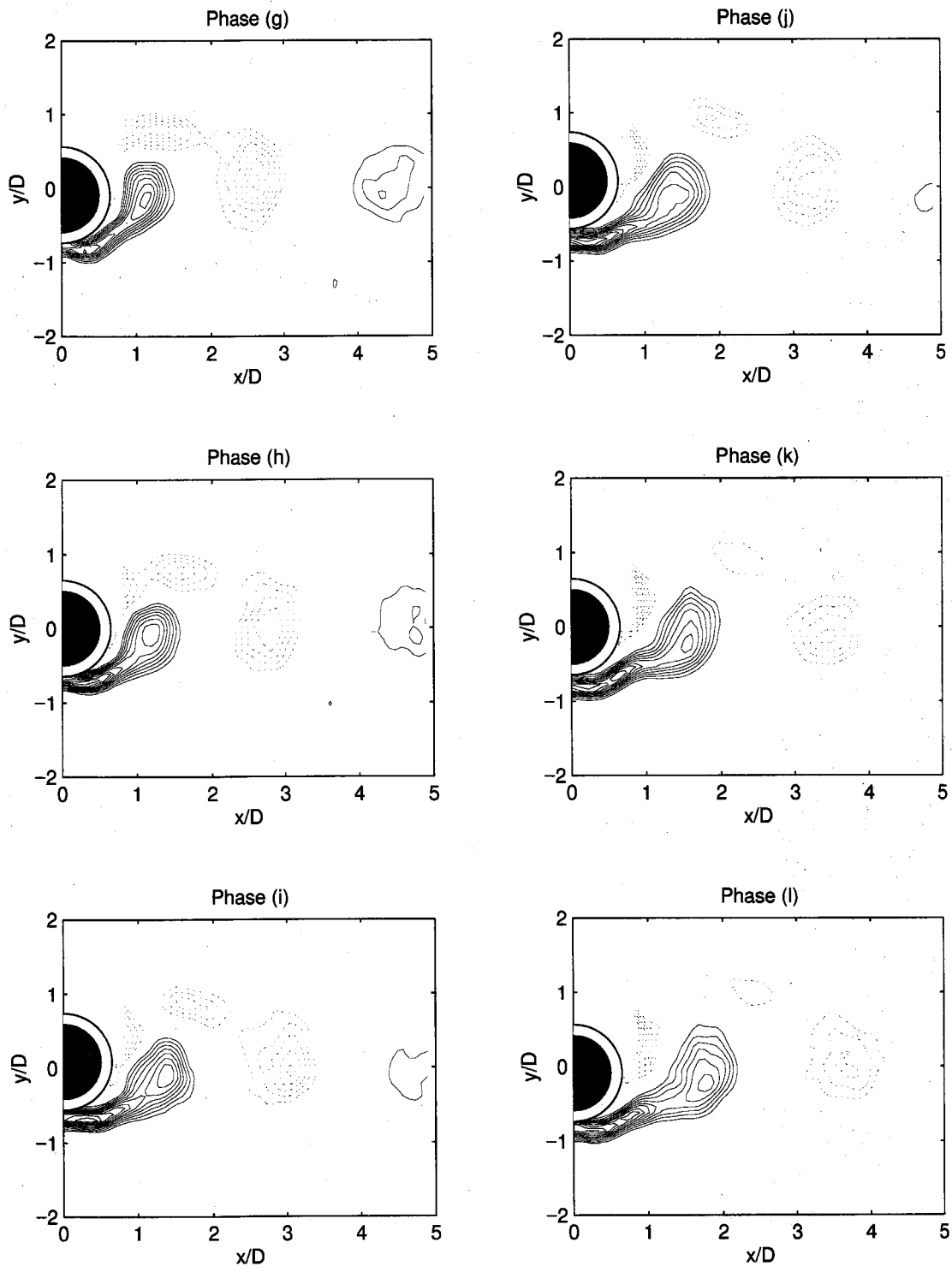


Figure 6.22(b) Sequence of phase averaged vorticity field for forced oscillating cylinder at $St_e$=0.58, A/D=0.1 (Case IV). ($|<\omega_z>D/U_\infty|>1.0$, contour increment 0.5) The y-displacement of the cylinder corresponding to each letter is shown in Fig. 6.60.

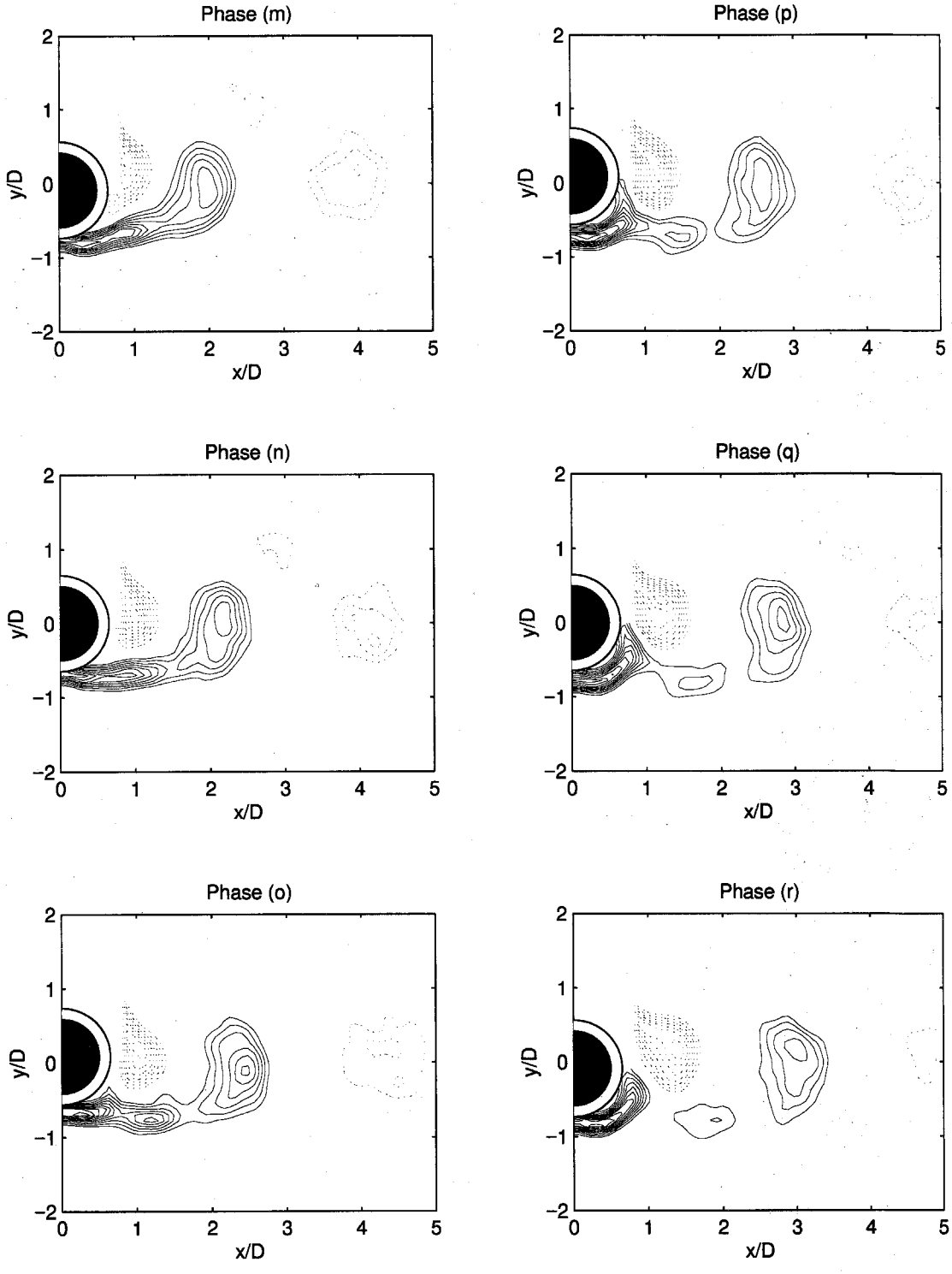


Figure 6.22(c) Sequence of phase averaged vorticity field for forced oscillating cylinder at $St_e$=0.58, A/D=0.1 (Case IV). ($|<\omega_z>D/U_\infty|>1.0$, contour increment 0.5) The y-displacement of the cylinder corresponding to each letter is shown in Fig. 6.60.

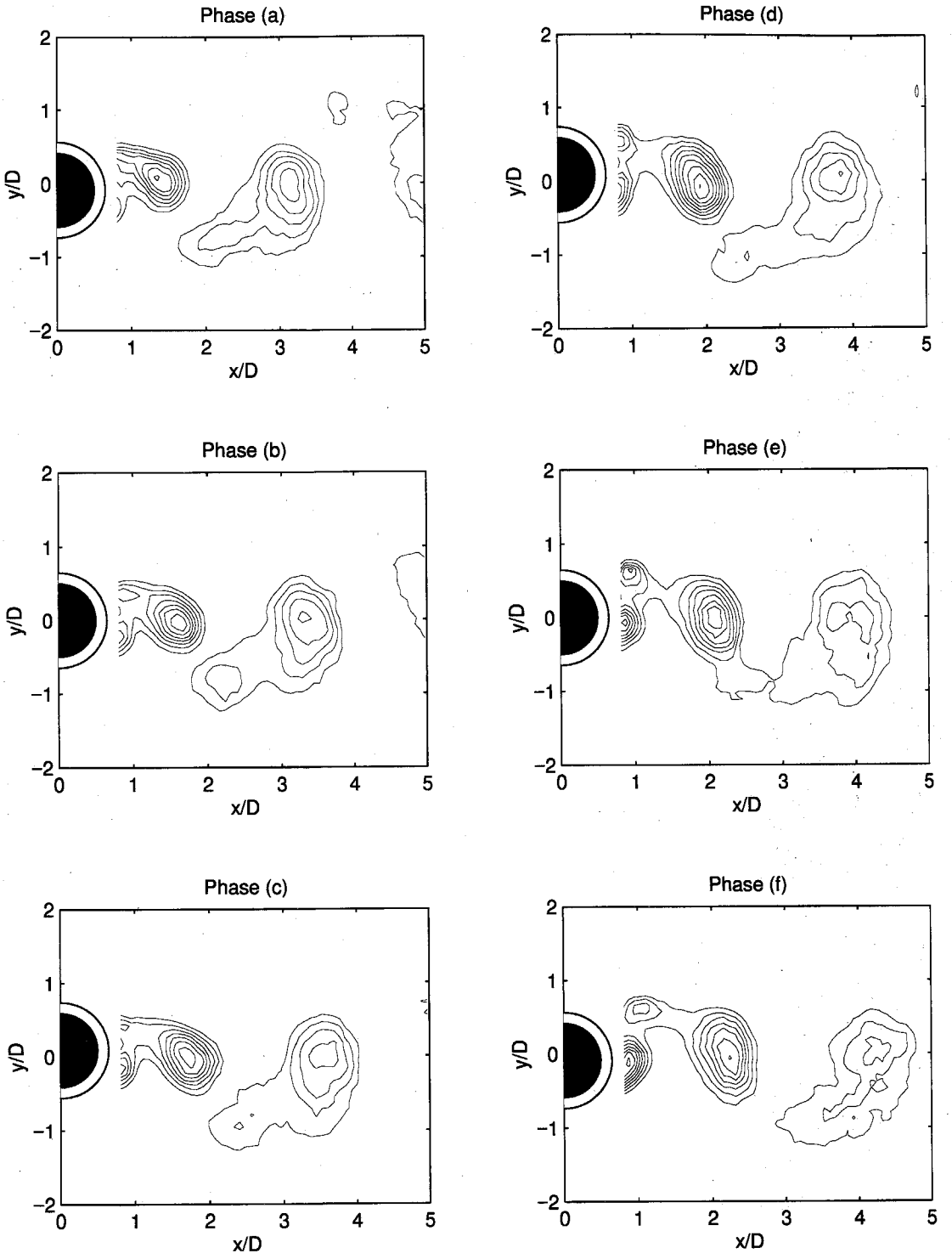


Figure 6.23(a) Sequence of phase averaged temperature field for forced oscillating cylinder at $St_c$=0.58, A/D=0.1 (Case IV). ($(<T> - T_\infty)/(T_c - T_\infty)>0.01$, contour increment 0.005) The y-displacement of the cylinder corresponding to each letter is shown in Fig. 6.60.

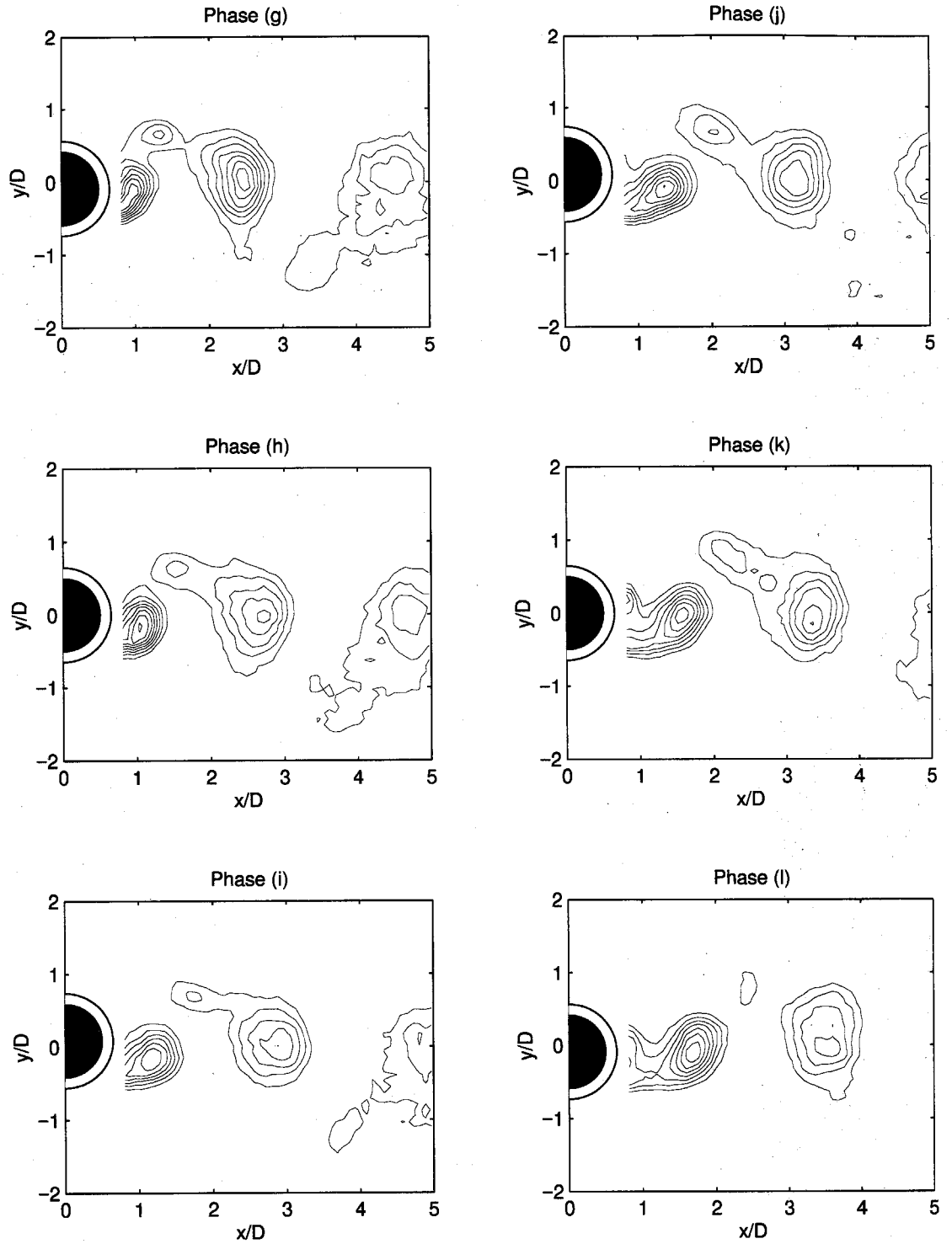


Figure 6.23(b) Sequence of phase averaged temperature field for forced oscillating cylinder at $St_c$=0.58, A/D=0.1 (Case IV). ($(<T> - T_\infty)/(T_c - T_\infty)>0.01$, contour increment 0.005) The y-displacement of the cylinder corresponding to each letter is shown in Fig. 6.60.

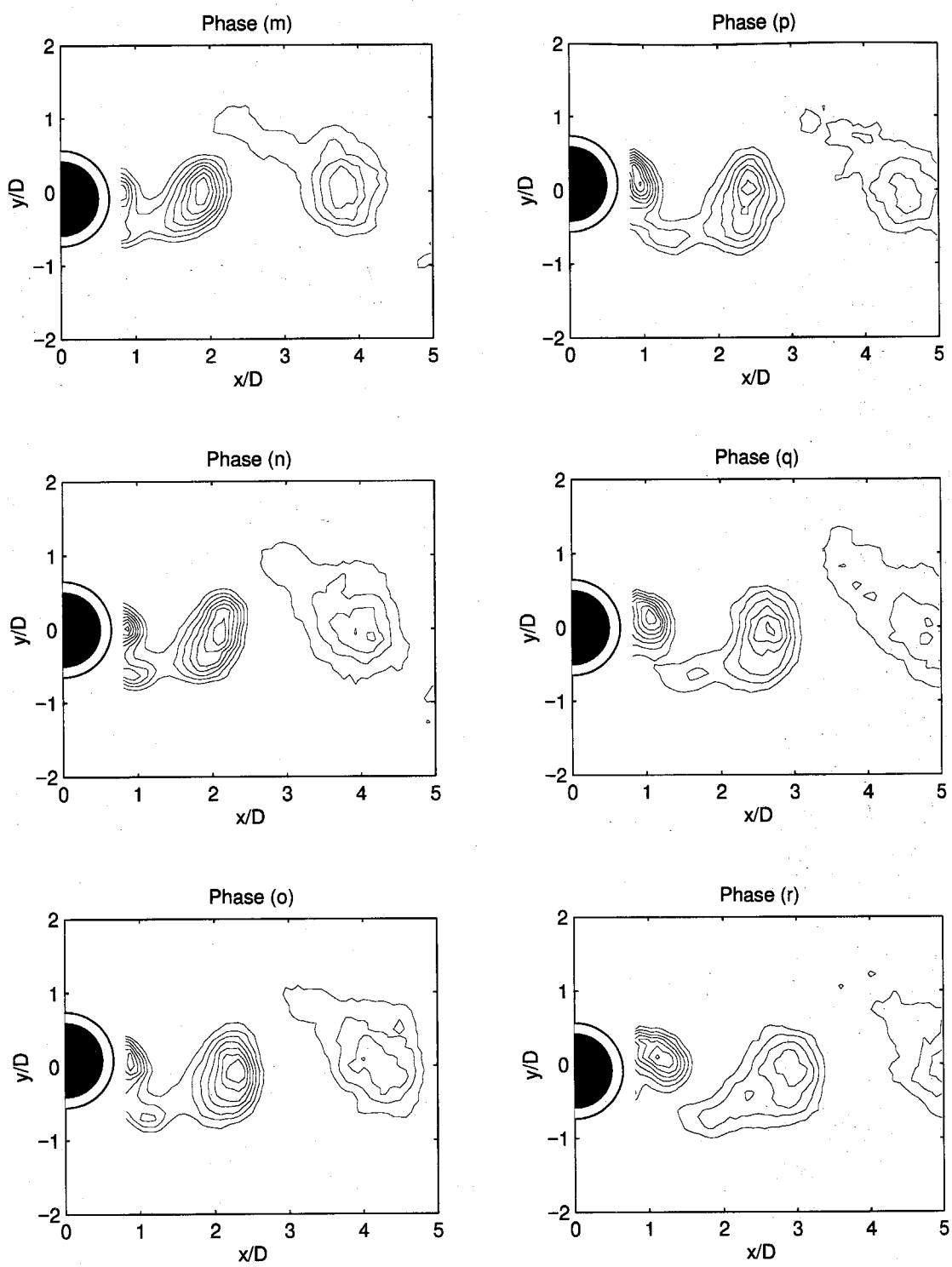


Figure 6.23(c) Sequence of phase averaged temperature field for forced oscillating cylinder at $St_c$=0.58, A/D=0.1 (Case IV). ($(<T> - T_\infty)/(T_c - T_\infty)>0.01$, contour increment 0.005) The y-displacement of the cylinder corresponding to each letter is shown in Fig. 6.60.

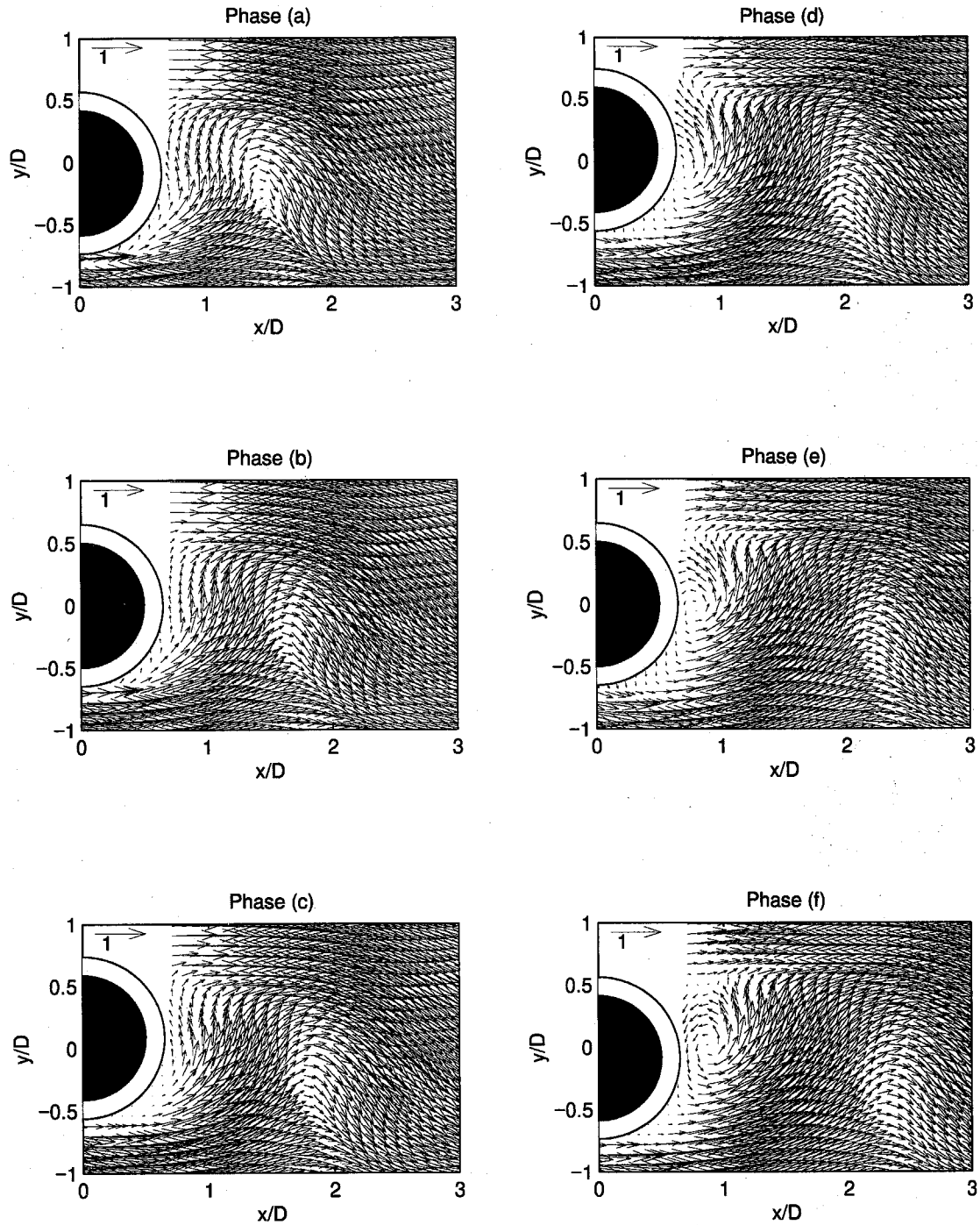


Figure 6.24(a) Sequence of phase averaged velocity field for forced oscillating cylinder at $St_c$=0.58, A/D=0.1 (Case IV). The y-displacement of the cylinder corresponding to each letter is shown in Fig. 6.60.

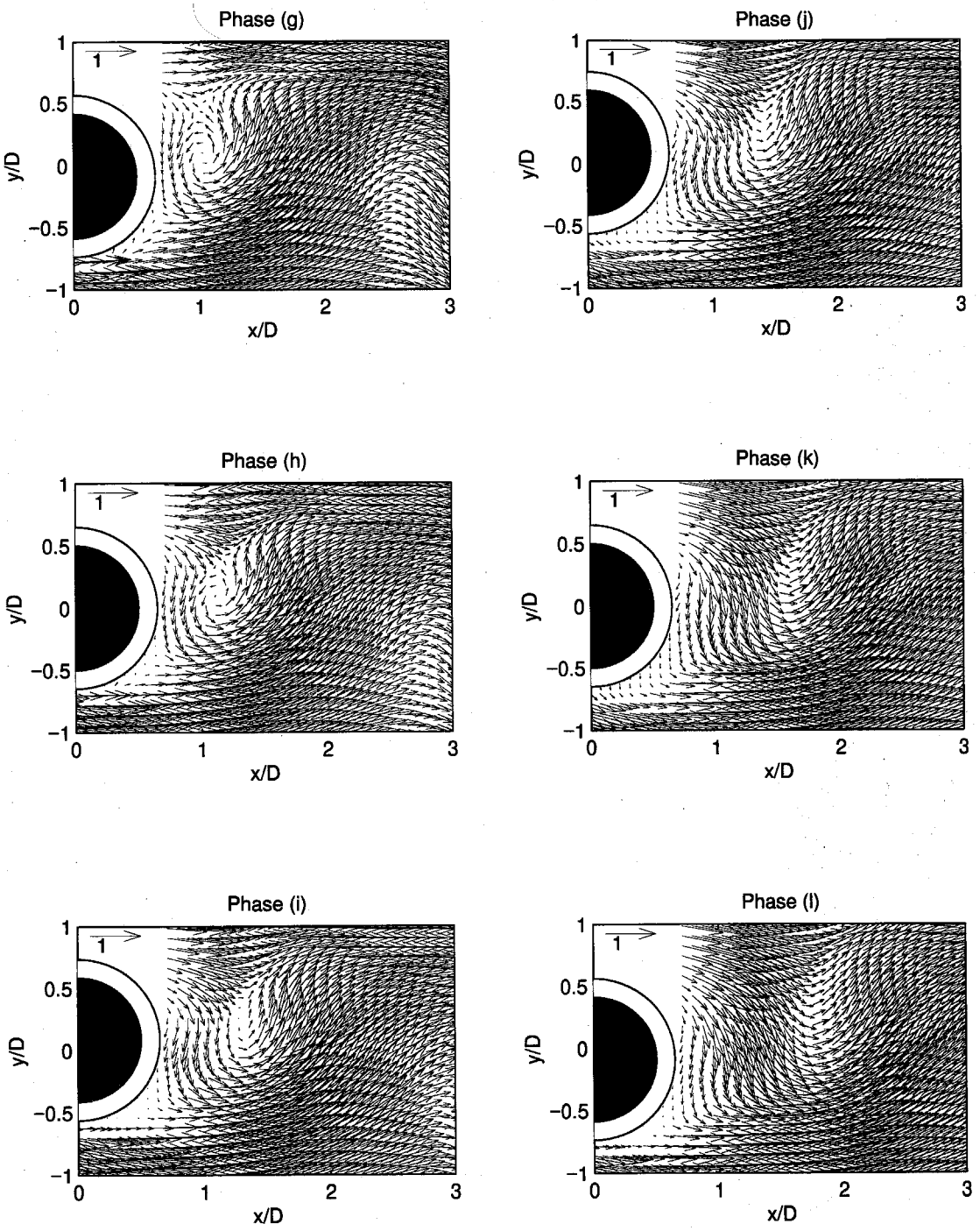


Figure 6.24(b) Sequence of phase averaged velocity field for forced oscillating cylinder at $St_c$=0.58, A/D=0.1 (Case IV). The y-displacement of the cylinder corresponding to each letter is shown in Fig. 6.60.

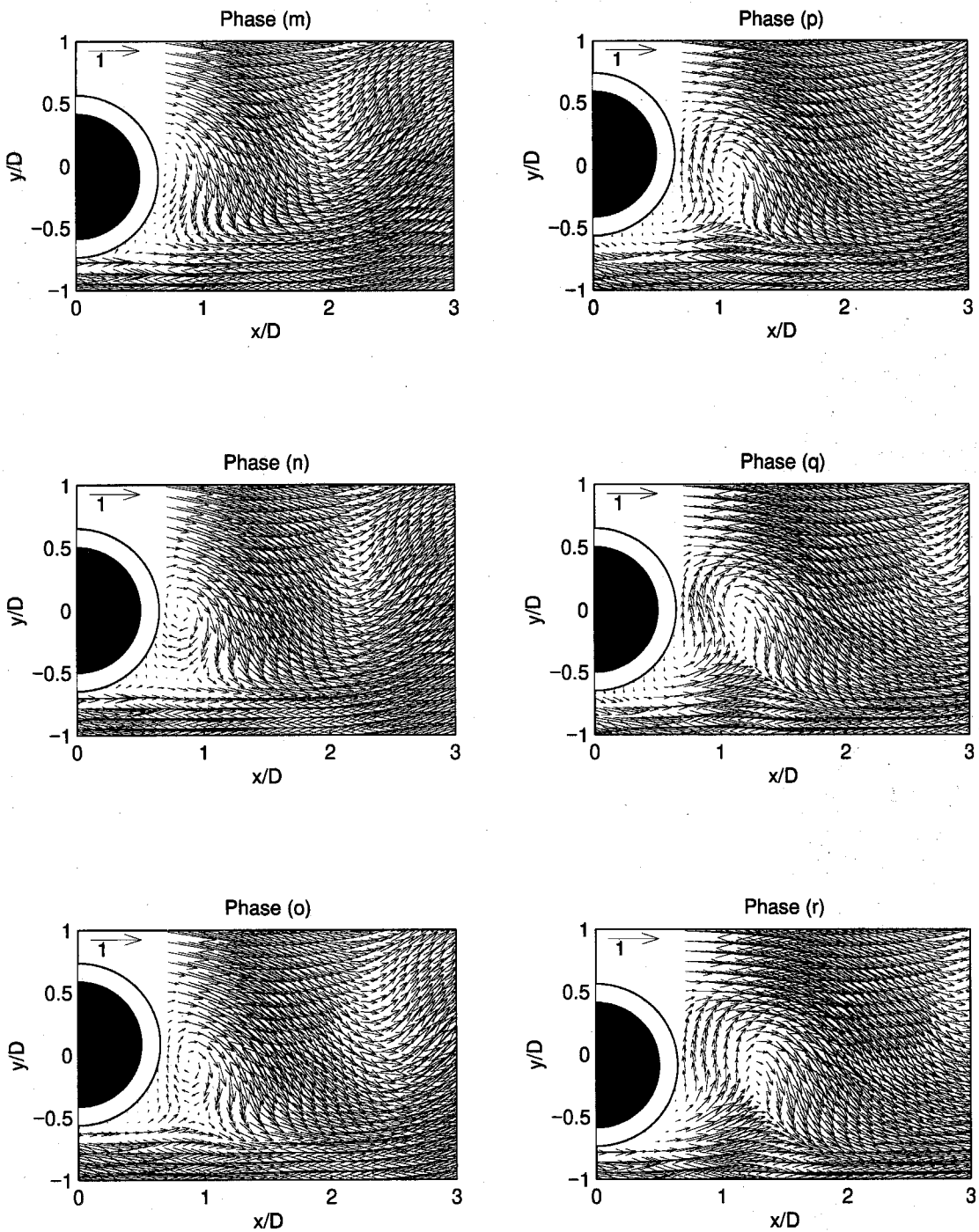


Figure 6.24(c) Sequence of phase averaged velocity field for forced oscillating cylinder at $St_c$=0.58, A/D=0.1 (Case IV). The y-displacement of the cylinder corresponding to each letter is shown in Fig. 6.60.

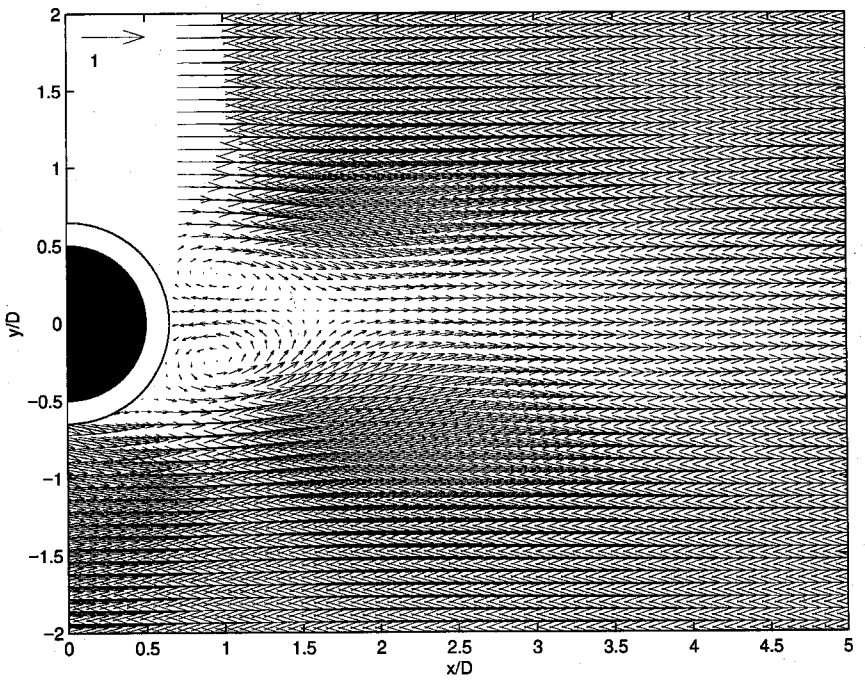


Figure 6.25 Mean vorticity field of forced oscillating cylinder at $St_c$=0.21, A/D=0.2 (Case V).

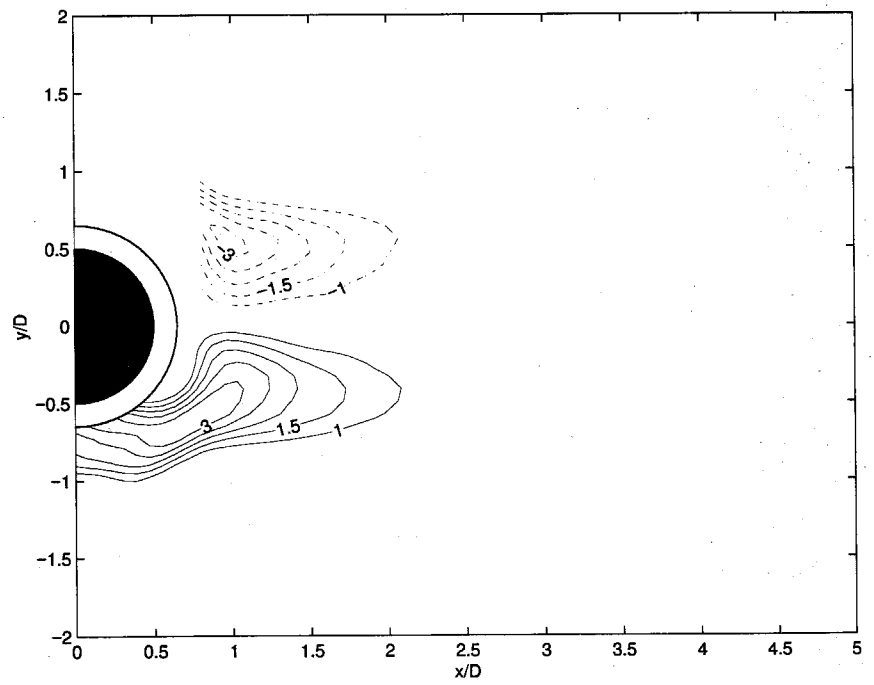


Figure 6.26 Mean vorticity field of forced oscillating cylinder at $St_c$=0.21, A/D=0.2 (Case V).

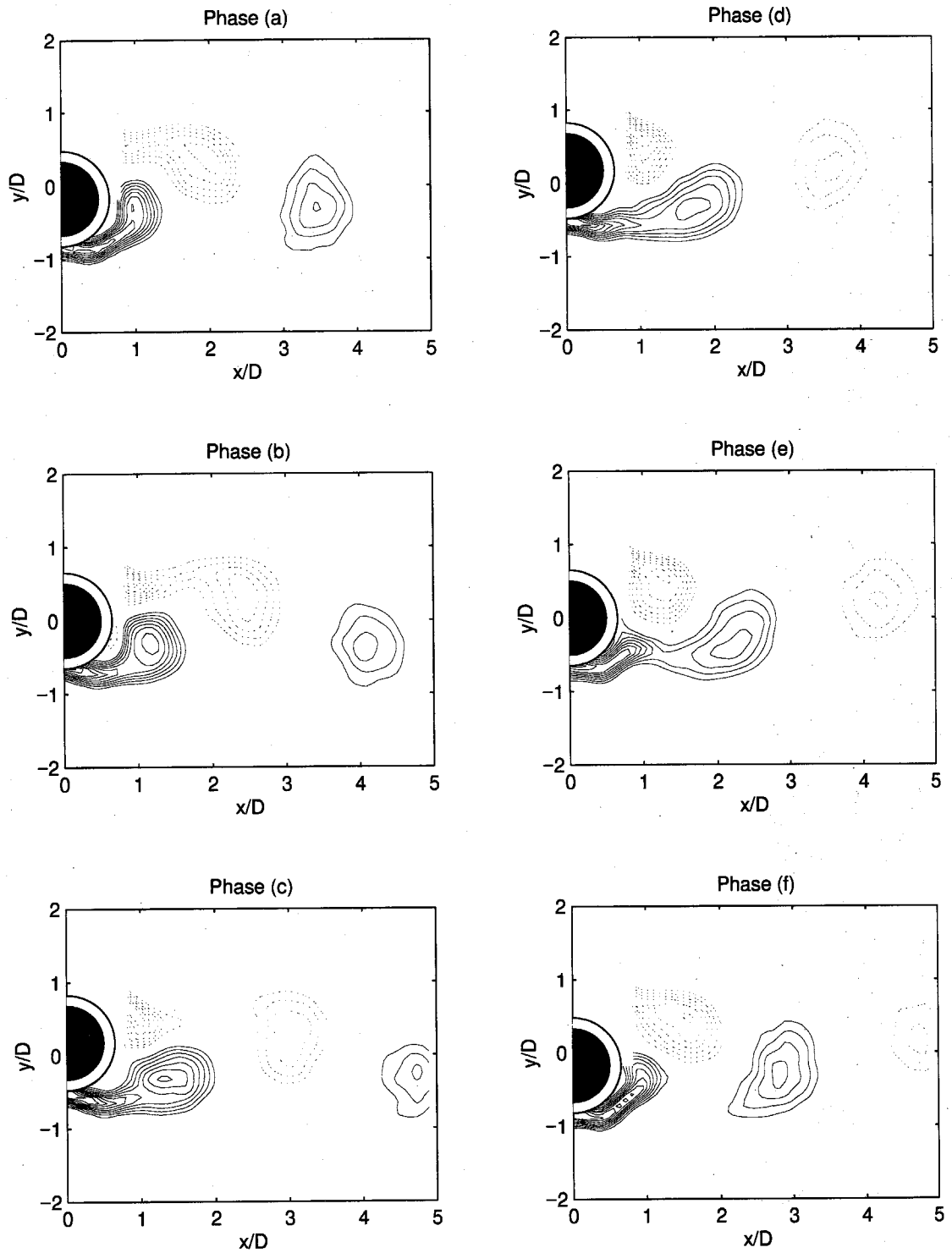


Figure 6.27 Sequence of phase averaged vorticity field for forced oscillating cylinder at $St_c$=0.21, A/D=0.2 (Case V). ($|<\omega_z>D/U_\infty|>1.0$, contour increment 0.5) The y-displacement of the cylinder corresponding to each letter is shown in Fig. 6.60.

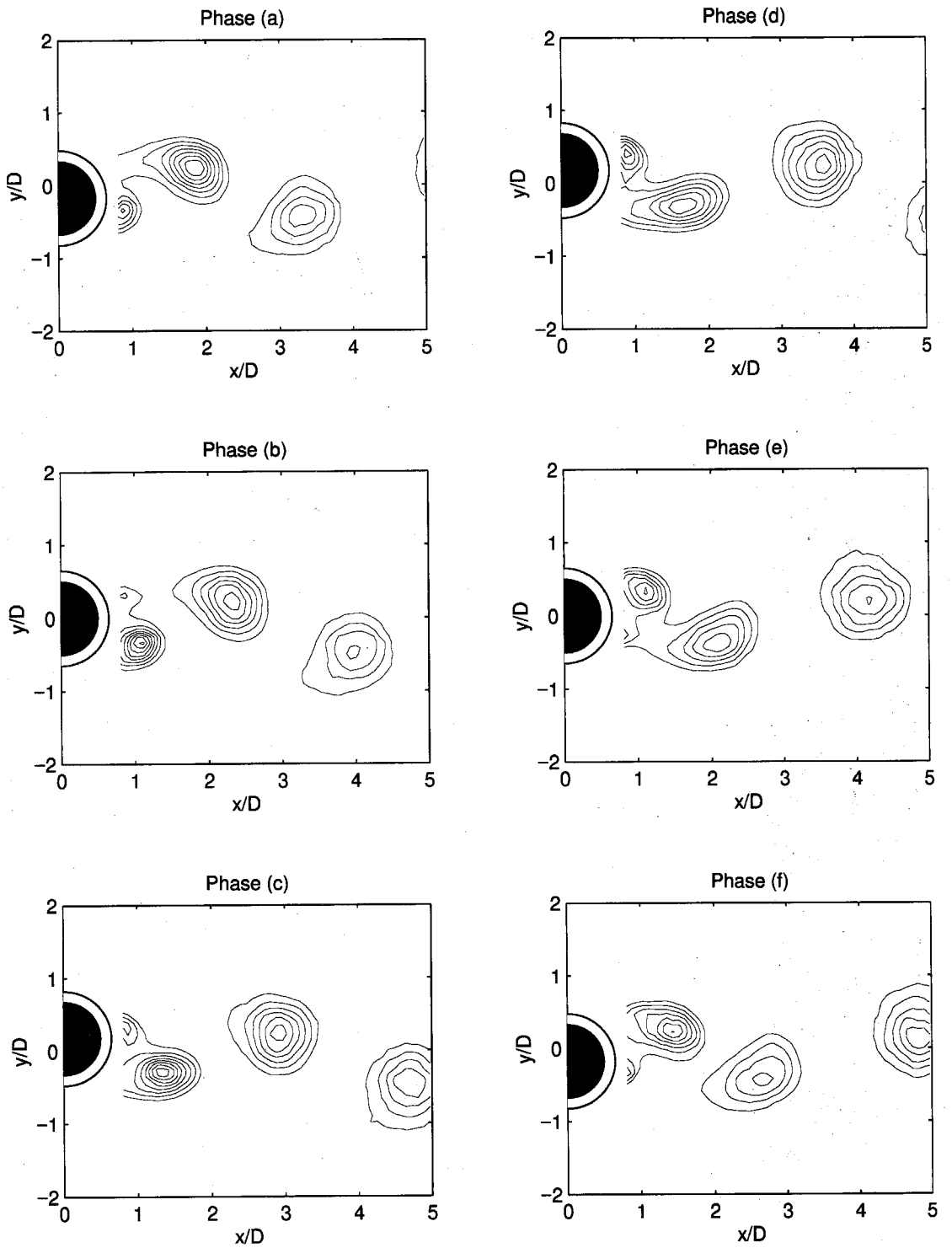


Figure 6.28 Sequence of phase averaged temperature field for forced oscillating cylinder at $St_c$=0.21, A/D=0.2 (Case V). ((<T> - $T_\infty$)/($T_c$ - $T_\infty$)>0.01, contour increment 0.005) The y-displacement of the cylinder corresponding to each letter is shown in Fig. 6.60.

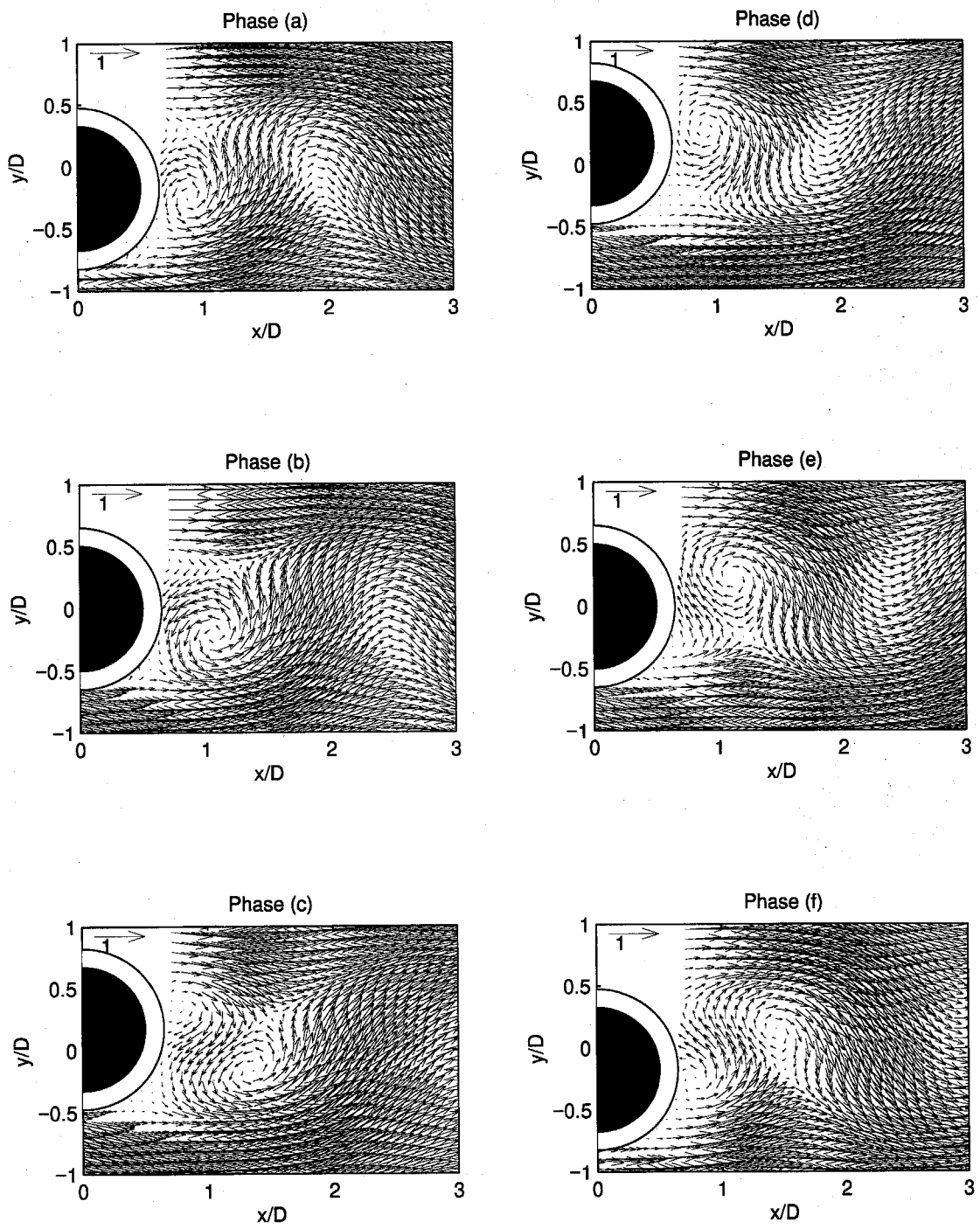


Figure 6.29 Sequence of phase averaged velocity field for forced oscillating cylinder at $St_c$=0.21, A/D=0.2 (Case V). The y-displacement of the cylinder corresponding to each letter is shown in Fig. 6.60.

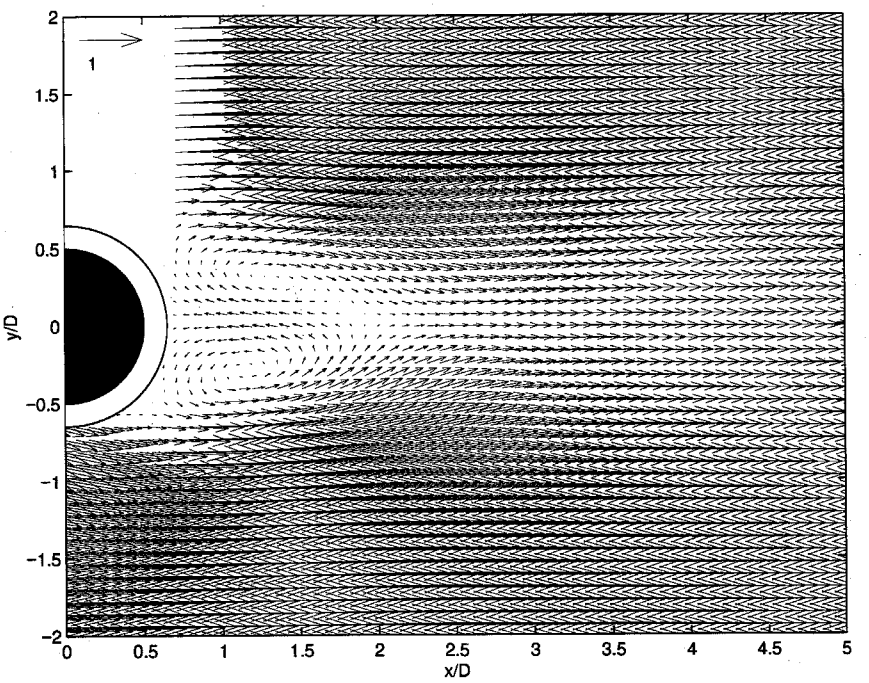


Figure 6.30 Mean velocity field of forced oscillating cylinder at $St_c$=0.30, A/D=0.2 (Case VI).

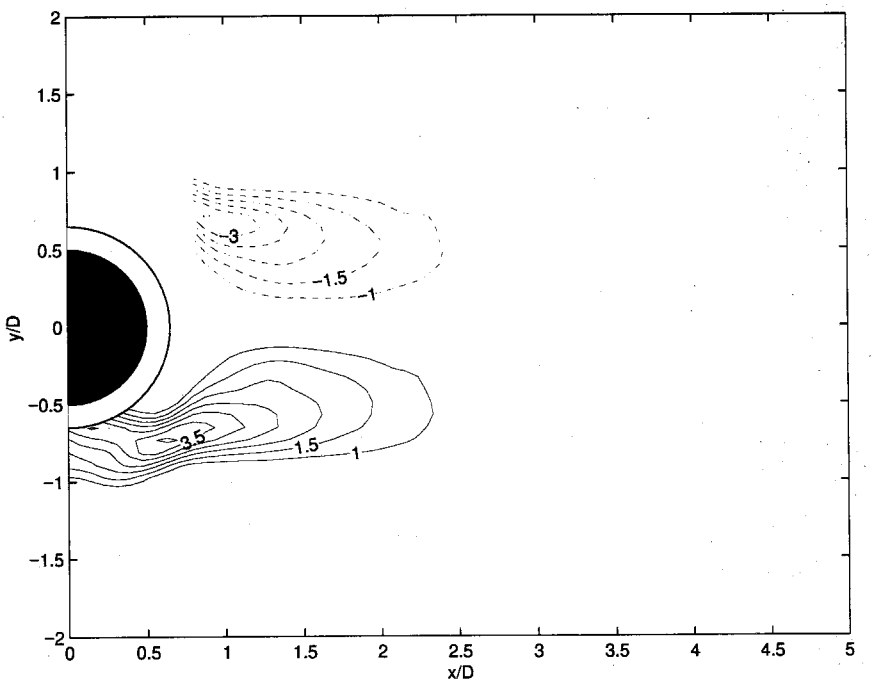


Figure 6.31 Mean vorticity field of forced oscillating cylinder at $St_c$=0.30, A/D=0.2 (Case VI).

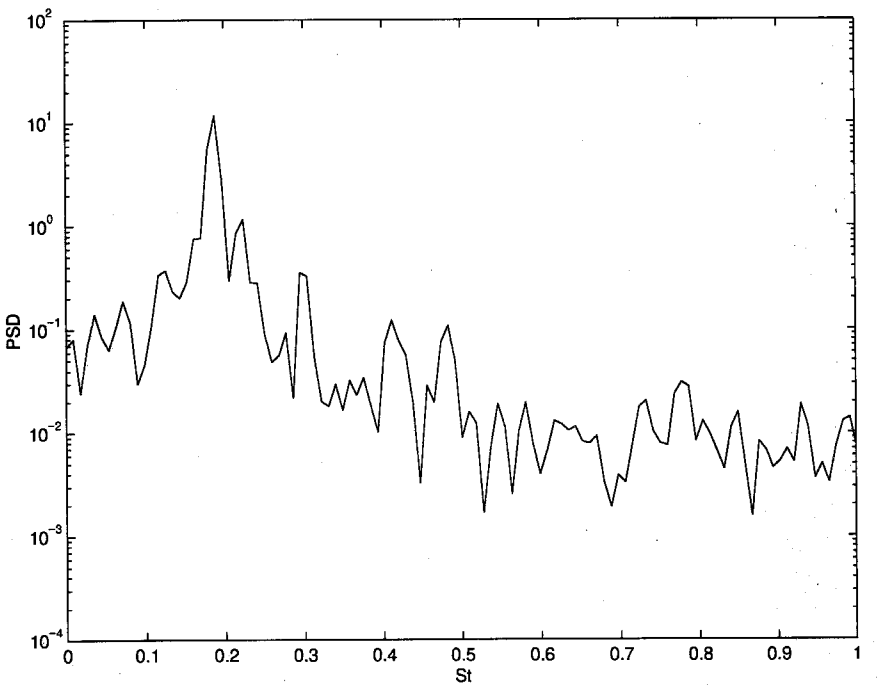


Figure 6.32 PSD of $u_y$ at location of maximum $u_y$ fluctuations on the wake centerline for forced oscillating cylinder at $St_c$=0.30, A/D=0.2 (Case VI).

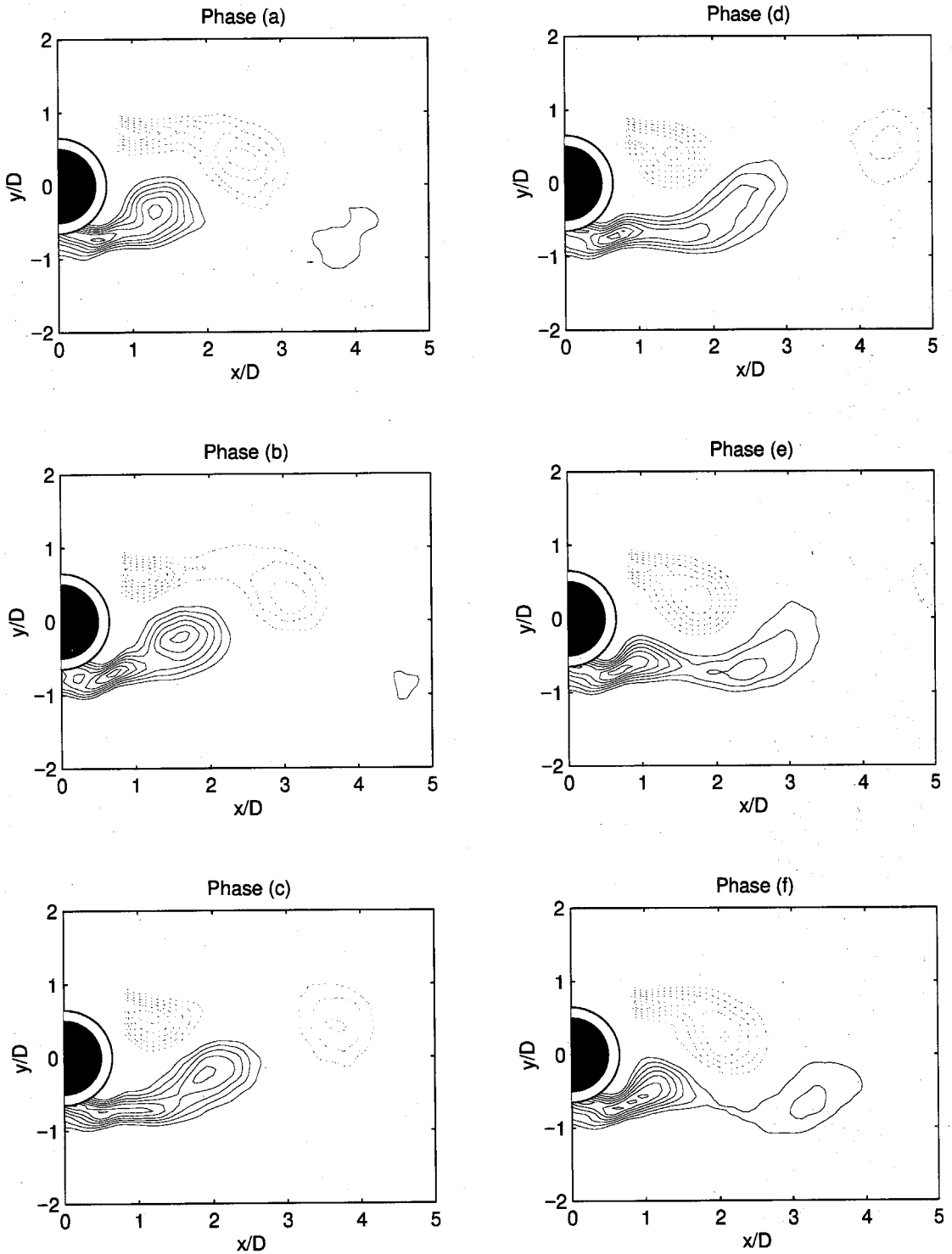


Figure 6.33 Sequence of phase averaged vorticity field for forced oscillating cylinder at $St_c$=0.30, A/D=0.2 (Case VI). ($|<\omega_z>D/U_\infty|>1.0$, contour increment 0.5) The phase averaging is done respect to $u_y$ at location of maximum $u_y$ fluctuations on the wake centerline. The value of the reference phase velocity ($u_y$ at location of maximum fluctuations) corresponding to each letter is shown in Fig. 6.60.

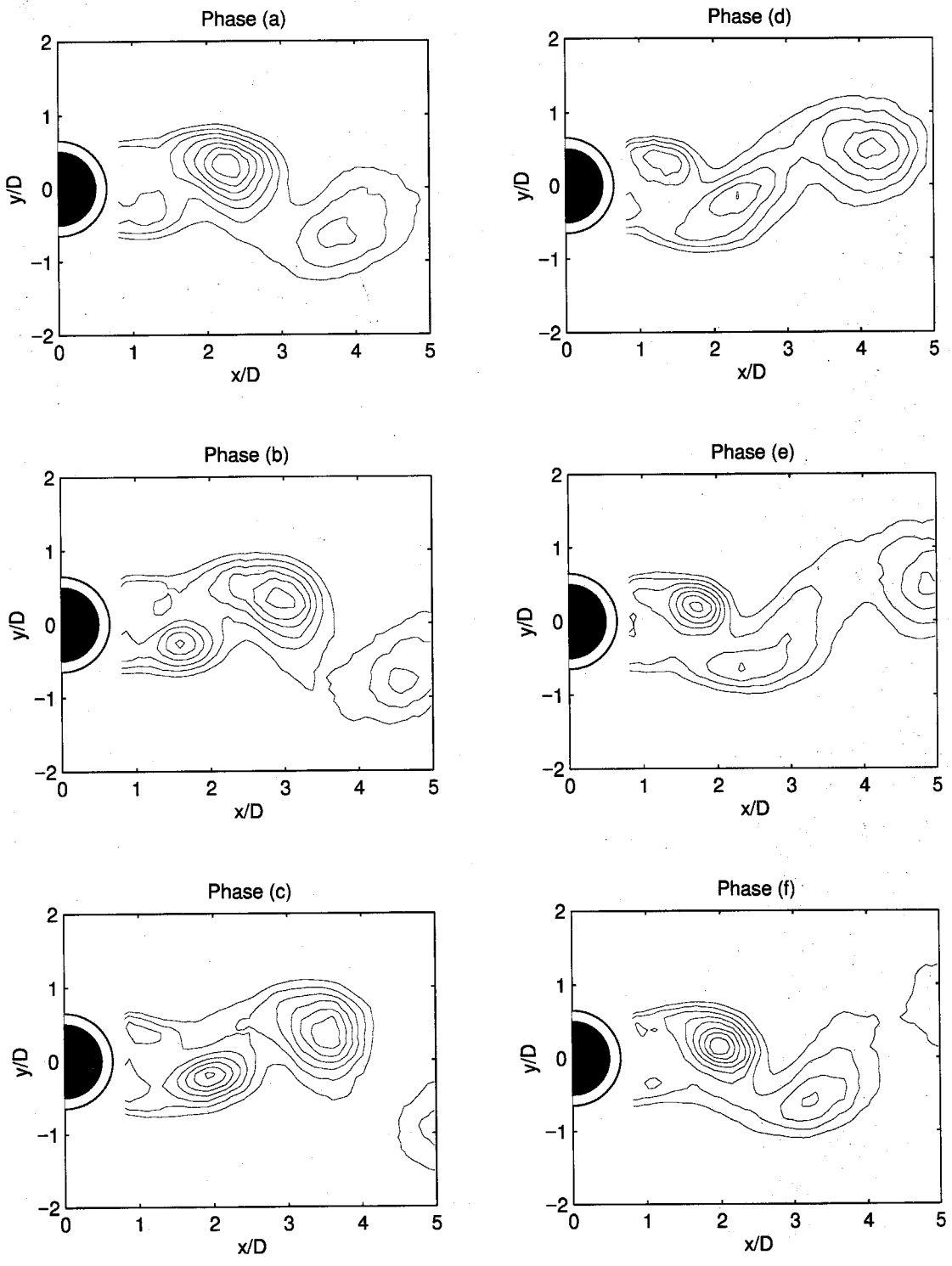


Figure 6.34 Sequence of phase averaged temperature field for forced oscillating cylinder at $St_c$=0.30, A/D=0.2 (Case VI). ((<T> - $T_\infty$)/($T_c$ - $T_\infty$)>0.01, contour increment 0.005) The phase averaging is done respect to $u_y$ at location of maximum $u_y$ fluctuations on the wake centerline. The value of the reference phase velocity ($u_y$ at location of maximum fluctuations) corresponding to each letter is shown in Fig. 6.60.

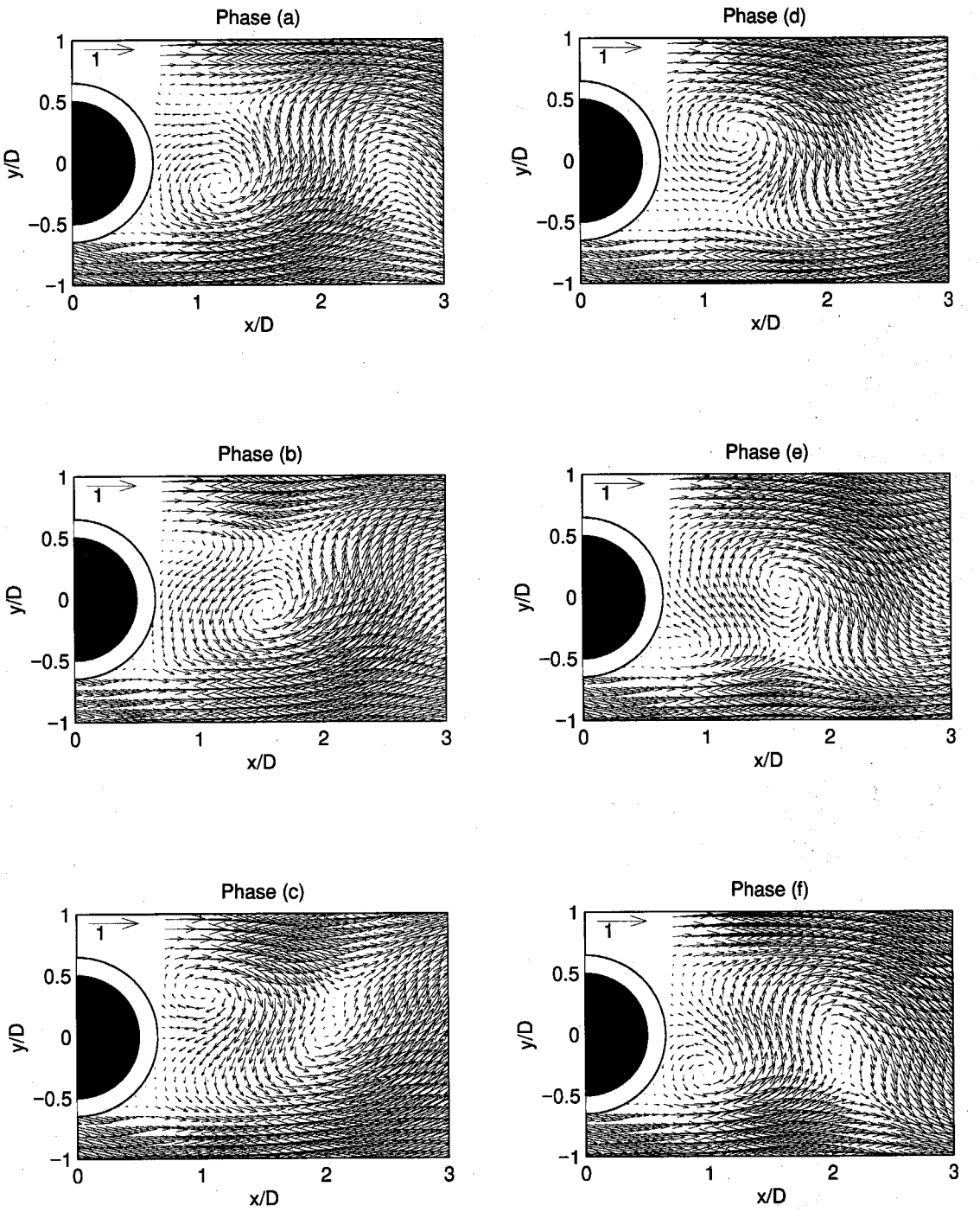


Figure 6.35 Sequence of phase averaged velocity field for forced oscillating cylinder at $St_c$=0.30, A/D=0.2 (Case VI). The phase averaging is done respect to $u_y$ at location of maximum $u_y$ fluctuations on the wake centerline. The value of the reference phase velocity ($u_y$ at location of maximum fluctuations) corresponding to each letter is shown in Fig. 6.60.

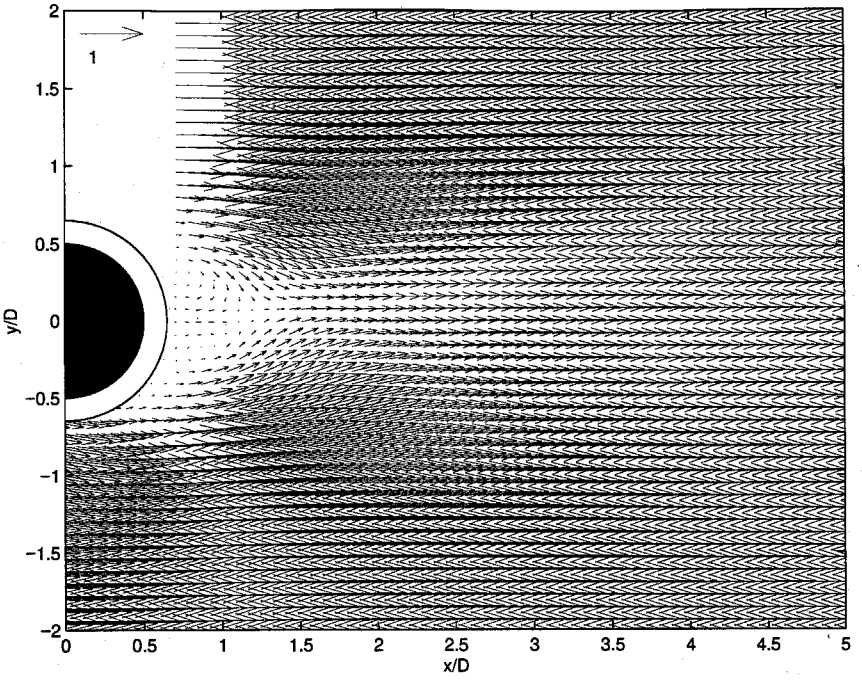


Figure 6.36 Mean velocity field of forced oscillating cylinder at $St_c$=0.37, A/D=0.2 (Case VII).

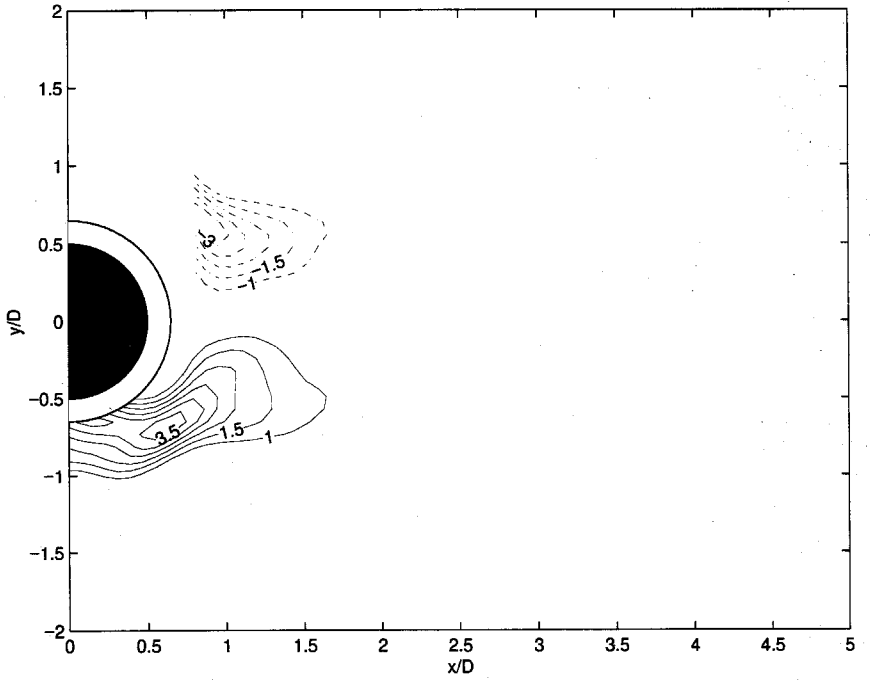


Figure 6.37 Mean vorticity field of forced oscillating cylinder at $St_c$=0.37, A/D=0.2 (Case VII).

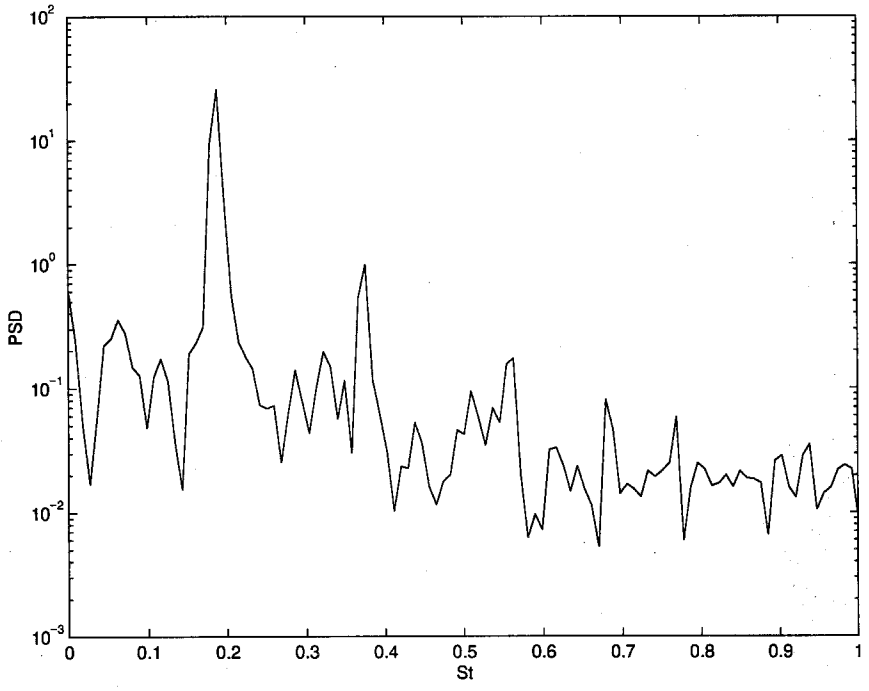


Figure 6.38 PSD of $u_y$ at location of maximum $u_y$ fluctuations on the wake centerline for forced oscillating cylinder at $St_c$=0.37, A/D=0.2 (Case VII).

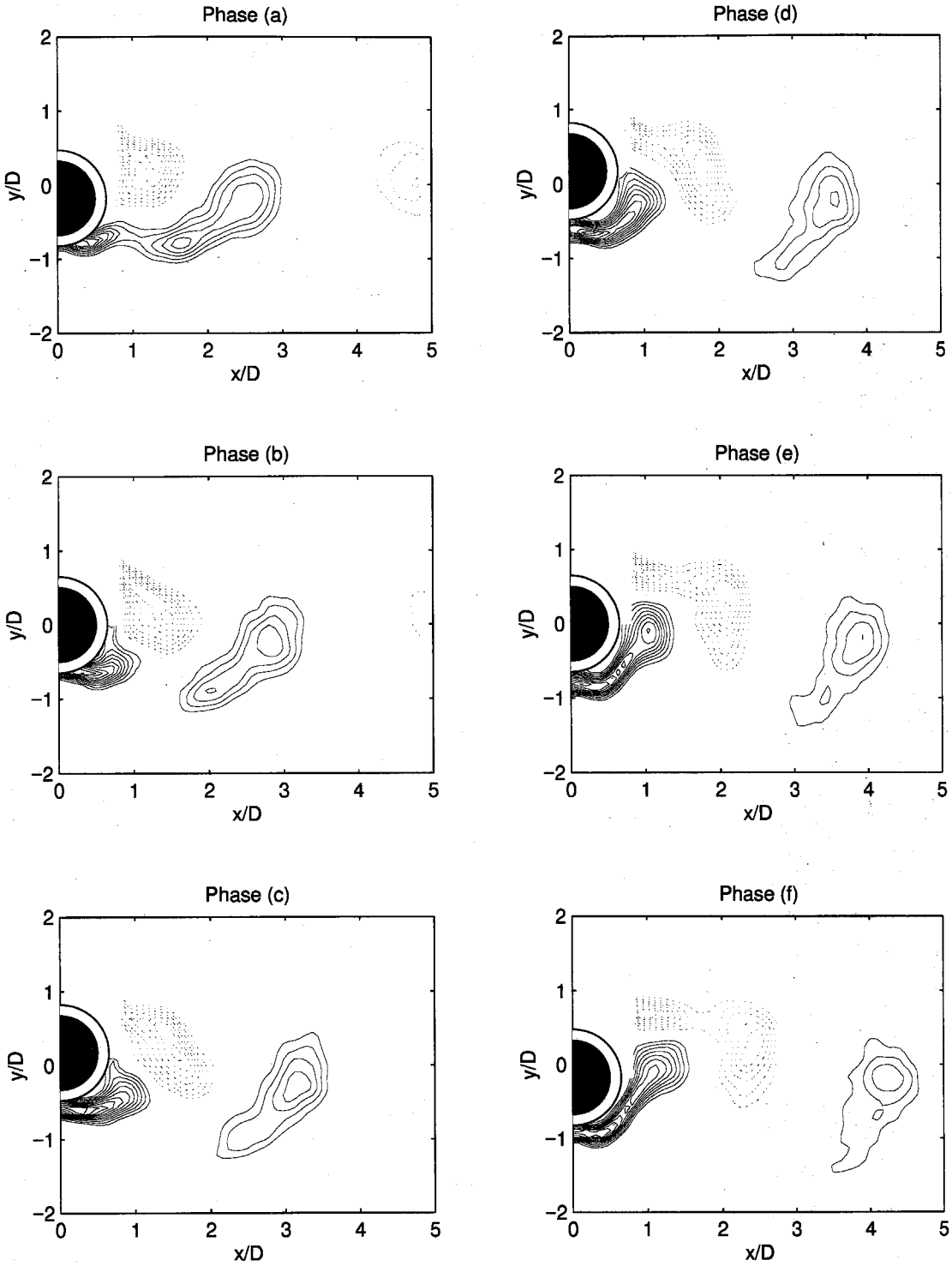


Figure 6.39(a) Sequence of phase averaged vorticity field for forced oscillating cylinder at $St_c$=0.37, A/D=0.2 (Case VII). ($|<\omega_z>D/U_\infty|>1.0$, contour increment 0.5) The y-displacement of the cylinder corresponding to each letter is shown in Fig. 6.60.

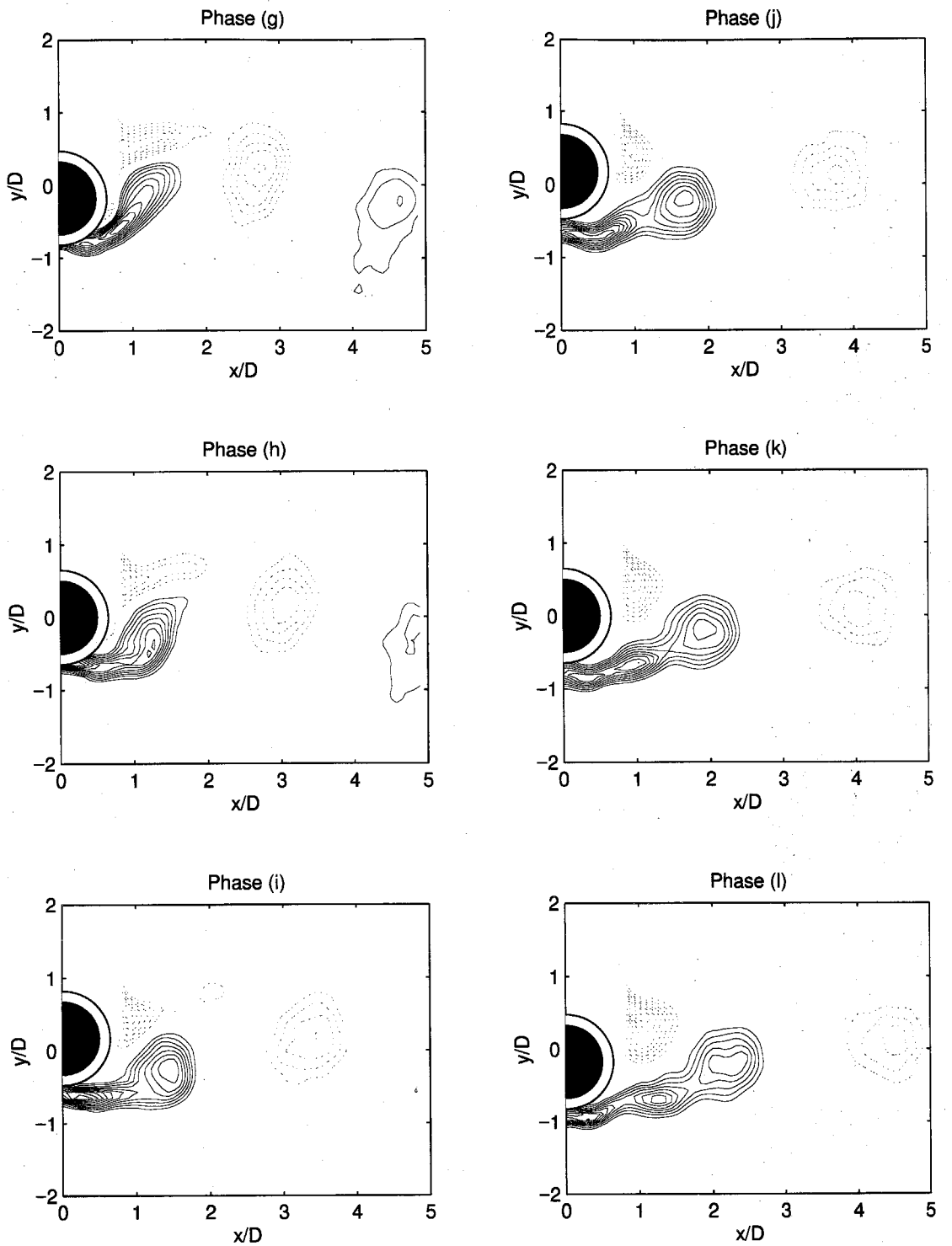


Figure 6.39(b) Sequence of phase averaged vorticity field for forced oscillating cylinder at $St_c$=0.37, A/D=0.2 (Case VII). ($|<\omega_z>D/U_\infty|>1.0$, contour increment 0.5) The y-displacement of the cylinder corresponding to each letter is shown in Fig. 6.60.

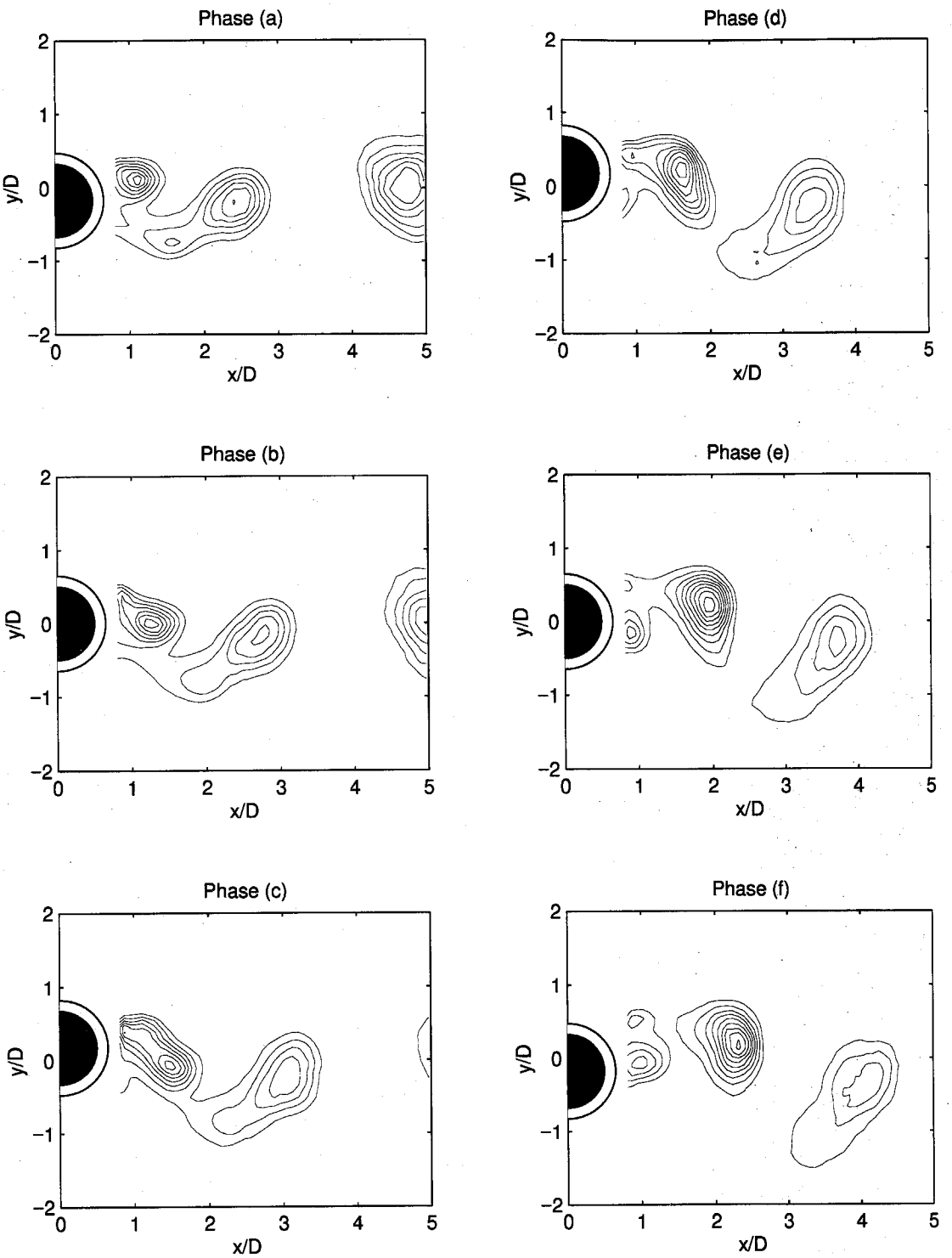


Figure 6.40(a) Sequence of phase averaged temperature field for forced oscillating cylinder at $St_c$=0.37, A/D=0.2 (Case VII). $((\langle T \rangle - T_\infty)/(T_c - T_\infty)>0.01$, contour increment 0.005) The y-displacement of the cylinder corresponding to each letter is shown in Fig. 6.60.

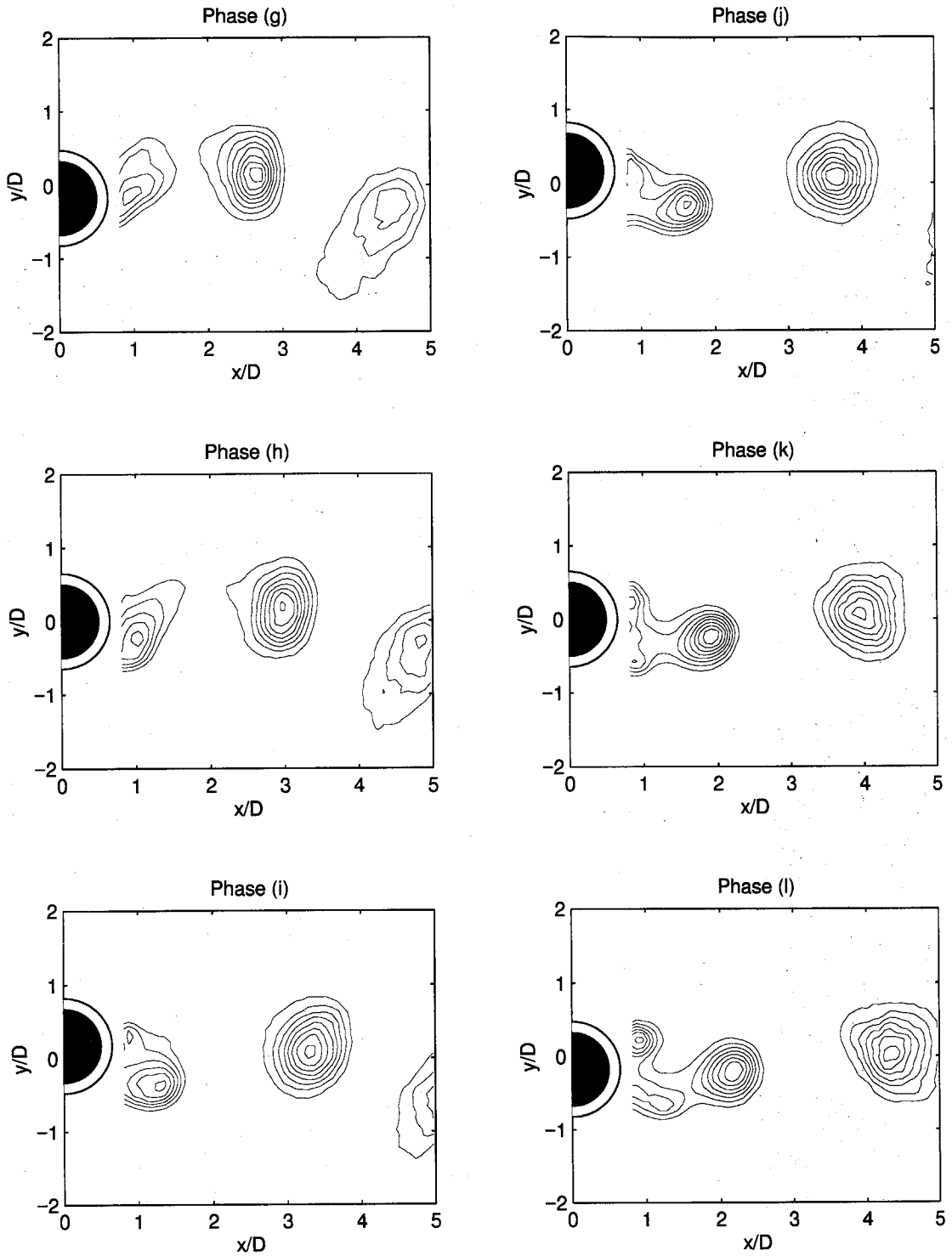


Figure 6.40(b) Sequence of phase averaged temperature field for forced oscillating cylinder at $St_c$=0.37, A/D=0.2 (Case VII). ($(<T> - T_\infty)/(T_c - T_\infty)>0.01$, contour increment 0.005) The y-displacement of the cylinder corresponding to each letter is shown in Fig. 6.60.

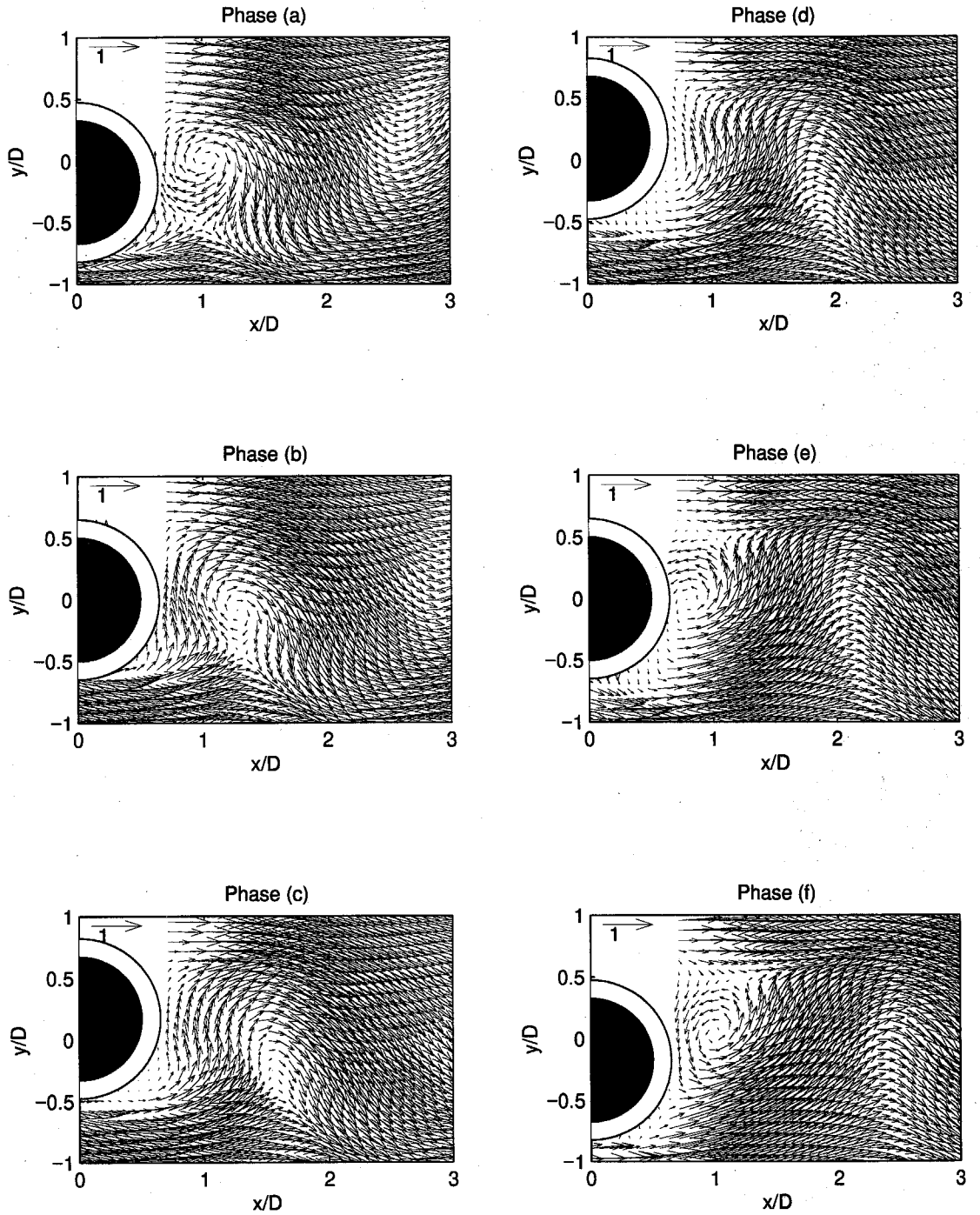


Figure 6.41(a) Sequence of phase averaged velocity field for forced oscillating cylinder at $St_c$=0.37, A/D=0.2 (Case VII). The y-displacement of the cylinder corresponding to each letter is shown in Fig. 6.60.

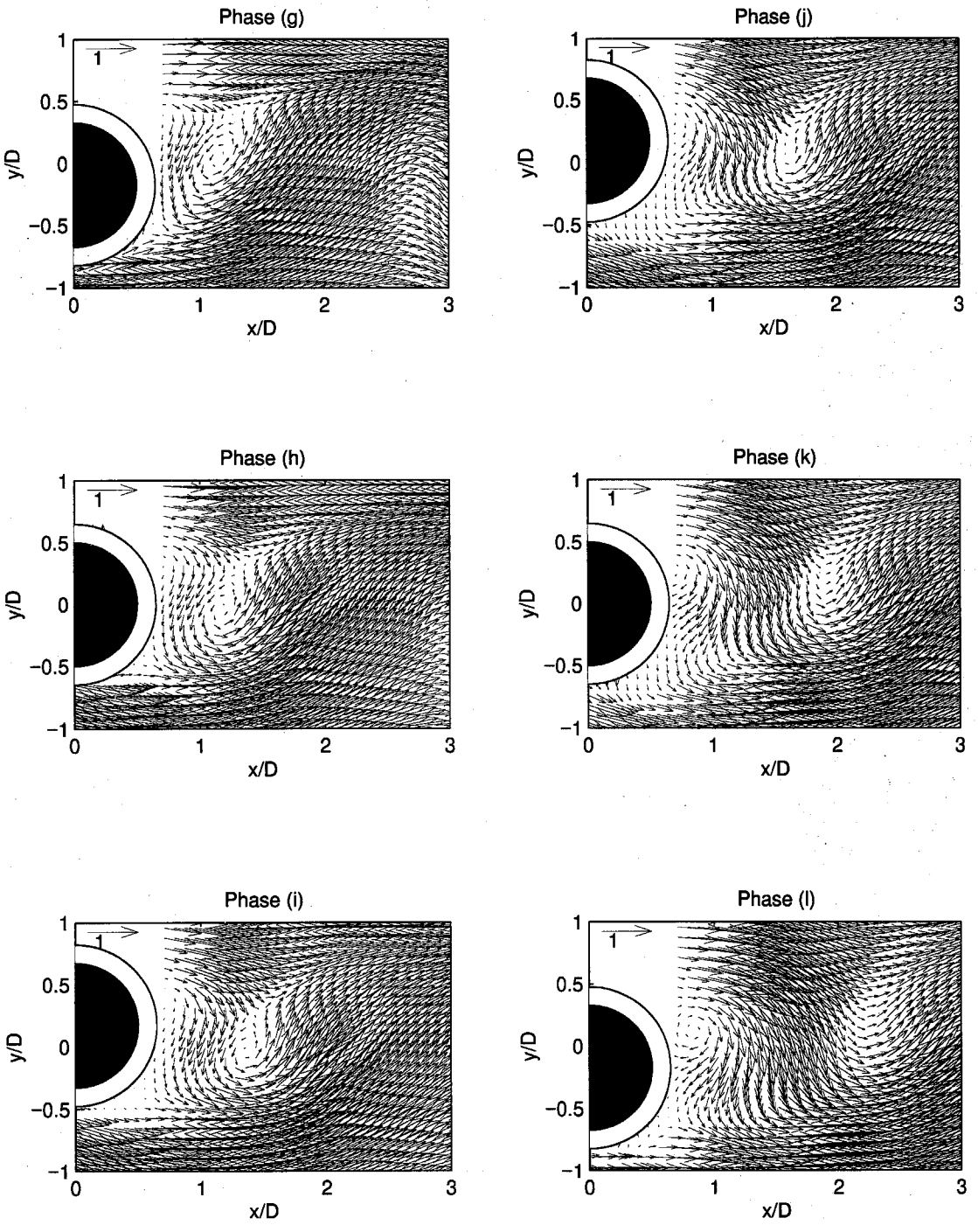


Figure 6.41(b) Sequence of phase averaged velocity field for forced oscillating cylinder at $St_c$=0.37, A/D=0.2 (Case VII). The y-displacement of the cylinder corresponding to each letter is shown in Fig. 6.60.

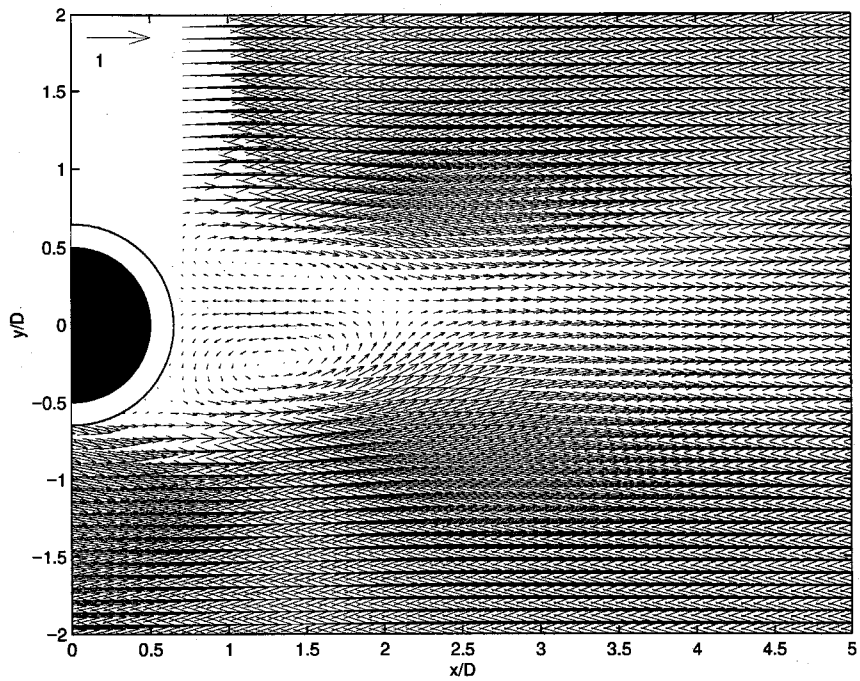


Figure 6.42 Mean velocity field of forced oscillating cylinder at $St_c$=0.42, A/D=0.2 (Case VIII).

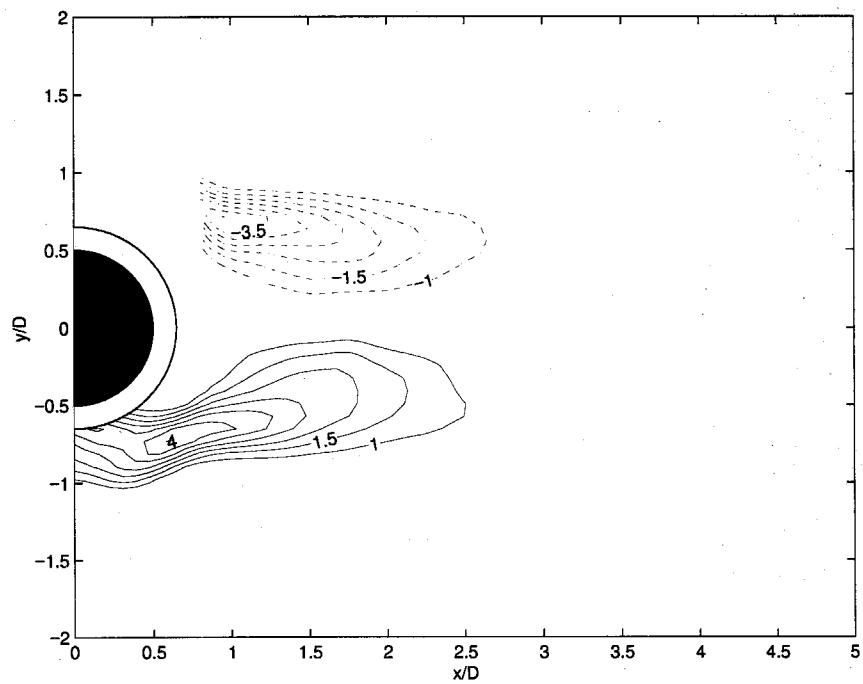


Figure 6.43 Mean vorticity field of forced oscillating cylinder at $St_c$=0.42, A/D=0.2 (Case VIII).

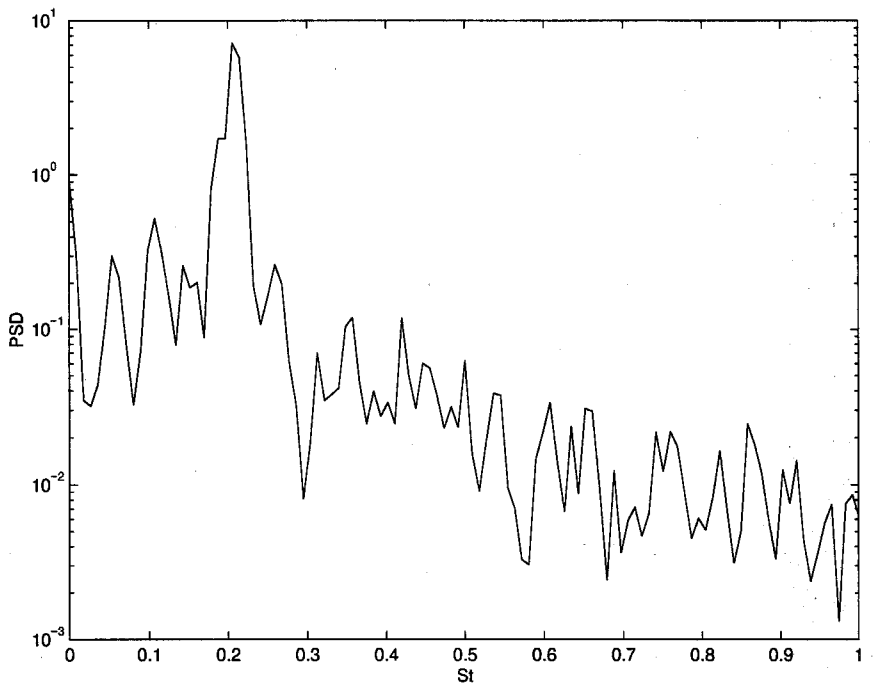


Figure 6.44 PSD of $u_y$ at location of maximum $u_y$ fluctuations on the wake centerline for forced oscillating cylinder at $St_e$=0.42, A/D=0.2 (Case VIII).

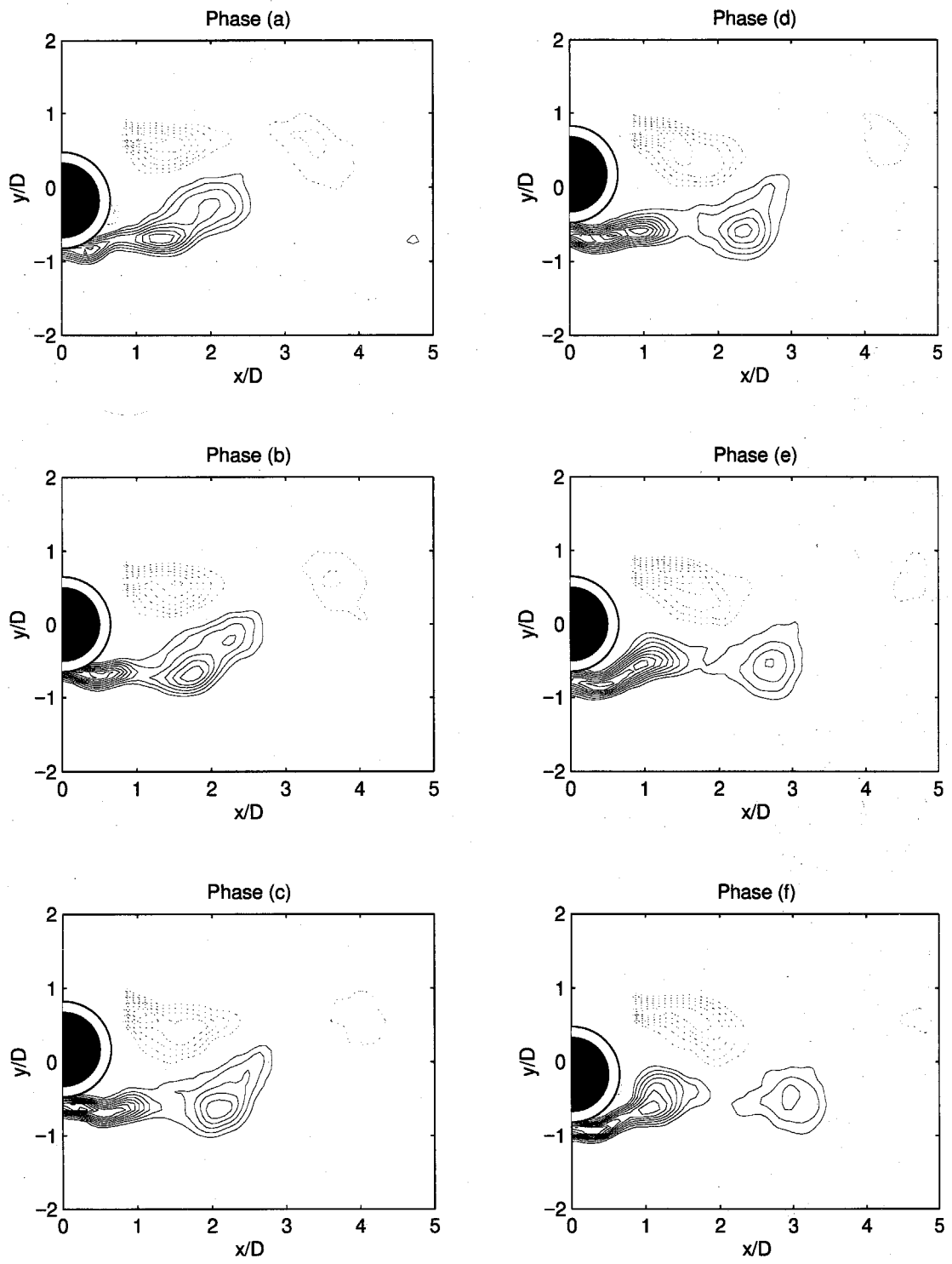


Figure 6.45(a) Sequence of phase averaged vorticity field for forced oscillating cylinder at $St_c$=0.42, A/D=0.2 (Case VIII). ($|<\omega_z>D/U_\infty|>1.0$, contour increment 0.5) The y-displacement of the cylinder corresponding to each letter is shown in Fig. 6.60.

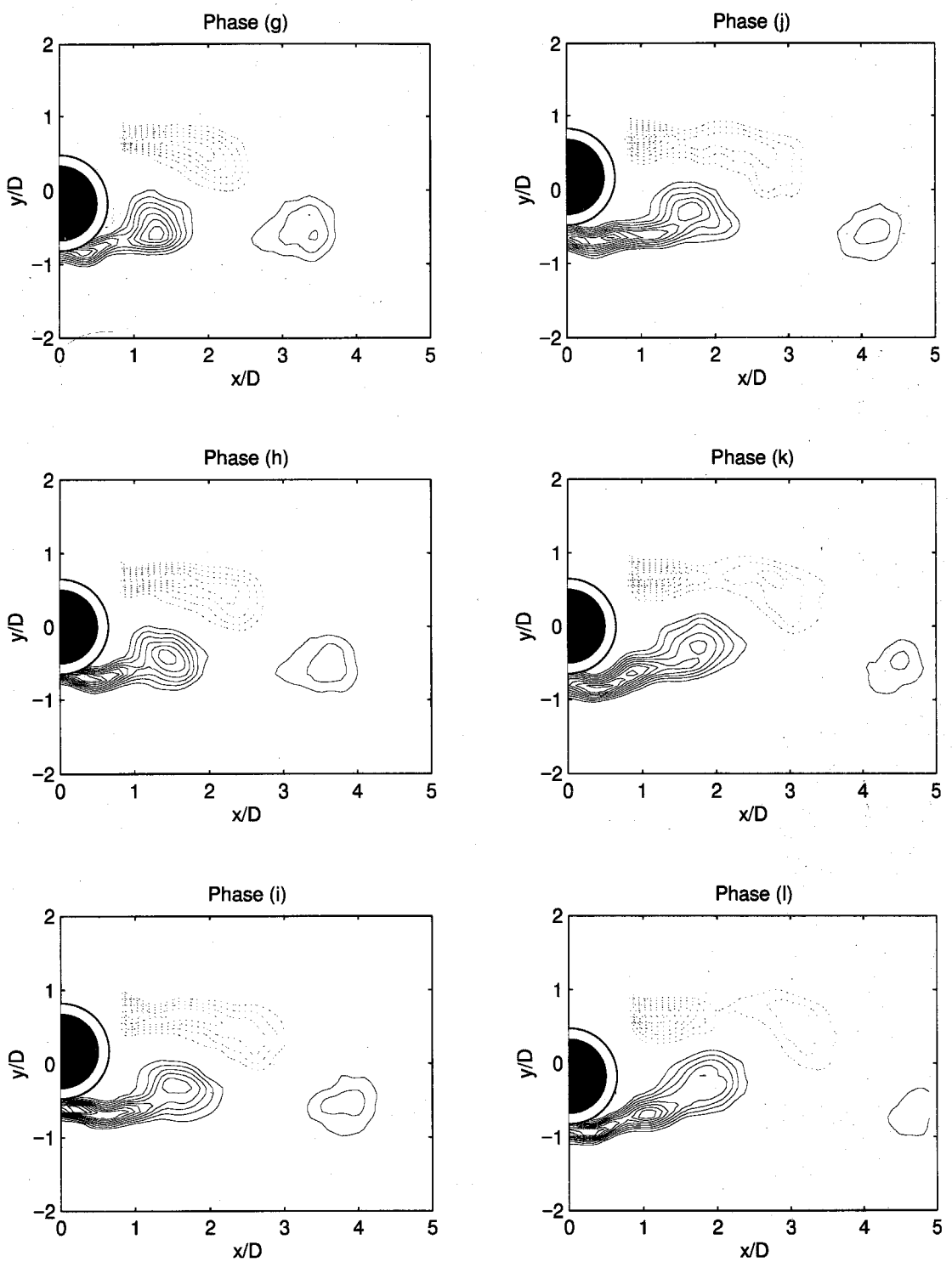


Figure 6.45(b) Sequence of phase averaged vorticity field for forced oscillating cylinder at $St_c$=0.42, A/D=0.2 (Case VIII). ($|<\omega_z>D/U_\infty|>1.0$, contour increment 0.5) The y-displacement of the cylinder corresponding to each letter is shown in Fig. 6.60.

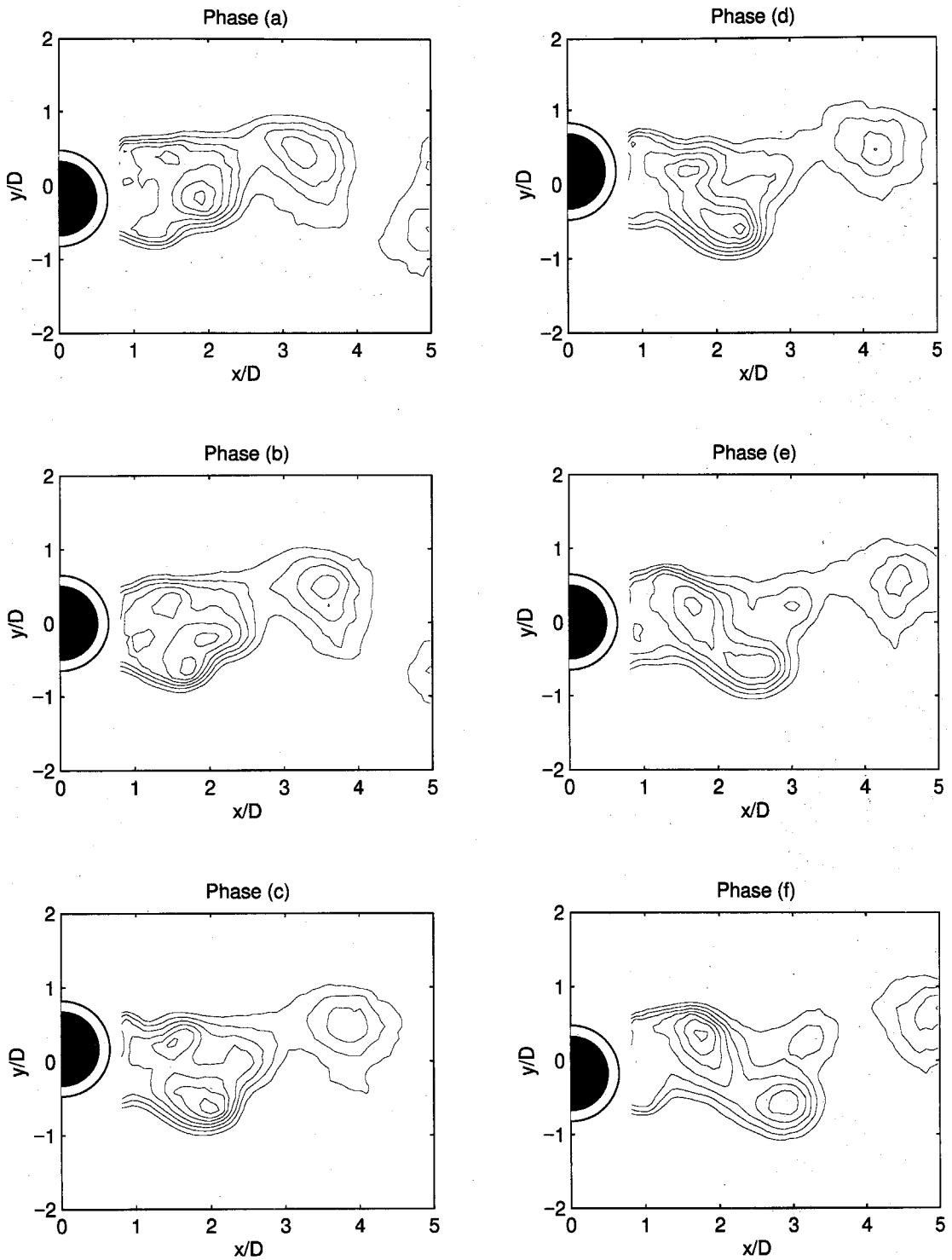


Figure 6.46(a) Sequence of phase averaged temperature field for forced oscillating cylinder at $St_c$=0.42, A/D=0.2 (Case VIII). ((<T> - $T_\infty$)/($T_c$ - $T_\infty$)>0.01, contour increment 0.005) The y-displacement of the cylinder corresponding to each letter is shown in Fig. 6.60.

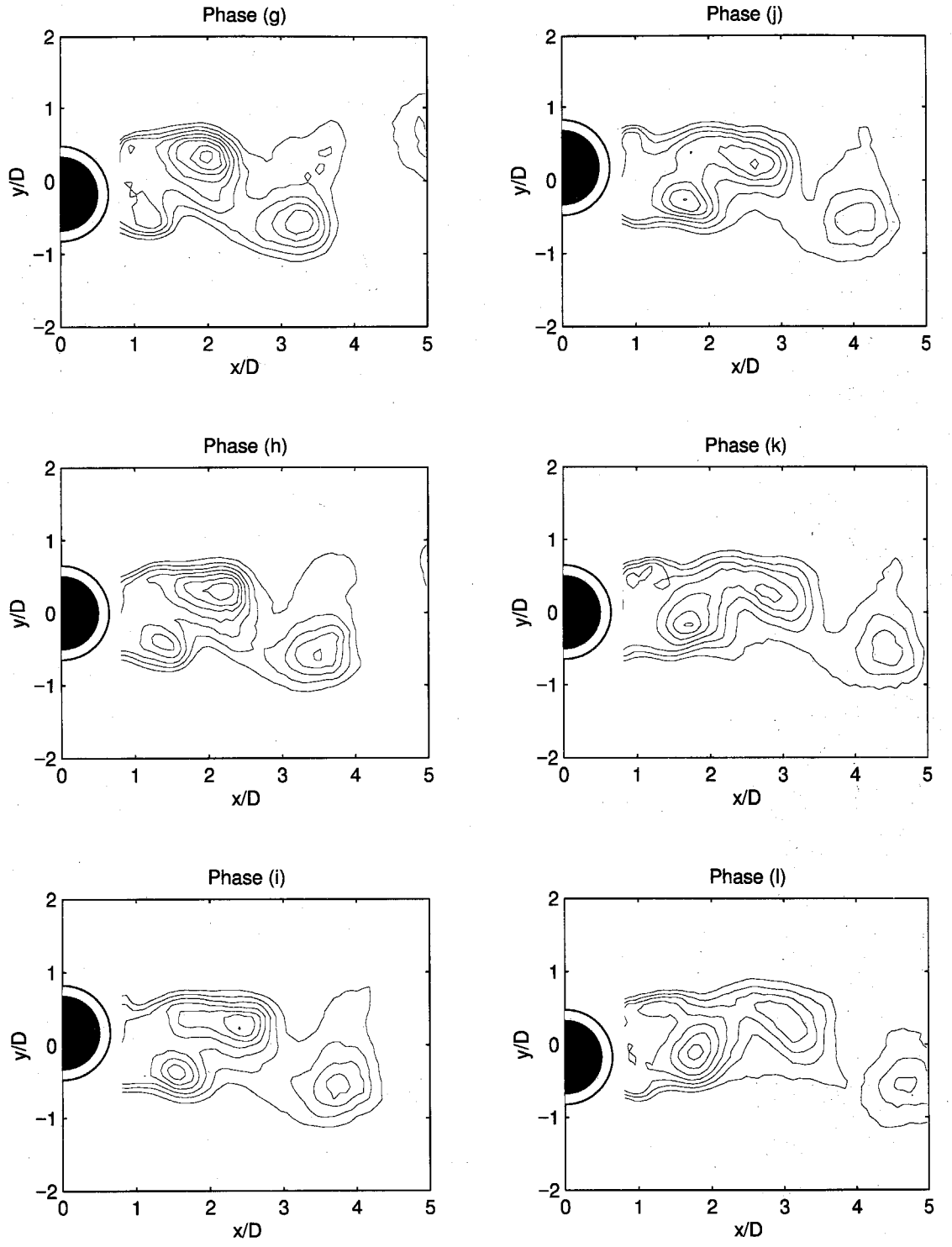


Figure 6.46(b) Sequence of phase averaged temperature field for forced oscillating cylinder at $St_c$=0.42, A/D=0.2 (Case VIII). ($(<T> - T_\infty)/(T_c - T_\infty)>0.01$, contour increment 0.005) The y-displacement of the cylinder corresponding to each letter is shown in Fig. 6.60.

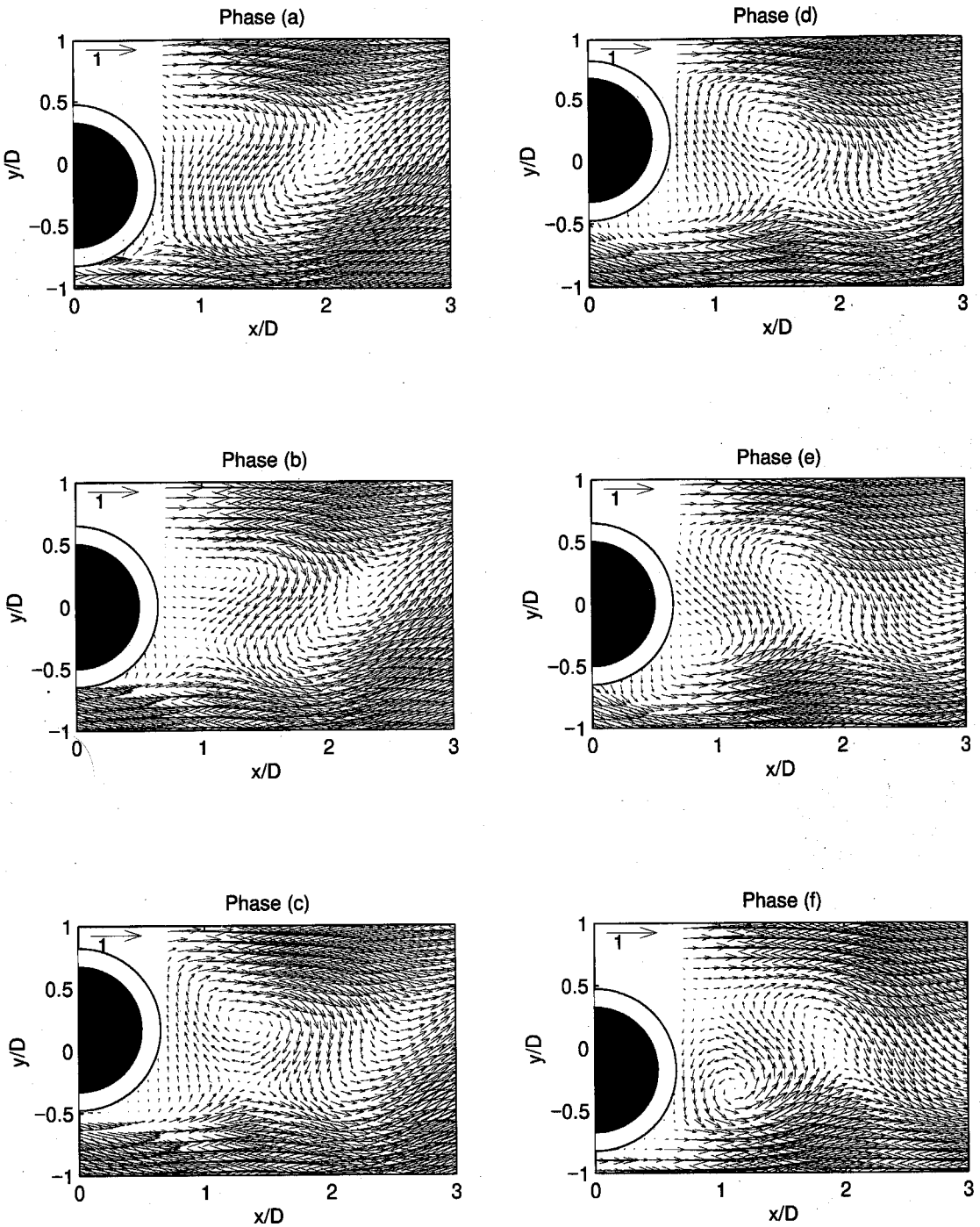


Figure 6.47(a) Sequence of phase averaged velocity field for forced oscillating cylinder at $St_c$=0.42, A/D=0.2 (Case VIII). The y-displacement of the cylinder corresponding to each letter is shown in Fig. 6.60.

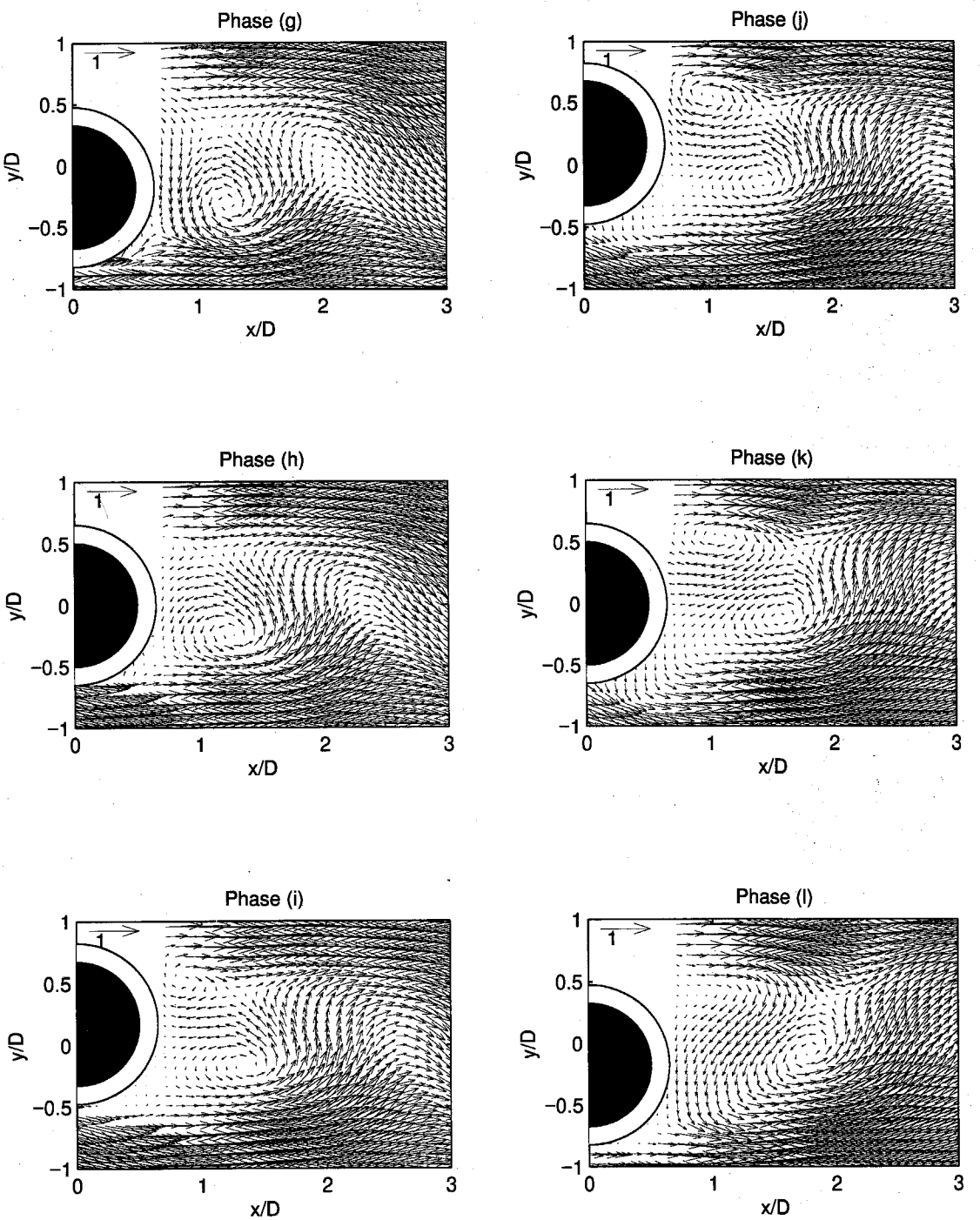


Figure 6.47(b) Sequence of phase averaged velocity field for forced oscillating cylinder at $St_c$=0.42, A/D=0.2 (Case VIII). The y-displacement of the cylinder corresponding to each letter is shown in Fig. 6.60.

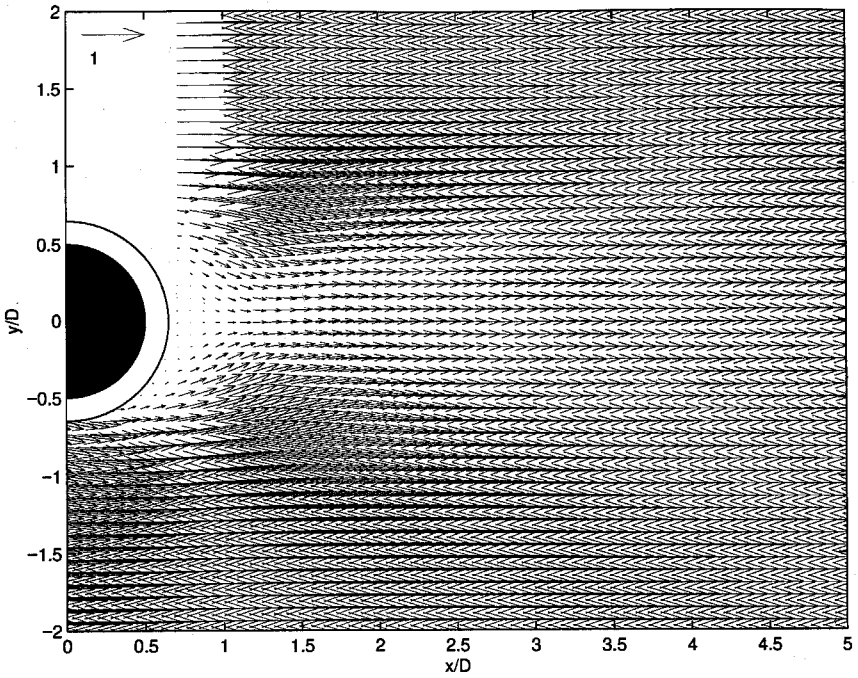


Figure 6.48 Mean velocity field of forced oscillating cylinder at $St_c$=0.51, A/D=0.2 (Case IX).

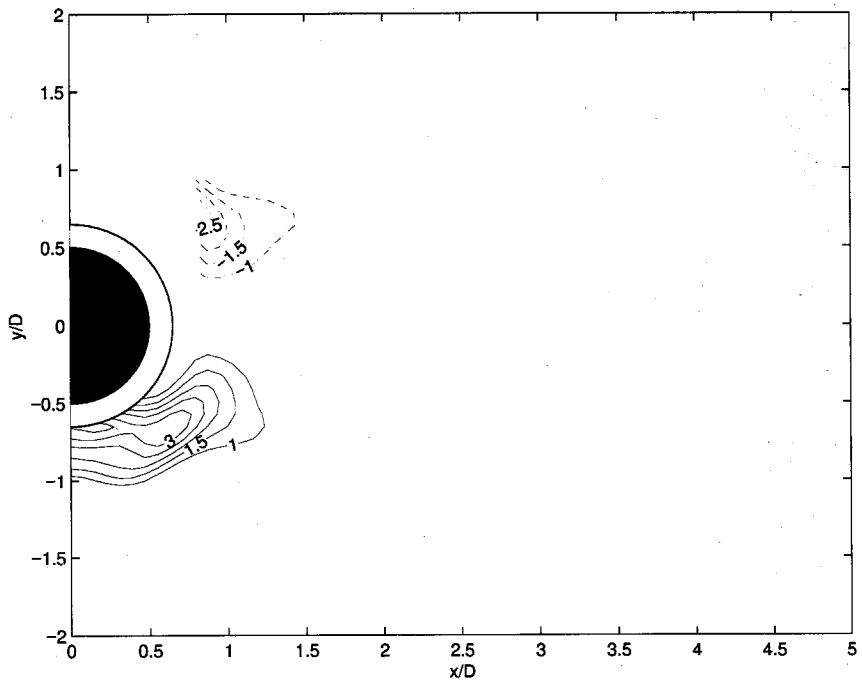


Figure 6.49 Mean vorticity field of forced oscillating cylinder at $St_c$=0.51, A/D=0.2 (Case IX).

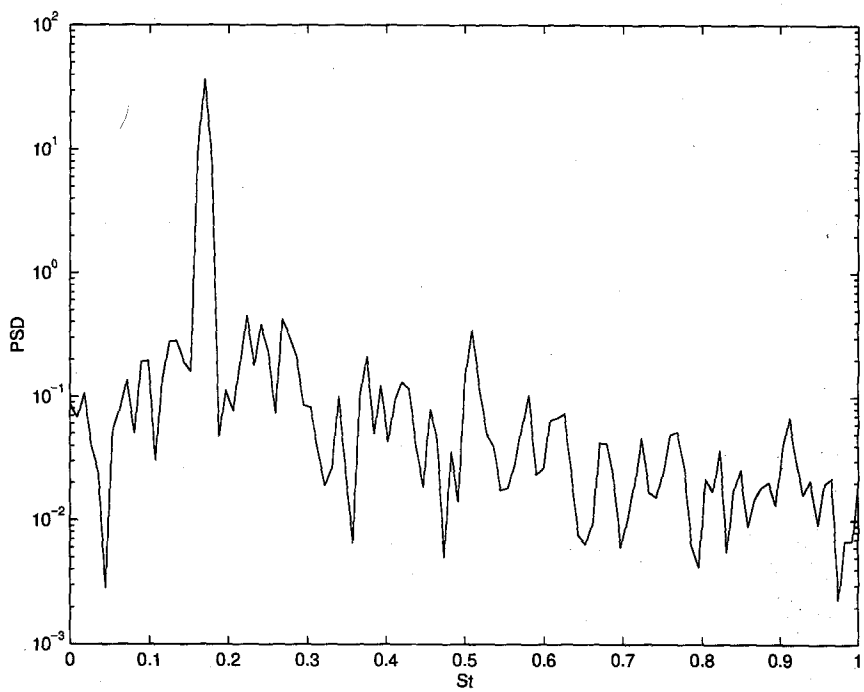


Figure 6.50 PSD of $u_y$ at location of maximum $u_y$ fluctuations on the wake centerline for forced oscillating cylinder at $St_e$=0.51, A/D=0.2 (Case IX).

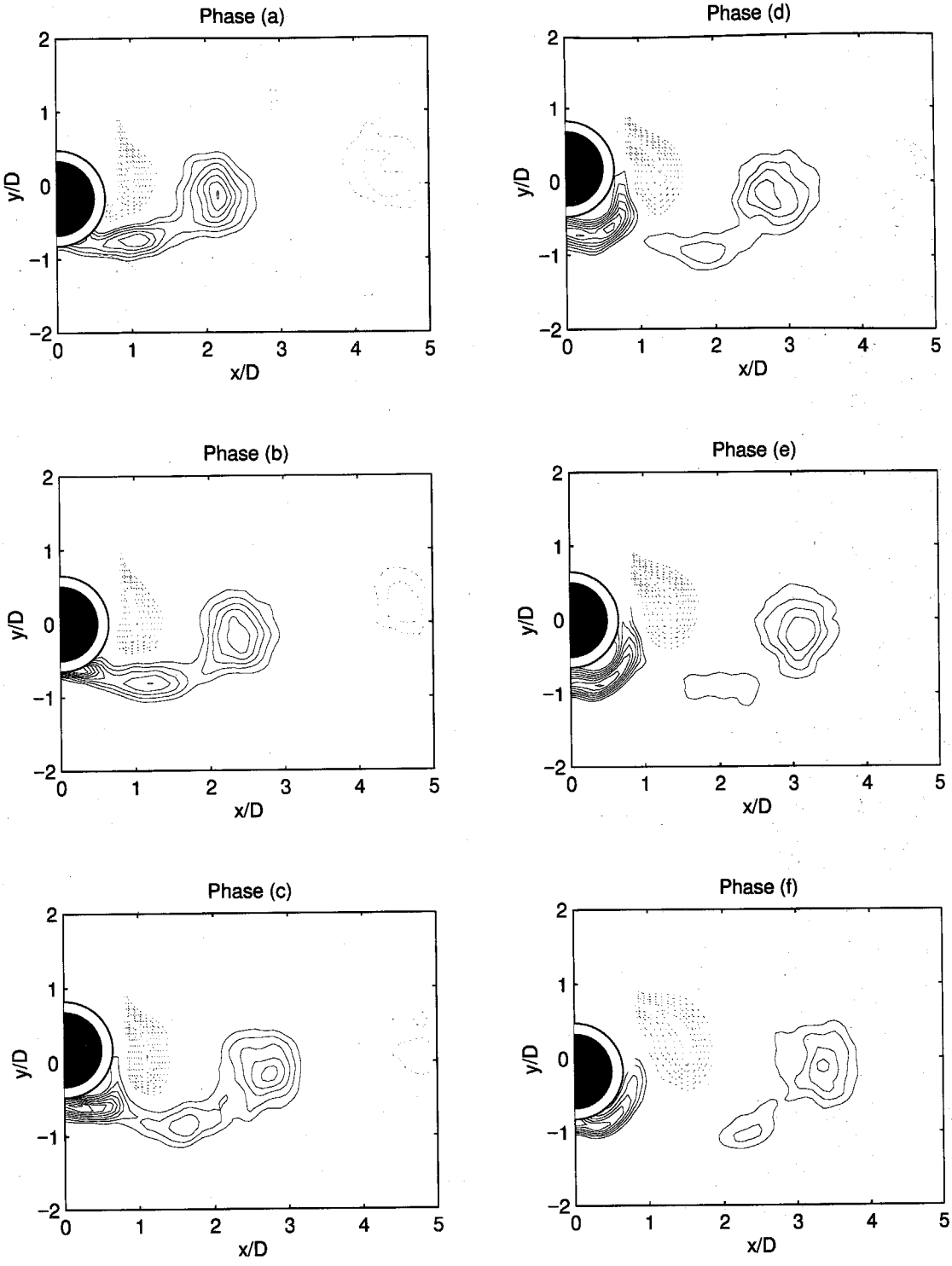


Figure 6.51(a) Sequence of phase averaged vorticity field for forced oscillating cylinder at $St_c$=0.51, A/D=0.2 (Case IX). ($|<\omega_z>D/U_\infty|>1.0$, contour increment 0.5) The y-displacement of the cylinder corresponding to each letter is shown in Fig. 6.60.

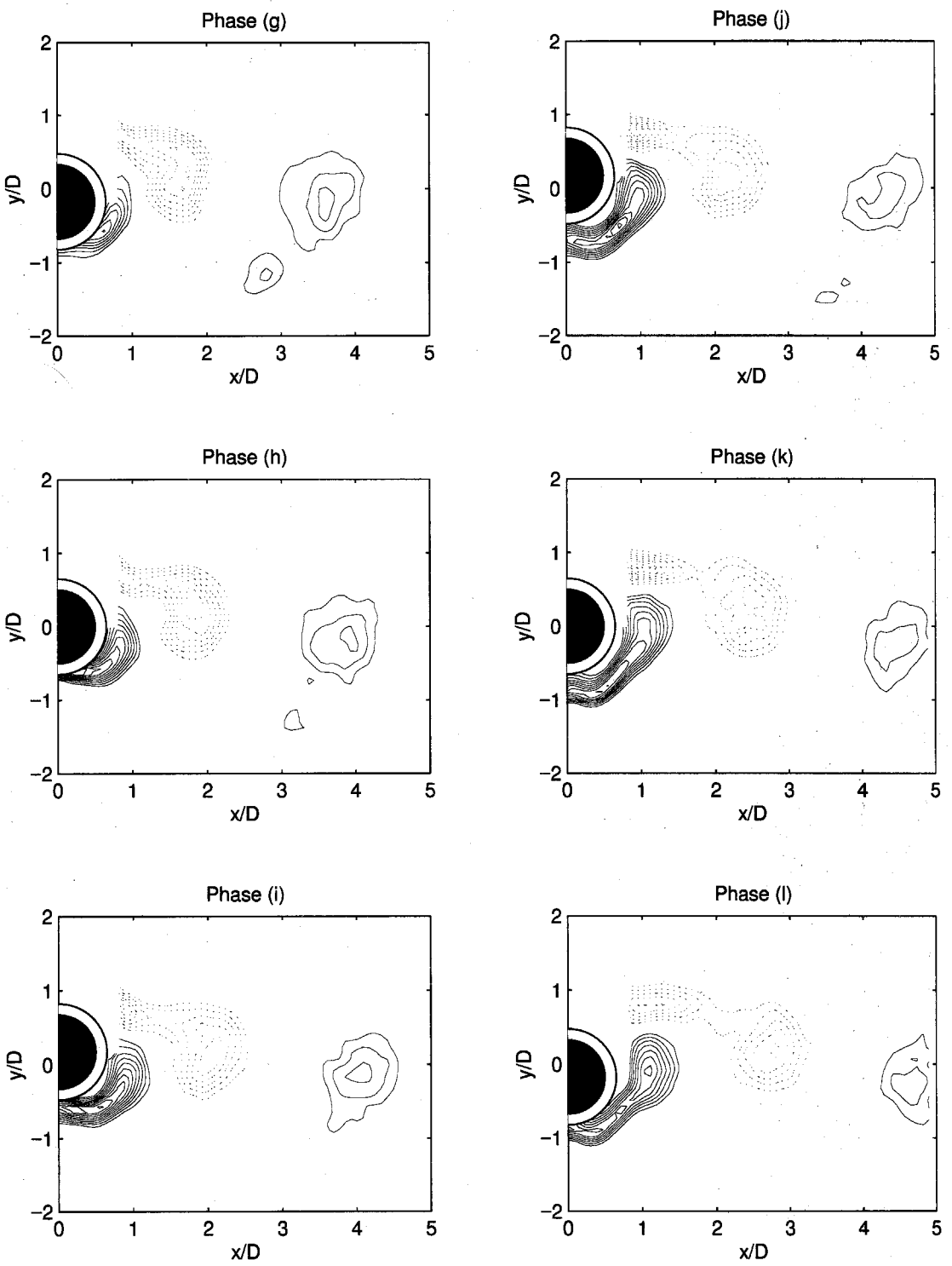


Figure 6.51(b) Sequence of phase averaged vorticity field for forced oscillating cylinder at $St_c$=0.51, A/D=0.2 (Case IX). ($|<\omega_z>D/U_\infty|>1.0$, contour increment 0.5) The y-displacement of the cylinder corresponding to each letter is shown in Fig. 6.60.

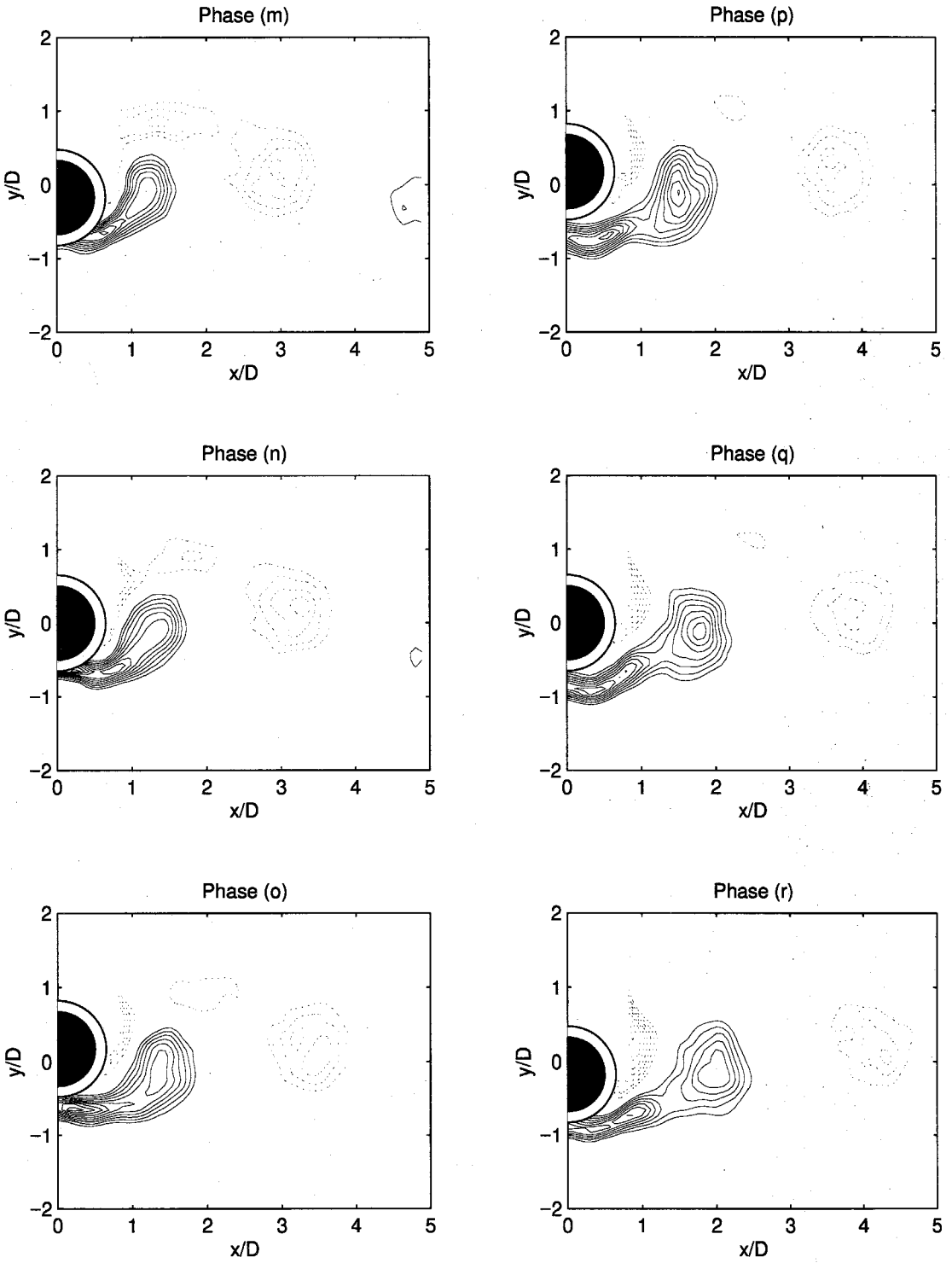


Figure 6.51(c) Sequence of phase averaged vorticity field for forced oscillating cylinder at $St_c$=0.51, A/D=0.2 (Case IX). ($|<\omega_z>D/U_\infty|>1.0$, contour increment 0.5) The y-displacement of the cylinder corresponding to each letter is shown in Fig. 6.60.

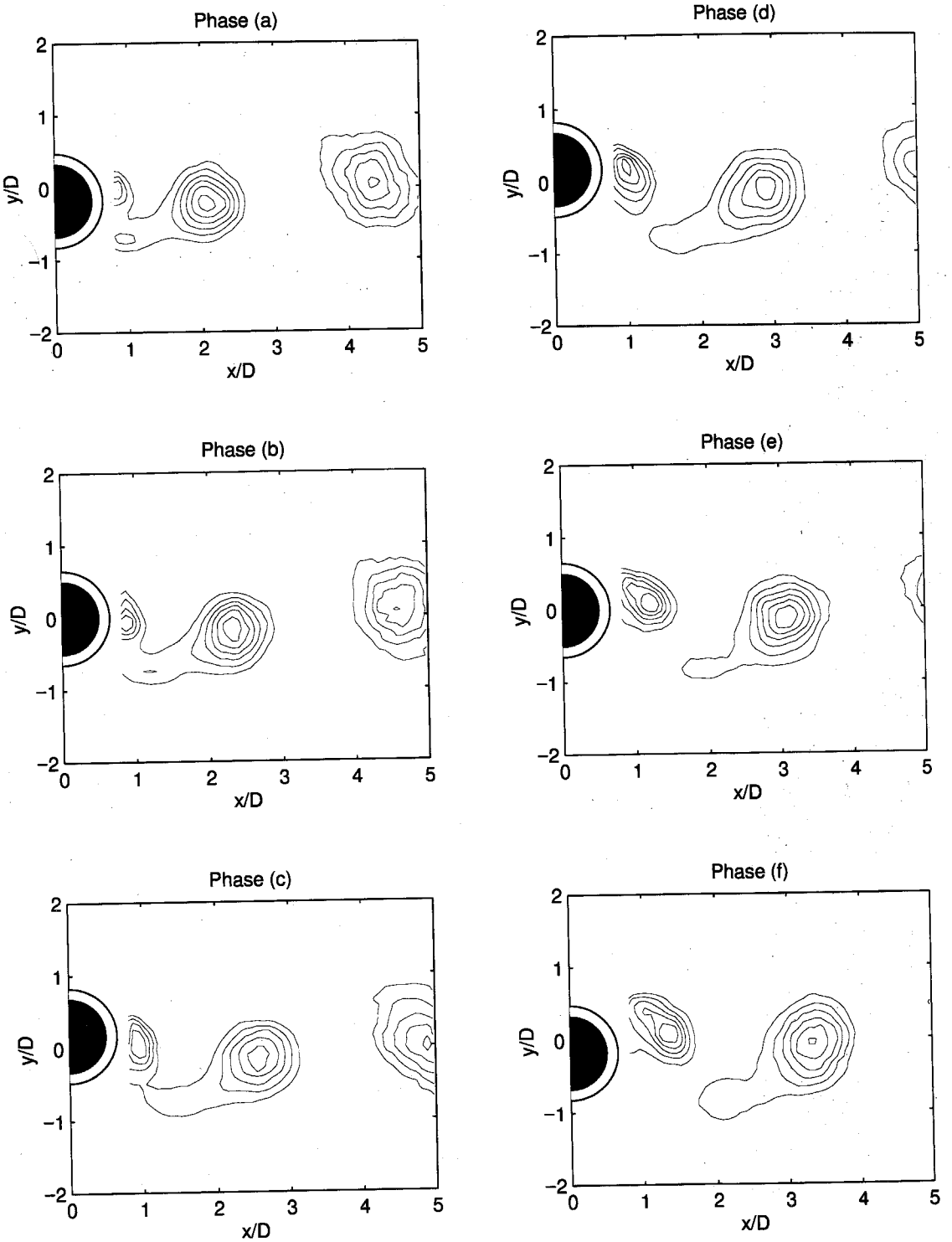


Figure 6.52(a) Sequence of phase averaged temperature field for forced oscillating cylinder at $St_c$=0.51, A/D=0.2 (Case IX). ($(<T> - T_\infty)/(T_c - T_\infty)>0.01$, contour increment 0.005) The y-displacement of the cylinder corresponding to each letter is shown in Fig. 6.60.

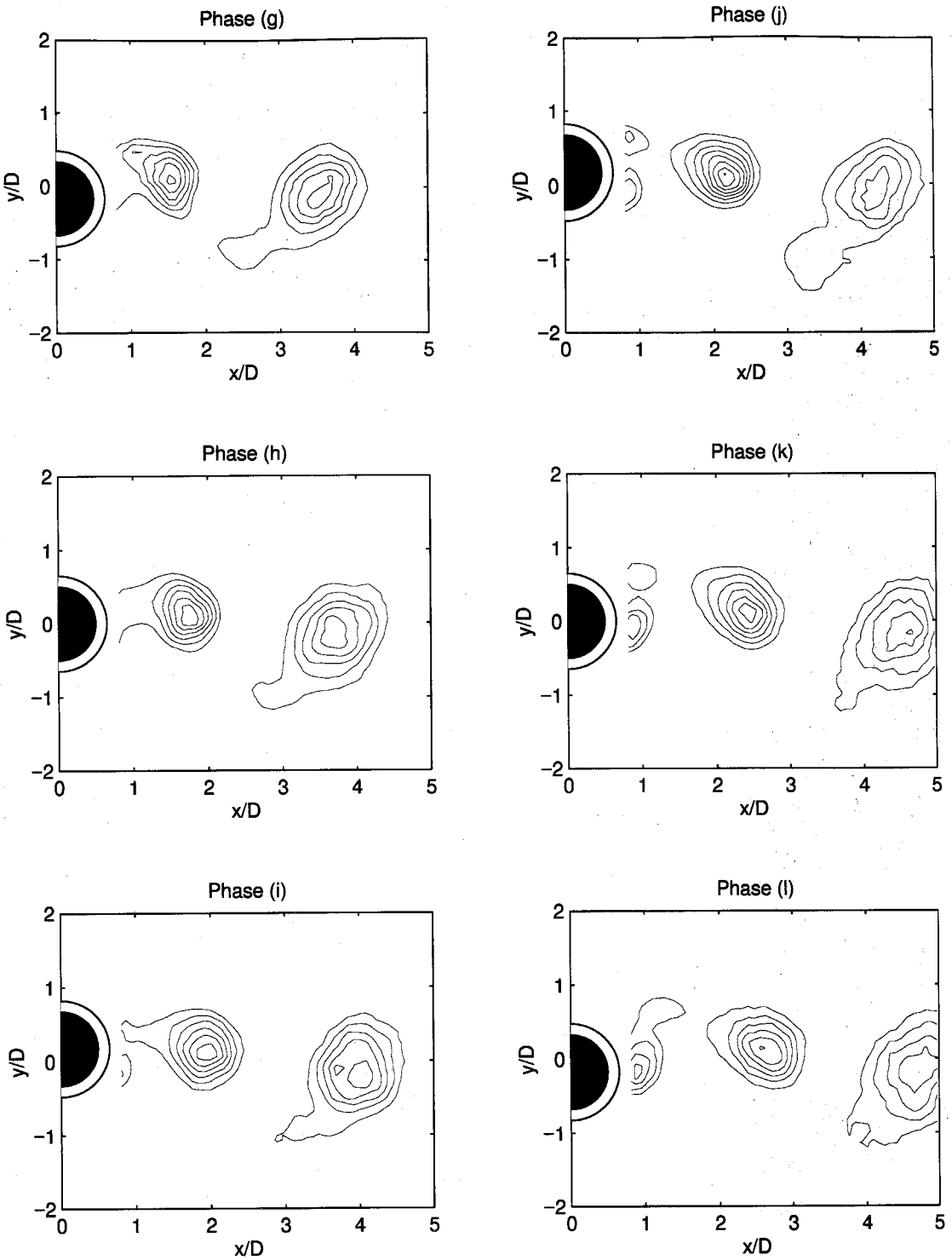


Figure 6.52(b) Sequence of phase averaged temperature field for forced oscillating cylinder at $St_c$=0.51, A/D=0.2 (Case IX). ((<T> - $T_\infty$)/($T_c$ - $T_\infty$)>0.01, contour increment 0.005) The y-displacement of the cylinder corresponding to each letter is shown in Fig. 6.60.

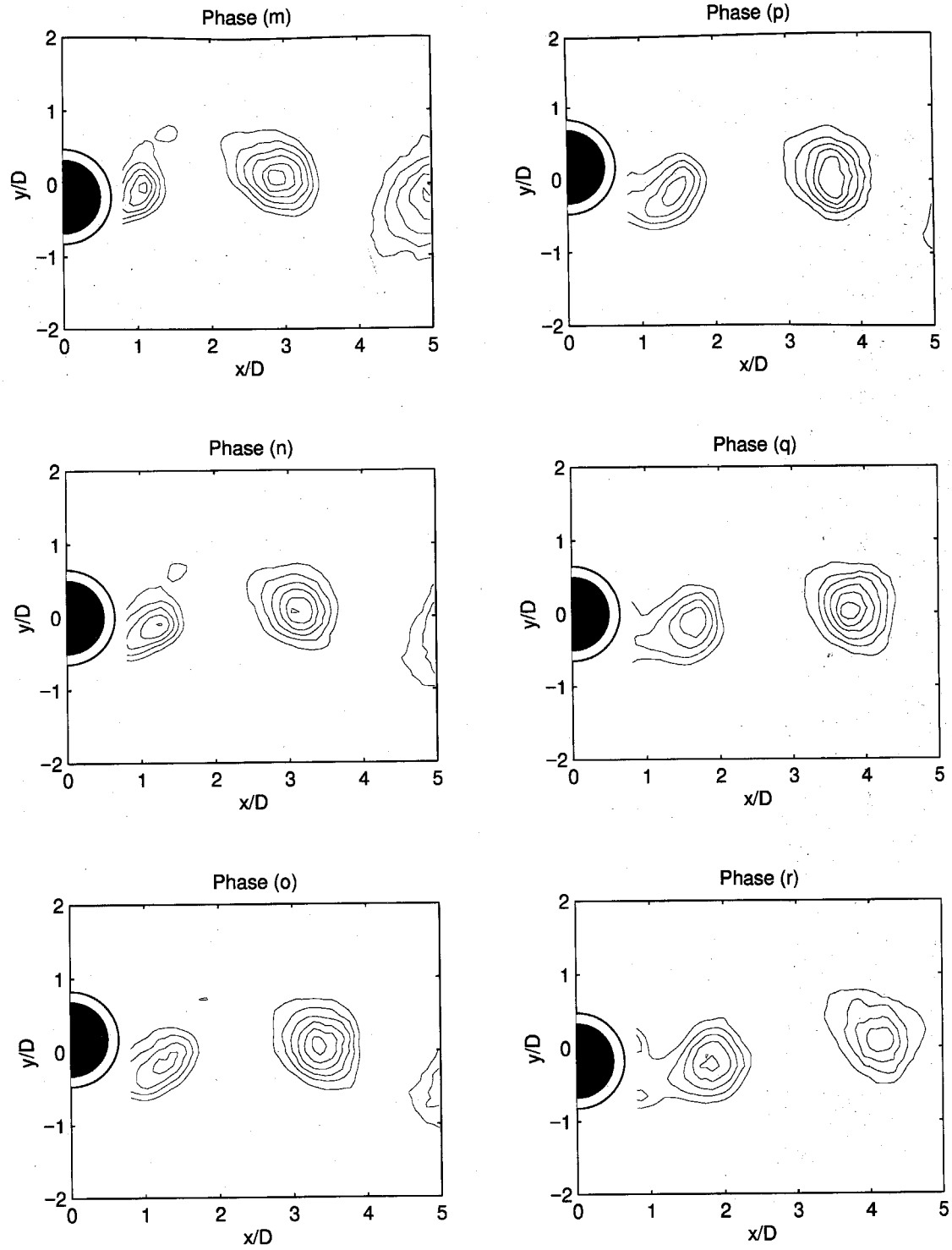


Figure 6.52(c) Sequence of phase averaged temperature field for forced oscillating cylinder at $St_c$=0.51, A/D=0.2 (Case IX). ($(<T> - T_\infty)/(T_c - T_\infty)>0.01$, contour increment 0.005) The y-displacement of the cylinder corresponding to each letter is shown in Fig. 6.60.

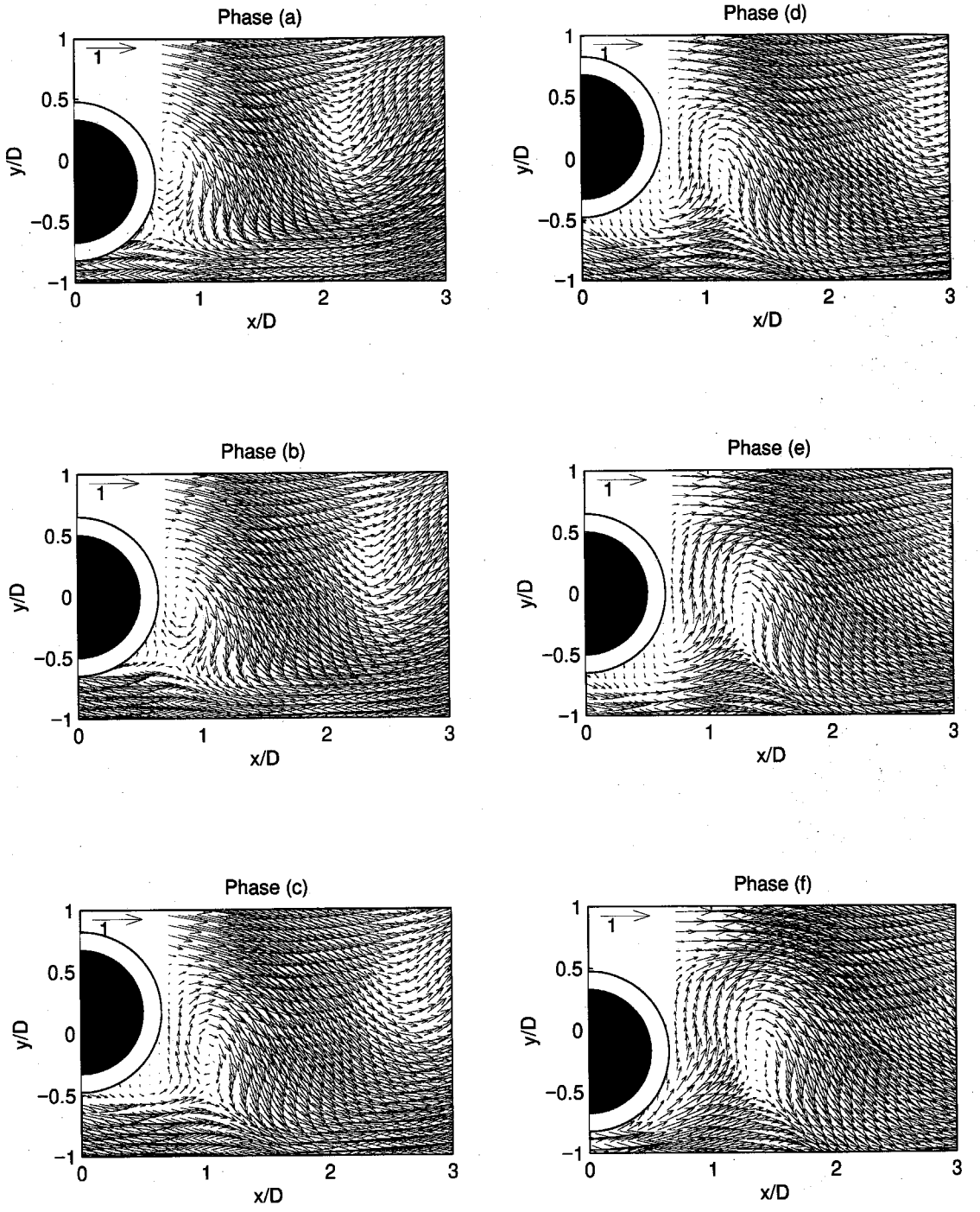


Figure 6.53(a) Sequence of phase averaged velocity field for forced oscillating cylinder at $St_e$=0.51, A/D=0.2 (Case IX). The y-displacement of the cylinder corresponding to each letter is shown in Fig. 6.60.

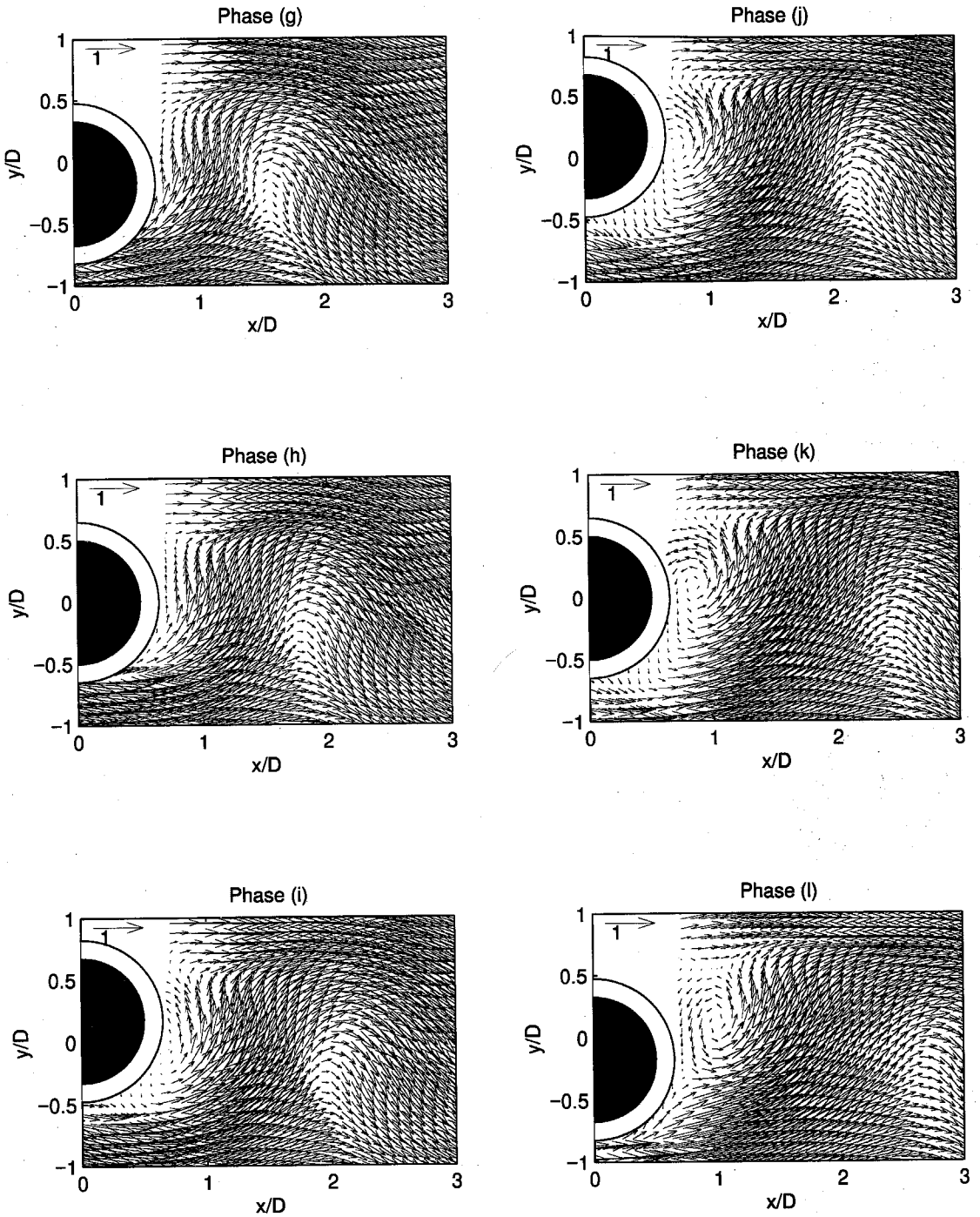


Figure 6.53(b) Sequence of phase averaged velocity field for forced oscillating cylinder at $St_c$=0.51, A/D=0.2 (Case IX). The y-displacement of the cylinder corresponding to each letter is shown in Fig. 6.60.

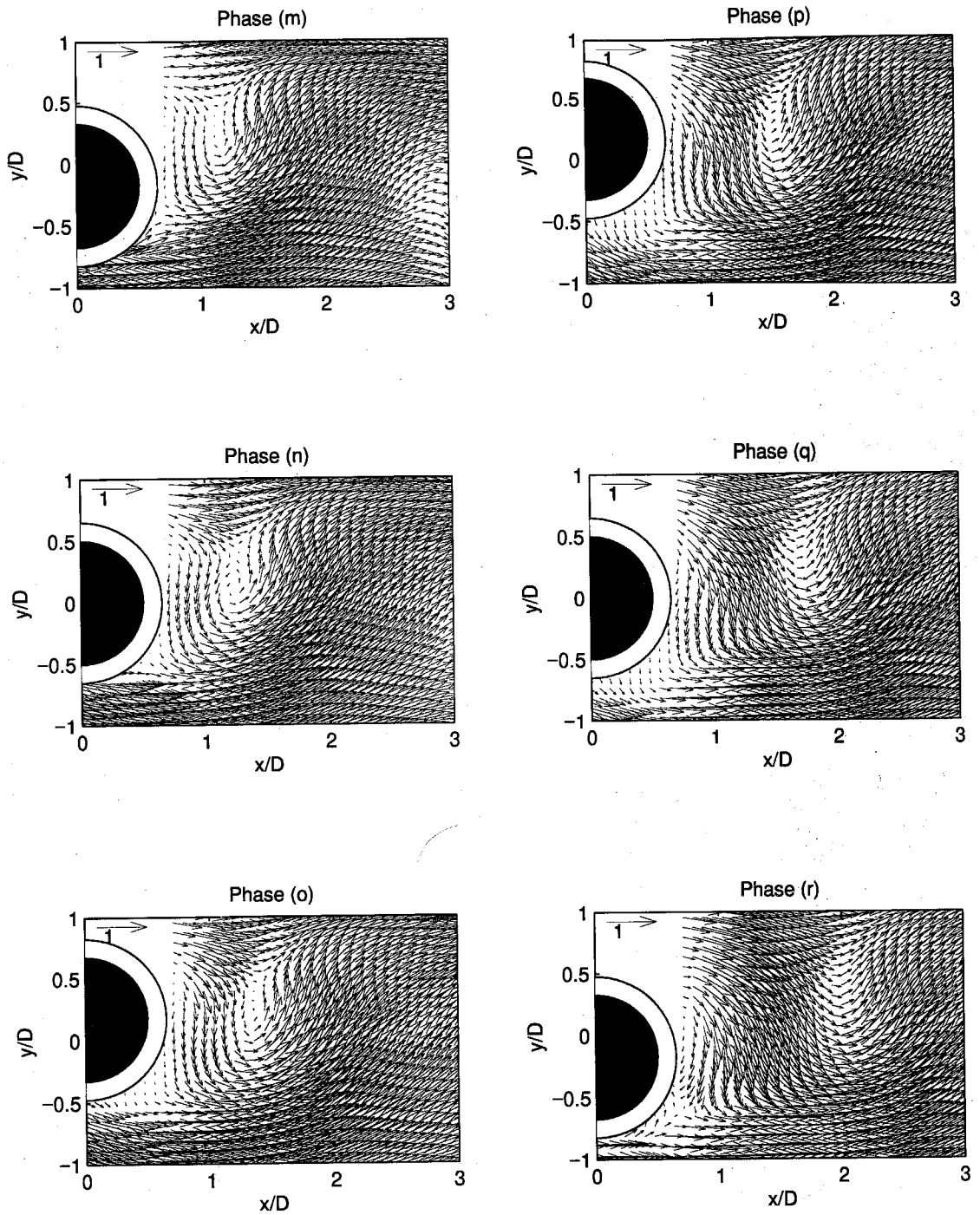


Figure 6.53(c) Sequence of phase averaged velocity field for forced oscillating cylinder at $St_c$=0.51, A/D=0.2 (Case IX). The y-displacement of the cylinder corresponding to each letter is shown in Fig. 6.60.

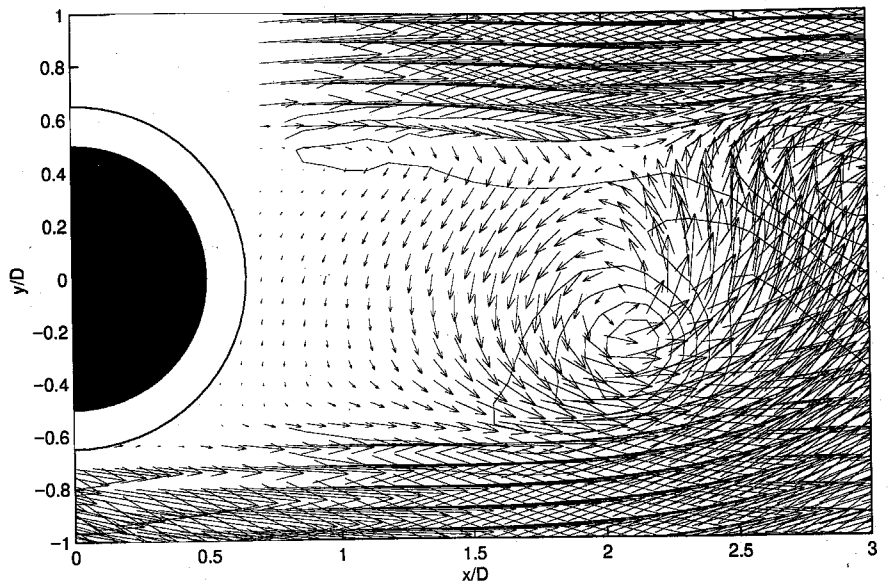


Figure 6.54 Stagnant and non-heat convecting fluid near the base of cylinder for Case (I). The velocity near the base of the cylinder is small as compared to the case of oscillating cylinder (Case II).

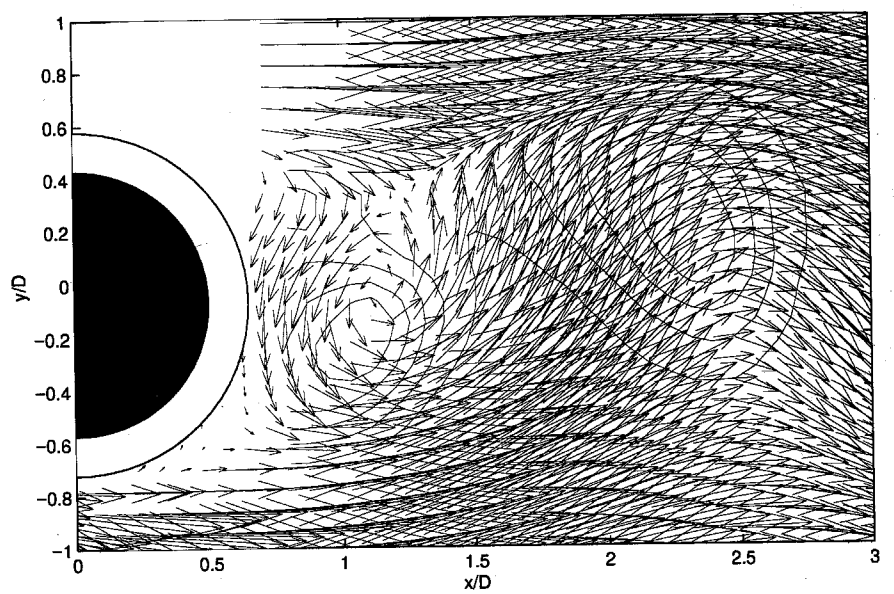


Figure 6.55 Vortices scrubbing away fluid near the base of the cylinder for Case (II). Note the close roll-up of the vortex and the large velocity near the base of the cylinder as compared to Case (I).

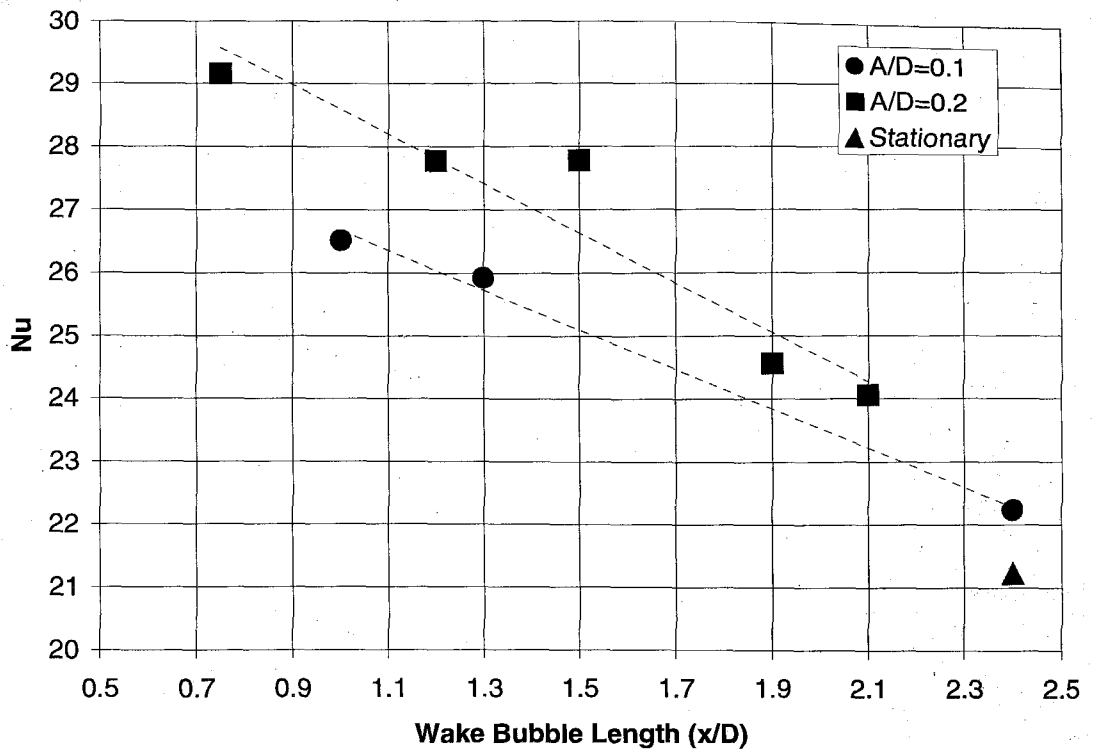


Figure 6.56 Nusselt number versus length of the mean wake bubble (Formation region).

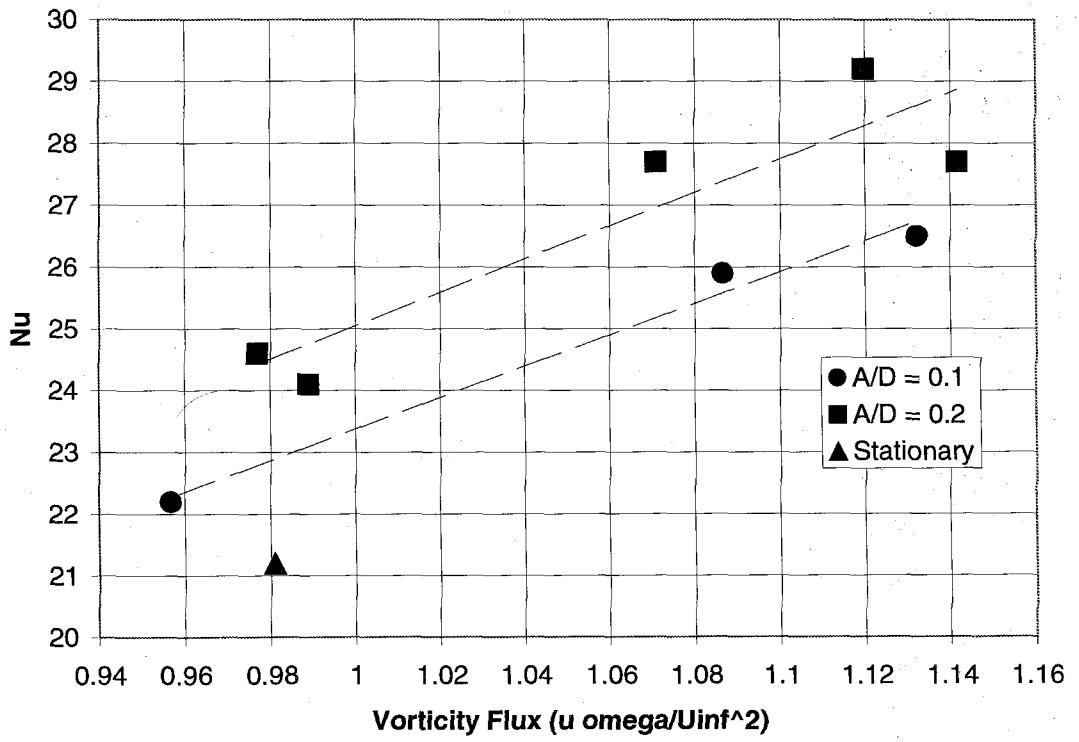


Figure 6.57 Nusselt number versus mean total vorticity flux of the lower shear layer at x/D=0.8.

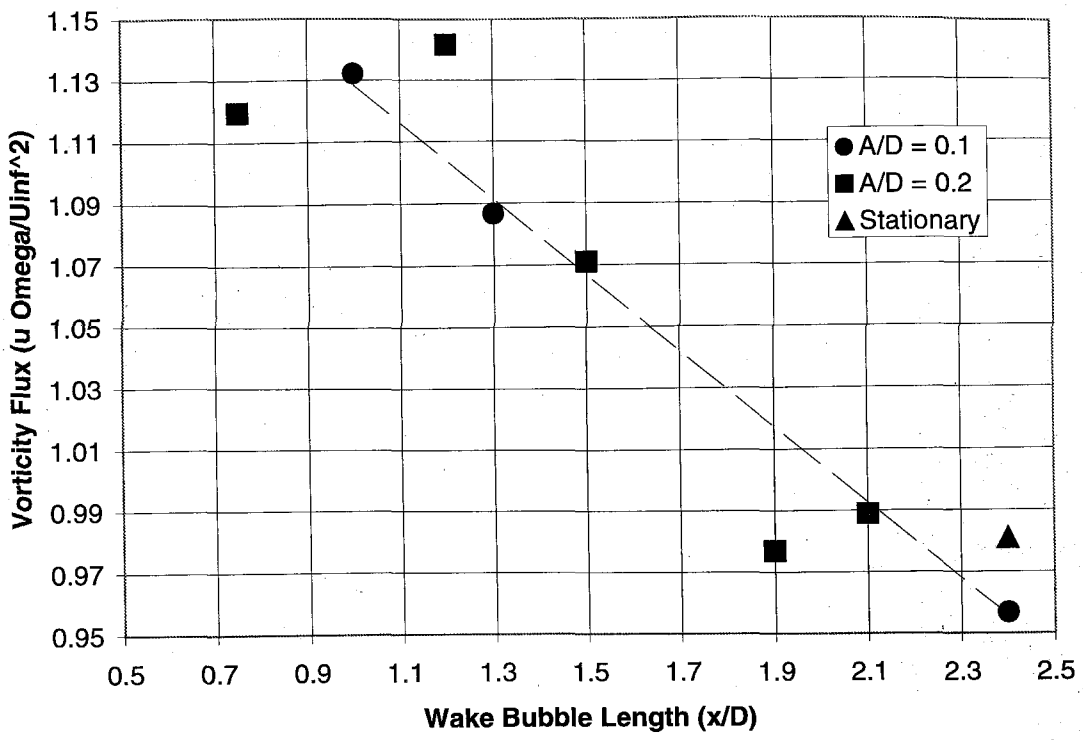


Figure 6.58 Vorticity flux versus the length of the mean wake bubble.

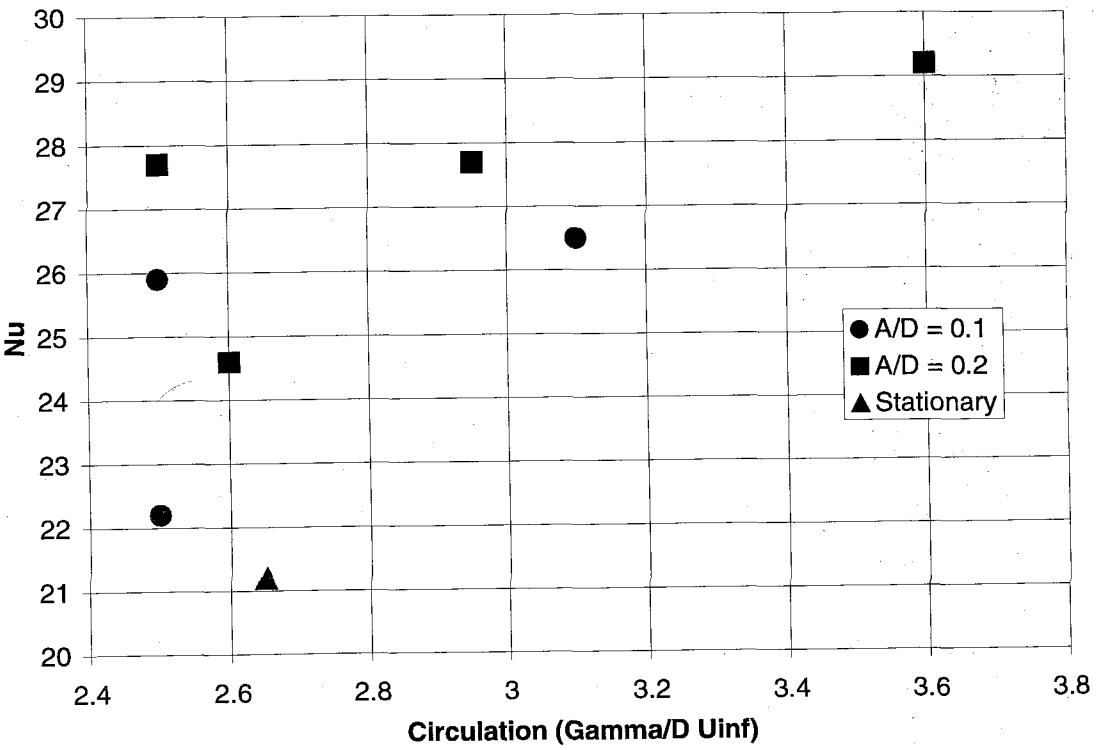


Figure 6.59 Nusselt number versus total circulation of the shed vortices.

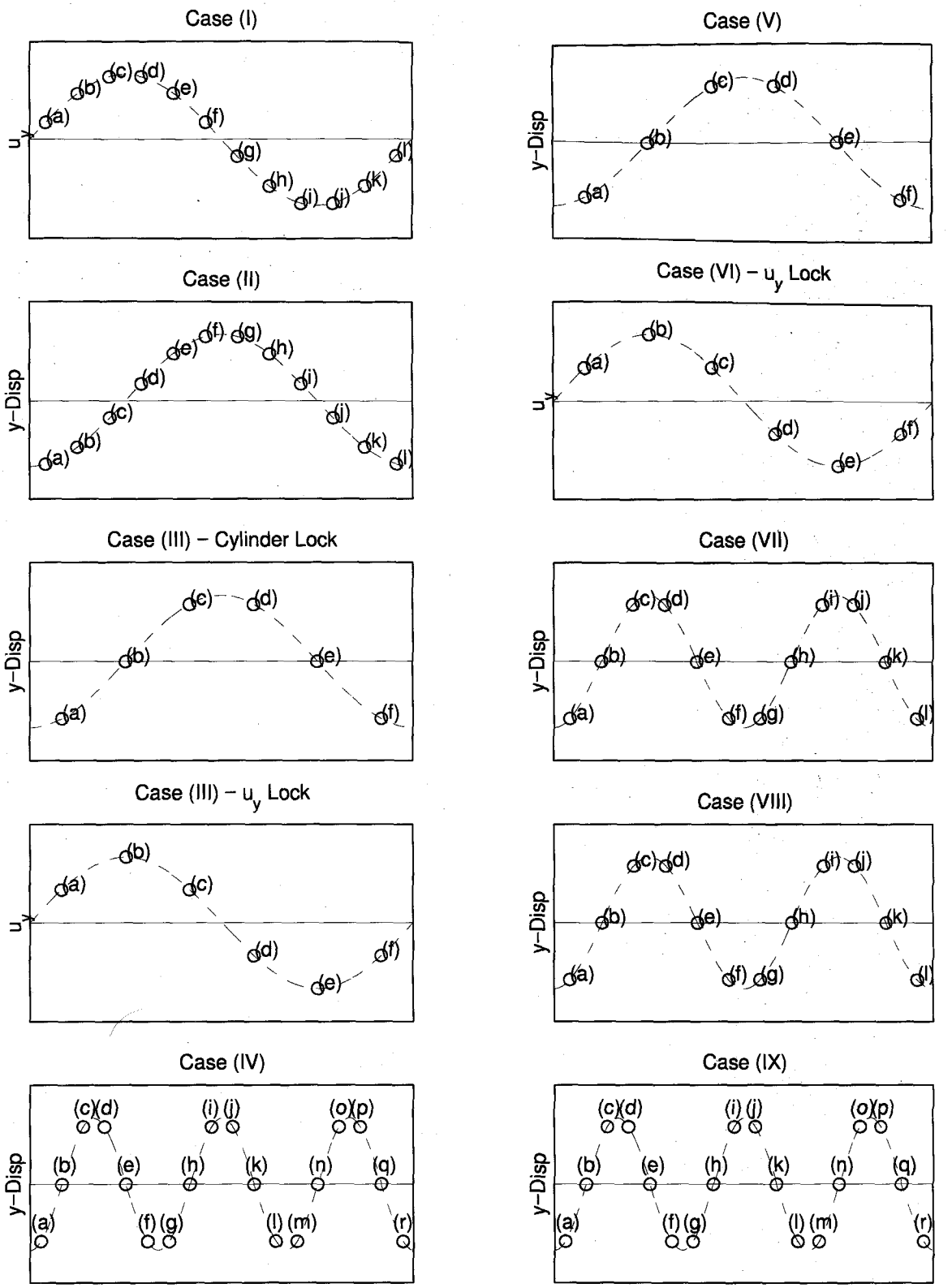


Figure 6.60 $u_y$ value and cylinder displacement corresponding to each letter of phase.

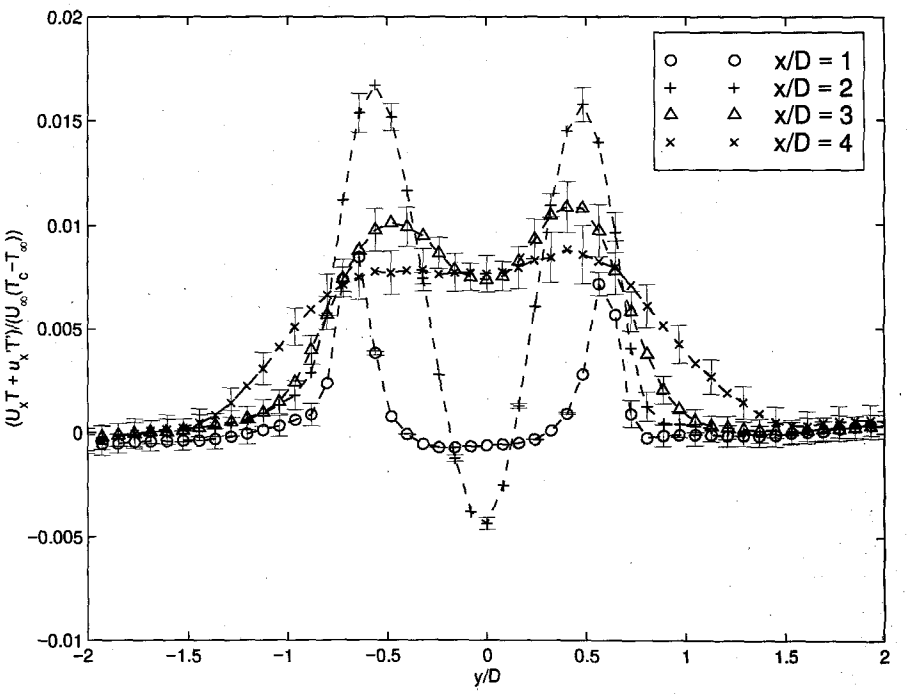


Figure A.1 Profiles of the total heat flux for different downstream locations.

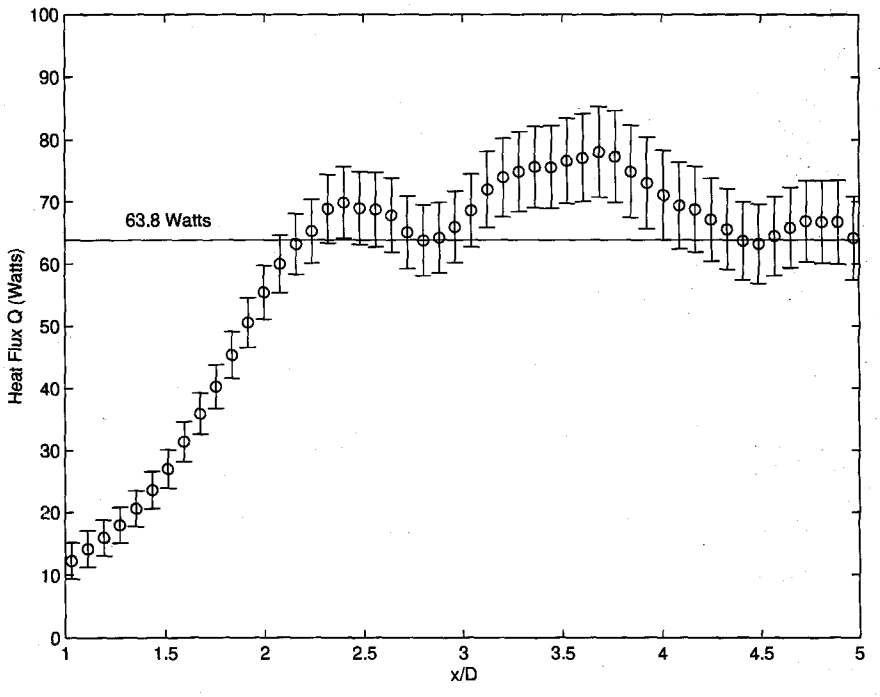


Figure A.2 Integral of the total heat flux for different downstream locations.

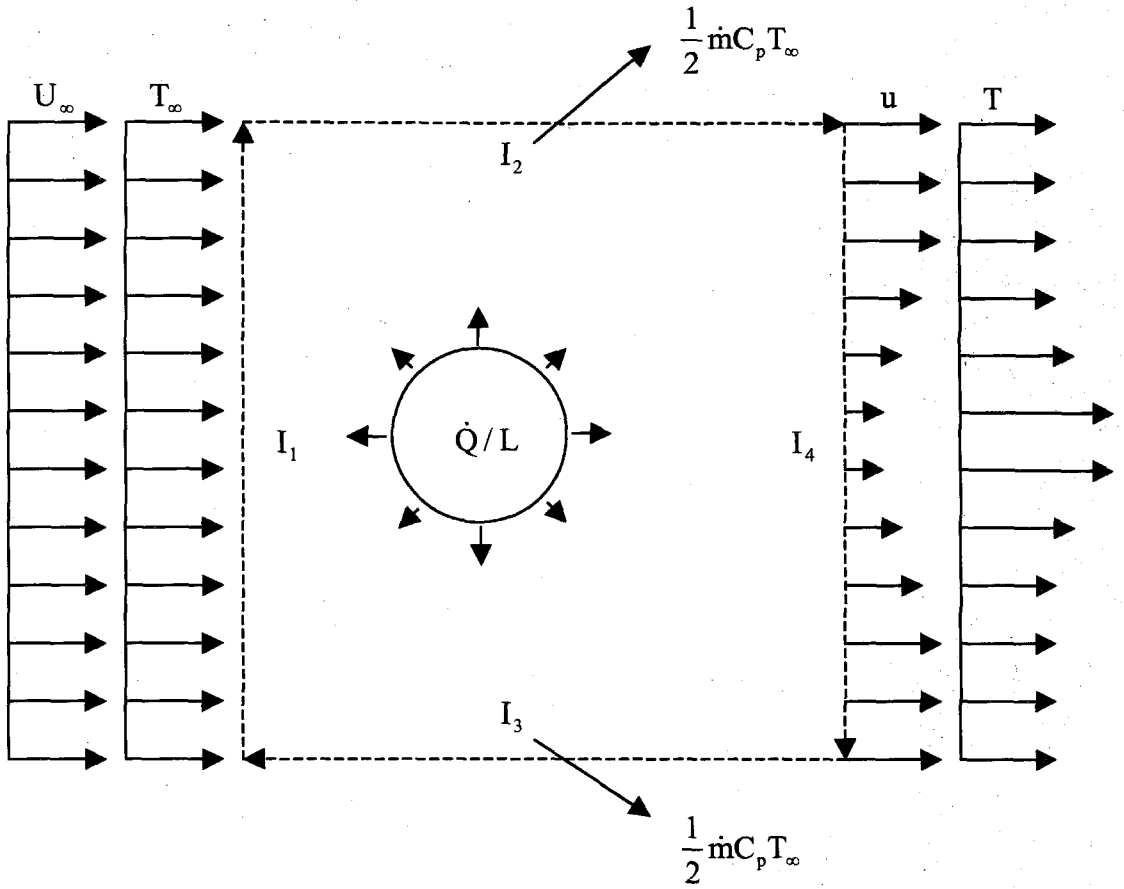


Figure C.1 Contour integral of the heat flux around a stationary control volume containing a heated cylinder.

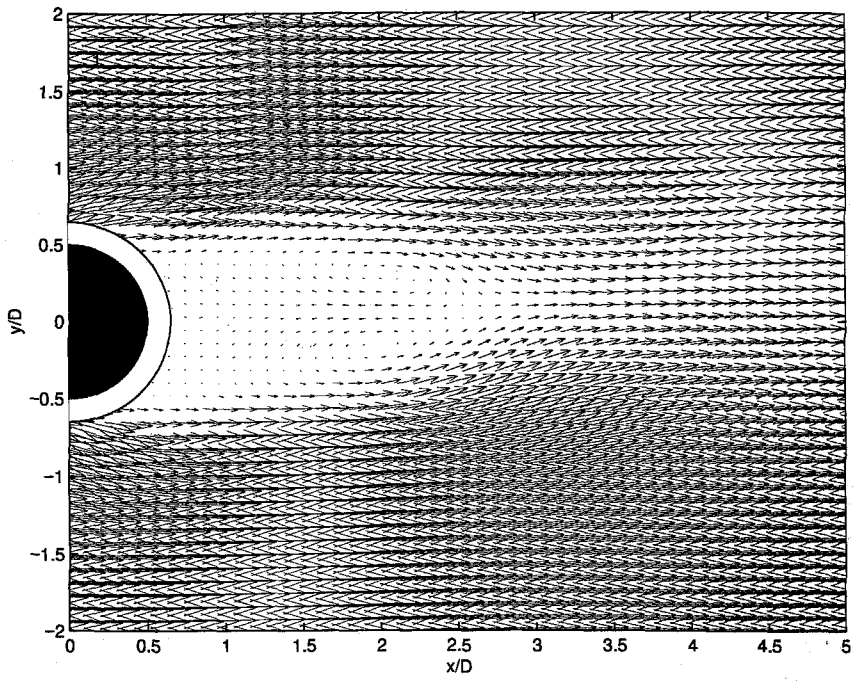


Figure D.1 Mean velocity field of heated cylinder.

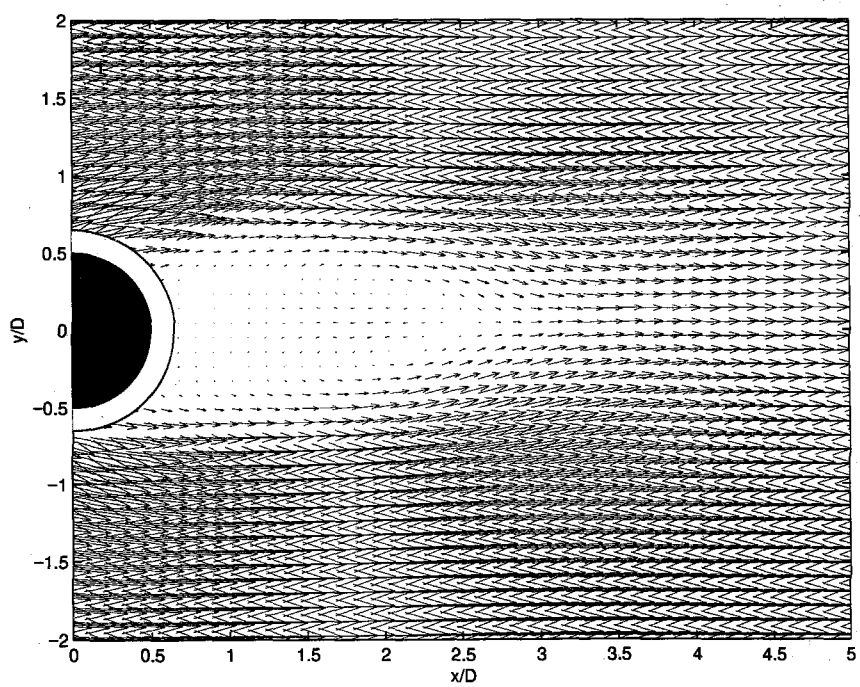


Figure D.2 Mean velocity field of unheated cylinder.

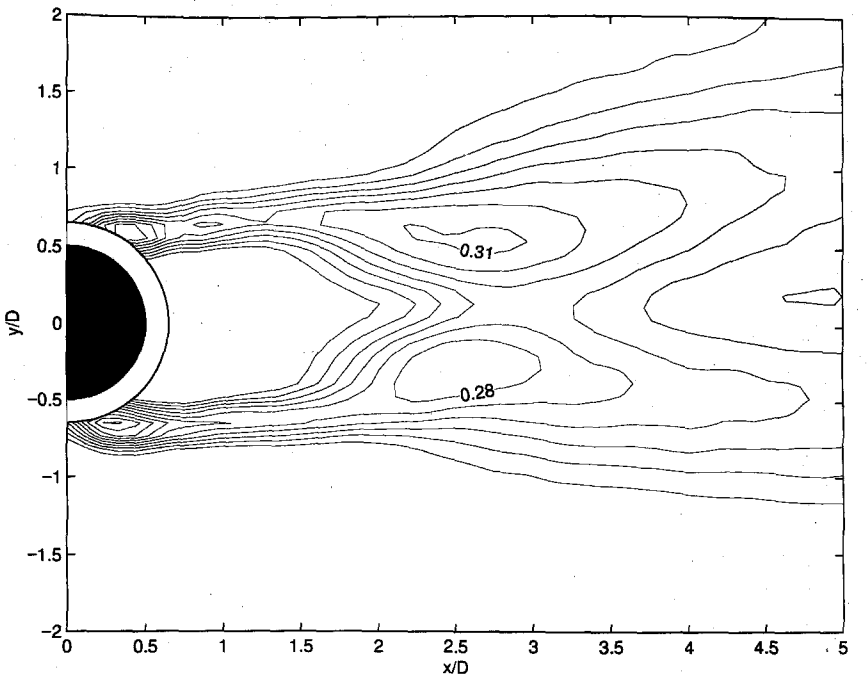


Figure D.3 RMS of $u_x$ of heated cylinder.

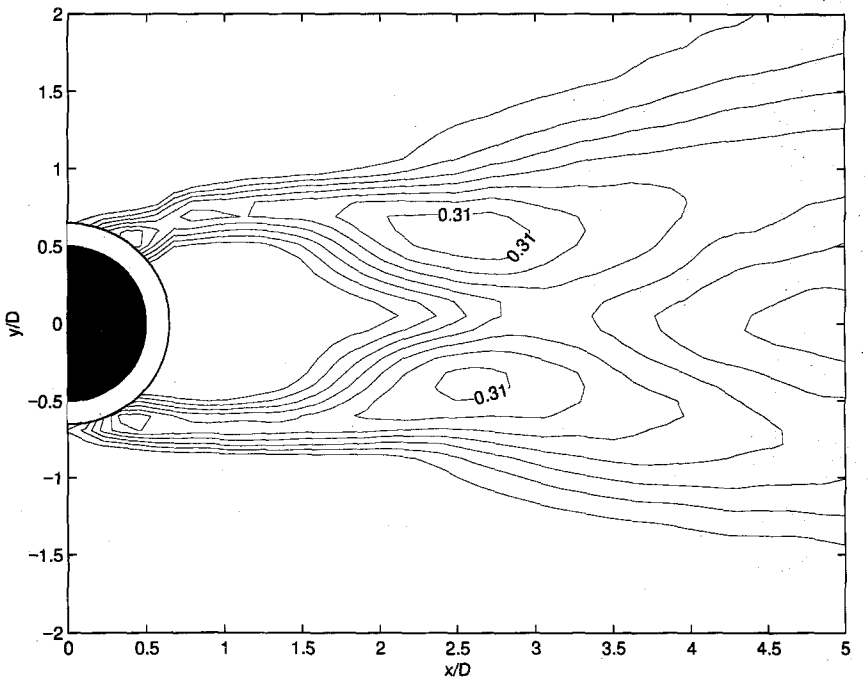


Figure D.4 RMS of $u_x$ of unheated cylinder.

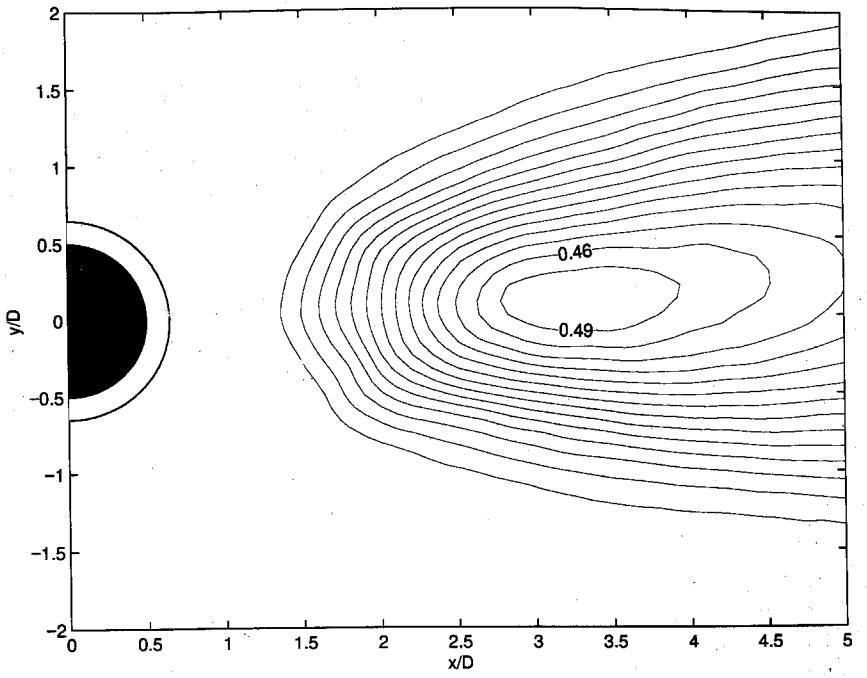


Figure D.5 RMS of $u_y$ of heated cylinder.

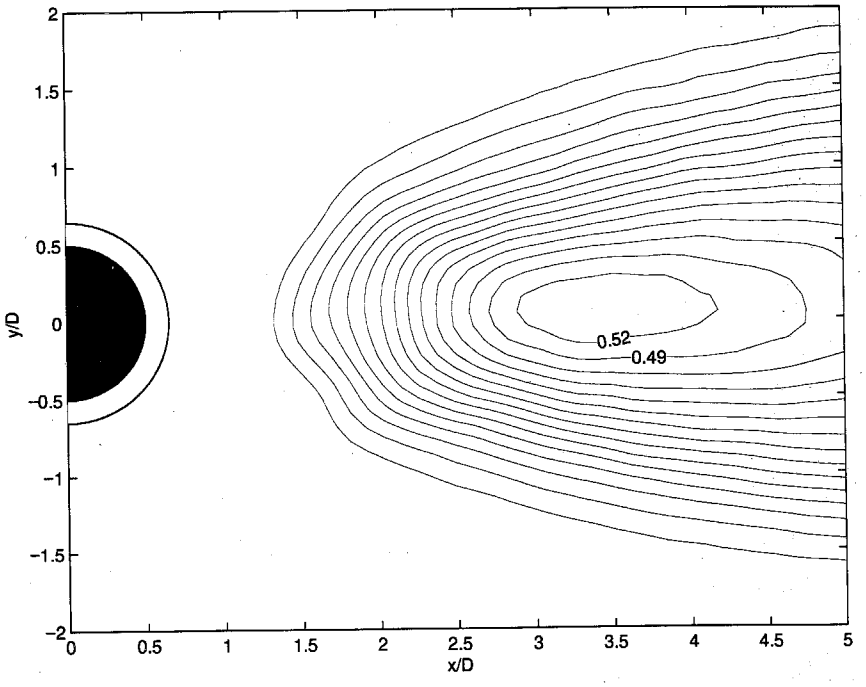


Figure D.6 RMS of $u_y$ of unheated cylinder.